UNIVERSITY OF SOUTHAMPTON

FACULTY OF NATURAL AND ENVIRONMENTAL SCIENCES

School of Ocean and Earth Science

Variability and Transport Methodology of the Atlantic Meridional Overturning Circulation at 26°N

by

Neela Morarji

Thesis for the degree of Doctor of Philosophy

December 2017

UNIVERSITY OF SOUTHAMPTON

ABSTRACT

FACULTY OF NATURAL AND ENVIRONMENTAL SCIENCES SCHOOL OF OCEAN AND EARTH SCIENCE

Thesis for the degree of Doctor of Philosophy

Variability and Transport Methodology of the Atlantic Meridional Overturning Circulation at 26°N

Neela Morarji

The importance of The Atlantic Meridional Overturning Circulation (AMOC) resides in its associated poleward movement of heat (Bryden et al., 2012). Projections of AMOC decline (IPCC, 2013) motivate continued investigation into AMOC transports. The AMOC baroclinic component has been monitored by infrequent hydrographic sections at 24.5°N and, since 2004, twice-daily measurements by the RAPID mooring array at 26°N. AMOC barotropic transports can be determined using bottom pressure data measured each month by the GRACE satellite system since 2003. During the first 4 years of RAPID observations the overturning circulation was, on average, 2.7 Sv stronger than in the subsequent 4 years (Smeed et al., 2014). RAPID transports also reveal downturn events, occurring in 2009-10, 2010-11 and 2013, typified by weak northward Ekman transports and weak southward transports below 3000m. Transports from hydrographic sections show contrasting results, with stronger overturning in 2010 than 2004. Causes for the discrepancy are explored. Hydrographic data are found to be inconsistent with the scale of flow variation captured by current meter absolute transports at the western boundary, an important region of large and highly changeable flow. The RAPID AMOC calculation is altered to include the deep western boundary current, allowing evaluation as to whether it carries a signal relevant to the observed AMOC weakening since 2004. An extra profile of mooring data located 500 km from the western boundary is added to the RAPID AMOC calculation and a shallow reference level is applied in the western region. Results indicate that the strong and highly variable western boundary baroclinic flow is accompanied by a strong and highly variable barotropic response. However, barotropic flow is difficult to observe directly and is therefore substituted with compensation transports that are calculated as a residual to ensure mass balance and distributed uniformly over the basin in the AMOC calculation. GRACE satellite data are employed to estimate deep barotropic transports, particularly below 5000 m. Potential is found for GRACE data to identify longitudinal variation in monthly-averaged barotropic transports across the basin. A future area of investigation lies in uncovering a method of non-uniform distribution of compensation transports, using GRACE-derived bottom pressure, in the RAPID AMOC calculation to fully incorporate the high-frequency western boundary flow and improve knowledge of the deep transports that counterbalance upper ocean changes. This study aims to improve understanding of AMOC measurements and trends at 26°N, which have implications for how the larger circulation is viewed.

Table of Contents

Table of Tables

Table of Figures

Academic Thesis: Declaration Of Authorship

I, Neela Morarji declare that this thesis, titled 'Variability and Transport Methodology of the Atlantic Meridional Overturning Circulation at 26°N', and the work presented in it are my own and has been generated by me as the result of my own original research.

I confirm that:

1. This work was done wholly or mainly while in candidature for a research degree at this University;
2. Where any part of this thesis has previously been submitted for a degree or any other qualification at this University or any other institution, this has been clearly stated;
3. Where I have consulted the published work of others, this is always clearly attributed;
4. Where I have quoted from the work of others, the source is always given. With the exception of such quotations, this thesis is entirely my own work;
5. I have acknowledged all main sources of help;
6. Where the thesis is based on work done by myself jointly with others, I have made clear exactly what was done by others and what I have contributed myself;
7. None of this work has been published before submission.

Signed: .....

Date: .....

Acknowledgements

I would like to acknowledge my PhD advisory panel: David Smeed, Gerard McCarthy and Eleanor Frajka-Williams and Harry Bryden. I am grateful for their support and suggestions with my research. Many thanks to all those involved in my project, your guidance when working through problems is very much appreciated. I would also like to thank the scientists and crews of JC103 and DY040 (particularly Brian King, Elaine McDonagh & Sinhue Torres-Valdes) for such highly enjoyable opportunities to experience work at sea. Thanks go out to my friends (especially Lissette, Lin, Jamie, Steve & Vlad) and family (most notably my mum and uncle for helping me move to Southampton) for their encouragement.

Definitions and Abbreviations

AABW	Antarctic Bottom Water
AAIW	Antarctic Intermediate Water
ADCP	Acoustic Doppler Current Profiler
AMOC	Atlantic Meridional Overturning Circulation
AMV	Atlantic Multidecadal Variability
BPR	Bottom Pressure Recorder
CTD	Conductivity Temperature Depth
Dbar	Decibar
Downturn	AMOC weakening, lasting between 1 and 3 months approximately, typified by northward Ekman transports that are more than 1 standard deviation weaker than the mean and southward LNADW transports that are more than 1 standard deviation weaker than the mean
DSOW	Denmark Straits Overflow Water
DWBC	Deep Western Boundary Current
EK	Ekman
FS	Florida Straits
GRACE	The Gravity Recovery and Climate Experiment
IPCC	Intergovernmental Panel on Climate Change
ISOW	Iceland Scotland Overflow Water
ITCZ	Intertropical Convergence Zone
LNADW	Lower North Atlantic Deep Water
LSW	Labrador Sea Water
MAR	Mid-Atlantic Ridge

MAReast	Mid-Atlantic Ridge eastern flank
MARwest	Mid-Atlantic Ridge western flank
Mascon	Mass concentration block
Millibar	Mbar
MOC	Meridional Overturning Circulation
NADW	North Atlantic Deep Water
NAO	North Atlantic Oscillation
OBP	Ocean Bottom Pressure
RAPID	RAPID/MOCHA/WBTS mooring array
RAPID4820	RAPID geostrophic data with reference level 4820 dbar
RAPID1000|4820	RAPID geostrophic data with western boundary reference level 1000 dbar and main basin reference level 4820 dbar
Ref	Reference level
RMS	Root Mean Square
SD	Standard Deviation
SLSW	Shallow Labrador Sea Water
SST	Sea Surface Temperature
Sv	Sverdrup
TPUD	Transport Per Unit Depth
UMO	Upper Mid-Ocean
UNADW	Upper North Atlantic Deep Water
WBW	Western Boundary Wedge

Chapter 1: Introduction

The Atlantic Meridional Overturning Circulation (AMOC) is a system of northward warm water flow in the top ~1000 m and southward return flow of cold, deep water. The AMOC is a key component of the global overturning circulation but there are concerns over AMOC weakening (Robson et al., 2014). The AMOC plays a vital role in maintaining Western Europe's moderate climate due to its associated large heat transfer to high northern latitudes (Vellinga and Wood, 2002). A weak AMOC will influence the regional and global climate (McCarthy et al., 2017).

The AMOC is a complex system, its trends and variability are subjects of ongoing research. Observational data, such as hydrographic surveys and the RAPID array, have improved our knowledge of the AMOC. The RAPID array across the basin at 26°N, deployed in 2004, delivers our best measurement of the AMOC (Cunningham et al., 2007; McCarthy et al., 2015a). A latitude of 26°N is a convenient and salient choice for such an array for four reasons: it coincides with the location of several hydrographic surveys; the Gulf Stream is confined to the Florida Straits allowing separate measurement; it is near the latitude of maximum meridional heat transport; the western boundary wall is relatively steep allowing measurement of ocean properties close to the boundary (Rayner et al., 2011). The AMOC was observed to weaken by 30% in strength for ~18 months around winter 2009-10 (McCarthy et al., 2012). Observations of AMOC weakening, of magnitude 0.5 ±0.2 Sverdrups (Sv) per year over the period 2002-2012 (Smeed et al., 2014), motivate ongoing investigation into its variability.

The goals of this study are to improve understanding of ongoing AMOC measurements and the methodological variations of its calculation. The work presented here has three themes, covered by three chapters. The first theme is a detailed investigation of the calculation methodology employed for hydrographic transports at 25°N from 2004, where the hydrographic method of calculation is evaluated against that of the RAPID method. Chapter 3 investigates and discusses RAPID data and an alternative methodology to represent variability of the Deep Western Boundary Current (DWBC) within the internal transports and the extent to which this alters the MOC. Chapter 4 presents estimates of external transports using data from the Gravity Recovery and Climate Experiment (GRACE) to quantify

variation in the deep layers and considers their inclusion in the calculation of the RAPID MOC. Chapter 5 discusses and summarises the main findings of this study.

1.1 The Atlantic Meridional Overturning Circulation

The Atlantic Meridional Overturning Circulation (AMOC) is characterised by:

- At 26°N in the Atlantic, northward Ekman flow within the surface layer, the Antilles Current and Florida Straits flow, which may recirculate southwards in the gyre or contribute to the net northward flow of relatively warm, saline water to high latitudes (McCarthy et al., 2015a);
- Buoyancy loss at high northern latitudes leading to North Atlantic Deep Water (NADW) formation and deep southward movement of NADW predominantly along the Deep Western Boundary Current (DWBC) (Bryden et al., 2005b);
- In the Southern Ocean, wind-driven upwelling fed by water-masses that include NADW (Marshall and Speer, 2012);
- Formation of Antarctic Bottom Water (AABW) and Antarctic Intermediate Water (AAIW) that are carried northward (Talley, 2013);
- Vertical mixing of heat downward within the ocean interior and the gradual rise of deep water-masses to the surface (Polzin et al., 1997);
- Northward movement of heat throughout the Atlantic (Wunsch & Heimbach, 2013).

A diagram of global ocean circulation, with focus on the Atlantic, is shown in Figure 1.1. An illustration of the AMOC north of 26°N, indicating the shallow currents and deep southward flow, can be found in Figure 1.2.

Understanding AMOC variability is important due to the wide-ranging ramifications of a weakening (Intergovernmental Panel on Climate Change (IPCC), 2013), including a change in the corresponding northward movement of heat that moderates the climate of North-West Europe (Talley, 1999; Bindoff & McDougall, 1994; Bryden et al., 2012). The AMOC has traditionally been viewed as a predictor of interannual and decadal climate variability (www.rapid.ac.uk; Srokosz et al., 2012; Yeager and Robson, 2017). Long-term climate variability is relevant due to associated impacts, such as ocean acidification, drought and extreme weather events (IPCC, 2013). There are links between the variable inflow of warm upper ocean waters to high latitudes and mass loss from the Greenland Ice Sheet (Rignot and Kanagaratnam 2006; Holland et al. 2008; Straneo & Heimbach,

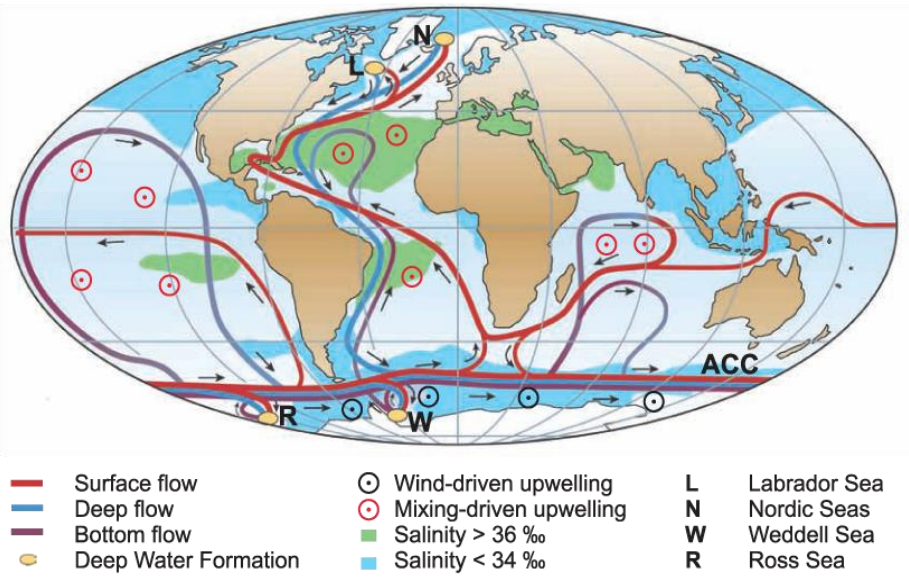

Figure 1.1: Simplified schematic of the global overturning circulation system. In the Atlantic, warm and salty waters flow northward into the Labrador and Nordic Seas before becoming NADW. Deep waters formed in the Southern Ocean are denser than NADW and thus spread to greater depth. Areas of mixing-driven upwelling are widespread relative to localised deep water formation. Along the Antarctic Circumpolar Current (ACC) wind-driven upwelling is intense. From Kuhlbrodt et al. (2007).

2013), as well as the reduction of Arctic sea ice cover (Serreze et al. 2007), leading to sea-level rise. Flooding, drought and food shortages could lead to human migration, associated with increasing political instability and international conflict (Reuveny, 2007; Black et al., 2011). Smeed et al. (2018) report that the AMOC has been slowing since 2008, relative to the period spanning 2004 to 2008, which coincides with a shift in North Atlantic Sea Surface Temperatures (SSTs). This SST shift alters ocean-atmosphere heat exchange and is a result of a reduction in northward Atlantic Ocean heat transport. SST pattern changes resulting from AMOC variability are important on varying time and spatial scales (McCartney, 1997; Marshall et al., 2001; Buckley & Marshall, 2016).

For 14 months covering the winter of 2009–10, an AMOC weakening of 30% occurred, reducing northward ocean heat transport across 25°N by 0.4 PW (McCarthy et al., 2012; Bryden et al., 2014). A divide was found at 25°N, where ocean waters in the top 1000 m were colder above this latitude due to a 5.6 Sv reduction in net warm water flow (Bryden et al., 2014). Below the 25°N latitude band, upper ocean waters were warmer owing to reduced northward heat transport (Bryden et al., 2014). This SST pattern resulted in an unprecedented low

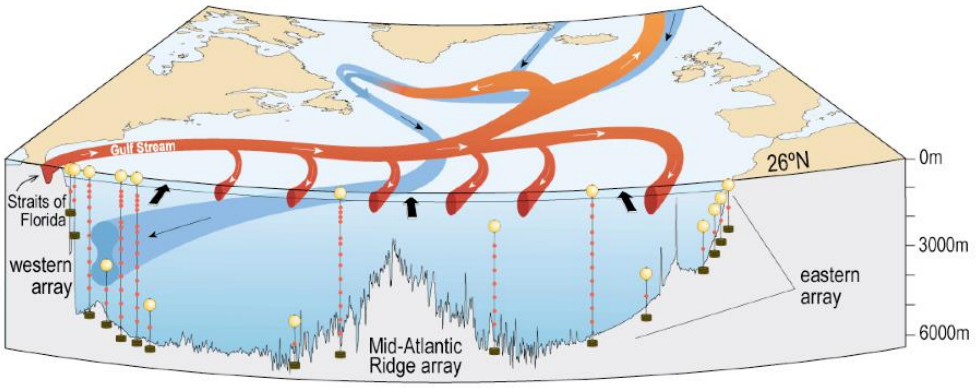

Figure 1.2: Representation of the North Atlantic MOC. The Gulf Stream / North Atlantic Current and subpolar and subtropical gyres (red) as well as the western boundary deep return flow (blue) are indicated. Near-surface wind-driven Ekman transports (broad black arrows) arising from the zonal wind stress are also indicated. The RAPID mooring array is illustrated. Moorings are concentrated at the four boundaries: east, west and either side of the MAR. Modified figure by Neil White and Lisa Bell, CSIRO.

negative North Atlantic Oscillation (NAO), with associated harsh winter weather across North-West Europe (Osborn, 2011; Bryden et al., 2014) and greater European summer precipitation (Sutton & Dong, 2012; Folland et al., 2009). South of 25˚N, across the tropical Atlantic, warmer upper ocean waters provide energy to stronger summer hurricane seasons (Elsner et al., 2008; Goni et al., 2009; Sutton and Hodson, 2007; Bader et al., 2011; Wang et al., 2012; Dong et al., 2013). Thus, anticipation of the SST patterns that follow AMOC changes comes with the potential for improving seasonal forecasts of Atlantic hurricanes and North-West European extreme weather events (Keenlyside et al., 2008; Duchez et al., 2016).

Two months after the 2009-10 AMOC weakening of 30%, a 10 cm sea-level rise in New York was recorded (Goddard et al., 2015), with societal and economic impacts due to coastal erosion, flooding and groundwater contamination. This increase in sea-level was related to both the weakened AMOC and negative NAO phase (Goddard et al., 2015). The sea-level gradient along the USA east coast reflects both gyre and AMOC transport variation (Ezer, 2013; McCarthy et al., 2015b). McCarthy et al. (2015b) utilise observational data to show that USA east coast sea-level differences serve as a guide to ocean circulation changes that act as a precursor to Atlantic Multidecadal Variability (AMV) changes. Proxy SST data spanning multiple centuries also indicate that AMOC induced SST patterns are a

driver for the AMV (Delworth and Mann, 2000; Delworth et al., 2007). Tree-ring reconstructions of the AMV show a connection between North Atlantic terrestrial climate and Atlantic SST patterns (Gray et al., 2004). Arctic sea ice cover appears linked to the NAO on interannual to decadal timescales (Visbeck et al., 2003; Bader et al., 2011; Straneo & Heimbach, 2013) and the AMV on multidecadal timescales (Miles et al., 2014; Straneo & Heimbach, 2013). AMV fluctuations are also linked to both drought and flooding in the USA (Enfield et al., 2001; McCabe et al., 2004; Delworth et al., 2008).

A weakened AMOC alters the cross-equatorial pressure gradient and modifies the position of the Intertropical Convergence Zone (ITCZ) southward in the tropical Atlantic (Hastenrath & Greischar, 1993; Black et al., 1999; Peterson et al., 2000), inducing a host of climate impacts. Levels of rainfall increase for the Australian-Indonesian and South American (northeast Brazil) monsoon systems correlate to the SST pattern of a cold AMV phase that displaces the ITCZ southward (Servain, 1991; Hastenrath & Greischar, 1993; Marshall et al., 2001; Mohtadi et al., 2016). Whereas, a southward ITCZ shift corresponds to dryer conditions for the North African (Sahel) and South Asian (India) monsoon regions (Ward, 1999; Feng & Hu, 2008; Mohtadi et al., 2016). Atlantic SST can also influence the tropical Pacific, with implications for the El Ninõ Southern Oscillation (Enfield et al., 2001; Polonsky et al., 2004; Kang et al., 2014), another driving mechanism of climate variability.

A continually weakening AMOC will likely yield shifts and declines in marine ecosystems due to reduced upwelling of nutrient-rich deep water and reduced upper ocean nutrient concentrations (Schmittner, 2005; Palter & Lozier 2008; Kuhlbrodt et al., 2009). The present warming climate (relative to the 1960's and 1970's) has already moved zooplankton groups northward to dominate places such as the North Sea (Beaugrand et al., 2002). The outcome of this is a move of fish species, as well as a reduction of boreal species accompanied by an increase in temperate species (Beaugrand et al., 2002; Kuhlbrodt et al., 2009). In the event of abrupt change, marine organisms would be left without the requisite time to adapt and the results would be difficult to predict (Ottersen and Stenseth, 2001).

Nearly 50% of anthropogenic CO_2 is taken and stored by the ocean (Sabine et al., 2004; Waugh et al., 2006), reducing the effects of greenhouse gas emissions. A weakened AMOC affects the North Atlantic sink for CO_2 (Schuster and Watson, 2007). The Atlantic is the biggest global deep store of anthropogenic carbon (Sabine et al., 2004; Takahashi et al., 2009) due to the northward upper flow of

the Meridional Overturning Circulation (MOC) (Steinfeldt et al. 2009). AMOC changes could alter air-sea CO_2 flux due to the change in northward water flow, though interannual variability is great and thus the degree of influence is difficult to quantify (Schuster and Watson, 2007; Watson et al., 2009). Understanding variability of the ocean CO_2 sink and its future change is vital to estimating the rate of ocean acidification and the effect on marine life (Metzl et al., 2010; Bates, 2012). Paleo-climate reconstructions confirm the importance of AMOC variations with regard to climate change (McManus et al., 2004; Buizert et al., 2014).

1.2 AMOC driving mechanisms at 26°N

The AMOC is subject to two principle drivers, buoyancy forcing and wind forcing (Kuhlbrodt et al., 2007). Variability of these drivers affects MOC estimates.

A weak AMOC is generally associated with weak convection (Gelderloos et al., 2012; Häkkinen and Rhines, 2004). Deep water formation processes set the interhemispheric shape and strength of the overturning cell (Kuhlbrodt et al., 2007). The DWBC is the principal conduit of deep water-mass changes to 26°N (Molinari et al., 1998; Atkinson 2012), though this is countered by the notion that southward flow is driven by eddies (Lozier, 2010). Water-mass analysis can aid in determination of advection timescales and pathways, though this is obscured by eddy mixing, entrainment and interior recirculation (Sebille et al., 2011). Understanding the degree to which water-masses are changing will be essential in gauging how the AMOC could alter under continued atmospheric warming (Cronin & Sprintall, 2009; Anderson et al., 2009; Cunningham et al., 2013).

Whilst deep convection occurs in small regions, wind-driven changes occur across larger regions (Talley, 2003). Wind forcing imparts surface momentum resulting in Ekman transport and upwelling/downwelling, which drive the ocean gyres (Cronin & Sprintall, 2009). Sverdrup transport resulting from changeable surface wind stress curl is complicated by factors such as basin topography and eddies (Wunsch & Roemmich, 1985). Wind-driven circulation and other processes that change the zonal integral of meridional transport, such as eddies at the basin boundaries, have an impact on the AMOC. Due to the seasonality of the winds, upwelling/downwelling and associated heave of isopycnals also display seasonality, which leads to density change within a particular depth range that isn't linked to salinity or temperature (Bindoff & McDougall, 1994). Wind stress curl can generate Rossby waves that can strengthen the geostrophic flow (Zhao &

Johns, 2014). Wind forcing also results in Ekman flow that is counterbalanced by transports in the deep ocean due to density changes at the western boundary (Frajka-Williams et al., 2016).

From an energy perspective it has been argued that, unlike wind forcing, buoyancy fluxes cannot drive the AMOC because they merely set ocean stratification (Munk & Wunsch, 1998). However, buoyancy plays a major role in setting the properties of the abyssal ocean but the extent to which this affects the AMOC is difficult to gauge (Johnson et al., 2008; Cronin & Sprintall, 2009). The weight of each driving mechanism is a matter of timescale. Polo et al. (2014) find that AMOC change resulting from buoyancy forcing is important for interannual and decadal timescales. Wind forcing affects the AMOC on subannual timescales, through processes such as coastal upwelling and Ekman transports, as well as interannual and decadal timescales, through processes such as the excitation of Rossby waves (Polo et al., 2014).

Understanding AMOC driving mechanisms is important because of the differing sensitivities of the AMOC to varying surface forcing, thus climate change will alter the AMOC in many different ways. Variability of these driving mechanisms may hide or enhance different aspects of anthropogenic warming, adding further uncertainty to the attribution of AMOC variation to man-made or natural warming.

1.3 Measuring the AMOC at 26°N

Mid-ocean flow is composed of two parts: depth-dependent geostrophic baroclinic flow created by density variations (as captured by hydrographic data, for example) and barotropic flow, caused by the tilt of pressure surface such that the velocity is depth-independent. Zonal integrated geostrophic per-unit-depth internal transports are here defined as the transports calculated using vertical profiles of density relative to a reference level plus any absolute transports measured using current meters. Zonal integrated bottom-pressure differences between vertical basin profiles provide the depth-independent barotropic external transports. External transports are combined with internal transports, Ekman transports and Florida Straits transports to compute AMOC variability. An alternative approach to computing AMOC variability is to substitute the external transports for compensation transports, which are calculated as a residual such that mass is conserved (e.g. Kanzow et al., 2007; Kanzow et al., 2010; Frajka-

Williams et al., 2016). The MOC is the net flow above the streamfunction maximum at approximately 1000 m depth.

Herein, AMOC transports at 26°N are composed of four parts: Ekman transports, Gulf Stream transports, internal transports and compensation transports. The sum of the internal transports and compensation transports are referred to as mid-ocean transports. Ekman transports are calculated from satellite measurements of wind stress. Near-surface wind-driven Ekman transports at 26°N display no consistent annual or semi-annual cycle and the seasonal cycle is overridden by fluctuations of the Azores high and the NAO (Atkinson et al., 2010). Gulf Stream transports, hereafter referred to as Florida Straits transports (the region to which it is confined at 26°N), are estimated by means of the induced voltage of submerged telephone cables and calibrated with data gained from hydrographic sections (Larsen, 1992; Baringer and Larsen, 2001; Meinen et al., 2010). Florida Straits transports show an annual cycle as a result of meridional wind stress that is overridden by internal ocean variability (Atkinson et al., 2010). Internal geostrophic transports are computed from the difference in full depth density profiles across the Atlantic relative to a level of no motion, with the addition of absolute transports from current meters where available. Compensation transports are added uniformly across the basin to ensure zero mass balance of internal transports added to Florida Straits transports and Ekman transports. Zero mass balance is a reasonable assumption owing to the inputs and outputs for the, essentially closed, basin being approximately equal. Kanzow et al. (2007) find that the volume for the North Atlantic is conserved above 26°N over short timescales (a few days). Furthermore, Kanzow et al. (2007) calculate external transports with in-situ bottom pressure data to find good agreement with the compensation component.

Density profiles are derived from temperature and salinity at discrete pressure levels. Both the hydrographic sections and RAPID array provide data for internal transports. GRACE OBP measurements provide data for external transports.

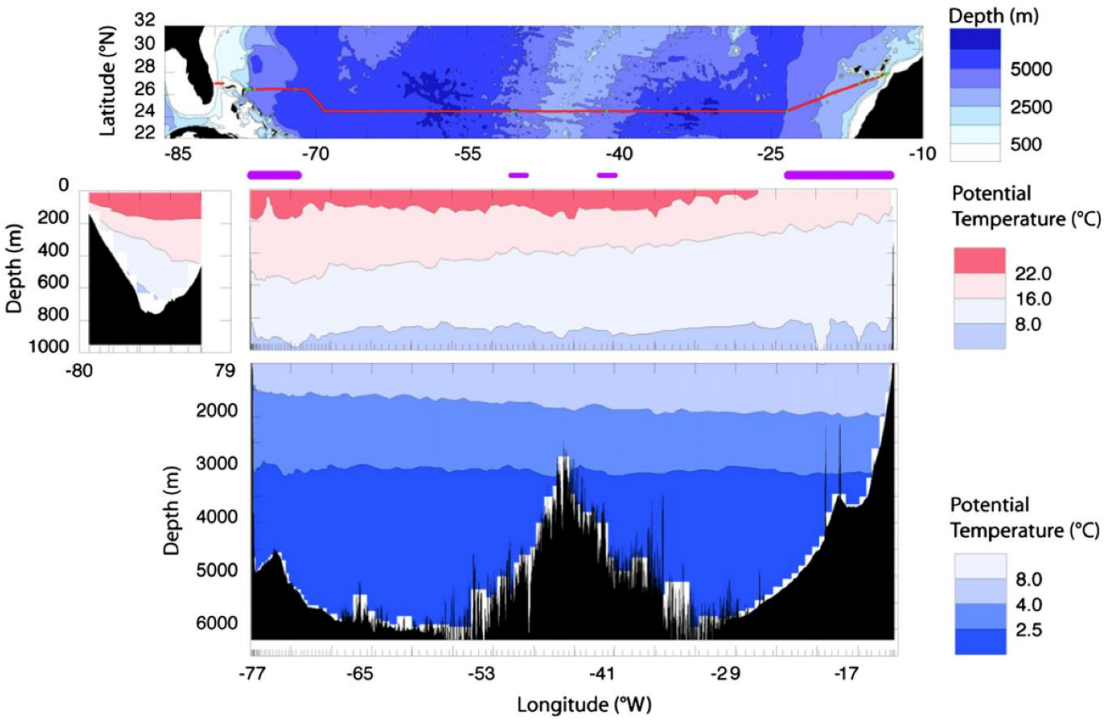

Figure 1.3: Bathymetry of the North Atlantic subtropical gyre region (top panel). The 2004 hydrographic section cruise track from the Bahamas to Africa (red line) is indicated. Magenta bars below the top panel denote the regions of the RAPID sub-arrays. The temperature data for the northward flowing Gulf Stream in the Florida Straits (middle left) and the top 1000 m of the mid-ocean (middle right) are shown. In the top 1000 m of the mid-ocean, the isotherms sloping up to the east are indicative of the southward flow of surface and thermocline water in the subtropical gyre. The temperature data for the lower 5000 m of the basin (lower panel) are also shown. From Cunningham (2005).

1.3.1 Hydrographic surveys at 25.5˚N

Hydrographic surveys across 25.5˚N in the Atlantic have been conducted since 1957, with a spacing of several years between each section. Four sections have been conducted since the installation of the RAPID moorings array in 2004 (Figure 1.3), 2010, 2011 and 2015. It should be noted that the 2011 hydrographic survey was conducted under the Malaspina project, aboard the research vessel Sarmiento de Gamboa, with Chief Scientist Alonso Hernández-Guerra (Universidad de Las Palmas de Gran Canaria, Spain) (Hernández-Guerra et al., 2014). The 2004, 2010 and 2015 hydrographic surveys were conducted aboard the RRS Discovery, supported by the UK Natural Environmental Research Council, and led by Principle Scientists Stuart Cunningham, Brian King and Brian

King, respectively (Bryden et al., 2005b; Atkinson et al., 2012). Each of the four sections consists of over 110 vertical station profiles of temperature, salinity, pressure and oxygen. Within the basin, the 2010 section cruise track shifts slightly in latitude over the Mid-Atlantic Ridge (MAR) to trace the main trench of the deep Kane Fracture Zone. Station profile spacing is concentrated at the boundaries and over the rough topography of the MAR. All hydrographic data are interpolated onto 20 decibar (dbar) levels. The problem associated with inferring decadal changes from the hydrography lies in long-term aliasing. See Table 1.1 summarises transports for 6 hydrographic sections conducted since 1957, by Atkinson et al., 2012, partitioned for each of the major water-masses: Upper Mid-Ocean (UMO) 0 - 800 m, Antarctic Intermediate Water (AAIW) 800 – 1100 m, Upper North Atlantic Deep Water (UNADW) 1100 – 3000 m, Lower North Atlantic Deep Water (LNADW) 3000 – 5000 m and Antarctic Bottom Water (AABW) below 5000 m. Despite the sparse temporal nature of the section data, the high spatial resolution offers the opportunity to evaluate property changes in the deep ocean.

		1957	1981	1992	1998	2004	2010
Upper	Ekman	4.5	3.7	4.6	5.2	4.5	2.1
	Florida Straits	31.1	31.1	30.3	34.0	31.8	30.5
	Mid-Ocean	−15.9	−18.0	−17.2	−22.2	−23.4	−17.2
	Total	19.7	16.8	17.7	17.0	12.9	15.4
Lower	Intermediate	1.6	1.1	0.7	−0.3	0.8	0.7
	UNADW	−11.8	−9.3	−11.1	−12.9	−10.4	−14.7
	LNADW	−12.6	−12.2	−10.5	−5.8	−6.6	−4.5
	AABW	2.3	2.9	2.4	1.1	2.5	2.3
	Total	−20.5	−17.5	−18.5	−17.9	−13.7	−16.2

Table 1.1: Transports (Sverdrups) for six hydrographic sections. The upper ocean comprises the Ekman layer, Florida Straits and upper mid-ocean (≤800 m); the lower ocean (>800 m) comprises the Intermediate, UNADW, LNADW and AABW layers. Ekman transports (zonally integrated across the section) are annual averages calculated from wind stress climatologies. Florida Straits transports are annual averages calculated from cable observations. The net imbalance between upper and lower layer total transports is due to the approximate 0.8 Sv Bering Straits inflow to the North Atlantic. From Atkinson et al. (2012).

1.3.2 The RAPID-AMOC programme at 26°N

The goal of the RAPID programme is to sustainably observe MOC variability in the North Atlantic, at 26°N since 2004, and improve forecasting of AMOC driven

climate change (http://www.rapid.ac.uk/rapidmoc/overview.php) (Figures 1.4 & 1.5). This involves shipboard deployment and recovery of moored instruments fitted with temperature, salinity and current sensors. The instruments are positioned east of the Bahamas, west of the African coastline, and on either side of the MAR. At the eastern boundary, the topographical slope is gradual and so a number of shorter moorings are spread along the slope to gain measurements as close to the boundary as possible, the data are merged to form the eastern boundary profile. The four boundary positions allow continuous estimation of the largely southward mid-ocean flow (Cunningham et al., 2007; Kanzow et al., 2007). These profiles are referred to as the west, MARwest, MAReast and east profiles throughout this thesis. The twice-daily (10-day filtered) time-series transports from 2004 for the major components and water-masses can be seen in Figures 1.6 & 1.7.

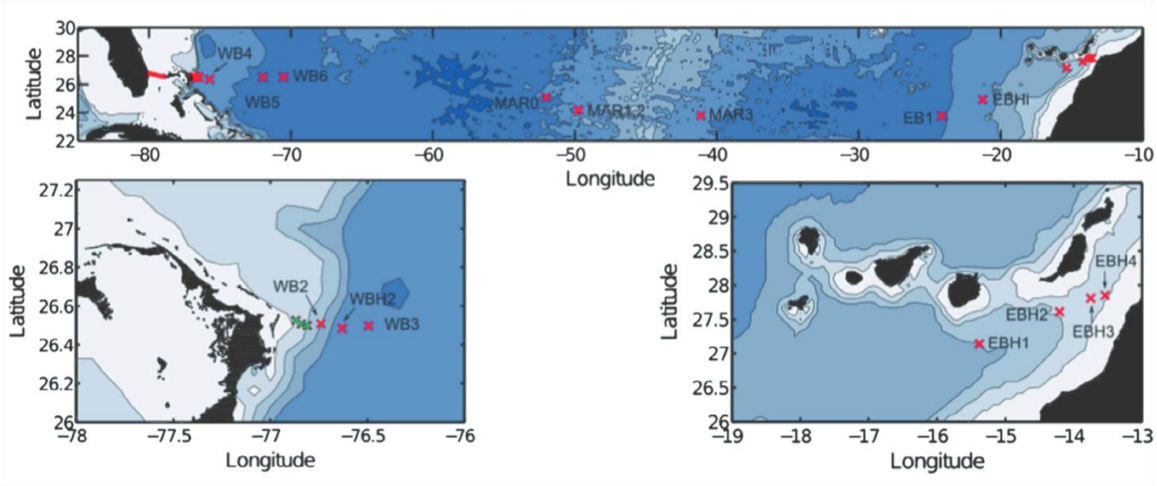

Figure 1.4: Top-down view of the dynamic height (red crosses) and current meter (green crosses) mooring locations across the 26°N section (top panel). Concentrated views of the western and eastern moorings are shown in the lower panels. Cable measurements of the Gulf Stream in the Florida Straits are indicated with a red line. From McCarthy et al. (2015a).

The Western Boundary Wedge (WBW) is a region located from the western coast of the Bahamas to the position of RAPID mooring WB2 at ~77°W (Figure 1.8). WBW transports over the steep continental shelf are calculated from direct velocity measurements from current meters (Johns et al., 2008). Data are filtered to remove unwanted signals such as those from internal waves and tides. Currents in this region typically consist of northward flow above 1000 m and southward flow below. Absolute transports for the WBW region partially negate the need for a shallow reference level at the western boundary that would be needed with

dynamic height data. RAPID internal transports are comprised of WBW data from the western coast to ~77°W and geostrophic flow estimated from dynamic height moorings relative to a 4820 dbar reference level.

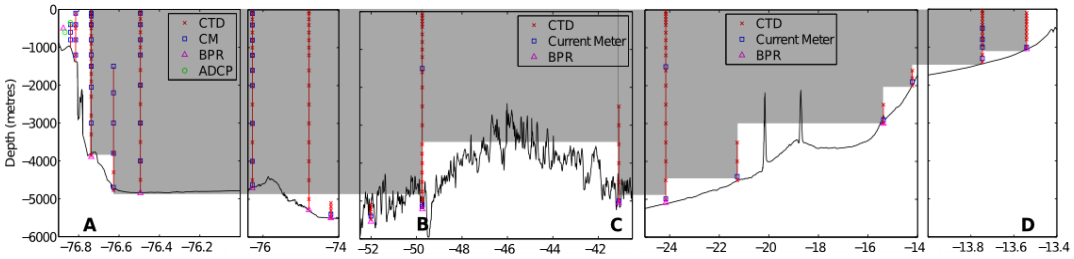

Figure 1.5: Cross-section view of mooring locations (red lines) across 26°N, as deployed in October 2012. Instruments are as indicated in the legend. Locations A, B, C and D refer to the western, MARwest, MAReast and eastern boundary sub-arrays respectively. Note the x-axis is unevenly scaled. Where the bathymetry is steep, moorings are combined at the boundary location to provide a profile that extends from near the surface to 4820 dbar. From McCarthy et al. (2015a).

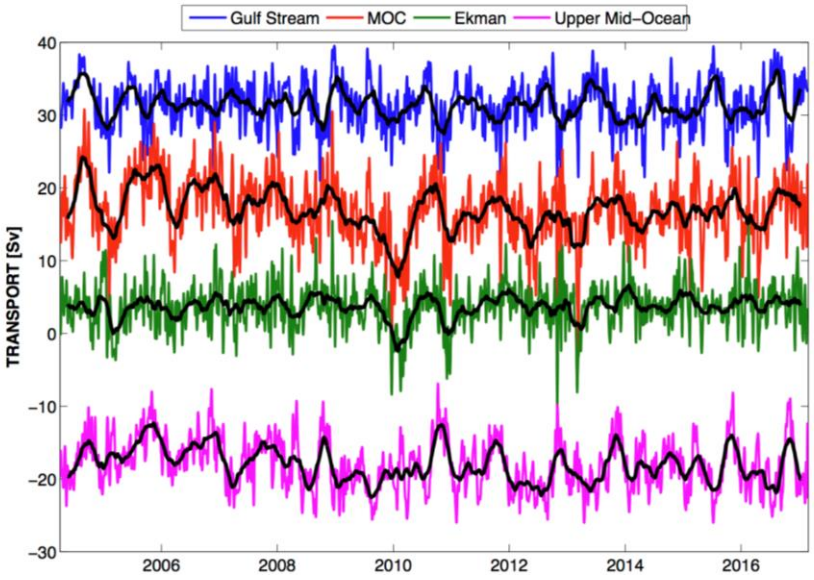

Figure 1.6: Ten-day (colours) and three-month (black) low-pass filtered time-series transports (Sverdrups) for the Florida Straits (blue), Ekman (green), UMO (magenta) and MOC (red) components from April 2004 to February 2017. RAPID UMO transports are the vertical integral of the transport per unit depth down to the deepest northward velocity (at approximately 1100 m). MOC transports are the sum of the Florida Straits, Ekman and UMO transports. Positive transports correspond to northward flow. From www.rapid.ac.uk.

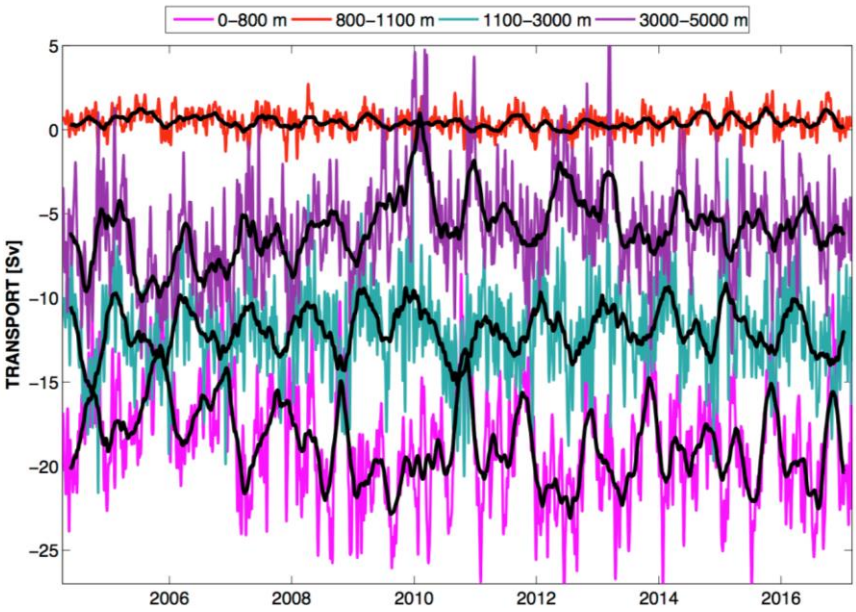

Figure 1.7: Ten-day (colours) and three-month (black) low-pass filtered time-series transports (Sverdrups) for the UMO (magenta – 0 m to 800 m), AAIW (red – 800 m to 1100 m), UNADW (turquoise – 1100 m to 3000 m) and LNADW (purple – 3000 m to 5000 m) layers. Negative transports correspond to southward flow. From www.rapid.ac.uk.

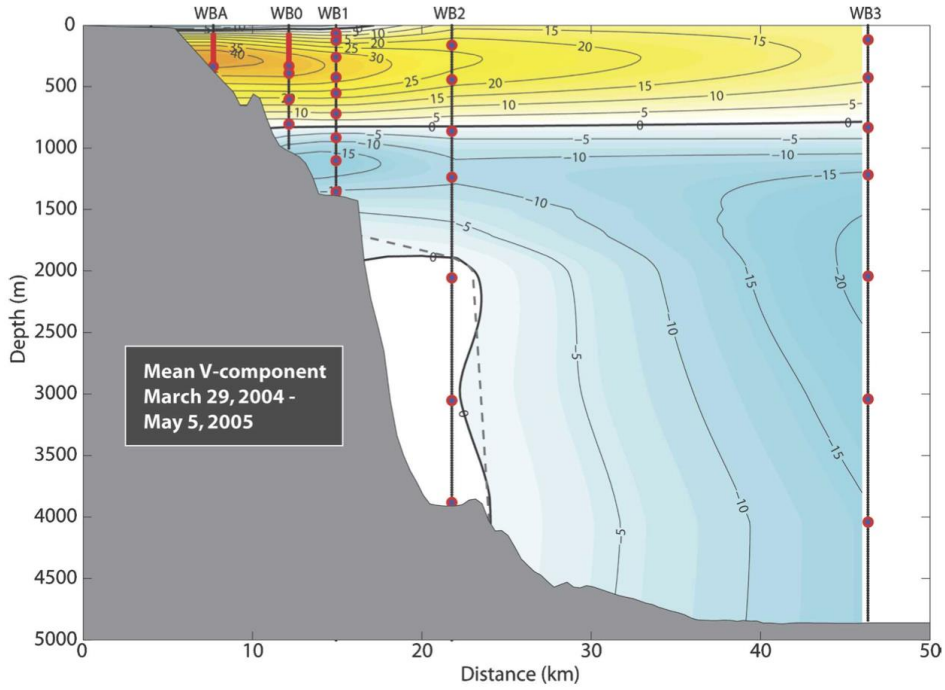

Figure 1.8: Cross-section view of the RAPID western boundary sub-array over topography near the Bahamas escarpment. The velocity contours (cm/s) denote the mean northward velocity from the gridded current meter data shoreward of WB3. The red markers show Acoustic Doppler Current Profiler (ADCP) locations. From Johns et al. (2008).

1.3.3 GRACE ocean bottom pressure

Since 2002 the Gravity Recovery and Climate Experiment (GRACE) twin satellites have made measurements of gravity field changes. GRACE ocean data were processed by Don P. Chambers, supported by the NASA MEaSUREs Program, and are available at https://grace.jpl.nasa.gov. These observed gravity field changes are the result of mass variation caused by changes in water storage (ignoring mass distribution by earthquakes or glacial isostatic adjustment). All data are processed to filter out noise (Wahr et al. 1998; Chambers & Bonin, 2012). GRACE Release-05 (RL05) has a reduced level of noise and is the version employed here (Watkins et al., 2015). The vertical extent of the monthly-averaged mass change is measured in equivalent water thickness (cm) relative to the time-mean baseline from 2004 to 2009, inclusive. The monthly mean data are gridded, where each element is a mass concentration block (mascon). Each mascon has a specific location and covers 3˚ longitude, ~300 km, at 26˚N. Equivalent water thickness (cm) data are convertible to ocean bottom pressure (OBP) using the equation for hydrostatic pressure (Figure 1.9). However, both temporal and spatial resolutions are sparse.

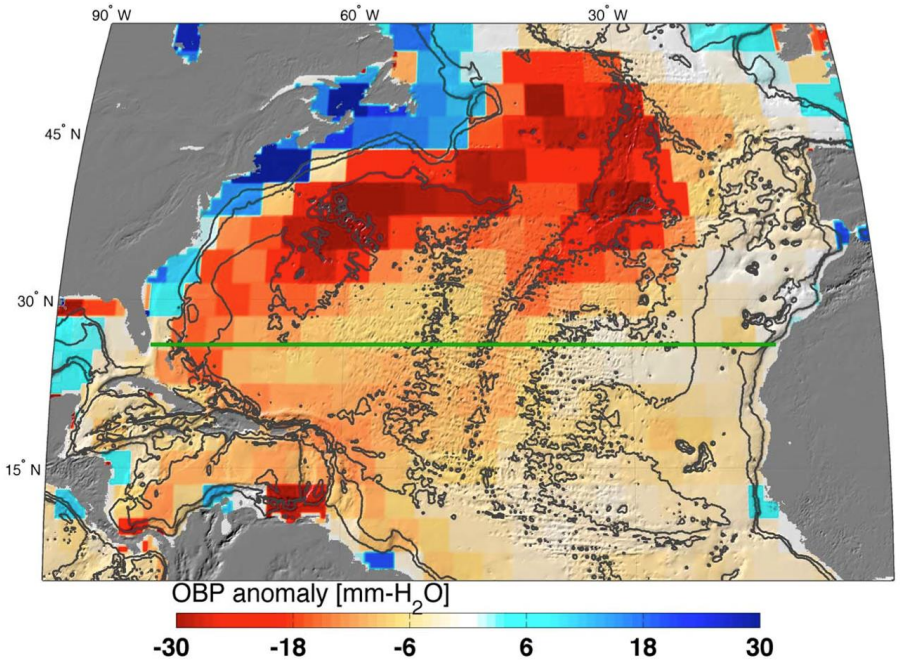

Figure 1.9: Bottom pressure anomalies (the November 2009 to March 2010 mean, relative to the 2005–2012 mean) across the North Atlantic for mascons from the GRACE JPL RL05M solution. The location of the RAPID mooring array is indicated (green line). Bottom pressure signals are larger on the western side of the basin. One mm-H_2O OBP is equal to approximately 10 Pascals. From Landerer et al. (2015).

Bottom pressure sensors are deployed at the base of RAPID moorings. Due to the need for maintenance each instrument is only deployed for up to three years. The resultant OBP measurements are subject to drift that is exponential-linear in form (Watts and Kontoyiannis, 1990). The drift is removed with a least-squares fit using an exponential-linear function, though this can remove some of the real low-frequency signal. Assembling the measurements from different instruments is also a task that produces imperfect results given that the start and end points of adjoining instruments may not match. GRACE data provides both an alternative to and a comparison with in-situ OBP. A good correlation (r = 0.7 to 0.8) is found between filtered GRACE Release-04 (RL04) OBP and sensor measurements between the Crozet Islands and Kerguelan by Rietbroek et al. (2006). Similarly, Park et al. (2008) find good correlation between GRACE OBP and in-situ data in the Kuroshio Extension. Watkins et al. (2015) conclude that better correlation between GRACE OBP and in-situ data is found at higher latitudes.

In a manner similar to Kanzow et al. (2007), vertically averaged differences of OBP fluctuations between adjacent basin depth-levels are referred to as external transports. Estimates of deep transports between 3000 m and 5000 m at 26˚N were made by Landerer et al. (2015) using GRACE release-05 (RL05) OBP to reveal good correlation (r = 0.69) with deep internal transports from the RAPID array (Figure 1.10).

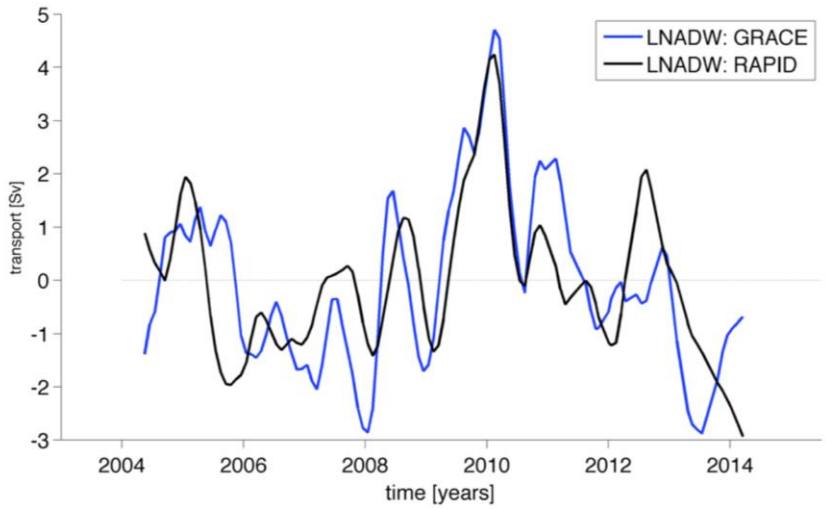

Figure 1.10: Transports (Sverdrups) estimated using GRACE OBP anomalies on the eastern and western boundaries integrated over 3000 m to 5000 m at 26.5˚N (blue line), compared to the RAPID estimate of LNADW transports (black line). The RMS difference between the two estimates is 1.2 Sv and the correlation is 0.69. The 1 sigma error of GRACE LNADW transports is ±1.1 Sv. From Landerer et al. (2015).

1.4 AMOC weakening

Over the past ~60 years average AMOC transports tend to fall within 15-19 Sverdrups (where 1 Sverdrup is equal to 1,000,000 cubic metres per second). This estimate is derived from numerous transoceanic hydrographic sections (Hall and Bryden, 1982; Roemmich and Wunsch, 1985; Lavin et al., 1998; Bryden et al., 2005b; Atkinson et al., 2012) and continuous time-series observations (Cunningham et al., 2007; Kanzow et al., 2010; McCarthy et al., 2012; Smeed et al., 2014; McCarthy et al., 2015a). Model studies show a 90-100% probability of an AMOC weakening over the next century that is interpreted by the IPCC to be very likely (IPCC, 2013). This AMOC weakening could be a result of man-made climate change as well as natural variability. The observed weakening of the AMOC, from 2004 to 2012, is described by Smeed et al. (2014). This weakening exceeds the long-term decline predicted by climate models in response to anthropogenic warming (IPCC, 2013). The AMOC decline is associated with stronger southward transports in the top 1100 m and weaker southward transports below 3000 m (Smeed et al., 2014). Buoyancy changes are expected in association with long-term AMOC changes (e.g. Robson et al., 2014).

AMOC Interannual fluctuations at 26.5˚N were reported by McCarthy et al. (2012) with an AMOC decrease in the winter of 2009-10 (Figure 1.11). This 2009-10 event was the result of reversed Ekman transports and stronger southward UMO geostrophic flow. The controlling mechanisms for these interannual variations are specified as low NAO phases that boosted subtropical trade winds and increased northward Ekman transports by Zhao & Johns (2014). Zhao & Johns (2014) attribute the strengthened southward UMO flow to wind-driven Rossby waves. Two similar events occurred in winter 2010-11 and early 2013. Frajka-Williams et al. (2016) attribute the cause of these events to surface Ekman flow anomalies that result in isopyncnal displacements at the western boundary and a deep basin response. This deep internal basin response weakens southward LNADW transports such that it flows northward (Figure 1.12). Herein, these events are referred to as ‘downturns’. Downturn events feature a large weakening of Ekman transports such that there are brief periods of net southward Ekman flow (mean Ekman flow from 2004 to 2014 is 3.6 ±3.4 Sv), a short-term reduction in northward flowing Florida Straits transports and a weakening of the southward LNADW flow below 3000 m such that there are brief periods of net northward flow (mean RAPID 2004-2014 LNADW flow is -8.7 ±3.4 Sv). These coinciding anomalies result in very brief reversals of the MOC (Frajka-Williams et al., 2016),

such that each reversal forces the (normally negative) compensation velocity to reverse sign and become briefly positive. The time-span for such reversals is typically no more than a few days. On average, for each downturn event duration, both northward Ekman flow and southward LNADW are more than 1 standard deviation weaker than their respective 2004-2014 means.

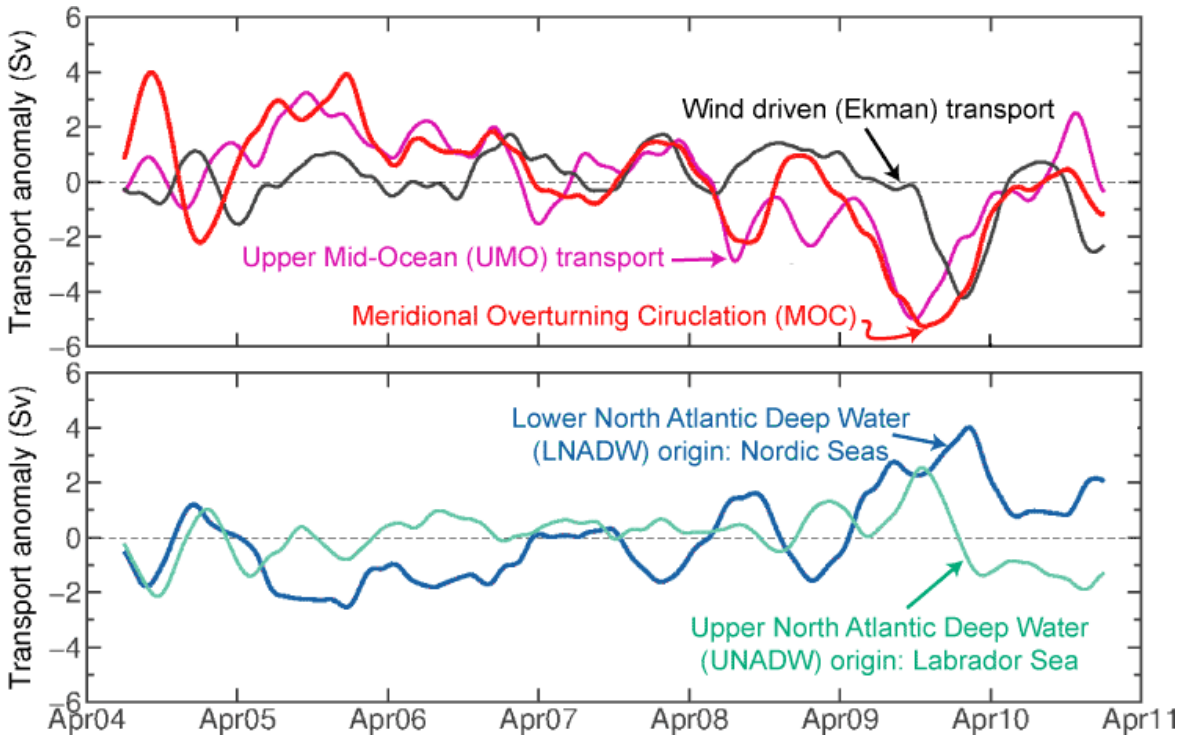

Figure 1.11: RAPID anomaly transports (Sv) after removal of the seasonal cycle and smoothing with a 180-day low-pass Tukey filter. Upper transports include Ekman (black line), UMO with fixed Ekman (magenta line) and overturning with fixed Ekman (red line). Lower transports include UNADW (1100–3000 m, cyan) and LNADW (3000–5000 m, dark blue) calculated with fixed Ekman. The 2009-10 downturn, driven by increased UMO southward transports and anomalous southward Ekman transports, is evident. From McCarthy et al. (2012).

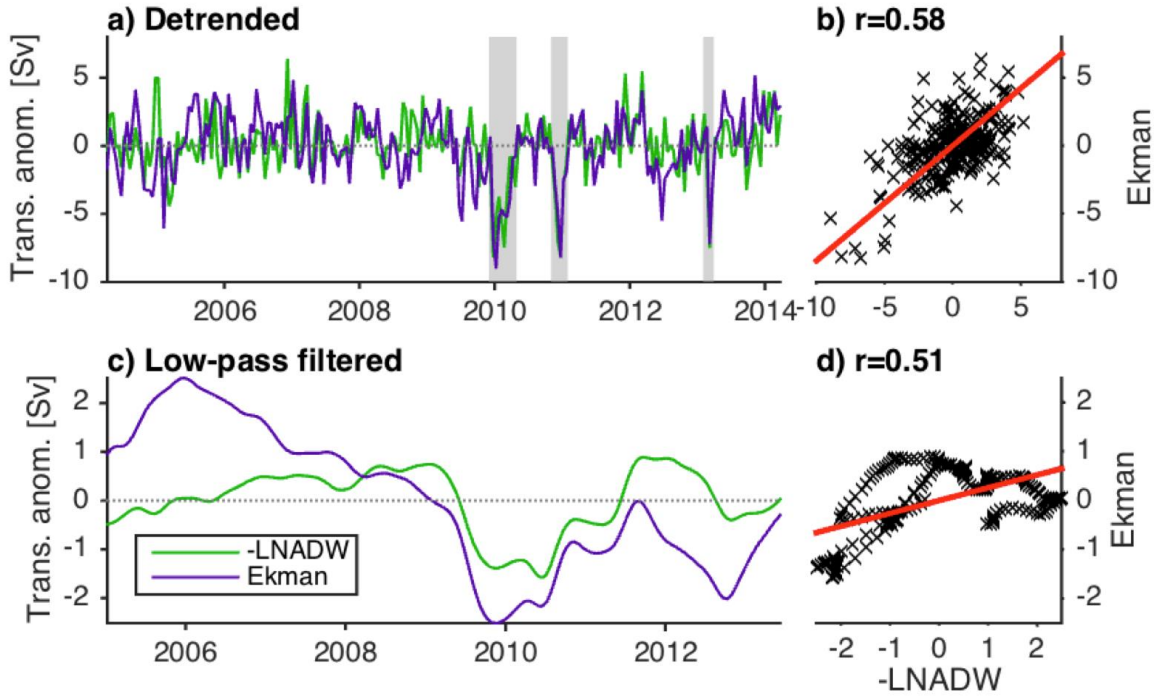

Figure 1.12: RAPID anomaly transports (Sv) (left side) for Ekman (purple) and −LNADW (green). Scatter plots of the same (right side) with correlation coefficients. In the top plot the data are de-trended. In the bottom plot the data are also de-seasonalised and low-pass filtered. The regression line is overlaid in the scatter plots. Grey regions denote downturn events in 2009-10, 2010-11 and 2013. From Frajka-Williams et al. (2015).

1.5 Summary

Chapter 1 provides an overview of the driving mechanisms of the AMOC as well as systems to measure transports at 26˚N. Mean AMOC strength and variation are accurately measured by the RAPID array and the important role of the AMOC for the climate system is acknowledged. The gradual weakening of the AMOC will be best understood through exploration of concurrent datasets, the methods to compute transports and the AMOC driving mechanisms. Attribution of the driving mechanisms will help to distinguish short-term and natural AMOC variability from long-term AMOC changes as a result of global climate change.

This thesis evaluates three different data sources with which to calculate transports: hydrographic data, RAPID data and GRACE data. The key objectives are:

1. To investigate the 2.7 Sv weaker overturning circulation in the second 4-year interval of RAPID observations relative to the first 4 years (Smeed et al., 2014);
2. To investigate downturn events, revealed by RAPID transports, in 2009-10, 2010-11 and 2013 that are typified by weak northward Ekman transports and weak southward flowing LNADW (Frajka-Williams et al., 2015);
3. To attempt to attribute AMOC changes to the driving mechanisms;
4. To uncover methodological choices and restrictions in AMOC component transports that could be altered to improve our understanding of the layer transports, particularly those in the deep basin.

Chapter 2 investigates why the hydrographic data in 2004 and 2010 convey an opposing signal to that of RAPID transports. The methodology to calculate transports typically employed for hydrographic and RAPID data will be compared. Hydrographic data have great spatial resolution and can be easily manipulated to explore the calculation methodology. Hydrographic sections also provide a set of additional parameters, such as oxygen concentration, that inform our knowledge of water-mass changes that can be used to complement quantifiable transports. Chapter 2 will therefore also use hydrographic basin properties to infer signals relevant to the observed AMOC downturns and weakening since 2004.

Chapter 3 explores the possibility of increasing the spatial complexity of the boundary transports by introducing data from an additional mooring located at the eastern edge of the DWBC. RAPID data will then be employed to highlight the variability of the DWBC to discover whether changes in the deep transports can be linked to the weakening AMOC. Chapter 3 also investigates the level of no motion, its impact on deep transports and compensation velocity.

In Chapter 4, GRACE data are employed to measure external transports for the deep layers, primarily AABW. These external transports are subject to wind stress variation. There is approximate compensation between internal and external transports and so the weakening of the MOC should be evident in GRACE-derived bottom pressure data. However, GRACE-derived transports are anomalies relative to an arbitrary mean, so an attempt will be made to convert these into transports for incorporation into the RAPID MOC calculation.

The aim of this study is to better understand the methodological choices employed to calculate transports and to use this understanding to gain insight

into AMOC variation, as well as to combine different datasets to build on knowledge of the mid-ocean flow.

Chapter 2: Atlantic Meridional Overturning Circulation (AMOC) geostrophic transports and methods: a comparison of hydrography with the RAPID time-series for 2004-2015

2.1 Introduction

The AMOC has emerged as a focal point in the study of climate change due to its capacity to move heat and other properties. Projections of AMOC decline (IPCC, 2013) motivate continued investigation into AMOC driving mechanisms and transports. The AMOC has been measured at 26°N by infrequent hydrographic sections and, since 2004, continuous measurements by the RAPID array.

The major AMOC components at 26°N are Florida Straits transports, Ekman transports, internal transports and compensation adjustment applied to ensure mass balance (e.g. Hall and Bryden, 1982; Longworth, 2007). The compensation acts as a proxy for external transports arising from ocean bottom pressure (OBP) fluctuations (Kanzow et al., 2007).

A series of intermittent hydrographic sections and the RAPID/MOCHA/WBTS array (hereafter referred to as RAPID) allow calculation of AMOC internal transports. The methods to calculate transports with these two datasets will hereafter be referred to as the hydrographic method and the RAPID method. Data from the RAPID project form a continuous time-series that allows estimation of temporal variability. Changes to the array over time have been documented by McCarthy et al. (2015a). The moorings are sparsely located across the basin and concentrated at the boundaries. Conversely, hydrographic surveys provide a spatially comprehensive set of profiles across the basin. Data collection is constrained by the time taken for a research vessel to traverse the basin, intermittently pausing for casts of a Conductivity Temperature Depth (CTD) rosette, and may therefore suffer from short-term aliasing. Moreover, trends are hard to detect due to long-term aliasing of the signal given the infrequency with which the surveys are conducted. Four such surveys have been conducted during the life of the RAPID array in 2004, 2010, 2011 and 2015. The 2011 hydrographic survey was conducted under the Malaspina project, aboard the research vessel Sarmiento de

Gamboa, led by Chief Scientist Alonso Hernández-Guerra (Universidad de Las Palmas de Gran Canaria, Spain) (Hernández-Guerra et al., 2014). The 2004, 2010 and 2015 hydrographic surveys were conducted aboard the RRS Discovery, supported by the UK Natural Environmental Research Council, and led by Principle Scientists Stuart Cunningham, Brian King and Brian King, respectively (Bryden et al., 2005b; Atkinson et al., 2012). Figures 2.1 & 2.2 detail the location of the hydrographic sections through the Atlantic Ocean, as well as the approximate RAPID boundary locations.

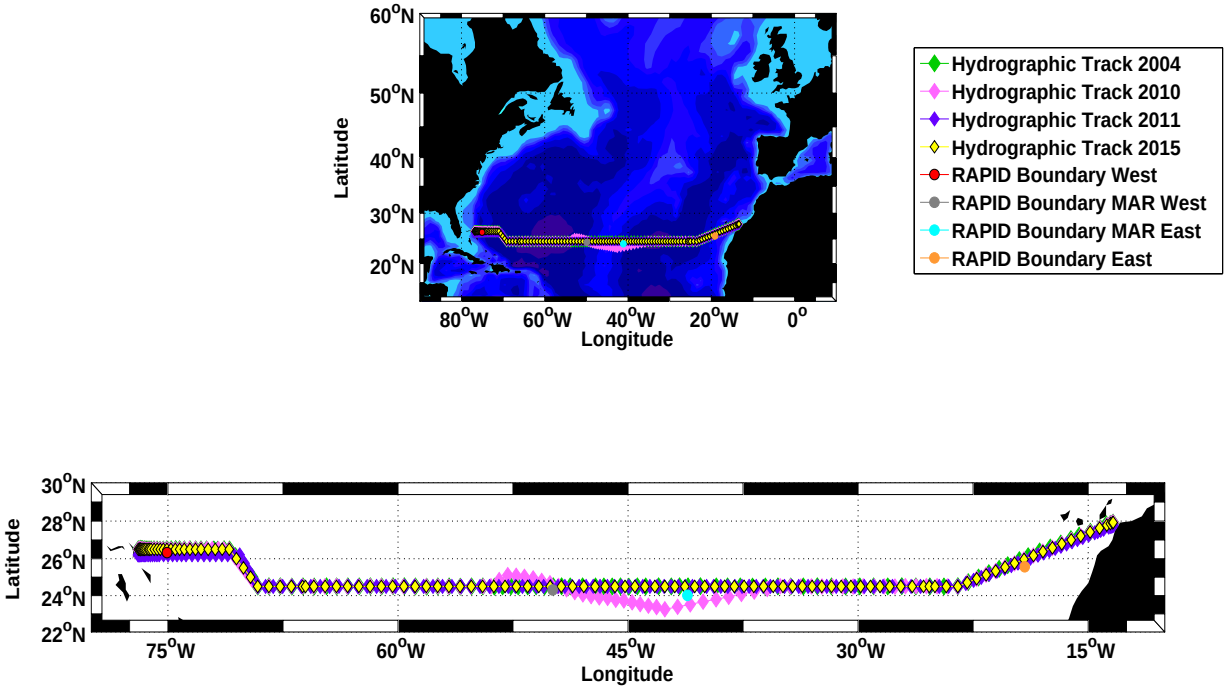

Figure 2.1: Bathymetric map of the mid-tropical North Atlantic with overlaid CTD stations for the 2004, 2010, 2011 and 2015 hydrographic sections. Station locations pertain to the main basin (east of the Florida Straits). RAPID boundary profile locations are also indicated. The top plot shows the station locations in relation to the larger Atlantic Ocean.

Atkinson et al. (2012) employ hydrographic sections to calculate transports and find that 2010 MOC strength is comparable to that of pre-2004 values. Atkinson et al. (2012) conclude that the 2010 MOC represents a return to form given the relatively weaker 2004 MOC. Atkinson et al. (2012) also conclude that UNADW transports compensate for flow variation in the top 800 m. In opposition to this, Smeed et al. (2014) observe an ongoing decline in the AMOC from 2004 to 2012, with 2009-10 showing the most substantial slowdown. Smeed et al. (2014) show that greater southward flow above the thermocline was compensated by

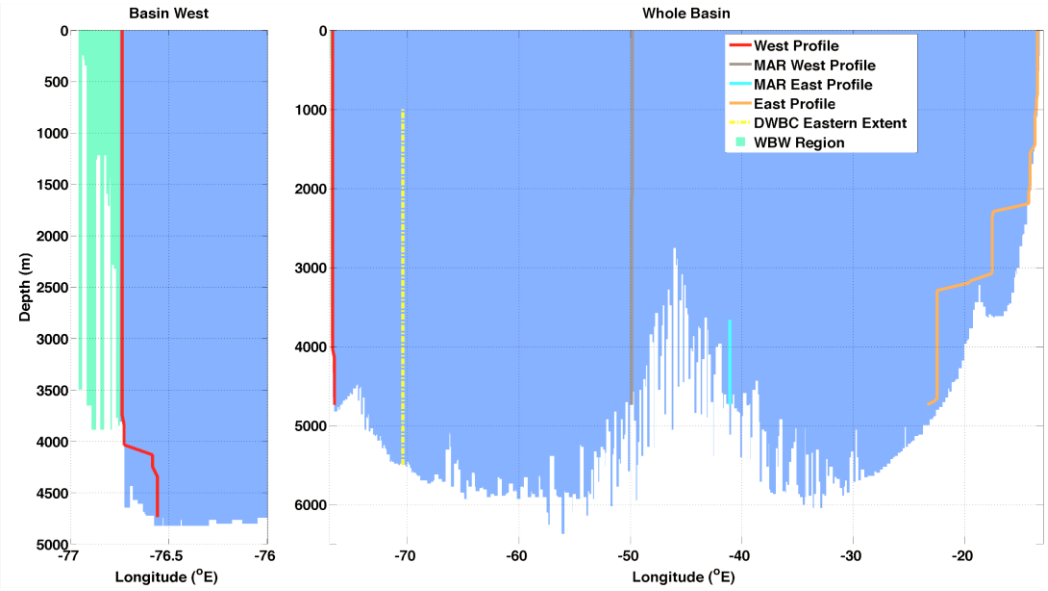

Figure 2.2: Basin cross-section composed of a composite of the profiles from hydrographic cruises in 2004, 2010, 2011 and 2015 for the whole basin (right subplot) and the western edge (left subplot). The WBW region and the eastern extent of the DWBC are indicated. RAPID boundary locations are also marked.

decreased southward LNADW flow. McCarthy et al. (2012) report a 30% decline in the annual average MOC for the period from April 2009 to March 2010. McCarthy et al. (2012) highlight associated strong southward thermocline flow and weakened Ekman transports from December 2009 to March 2010. This event is referred to as the 2009-10 downturn event. Two similar downturn events occur again in November 2010 to January 2011 and February 2013 to March 2013 (Frajka-Williams et al., 2016) and are referred to as the 2010-11 and 2013 downturns, respectively. The conclusion of Atkinson et al. (2012) that the AMOC is not weakening is further challenged by Robson et al. (2014). Robson et al. (2014) hypothesise that the 2004-12 AMOC decline seen in RAPID transports is demonstrative of decadal decline.

During the first 4 years of RAPID observations the overturning circulation was, on average, 2.7 Sv stronger than in the subsequent 4 years (Smeed et al., 2014). Transports from hydrographic sections show contrasting results, with stronger overturning in 2010 than 2004 (Atkinson et al., 2012). Causes for the apparent discrepancy between the RAPID mooring array and hydrography are explored. These two estimates of the overturning are based on different data and different calculation methods. The limitations and assumptions of the data and methods are examined.

The hydrographic and RAPID datasets are compared to quantify the extent to which the relatively poor temporal resolution of the hydrography affects MOC transports. The hydrographic sections provide a spatially comprehensive discrete set of MOC snapshots that may be experimented with and analysed zonally. The hydrography is processed with a RAPID methodology, preceded by an evaluation of each step-by-step alteration, to determine the major differences. The sections are then examined to ensure they fall within average transports as calculated with RAPID data. The methodology is discussed in greater detail within Section 2.2.5 and summarised in Table 2.4.

Hydrographic internal flow is separated into water-mass layers based on both depth and potential temperature classes to see if the two are consistent. RAPID internal flow is also broken into water-mass layers to see how changes for a particular layer can affect the others, as well as overall MOC strength. Methodological factors pertinent to the hydrographic transports are addressed with regard to RAPID transports. This is achieved by holding certain components constant in order to reveal the variability of the other components. Here, Ekman transports and Florida Straits transports are held at their long-term mean values (until Section 2.3.9). This enables an examination of the external adjustment that leads to mass conservation.

The principal aims are to investigate the calculation methods of AMOC transports and determine whether the 2009-10 downturn event evident in the RAPID time-series is contradicted by the hydrographic data. Areas of investigation include variability and correlation of AMOC transports, the factors most important in identifying downturn events and the usefulness of hydrographic transports to discern long-term trends.

2.2 Data and methods

2.2.1 Hydrographic data

The hydrographic data analysed in this thesis originate from four cruises conducted in April-May 2004, January-February 2010, January-March 2011 and December-January 2015/6 (Table 2.1). The 2010 section falls within the AMOC downturn event from December 2009 to April 2010 seen in the RAPID transports. The first half of the 2011 section, approximately, falls within another downturn event from November 2010 to January 2011.

Year	2004	2010	2011	2015
Start - Finish	8 Apr - 9 May	10 Jan - 15 Feb	28 Jan - 10 Mar	13 Dec - 20 Jan
Stations East of -77°E	113	122	148	120
Section Area East of -77°E (10^8 m^2)	315.7	331.6	318.6	315.0
Western extent of DWBC (°E)	-69.9	-69.5	-69.7	-71.0

Table 2.1: Hydrographic section details. Section area excludes bottom triangles and the Florida Straits region. The eastern extent of the DWBC is characterised by a steep switch from high to low oxygen concentrations below 1000 m (Longworth, 2007; Atkinson et al., 2012).

At each station full-depth CTD casts captured data and these raw files were processed to create a calibrated series of profiles. The surveys were conducted approximately on a line of constant latitude, but stations vary from 26.5˚N at the Bahamas, to 24.5˚N over the MAR and arrive on the eastern edge at 27˚N. The latitude of the western extent of the hydrography coincides with the location of Florida Straits transports gained from cable data. Station spacing is concentrated at the boundaries and over the MAR. Hydrographic temperature and salinity data are averaged on a 2 dbar spacing grid ranging from 1 dbar to 6597 dbar. The profiles of station data are, in this analysis, linearly interpolated onto a 20 dbar grid. Where station spacing is too close, within 100m, one is eliminated where necessary to produce sections free of abnormally large property changes over a small distance. The TEOS-10 Gibbs Seawater Oceanographic Toolbox of the International Thermodynamic Equation of Seawater (GSW) is employed to compute thermodynamic properties including potential temperature and absolute salinity.

Potential temperature sections are shown in Figure 2.3. The overlaid contour defines the division between the major water-masses, enabling the depth range of each water-mass and its change over time to be analysed. Isotherms can be seen to distort near the western margin outlining the presence of the DWBC.

Potential temperature class definitions were obtained from Longworth (2007) and Atkinson et al. (2012) with the exception of the upper extent of the Antarctic Bottom Water (AABW) layer. The upper boundary of AABW is usually determined by locating the upper limit of northward velocity after eliminating DWBC recirculation. Regarding the 2004 section, the start of northward AABW velocity coincides with a potential temperature of 1.75˚C (rounded to the nearest 0.05˚C).

For the 2010, 2011 and 2015 sections, northward velocities correspond to a potential temperature of 1.90˚C. For direct comparison with the other sections, the 2004 AABW upper potential temperature is adjusted to 1.90˚C (Figure 2.3). This selection slightly reduces southward flow for the 2004 LNADW layer. This higher AABW border for the later sections, in potential temperature classification, results in a reduction in the section area attributed to LNADW. The potential temperature boundary between AABW and LNADW (Figure 2.3) displays the greatest depth variance of all the water-mass boundaries from one section to another.

Figure 2.4 shows potential temperature differences from the mean for each section separated into depth layers. The UMO layer occupies the top 800m, below this Antarctic Intermediate Water (AAIW) takes up the 800 m - 1100 m depth range, UNADW resides in the 1100 m - 3000 m range, LNADW takes up the 3000 m - 5000 m range and AABW is below 5000 m.

The mean potential temperature below 5000 m (Figure 2.4 and Table 2.2), where the mean is calculated as the average of all 4 sections, increased from 2004 to 2015. This is consistent with the progressive warming of AABW at 24˚N since 2004 found by Johnson et al. (2008). Deeper and cooler AABW is linked to greater northward flow (Lavin et al., 1998). Strong northward AABW flow in 2004, followed by a gradual decrease, is therefore indicated.

The UNADW depth layer mean potential temperature (Figure 2.4 and Table 2.2) increased from 2004 to 2015. LNADW mean temperature for each section fluctuates but shows no trend.

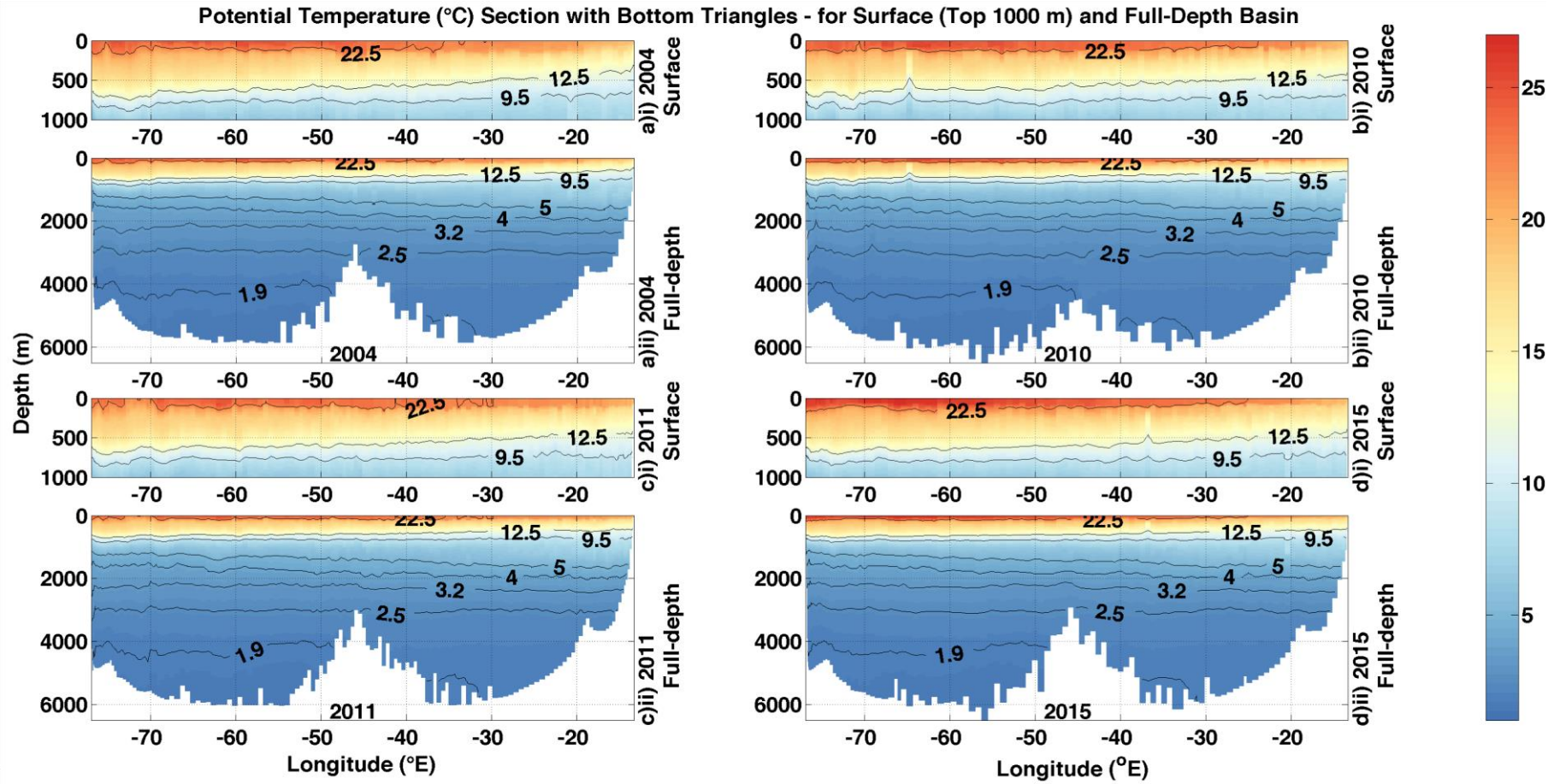

Figure 2.3: Hydrographic sections of potential temperature (°C): a) 2004; b) 2010; c) 2011; d) 2015. Each section is divided to show i) the top 1000 m and ii) the full basin. Contours represent potential temperature layers (defined in Table 2.6). With regard to the 2010 section, an upward spike of relatively cool potential temperature can be seen at ~65°W (plot b, surface) above 1000 m depth.

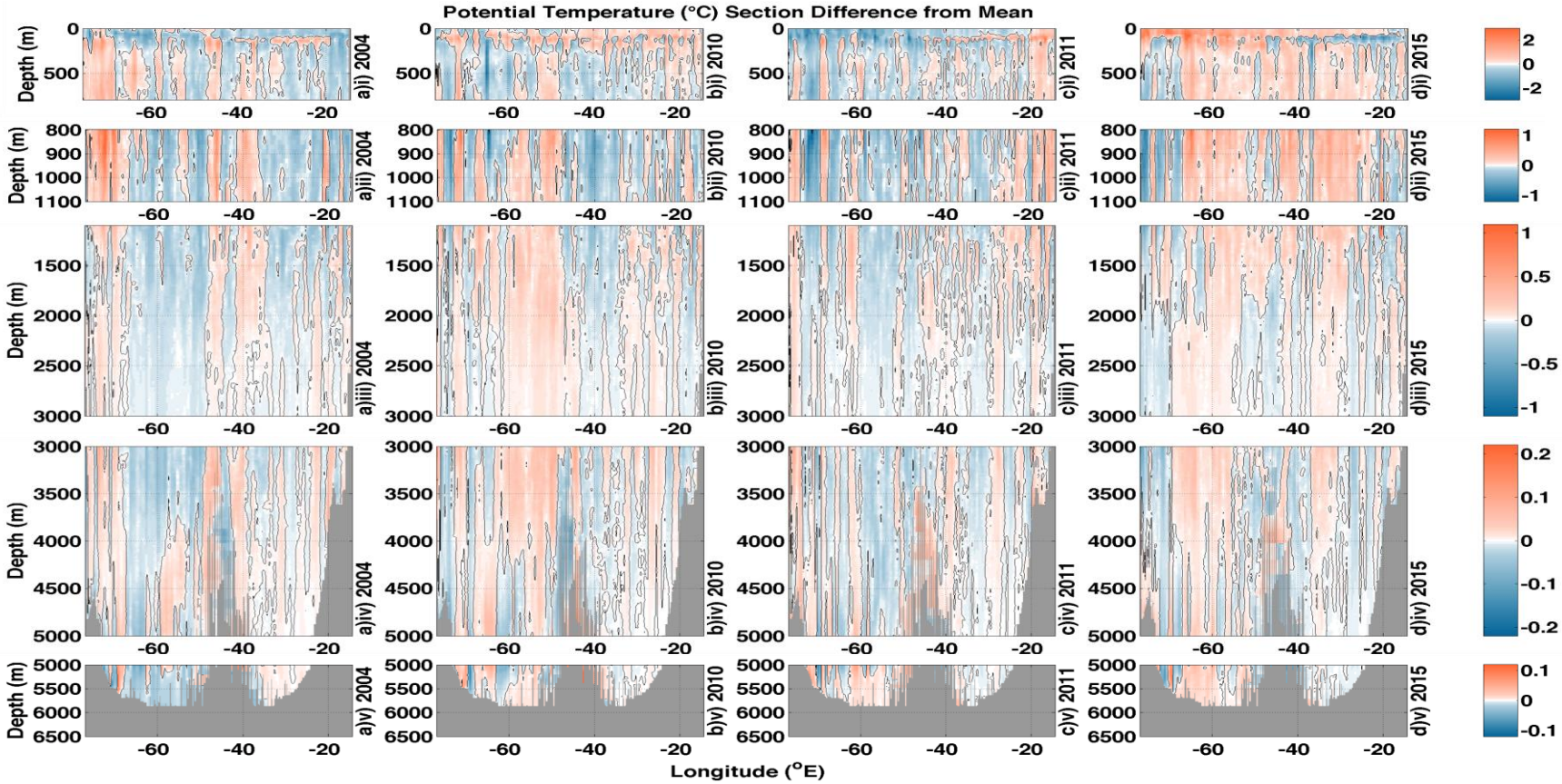

Figure 2.4: Hydrographic sections of potential temperature (°C) relative to the mean: a) 2004; b) 2010; c) 2011; d) 2015. The mean is calculated as the average of all four hydrographic sections of potential temperature. Contours within each plot represent the divide between positive and negative values. Each section is divided into depth layers (defined in Table 2). Each depth layer has its own colour bar and scale.

		Apr-May 2004	Jan-Feb 2010	Jan-Mar 2011	Dec-Jan 2015
		Mean	Mean	Mean	Mean
Mean Layer Potential Temperatures (°C)	**UMO** z ≤ 800 m	16.34 ± *0.50*	16.31 ± *0.55*	16.04 ± *0.59*	16.51 ± *0.61*
	AAIW 800 m < z ≤ 1100 m	7.44 ± *0.34*	7.40 ± *0.31*	7.39 ± *0.27*	7.43 ± *0.26*
	UNADW 1100 m < z ≤ 3000 m	3.78 ± *0.22*	3.83 ± *0.24*	3.81 ± *0.22*	3.84 ± *0.24*
	LNADW 3000 m < z ≤ 5000 m	2.09 ± *0.05*	2.07 ± *0.05*	2.11 ± *0.05*	2.09 ± *0.05*
	AABW >5000m	1.69 ± *0.02*	1.71 ± *0.02*	1.71 ± *0.02*	1.72 ± *0.02*

Table 2.2: Hydrographic section (excluding the Florida Straits region) mean layer potential temperatures (°C). Standard deviations are in italics.

		Apr-May 2004	Jan-Feb 2010	Jan-Mar 2011	Dec-Jan 2015
		Mean	Mean	Mean	Mean
Mean Layer Absolute Salinities (g/kg)	**UMO** z ≤ 800 m	36.40 ± *0.12*	36.40 ± *0.13*	36.40 ± *0.11*	36.38 ± *0.11*
	AAIW 800 m < z ≤ 1100 m	35.32 ± *0.03*	35.32 ± *0.03*	35.30 ± *0.02*	35.32 ± *0.03*
	UNADW 1100 m < z ≤ 3000 m	35.19 ± *0.03*	35.19 ± *0.03*	35.19 ± *0.03*	35.19 ± *0.03*
	LNADW 3000 m < z ≤ 5000 m	35.08 ± *0.00*	35.08 ± *0.00*	35.07 ± *0.00*	35.08 ± *0.00*
	AABW >5000m	35.04 ± *0.00*	35.04 ± *0.00*	35.04 ± *0.00*	35.04 ± *0.00*

Table 2.3: Hydrographic section (excluding the Florida Straits region) mean layer absolute salinity (g/kg). Standard deviations are in italics.

Absolute salinity sections are shown in Figure 2.5 (summarised in Table 2.3). The 35.1 g/kg salinity contour matches neatly with the 2.5°C potential temperature contour (Figure 2.3) for each section and both coincide with the 3000 m depth level. This highlights the appropriateness of the 3000 m divide between the UNADW and LNADW water-masses.

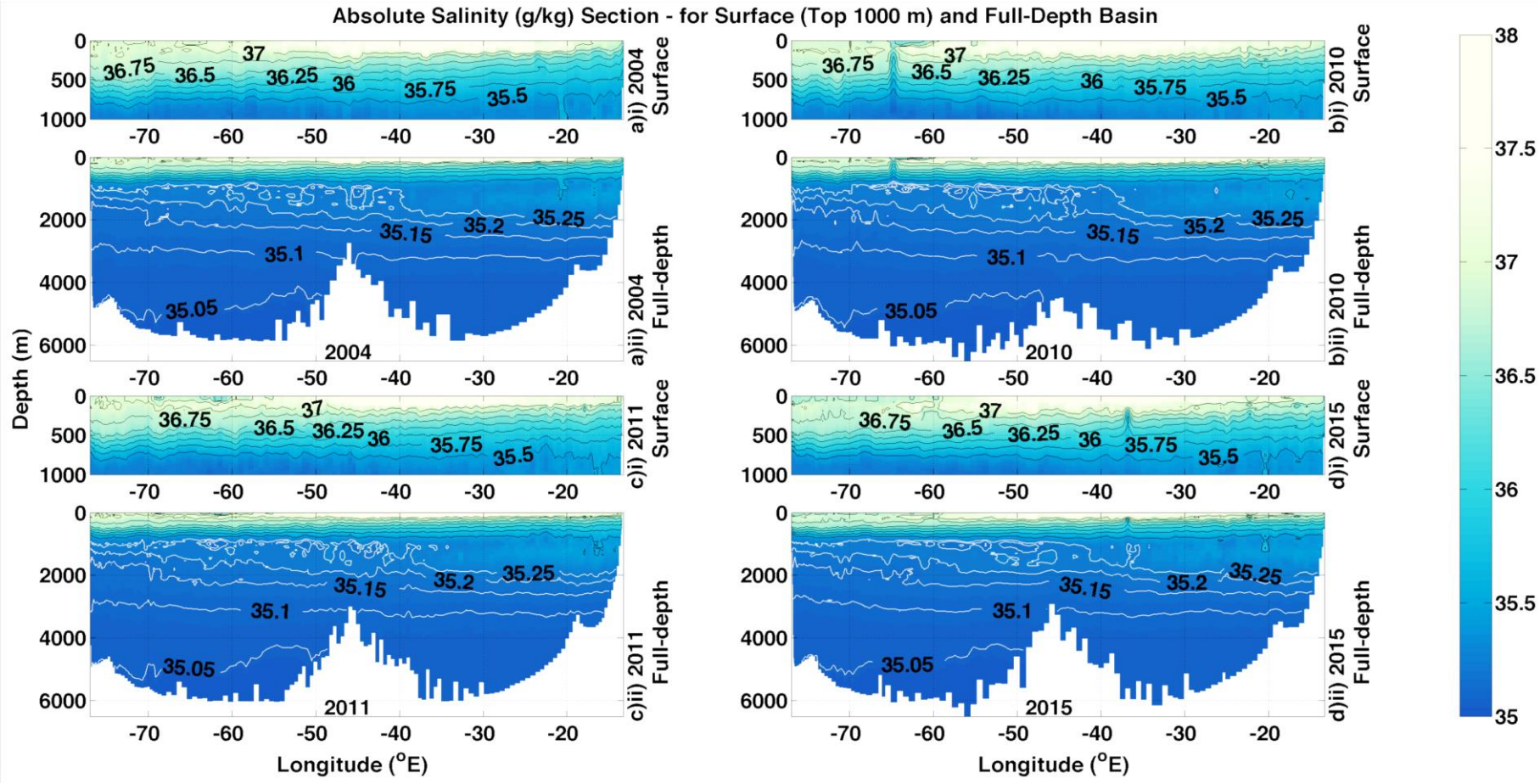

Figure 2.5: Hydrographic sections of absolute salinity (g/kg): a) 2004; b) 2010; c) 2011; d) 2015. Each section is divided to show i) the top 1000 m and ii) the full basin. Black contours represent every 0.5 g/kg change in the top 1000 m. White contours represent every 0.05 g/kg change in the main basin. In the 2010 section, a spike of low salinity can be seen at ~65°W above 1000 m depth.

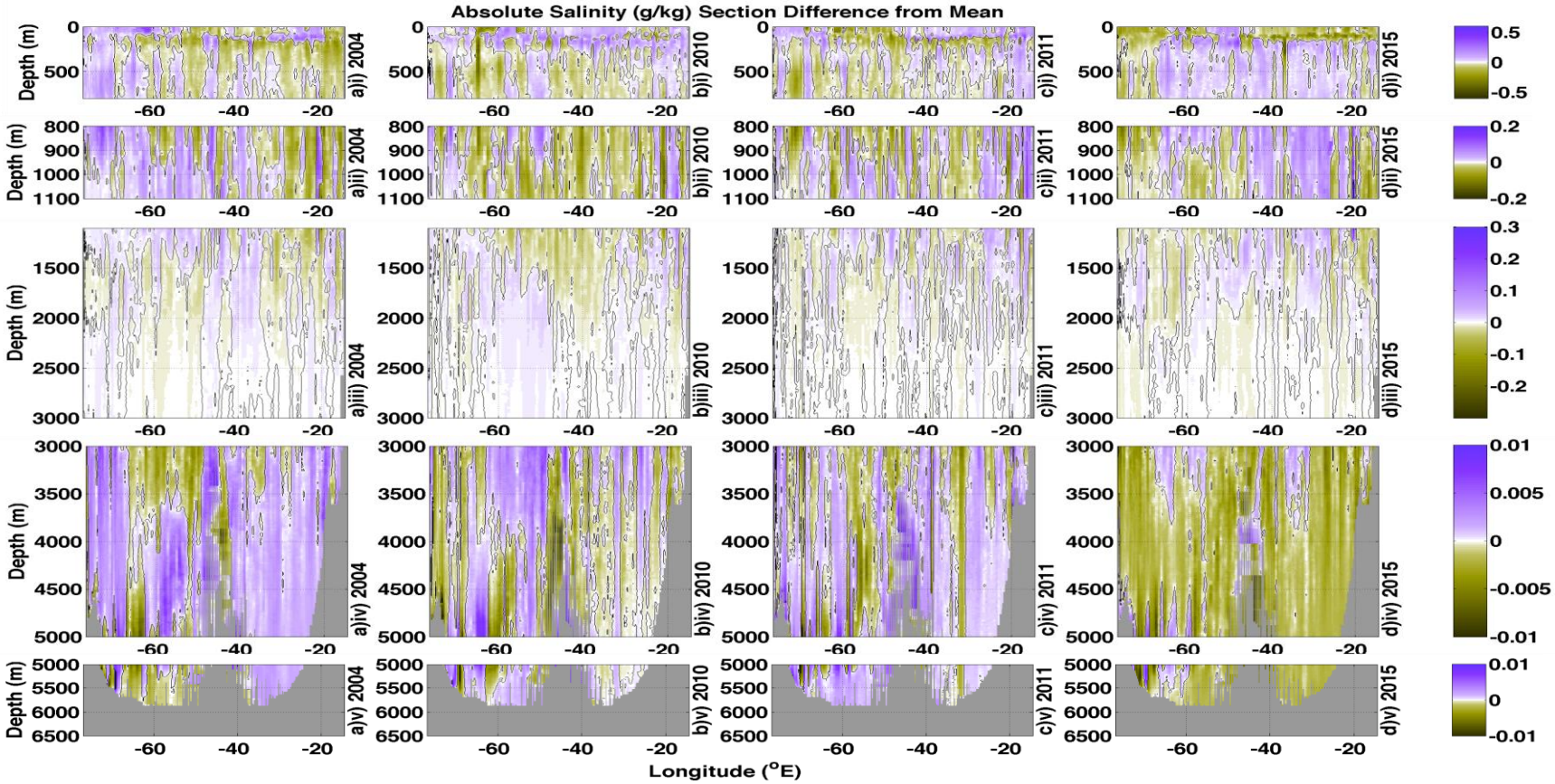

Figure 2.6: Hydrographic sections of absolute salinity (g/kg) relative to the mean: a) 2004; b) 2010; c) 2011; d) 2015. The mean is calculated as the average of all four hydrographic sections of absolute salinity. Contours represent the divide between positive and negative values. Each section is divided into depth layers (defined in Table 2). Each depth layer has its own colour bar and scale.

Absolute salinity section difference from the mean for each water-mass layer, where the mean is calculated as the average of all 4 sections, can be seen in Figure 2.6. Mean salinity for the AABW and UNADW layers remains consistent for all four sections. With regard to the LNADW and AAIW layers, there has been little change and no discernable trend in absolute salinity (note the small colour bar range). The UMO layer absolute salinity has decreased from 2004 to 2015.

Potential temperature / absolute salinity curves for each section are displayed in Figure 2.7. The highest mean surface temperatures are found in the 2004 (16.34˚C) and 2015 (16.51˚C) sections relative to 2010 (16.31˚C) and 2011 (16.04˚C), with these extremes appearing on the western side of the basin. A slight freshening of surface waters with each section is evident. 2015 surface temperatures are the warmest and freshest. The west-to-east temperature gradient (ignoring the middle) is greater for the 2004 and 2015 sections, suggestive of a stronger AMOC. The east-west temperature difference for the top 120 m is relevant due to the effect this has on the basin-wide thermocline slope. Strong internal southward flow is associated with a steep basin-wide thermocline slope (Longworth et al., 2011). The difference in mean east (<20˚W) to west (>70˚W) surface temperature (top 120 m) is 4.7˚C, 3.8˚C, 2.1˚C and 6.0˚C for 2004, 2010, 2011 and 2015, respectively (Figure 2.7). This indicates a stronger MOC for the 2004 and 2015 sections. Pérez-Hernández et al. (2015) indicate an east-west temperature difference of <1˚C for winter/spring for the top 120m (inferred from their Figure 5) for the seasonal temperature cycle calculated from RAPID mooring data. Here, each section east-west surface temperature difference exceeds 1˚C. Lower density UMO in 2010 and 2011 could be linked to the winter downturn events in 2009-10 and 2010-11. However, firm deductions are difficult given temporal aliasing. The high-frequency variability of upper ocean temperatures prevents the use of hydrographic UMO potential temperatures as a meaningful proxy for UMO transports. A source of continuous temperature measurements would provide a more meaningful proxy, yet their usefulness is limited given that UMO transports can be measured.

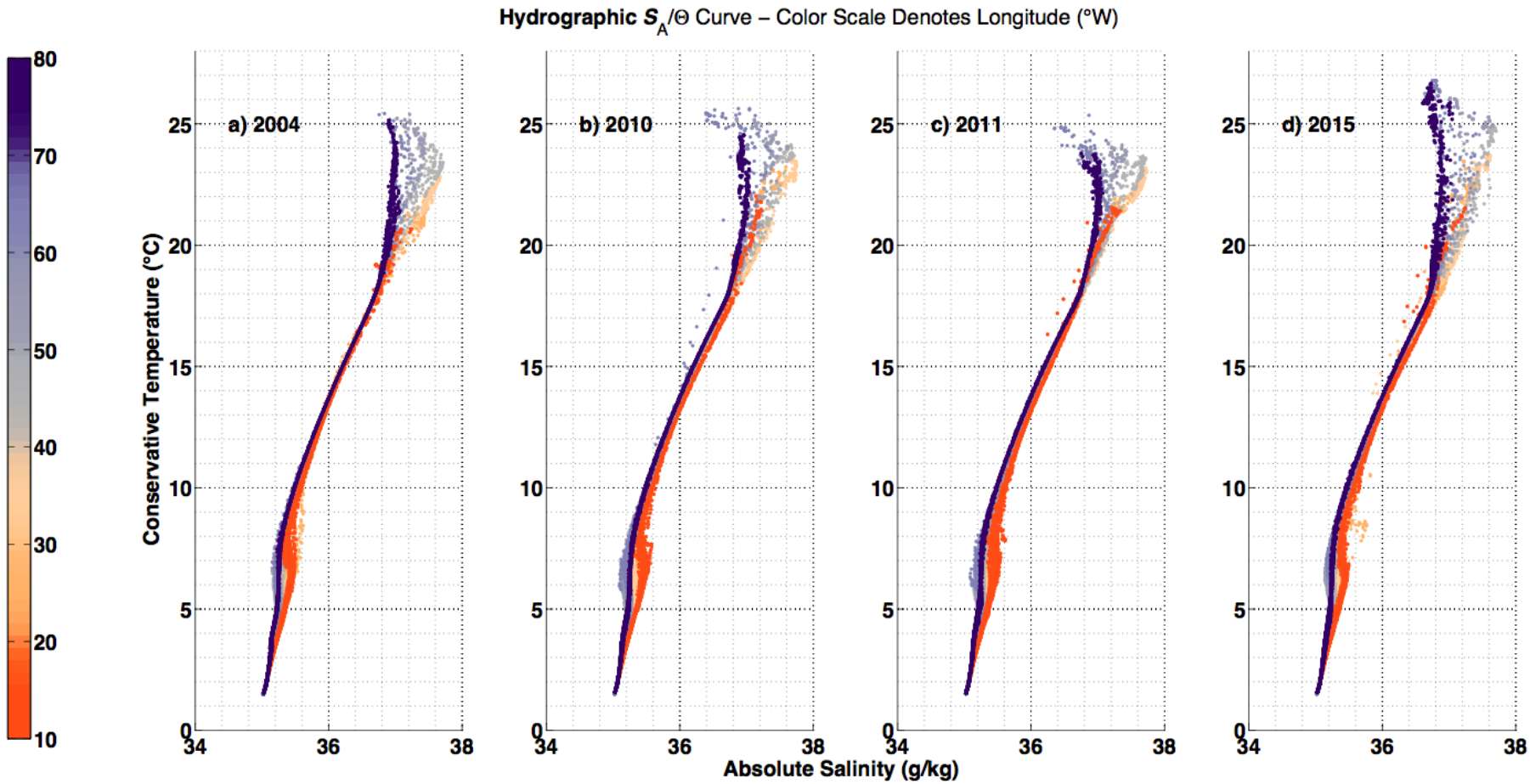

Figure 2.7: θ/S_A (°C and g/kg) plots for the hydrographic data: a) 2004; b) 2010; c) 2011; d) 2015. The colour scale denotes longitude (°W).

Oxygen concentration is shown in Figure 2.8. Meaningful inferences from oxygen concentrations can be difficult given that it is a non-conservative property. However, a steep switch from high to low oxygen concentrations below 1000 m at approximately 70°W is indicative of the eastern extent of the DWBC (Longworth, 2007; Atkinson et al., 2012). The transition out of the DWBC has, for the 2015 section, moved westward (Table 2.1 & Figure 2.8). The DWBC core and its eastern extent meander, so any movement could be due to aliasing of that motion through the sparse temporal resolution of the hydrography (Pickart, 1994; Lee et al., 1990).

Highly oxygenated, young water is found within the core of the DWBC and its recirculation gyre with mixing across the rest of the main basin (Figure 2.8). The DWBC displays greater mixing and a broader spread of recirculation in the 2004 and 2015 sections. This is inferred from the distribution of highly oxygenated waters beyond the DWBC into the main basin. Meinen et al. (2013) find NADW recirculation to be primarily between 75°W and 72°W with lesser counter-flow up to 49°W. Greater oxygenation in the deep basin may not necessarily be indicative of a stronger AMOC in 2004 and 2015, as it could instead simply imply greater recirculation into the interior (Johns et al., 1997). Lower DWBC oxygen concentrations and reduced spread are evident in the 2010 and 2011 sections. These hydrographic sections coincide with AMOC downturn events.

Oxygen concentration spikes in the thermocline can be seen in the 2010 section at ~64°W and the 2015 section at ~37°W (Figure 2.8). These spikes are echoed in the potential temperature and absolute salinity data. These anomalies are attributed to eddies. The net flow of these cyclonic features is included in the final MOC calculation. They are fully contained in the section and do not alter the large-scale outcome.

Figure 2.9 shows the section-wide oxygen concentration difference from the mean. It is clear that the 2010 section has largely lower oxygen concentrations throughout the basin relative to the mean, where the mean is calculated as the average of all 4 sections. The 2011 section has the second lowest total basin oxygen concentration.

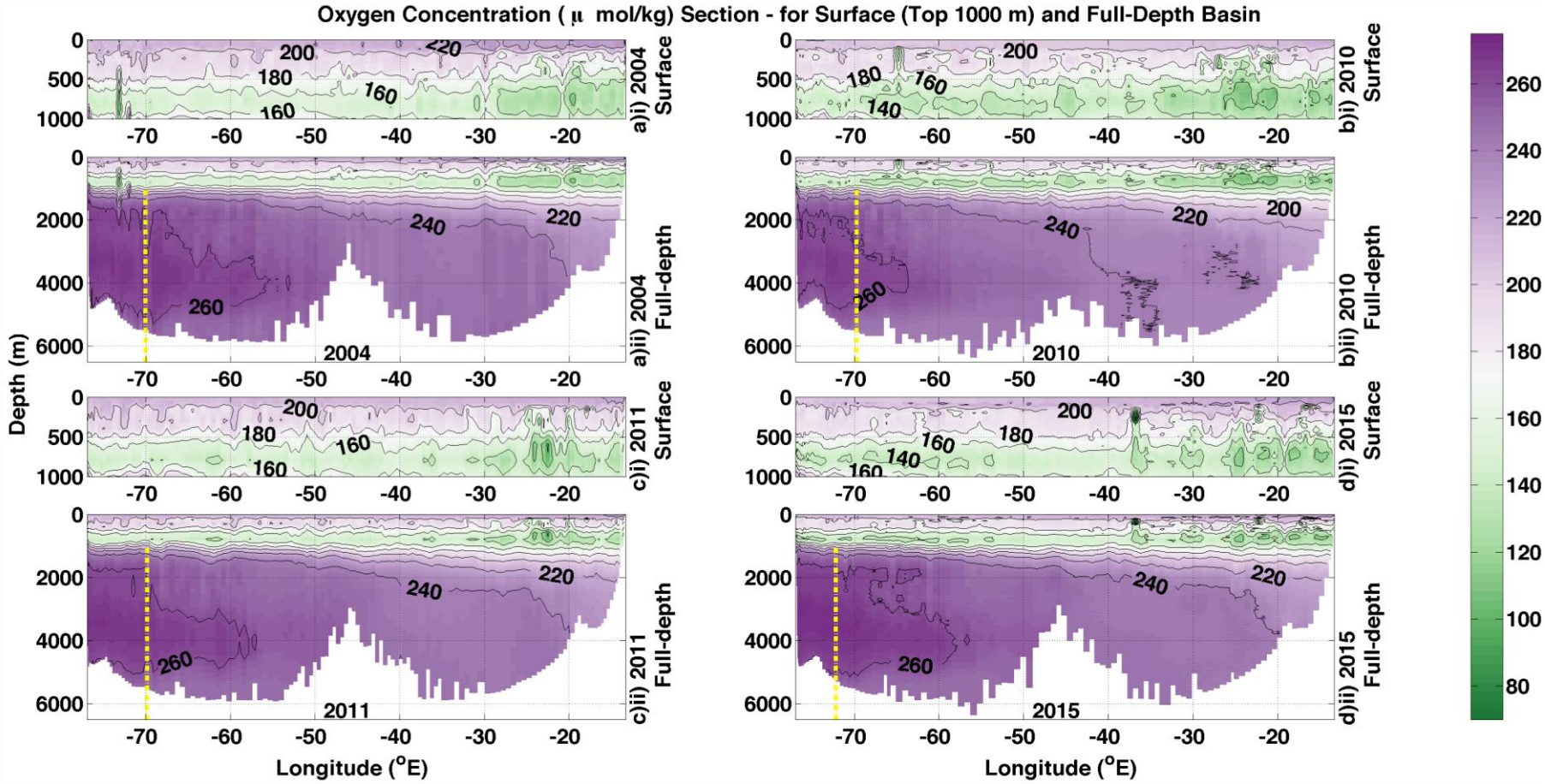

Figure 2.8: Hydrographic oxygen concentration (μmol/kg) sections: a) 2004; b) 2010; c) 2011; d) 2015. Each section is divided to show i) the top 1000 m and ii) the full basin. Contours convey each 20 μmol/kg change. For the 2010 section, a spike of low oxygen concentration can be seen at ~65˚W (plot b, surface) above 500 m. Yellow dashed lines denote the DWBC eastern extent.

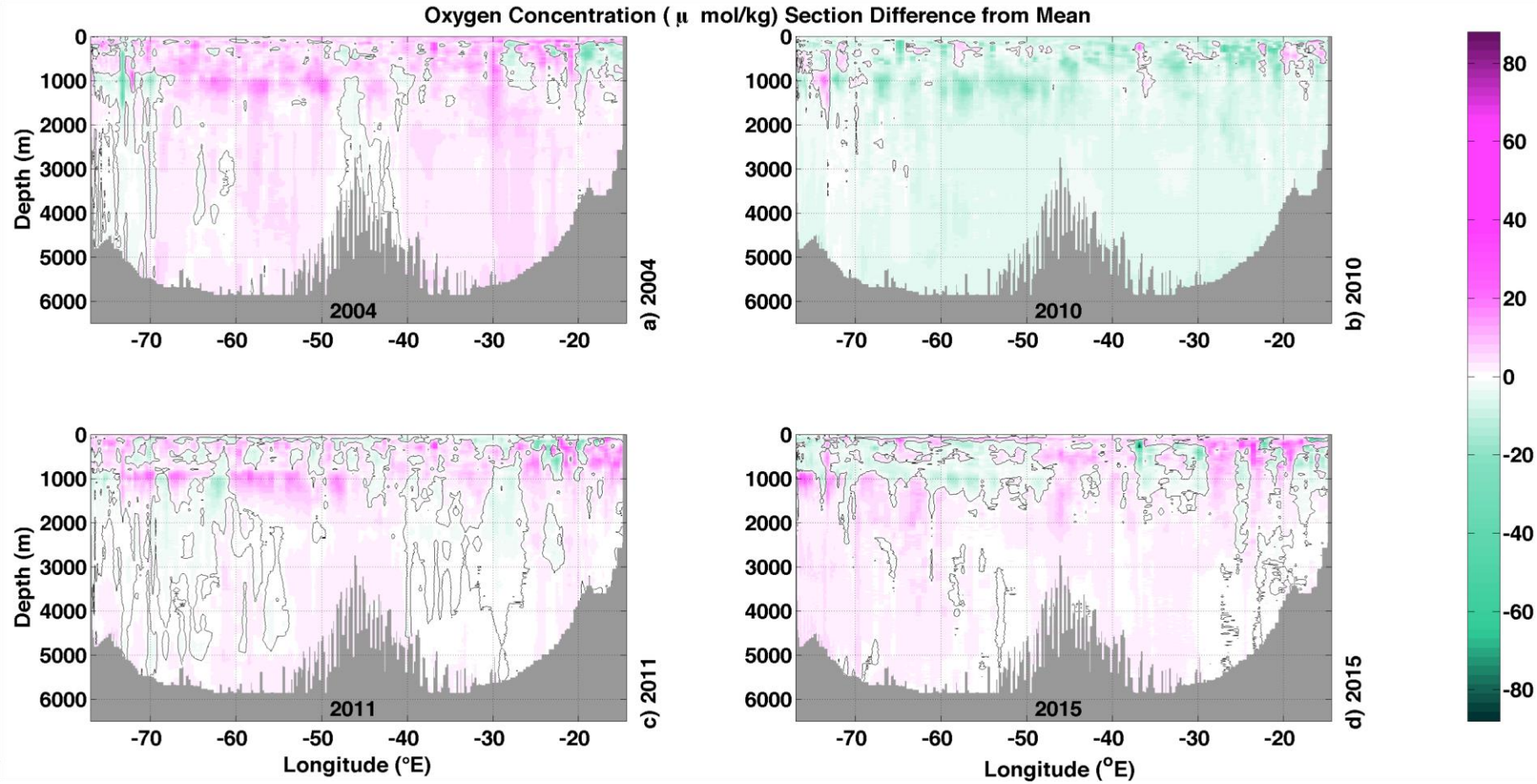

Figure 2.9: Hydrographic oxygen concentration (μmol/kg) sections relative to the mean: a) 2004; b) 2010; c) 2011; d) 2015. The mean is calculated as the average of all four hydrographic sections of oxygen concentration. Contours represent the divide between positive and negative values.

With regard to low oxygen concentration values in the 2010 hydrographic data, the same steep change in the gradient (Figures 2.8 & 2.9, plot b), conveyed by the 420 μmol/kg depth contour, is also found by Atkinson et al. (2012) (see their Figure 3). The lower oxygen concentration levels seen within the 2010 main basin convey 'older', less oxygenated, waters. A weaker DWBC and weaker re-circulation appear to be a genuine feature conveyed by the oxygen concentration data. Atkinson et al. (2012) show that the 2010 section features lower oxygen concentration values relative to hydrographic sections conducted in 1957, 1981, 1992, 1998 and 2004.

2.2.2 RAPID array data

RAPID array data, continuous since April 2004, is spatially sparse though temporally rich relative to the hydrography. Array moorings are located primarily at the boundaries and on either side of the MAR. Array data are calibrated using measurements from CTD dips performed when the moorings are recovered/deployed. The data are 10-day low-pass filtered to eliminate tidal and inertial effects. The data are then sub-sampled in time to produce twice-daily profiles on a grid with a 20 dbar spacing. A schematic of the RAPID array can be seen in McCarthy et al. (2015a).

Composite dynamic height profiles are created for the eastern and western boundaries from moorings data. Figure 2.2 shows approximate locations of the boundary profiles relative to the hydrographic profiles. RAPID array data doesn't extend to the surface, though several moorings reach up to 50 m below the surface at the western boundary and 100 m below the surface at the eastern boundary. The composite dynamic height profiles are extrapolated upward based on the typical shear in the upper ocean for the time of year. Extrapolation employs coefficients of typical shear on a monthly basis at three pivotal locations situated near the western boundary, the MAR and the eastern boundary. The mooring located on the eastern flank of the MAR, however, begins at 3700 dbar (the MAR peak). All boundary dynamic height profiles extend down to 4820 dbar. A detailed description of initial data processing can be found in McCarthy et al. (2015a).

2.2.3 The hydrographic method for calculating transports

The hydrographic method of calculating transports employed in this thesis is

similar to the process employed by Hall and Bryden (1982), Longworth (2007) and Atkinson et al. (2012), but with one difference being the use of TEOS-10, which has superseded the EOS-80 Seawater library (CSIRO). TEOS-10 is used to compute conservative temperature, absolute salinity and dynamic height for stations pairs. Geostrophic velocity shear is calculated from the dynamic height difference between each station pair. A reference level velocity is needed to determine absolute velocity. Velocities are calculated such that positive values represent northward flow through the section towards higher northern hemisphere latitudes.

The below equation is for the computation of velocity shear, where v is the average geostrophic velocity (m s^{-1}) between stations 1 and 2, with specific volume anomaly δ_1 and δ_2 (m^3 kg^{-1}) respectively (specific volume anomaly is defined as the difference between the in-situ specific volume and the specific volume of seawater and the same pressure with temperature equal to 0˚C and salinity equal to 35 g/kg), integrated from pressure P_r to P. The horizontal distance (m) between the stations, Δx, and the Coriolis parameter, f, are also accounted for:

$$(v - v_r) = \frac{1}{f\,\Delta x}\left(\int_{P_r}^{P} \delta_1\, dp - \int_{P_r}^{P} \delta_2\, dp\right).$$

As a function of dynamic height, where $\Delta D = \int_{P_r}^{P} \delta\, dp$, the above equation may be re-written:

$$(v - v_r) = \frac{1}{f\,\Delta x}\,(\Delta D_1 - \Delta D_2).$$

The reference level is set at 1000 dbar within the relatively highly oxygenated western boundary and 3200 dbar to the east of the DWBC. Lavin et al. (1998) justify this choice based on oxygen distribution from sections conducted in 1957, 1981 and 1992. On the west side of the basin, a 1000 dbar reference level ensures southward flow below this level and northward flow above as part of the Antilles Current. East of the DWBC, a reference level of 3200 dbar is chosen because a shallower level results in strong deep southward transports. This choice is ratified by Bryden et al. (2005a) and Johns et al. (2008). Should the shortest station of the pair not reach the requisite reference level pressure, the reference level is taken as the deepest common pressure level.

Geostrophic velocities are calculated as far down as the deepest common level for each station pair. Where one station is deeper than the other, the velocities within this triangle are filled, but only where the reference level is not shallower than the deepest common pressure level. The approach for filling these triangles is similar to that of Slater (2003). Within the bottom triangle, the velocity is assumed to be zero at the seabed. Thus, the deepest computed velocity, located directly above the triangle, descends to zero within the triangle. Velocity within the triangle is distributed according to area. The area is allocated to each cell in relation to its proportional area for the triangle at each pressure level. The potential temperature for each grid cell within the bottom triangle is determined by taking the bottom values for the shortest station and the longest station before allocating each value sandwiched between to produce a smooth transition.

Transports (m^2 s^{-1}) are calculated as the integral of velocities over the cross-section area. These internal transports are combined with long-term average Ekman transport and long-term average Florida Straits transport. Conservation of mass is achieved by imposing a compensation velocity. The compensation velocity is uniformly applied across the whole section area. Yearly average Bering Straits inflow of 0.8 Sv is ignored. The use of long-term mean Ekman transport and long-term mean Florida Straits transport allows the variability for the other components to be clearly discerned. This also ensures that the compensation velocity applied to ensure mass balance is only dependent on the cross-section area and geostrophic velocity. Cruise duration mean values are employed at the very last stage (Section 2.3.9) to allow comparison with RAPID transports.

2.2.4 The RAPID method for calculating transports

The RAPID method works with 4 dynamic height profiles: the western boundary, the western flank of the MAR, the eastern flank of the MAR and the eastern boundary. The merged data of several moorings form each boundary profile. Boundary profiles capture the basin-wide density gradient and therefore encompass the full zonal integral. Each boundary profile is matched by time/date to create a time-series of transports for each 12-hourly interval since 2004. There is no temporal offset across the basin unlike the hydrographic sections, which typically have a number of weeks between easternmost and westernmost profiles. All data are 10-day filtered (5^{th} order Butterworth design) prior to computing transports.

Geostrophic velocity is determined from the gradient between dynamic height profiles. To account for the presence of the MAR, geostrophic velocities are calculated in sections:

1. From the western boundary to the MARwest profile, above 4820 dbar;
2. From the MARwest profile to the eastern boundary, above 3700 dbar;
3. From the MAReast profile to the eastern boundary, below 3700 dbar.

A reference level of 4820 dbar was employed by McCarthy et al. (2012) and Smeed et al. (2014) to calculate geostrophic velocity with RAPID dynamic height data. This reference level coincides with the interface between LNADW and AABW, as well as matching the deepest mooring instrument level.

A mean AABW transport profile is appended from 5000 m downward. Net AABW northward transport is equal to 1 Sv. Frajka-Williams et al. (2011) justify this choice by concluding that there is a large degree of short-term variability in AABW flow that falls within the range of 1-5 Sv, with a mean transport of 1 Sv.

Internal transports include Western Boundary Wedge (WBW) absolute transports, located east of Abaco Island but west of ~76.6˚W (Figure 2.2). WBW absolute transports exhibit large magnitude and variability within a relatively small region (Johns et al., 2005; Johns et al., 2008). WBW transports are estimated from Acoustic Doppler Current Profiler (ADCP) data and moored current meter data. This partially negates the need for a shallow reference level at the western boundary.

Internal transports are added to time-variable Ekman transports derived from reanalysis data and Florida Straits transports obtained from cable measurements. Section-wide mass balance is ensured through the addition of a uniformly applied compensation component.

2.2.5 Methodology for comparing hydrographic transports with RAPID transports

The RAPID method will be applied to hydrographic data to quantify and mitigate bias resulting from methodological differences applied to the two datasets. However, the hydrographic profiles are offset in time from east-to-west, an offset that can be recreated with RAPID data for comparison. The evolution of each hydrographic profile can be tracked through each change to the RAPID method and is summarised in Table 2.4.

Section	2.3.1	2.3.2	2.3.3	2.3.4	2.3.5	2.3.6
Data Source	Hydrography	Hydrography	Hydrography	Hydrography	Hydrography subsampled to RAPID profile location	Temporally offset RAPID profiles
Method	Hydrographic method				RAPID method	RAPID method
Bottom Triangles & AABW	Bottom triangle velocity estimated and added to main basin, AABW transport calculated between profiles	Bottom triangles ignored & mean AABW transport profile substituted into basin	Bottom triangles ignored & mean AABW transport profile substituted into basin	Bottom triangles ignored & mean AABW transport profile substituted into basin	Bottom triangles ignored & mean AABW transport profile substituted into basin	Bottom triangles ignored & mean AABW transport profile substituted into basin
Section Area	Section area is specific to each hydrographic dataset and is dependent on station location / depth	Uniform area for each depth layer is applied to all basin hydrographic section data	Uniform area for each depth layer is applied to all basin hydrographic section data	Uniform area for each depth layer is applied to all basin hydrographic section data	Uniform area for each depth layer is applied to all basin hydrographic section data	Uniform area for each depth layer is applied to all basin section data
Reference Level	1000 dbar in the DWBC region and 3200 dbar in the main basin	1000 dbar in the DWBC region and 3200 dbar in the main basin	4820 dbar throughout the basin	4820 dbar throughout the basin	4820 dbar throughout the basin	4820 dbar throughout the basin
WBW	Geostrophic transport within WBW region is calculated between hydrographic profiles	Geostrophic transport within WBW region is calculated between hydrographic profiles	Geostrophic transport within WBW region is calculated between hydrographic profiles	WBW absolute transport profile (west of WB2) is substituted into the region for each section	WBW absolute transport profile (west of WB2) is substituted into the region for each section	WBW absolute transport profile (west of WB2) is substituted into the region for each section

Table 2.4: Summary of the evolution from the hydrographic method to the RAPID method, as applied to hydrographic data. A summary of the RAPID method, as applied to RAPID data (but temporally offset to match the hydrography), is included for comparison (red column). Each stage in the evolution will be addressed, in order (from black to yellow), within Chapter 2.3.

Evolution of the hydrographic method to the RAPID method, applied to hydrographic data, begins by replacing flow below 5000 m with the mean AABW transport profile utilised by the RAPID method. With regard to hydrographic transports, AABW displays large variability due to vastly different topography calculated between station profiles. The depth and distance between profiles determines the area calculated for the region. This source of variation is therefore easily eliminated. Next, bottom triangle velocities were removed, as the hydrographic profiles are relatively close and each triangle is small. Transports are dependent on section area and the area for each section is different (see Table 2.1). So, to eliminate this as a source of bias, each depth level was forced to equal the depth level area defined in the area profile employed by the RAPID methodology. Then, the reference level for the entire basin was altered to 4820 dbar. Where profiles do not extend down to the requisite pressure level, the deepest common level is chosen as the reference level. Whilst a relatively shallow level of no motion may be more appropriate within the DWBC region, this is mitigated by subsequently replacing profiles within the WBW region with absolute transports. Lastly, to investigate the extent to which sparse spatial sampling affects the outcome, the hydrography is sub-sampled to match the location of the boundary profiles.

The goal of the RAPID project is to produce a time-series of AMOC transports. Here, just four sets of data corresponding to the times of the hydrographic sections in 2004, 2010, 2011 and 2015 will be extracted from the time-series. To allow direct comparison with that of the hydrography, mooring data was offset in time to match the hydrographic west-east profile timing. To investigate the extent of short-term aliasing, mean transports with no temporal offset were also calculated for every RAPID 12-hourly profile falling within the four cruise durations.

2.3 Results

Long-term inferences from hydrographic transports are limited due to differing seasonal conditions at data collection, the large time gap between sections and differing methods of data collection. A comparison of the differences in the two datasets and methods of computing transports may, however, enable such inferences. Once disparities in the methodology are eliminated or reduced, a comparison with RAPID transports should be sensible. Long-term average Ekman

transport and long-term average Florida Straits transport are utilised to reduce the number of variables and highlight variation of the internal transports and the compensation transports. Each evolutionary stage in the methodology is cumulative.

2.3.1 Hydrographic transports calculated with the hydrographic method

Results for the hydrography processed with the hydrographic method show that mean MOC strength (Table 2.5) is 14.4 Sv across the four sections where layer transports are defined by depth. Relatively large southward UMO flow is evident in 2004 compared to 2010, 2011 and 2015 (Table 2.5). It cannot be determined whether this is a short-term (seasonal or less) event or otherwise. Stronger southward UMO flow results in a weaker MOC. The findings convey a stronger MOC in 2010 relative to the other sections. This echoes the results of Atkinson et al. (2012) (see their Table 4). This is despite minor differences in the methodology, such as their choice to account for Bering Straits inflow and use of annual average Ekman transports and annual average Florida Straits transports.

	Data	Hydrography			
	Year	2004	2010	2011	2015
	Compensation Velocity (m/s)	0.0000	-0.0015	-0.0021	-0.0007
Transports (Sv)	Ekman	3.5	3.5	3.5	3.5
	Florida Straits	31.5	31.5	31.5	31.5
	UMO z ≤ 800 m	-23.4	-18.3	-20.0	-20.5
	Upper Total	11.6	16.7	15.0	14.5
	AAIW 800 m < z ≤ 1100 m	0.8	0.3	-1.1	0.6
	UNADW 1100 m < z ≤ 3000 m	-10.3	-17.0	-15.8	-10.4
	LNADW 3000 m < z ≤ 5000 m	-4.7	-3.7	1.1	-6.6
	AABW >5000m	2.6	3.7	0.8	1.9
	Lower Total	-11.6	-16.7	-15.0	-14.5

Table 2.5: Hydrographic transports (Sv) in depth classes calculated using the hydrographic method. Transports employ long-term mean Florida Straits transport and long-term mean Ekman transport. Northward transports are positive. Bering Straits inflow (~0.8 Sv) is ignored. The following abbreviations apply: UNADW - Upper North Atlantic Deep Water, LNADW - Lower North Atlantic Deep Water, AABW - Antarctic Bottom Water.

Mean AABW flow across the four datasets is 2.3 ±1.0 Sv (Table 2.5). This sits within the 1 to 5 Sv estimated by Frajka-Williams et al. (2011). However, the AABW section area differs greatly for each year and so a straightforward assessment of a trend across each section is not possible without accounting for this bias. The addition, here, of bottom triangle transports also prevents straightforward comparison across sections. The slow warming found in the mean potential temperature data (Table 2.2) for this depth level suggests that AABW northward flow is decreasing with each section. However, there is no decreasing trend found in the section transports (Table 2.5).

The 2011 dataset reveals southward flow in the AAIW layer (Table 2.5). San Antolín Plaza et al. (2012) find that, from 1993 to 2010, there was a reduction in northward flowing AAIW due to an increase in deep water that is both warmer and saltier. However, AAIW for the 2011 section is forced, by the large negative compensation ensuring mass balance, to flow southward.

Separation of water-masses by potential temperature class is laid out in Table 2.6. Potential temperature classes provide a useful means of evaluating change in water-masses with time that are not confined to a predefined area. Water-mass divisions in potential temperature classes are reproduced from Longworth (2007), employed by Atkinson et al. (2012) and founded on the analysis of Schmitz & McCartney (1993) as well as Fine (1995), with the exception of the 22.5˚C and the 1.9˚C divisions. The 22.5˚C division between surface and thermocline waters was determined by Atkinson (2011) following analysis into the isotherm that best represents the bottom of the seasonal thermocline all the way across the upper mid-ocean. The 1.9˚C division between LNADW and AABW is set as the shallowest occurrence of northward flow for all four sections (within 0.05˚C intervals). It should be noted that Atkinson et al. (2012) employ a LNADW-AABW division that changes for each section, but here we have selected the shallowest divide for all four sections and used the same division for each to allow direct comparison.

Relatively large southward surface flow in 2015 is evident in Table 2.6, which corresponds to the largest surface temperatures of all four sections. It cannot be determined whether surface transports are short-term (seasonal or less) events or otherwise.

Table 2.6 shows that, when defined by potential temperature, AABW mean transport for the 4 sections is 2.7 ±1.4 Sv. This is very similar to the values obtained when the water-mass is calculated according to depth level, despite the

potential temperature divide sitting closer to 4000 m depth than 5000 m depth (Figure 2.3). This is because, whilst a 5000 m interface cuts-off AABW northward flow between 4000 m and 5000 m west of the MAR, it also incorporates flow below 5000 m on the eastern side of the MAR. This confirms 5000 m as an appropriate choice of depth level divide.

		Year	2004	2010	2011	2015
		Compensation Velocity (m/s)	0.0000	-0.0015	-0.0021	-0.0007
Transports (Sv)	Surface	Ekman	3.5	3.5	3.5	3.5
		Florida Straits	11.6	11.6	11.6	11.6
		UMO $> 22.5\ ^{\circ}C$	-0.3	-3.2	0.8	-6.0
		Total	14.8	11.9	15.9	9.1
	Thermocline	Florida Straits	15.1	15.1	15.1	15.1
		UMO $12.5\ ^{\circ}C < \theta \leq 22.5\ ^{\circ}C$	-22.6	-14.9	-19.7	-14.5
		Total	-7.5	0.2	-4.6	0.6
	Lower Thermocline	Florida Straits	2.8	2.8	2.8	2.8
		UMO $9.5\ ^{\circ}C < \theta \leq 12.5\ ^{\circ}C$	-1.0	-0.9	-1.6	-0.8
		Total	1.8	1.9	1.2	2.0
		Upper Total	9.1	14.0	12.5	11.7
Transports (Sv)	AAIW	Florida Straits	2.0	2.0	2.0	2.0
		UMO $5\ ^{\circ}C < \theta \leq 9.5\ ^{\circ}C$	1.8	-0.9	-3.2	0.4
		Total	3.8	1.1	-1.2	2.4
	UNADW	SLSW $4\ ^{\circ}C < \theta \leq 5\ ^{\circ}C$	-2.3	-3.9	-4.0	-1.8
		LSW $3.2\ ^{\circ}C < \theta \leq 4\ ^{\circ}C$	-5.9	-7.4	-4.9	-3.2
		ISOW $2.5\ ^{\circ}C < \theta \leq 3.2\ ^{\circ}C$	-2.5	-4.5	-4.3	-4.0
		Total	-10.6	-15.7	-13.2	-9.0
	LNADW	DSOW $1.9\ ^{\circ}C < \theta \leq 2.5\ ^{\circ}C$	-4.8	-3.8	-1.4	-5.8
		AABW $\theta \leq 1.9\ ^{\circ}C$	2.5	4.5	3.3	0.6
		Lower Total	-9.1	-14.0	-12.5	-11.7

Table 2.6: Hydrographic transports in potential temperature classes using the hydrographic method. Transports employ long-term mean Florida Straits transport and long-term mean Ekman transport. Northward transports are positive. Bering Straits inflow (~0.8 Sv) is ignored. The following abbreviations apply: SLSW – Shallow Labrador Sea Water, LSW – Labrador Sea Water, ISOW – Iceland Scotland Overflow Water, DSOW – Denmark Straits Overflow Water.

Labrador Sea Water (LSW) and Denmark Straits Overflow Water (DSOW) vary the most from section-to-section, with mean transports of -5.3 ±1.5 Sv and -3.9 ±1.6 Sv, respectively (Table 2.6). Inferences regarding which of these layers, if any,

compensate for changes in upper ocean flow is difficult given the time gap between sections and the high degree of short-term AMOC variability revealed by RAPID transports (Smeed et al., 2014).

Re-classification of water-masses to potential temperature (Table 2.6) enables a more realistic separation of AAIW from UNADW. AAIW exhibits an eastern-heavy wedge shape through the basin (Figure 2.3) that is not easily captured by simple classification according to depth. 2010 and 2011 AAIW transports are anomalously southward flowing due to large negative compensations that are possibly associated with downturn events.

The differing section areas least affect the UMO and UNADW layers for each year. When classified by depth class (Table 2.5), mean UMO transport is -20.6 ±1.8 Sv. When partitioned by potential temperature (Table 2.6), mean UMO transport (combined for the surface, thermocline and lower thermocline layers) is -21.2 ±1.8 Sv. Mean UNADW transport classified by depth class (Table 2.5) is -13.4 ±3.0 Sv. Mean total UNADW transport classified by potential temperature (Table 2.6) is -12.1 ±2.6 Sv. The similarity of mean transport for the UMO and UNADW layers, in depth class and potential temperature class, indicates that the depth layer divisions serve as good approximations for the water-mass interfaces.

2.3.2 Hydrographic transports with uniform section area

A large difference between sections is the area calculated between the profiles. This is most pronounced for the AABW layer. To enable a fairer comparison of transports, the AABW layer for each section is replaced by the mean profile utilised in the RAPID method. This alteration alone impacts the total MOC by an average of -0.2 Sv for the four sections. Next, bottom triangle transports added as part of the hydrographic method are omitted, as this has very little impact on the basin. Omission of bottom triangle transports alters the total MOC by -0.001 Sv, on average.

Transports for the first evolutionary stage from the hydrographic method to the RAPID method are largely reflective of forcing the total area for each depth level to match for each section. The total area is altered using a uniform section area to define the boundaries over which transports are evaluated. This uniform area grid is a composite of the profiles for all four sections, as well as the RAPID profile of section area.

The combined effect of all three changes (appending AABW mean transport, ignoring bottom triangles and enforcing the same area profile for each section) is an average increase in MOC strength by 3.4 Sv (Table 2.7). This change is due to correcting the area of the basin outer edges and over the MAR. The 2010 section, for example, extends down to ~4500 m over the MAR and thus oversamples this region due to station depth levels and spacing. Conversely, the 2004 section underestimates the basin area over the MAR. This is illustrated in Figure 2.10, where pink shaded regions denote oversampling and green shaded areas denote under-sampling. Furthermore, the use of a uniform area grid addresses section area differences resulting from cruise track latitude shifts (as both latitude and longitude are utilised in the calculation of area between station profiles). The 2010 section track, for example, shifts in latitude over the MAR to trace the main trench of the deep Kane Fracture Zone (Figure 2.1).

	Data	Hydrography			
	Method	1. Bottom triangles ignored & mean AABW 2. Uniform area for each depth layer			
	Year	2004	2010	2011	2015
	Compensation Velocity (m/s)	-0.0003	-0.0015	-0.0021	-0.0010
Transports (Sv)	Ekman	3.5	3.5	3.5	3.5
	Florida Straits	31.5	31.5	31.5	31.5
	UMO z ≤ 800 m	-17.8	-16.6	-17.1	-17.2
	Upper Total	**17.2**	**18.4**	**17.9**	**17.8**
	AAIW 800 m < z ≤ 1100 m	0.7	-0.1	-0.8	0.1
	UNADW 1100 m < z ≤ 3000 m	-11.2	-15.8	-16.2	-11.0
	LNADW 3000 m < z ≤ 5000 m	-7.8	-3.5	-1.9	-7.9
	AABW >5000m	1.0	1.0	1.0	1.0
	Lower Total	**-17.2**	**-18.4**	**-17.9**	**-17.8**

Table 2.7: Hydrographic transports (Sv) in depth classes with uniform area. Transports employ long-term mean Florida Straits transport and long-term mean Ekman transport. Methodological deviations from the hydrographic method are listed in the second row. Northward transports are positive.

Where an individual section oversamples a region due to the spacing of profiles (Figure 2.10, pink regions), application of a uniform area grid ensures that the outcome is not overinflated. Where an individual section under-samples a region

(Figure 2.10, green regions), the nearest velocity value is assumed to persist. Replacing each individual section area with a uniform area grid also redistributes the compensation velocity.

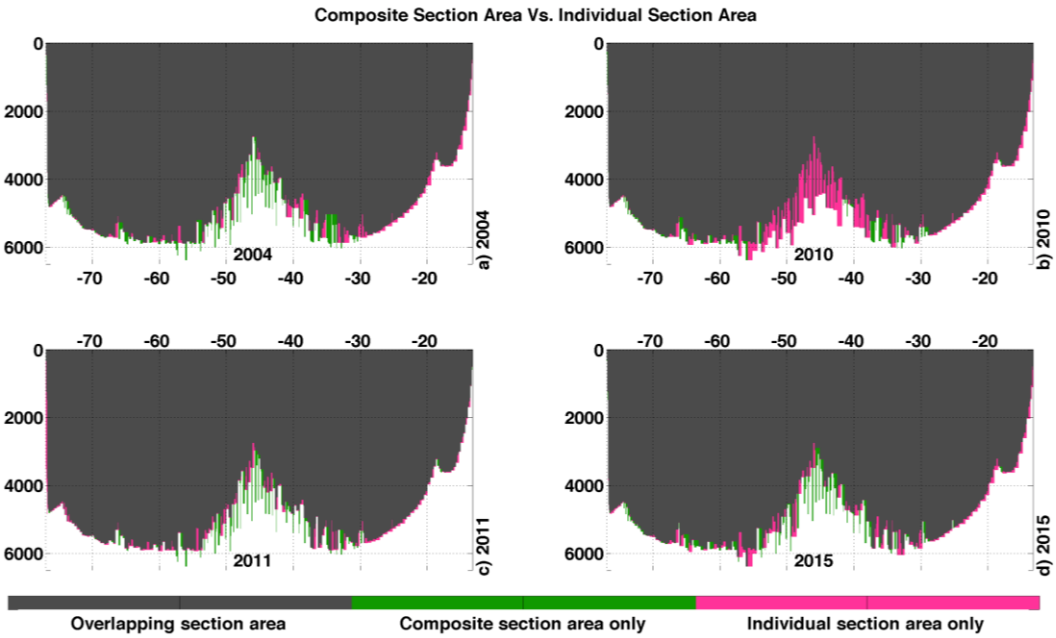

Figure 2.10: Hydrographic section area relative to the uniform section area: a) 2004; b) 2010; c) 2011; d) 2015. Overlapping areas are shaded in grey, section areas belonging to just the individual section are shaded in pink and section areas belonging to just the composite area are shaded in green.

Unifying the section areas has the largest impact on the 2004 MOC (Table 2.7), with an increase in the total MOC of 5.6 Sv. This increase brings the section in-line with the transports of the other three sections and eliminates the inference of the 2004 MOC being very weak relative to the other sections. The AAIW and UNADW layers are little altered, on average, for all sections. The LNADW layer sees an average -1.8 Sv change in flow.

Applying a uniform section area also alters the 2011 section so that LNADW is now southward flowing (Table 2.7). It should be noted that this change is not the outcome of AABW transports being forced to equal 1 Sv of northward flow. The cause is the change in transports over the MAR and subsequent redistribution of compensation transports.

The profiles of transport per unit depth (TPUD) for the hydrographic transports in Table 2.7 are plotted alongside those of Table 2.5, for comparison, in Figure 2.11. The TPUD profiles and streamfunctions include a long-term mean Florida

Straits transport profile for the top 800 m and long-term mean Ekman transport. Small plateau's where the TPUD profiles aren't smooth are the result of the termination of station profile data at varying depths across the basin. Each plot line is colour-matched to Tables 2.5 & 2.7. The 2004 and 2015 TPUD profiles reveal the two-lobed structure of southward flowing NADW, there is a positive curve separating UNADW (1100 m to 3000 m) from LNADW (3000 m to 5000 m). This two-lobed shape is much less evident in the 2010 and 2011 sections. This may be linked to the downturn events, as it is indicative of weaker LNADW southward flow.

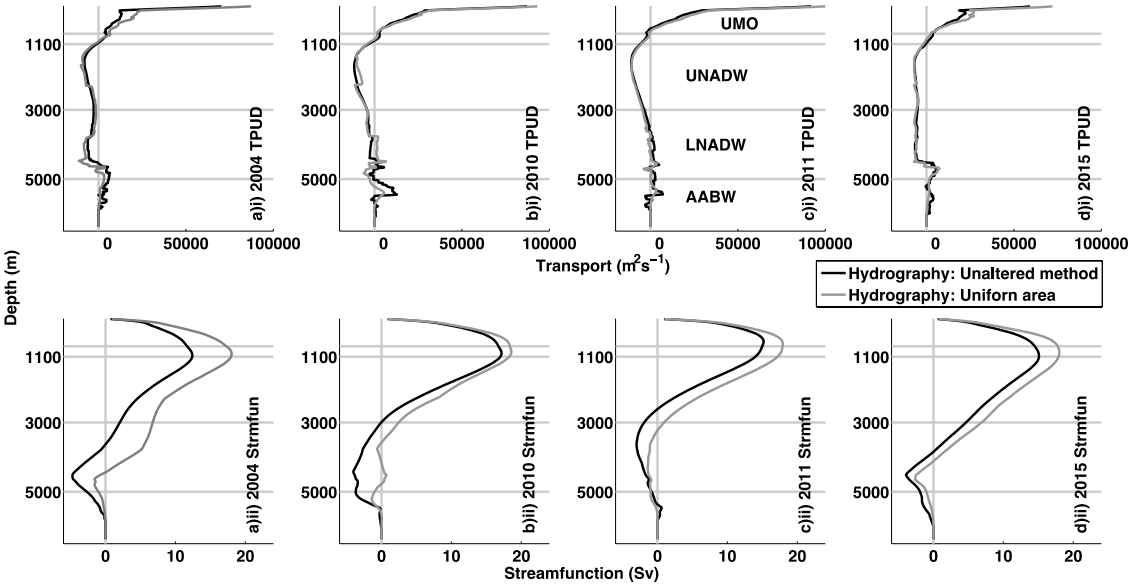

Figure 2.11: Hydrographic TPUD (m^2s^{-1}) profiles (top) and streamfunctions (bottom): a) 2004; b) 2010; c) 2011; d) 2015. All plots include a mean Florida Straits transport profile and mean Ekman transport. Black plotlines represent the unaltered hydrographic transports, whereas the grey plotlines show transports calculated after a uniform area is imposed.

2.3.3 Hydrographic transports with basin-wide deep reference level

In the second evolutionary change in the hydrographic method to the RAPID method, calculated with hydrographic data, the reference level is deepened to 4820 dbar across the basin (Table 2.8). Figure 2.12 shows the TPUD and streamfunction profiles for each section with comparison of the deep reference level (blue lines) with transports calculated with a reference level of 1000 dbar in the DWBC region and 3200 dbar within the main basin (grey lines). A shallow reference level of 1000 dbar ensures northward flow above 1000 dbar for the Antilles Current and southward flow below 1000 dbar that reflects the strong flow

of the DWBC that carries UNADW and LNADW (Bryden et al., 2005a). Lowering the reference level to 4820 dbar alters the ratio of the deep flow components. The deep return flow is pushed down in the basin, LNADW internal transports are altered and the compensation adjusts to ensure mass balance. The compensation is applied to the basin uniformly according to area. Thus, the larger the southward compensation, the greater the resemblance of the TPUD profile to that of the area profile after compensation is added.

	Data	Hydrography			
	Method	1. Bottom triangles ignored & mean AABW 2. Uniform area for each depth layer 3. Reference level 4820 dbar			
	Year	2004	2010	2011	2015
	Compensation Velocity (m/s)	-0.0007	-0.0005	0.0000	-0.0007
Transports (Sv)	Ekman	3.5	3.5	3.5	3.5
	Florida Straits	31.5	31.5	31.5	31.5
	UMO z ≤ 800 m	-17.5	-15.6	-17.4	-16.8
	Upper Total	**17.5**	**19.4**	**17.6**	**18.2**
	AAIW 800 m < z ≤ 1100 m	0.7	0.3	-0.9	0.3
	UNADW 1100 m < z ≤ 3000 m	-11.6	-14.7	-14.7	-10.3
	LNADW 3000 m < z ≤ 5000 m	-7.5	-6.0	-3.0	-9.1
	AABW >5000m	1.0	1.0	1.0	1.0
	Lower Total	**-17.5**	**-19.4**	**-17.6**	**-18.2**

Table 2.8: Hydrographic transports (Sv) in depth classes with reference level 4820 dbar. Transports employ long-term mean Florida Straits transport and long-term mean Ekman transport. Methodological deviations from the hydrographic method are listed in the second row. Northward transports are positive.

Deepening the reference level alters the MOC by just 0.3 Sv on average for the 4 sections. The negative compensation shifts in a positive direction toward zero (Table 2.8 relative to Table 2.7), due to the deeper reference level, with each section needing less negative compensation to ensure mass balance. This suggests that the deeper reference level (Table 2.8) is closer to a level of no motion between water-masses. The reduced negative compensation has an impact on all layers due to its uniform distribution over the section. An exception to this process is the 2004 section. With regard to the 2004 section, LNADW displays strong southward flow with a shallow reference level in the DWBC region

(Figure 2.12a, grey line). Deepening the 2004 section reference level reduces LNADW, which is then built back up to almost match its prior strength, but this necessitates a greater southward compensation (Figure 2.12a, blue line). The 2004 section compensation velocity shifts in a negative direction away from zero to ensure mass balance that is lost by a deeper reference level (Table 2.8).

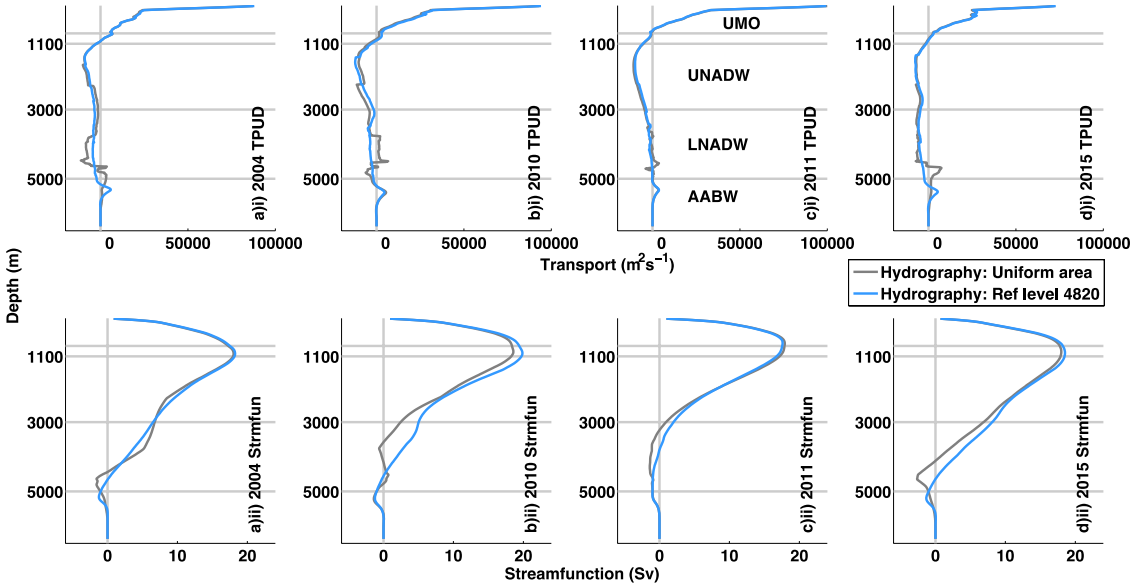

Figure 2.12: Hydrographic TPUD (m^2s^{-1}) profiles (top) and streamfunctions (bottom): a) 2004; b) 2010; c) 2011; d) 2015. All plots include a mean Florida Straits transport profile and mean Ekman transport. Grey plotlines show hydrographic transports for each section when a uniform area is imposed and blue plotlines represent the additional alteration of the shift to a deep reference level (4820 dbar).

Streamfunctions with a reference level altered to 4820 dbar (Figures 2.12a ii, 2.12b ii & 2.12d ii) resemble those produced by Smeed et al. (2014) where the deep return flow is pushed down within the basin. This streamfunction structure was also uncovered by Roberts et al. (2013) utilising model data and employing a RAPID methodology. Deepening the reference level changes the shape of the 2010 TPUD profile considerably (Figure 2.12b i). Once the reference level is deepened, the 2-lobed NADW shape emerges for the 2010 TPUD profile, as the deep return flow is redistributed lower down in the basin to the LNADW layer.

2.3.4 Hydrographic transports with WBW absolute transports

Absolute transports derived from current meters in the WBW region (from the western coast of the Bahamas to mooring WB2) are 10-day filtered before

inclusion with RAPID geostrophic transports. Here, these same absolute transports are picked to match the dates each hydrographic cruise collected data in this region and then averaged to produce a single profile for each section. Replacing the hydrography in the WBW region with absolute transports (Table 2.9 and Figure 2.13) weakens the 2010 MOC by 2.5 Sv but strengthens all other sections. The reduction in 2010 MOC strength almost mitigates the increase resulting from all previous alterations to the methodology (application of uniform section area and deepening of the reference level). The substantial reduction in the 2010 upper ocean total suggests that the WBW region is critical for determining downturn events. An overall MOC trend that matches the RAPID time-series is now visible, the trend conveys a weaker MOC in winter 2009-10 relative to spring 2004.

	Data	Hydrography			
	Method	1. Bottom triangles ignored & mean AABW 2. Uniform area for each depth layer 3. Reference level 4820 dbar 4. WBW absolute transport (west of WB2)			
	Year	2004	2010	2011	2015
	Compensation Velocity (m/s)	-0.0009	-0.0004	0.0000	-0.0008
Transport (Sv)	Ekman	3.5	3.5	3.5	3.5
	Florida Straits	31.5	31.5	31.5	31.5
	UMO z ≤ 800 m	-14.8	-18.1	-16.8	-16.3
	Upper Total	**20.2**	**16.9**	**18.2**	**18.7**
	AAIW 800 m < z ≤ 1100 m	0.5	0.1	-1.0	0.6
	UNADW 1100 m < z ≤ 3000 m	-12.9	-13.0	-15.5	-10.4
	LNADW 3000 m < z ≤ 5000 m	-8.7	-4.9	-2.7	-9.9
	AABW >5000m	1.0	1.0	1.0	1.0
	Lower Total	**-20.2**	**-16.9**	**-18.2**	**-18.7**

Table 2.9: Hydrographic transports (Sv) in depth classes with WBW absolute transports. Transports employ long-term mean Florida Straits transport and long-term mean Ekman transport. Northward transports are positive.

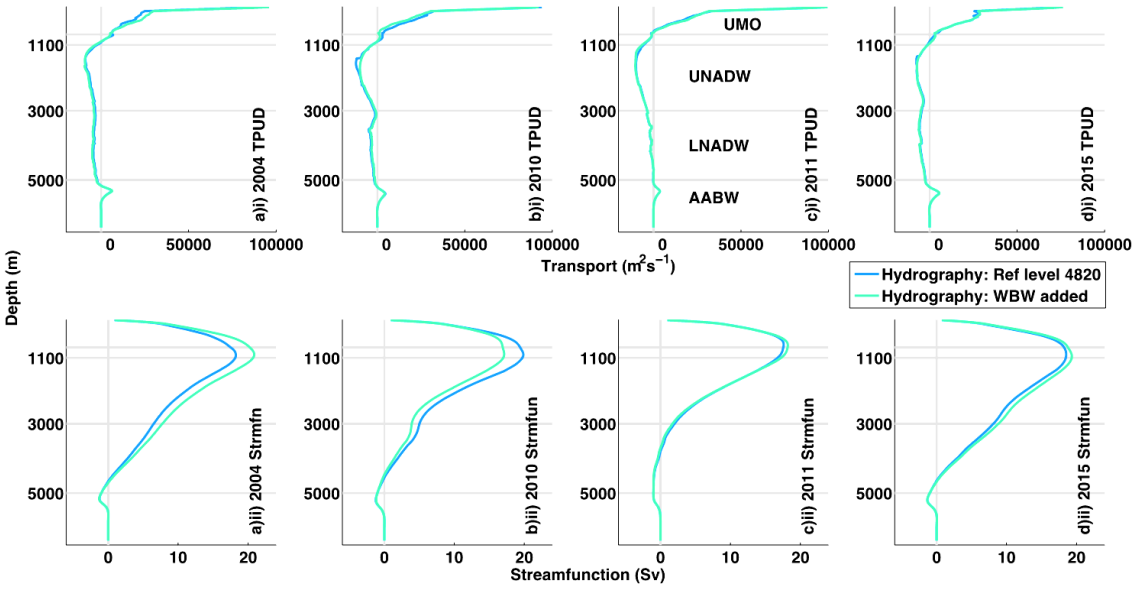

Figure 2.13: Hydrographic TPUD (m^2s^{-1}) profiles (top) and streamfunctions (bottom): a) 2004; b) 2010; c) 2011; d) 2015. All plots include a mean Florida Straits transport profile and mean Ekman transport. Blue plotlines represent hydrographic transports calculated with a deep reference level (4820 dbar) and green plotlines show the additional substitution of WBW absolute transports.

To explore the variation in WBW absolute transports, the time-series has been plotted along with the isolated hydrographic WBW transports (Figure 2.14). Mean WBW transports matching each hydrographic section, separated by depth class, can be compared with the hydrography in Table 2.10. It is evident that WBW absolute transports matched to the 2010 and 2011 sections are much lower than that of the data matched to the 2004 and 2015 sections. The 2010 and 2011 sections coincide with downturn events and the WBW region is likely key to defining such events.

Meinen et al. (2004) find that, near 26.5˚N, DWBC hydrographic geostrophic transports don't emulate absolute transports from Inverted Echo Sounder data, the correlation coefficient is 0.30. Meinen et al. (2004) then find the correlation coefficient between transports gained from Inverted Echo Sounder data and current meter data is 0.76. The practical constraints of collecting hydrographic profiles, such as the temporal gap between profiles, may limit capture of the large short-term variability in the WBW signal.

		2004		2010		2011		2015	
	Dataset	Hydrography	RAPID	Hydrography	RAPID	Hydrography	RAPID	Hydrography	RAPID
WBW Transports (Sv)	**UMO** z ≤ 800 m	0.6	3.9	4.1	1.1	1.3	1.8	1.2	2.1
	AAIW 800 m < z ≤ 1100 m	-0.1	0.0	0.4	0.0	-0.2	-0.4	-0.4	0.0
	UNADW 1100 m < z ≤ 3000 m	-0.6	0.2	-0.9	-0.3	0.8	-0.3	-0.9	-0.2
	LNADW 3000 m < z ≤ 5000 m	0.0	0.1	0.0	0.2	0.1	0.1	0.0	0.1
	Total	0.0	4.3	3.7	1.0	2.0	1.2	-0.2	2.0

Table 2.10: Cruise mean transports (Sv) in the WBW region for the hydrographic data compared to WBW absolute transports. Transports are displayed for each depth class. Northward transports are positive.

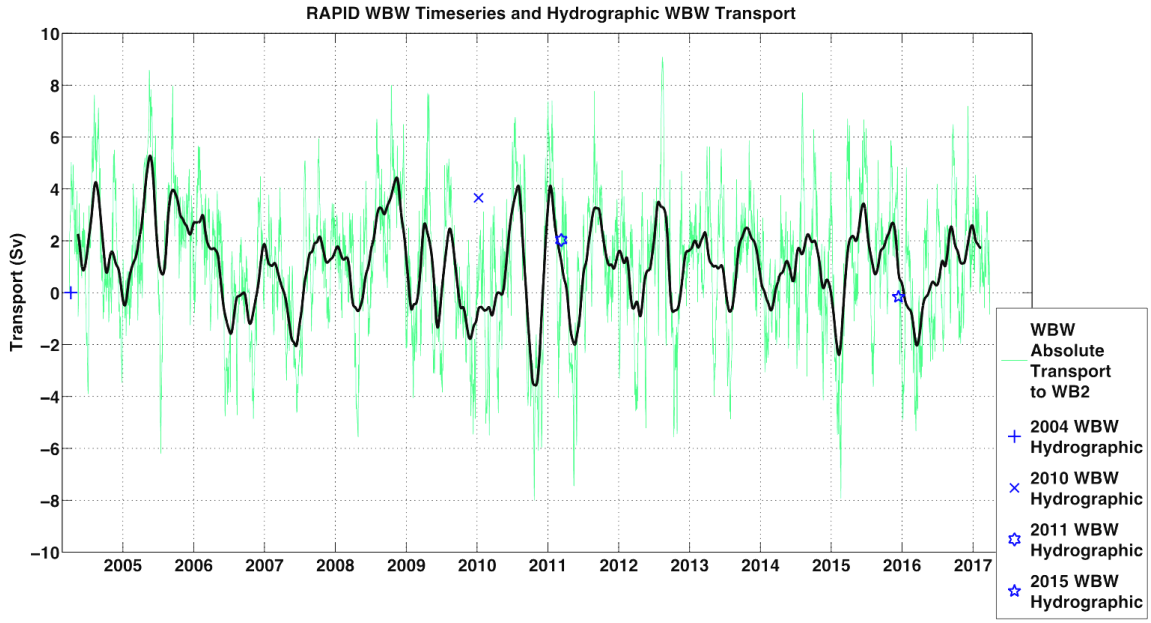

Figure 2.14: Total WBW absolute transports (Sv). Blue plot points represent hydrographic equivalents isolated to the same region of the basin. WBW Transports in green are 10-day low-pass filtered. Transports in black are 3-month low-pass filtered.

2.3.5 Hydrographic transports subsampled to RAPID boundary locations

The outcome of sub-sampling the basin to boundary locations, in the last stage of processing the hydrography, is found in Table 2.11 and Figure 2.15. The average MOC change for all four sections when subsampled to boundary locations is -1.9 ±1.3 Sv. These are substantial differences that are attributable to altering the eastern extent of the hydrographic section data to match the RAPID eastern boundary location (see Figures 2.2 & 2.16). This changes transports up to the eastern boundary by shifting the west-east dynamic height gradient.

	Data	Subsampled Hydrography			
	Method	1. Bottom triangles ignored & mean AABW 2. Uniform area for each depth layer 3. Reference level 4820 dbar 4. WBW absolute transport (west of WB2)			
	Year	2004	2010	2011	2015
	Compensation Velocity (m/s)	-0.0012	-0.0006	-0.0008	-0.0012
Transports (Sv)	Ekman	3.5	3.5	3.5	3.5
	Florida Straits	31.5	31.5	31.5	31.5
	UMO z ≤ 800 m	-18.5	-19.8	-19.1	-16.4
	Upper Total	**16.5**	**15.2**	**15.9**	**18.6**
	AAIW 800 m < z ≤ 1100 m	0.9	0.1	-0.8	1.2
	UNADW 1100 m < z ≤ 3000 m	-8.3	-11.3	-8.4	-8.9
	LNADW 3000 m < z ≤ 5000 m	-10.1	-5.1	-7.8	-11.9
	AABW >5000m	1.0	1.0	1.0	1.0
	Lower Total	**-16.5**	**-15.2**	**-15.9**	**-18.6**

Table 2.11: Hydrographic transports (Sv) in depth classes where data is sub-sampled to four boundary profiles. Transports employ long-term mean Florida Straits transport and long-term mean Ekman transport. Methodological deviations from the hydrographic method are listed in the second row. Northward transports are positive.

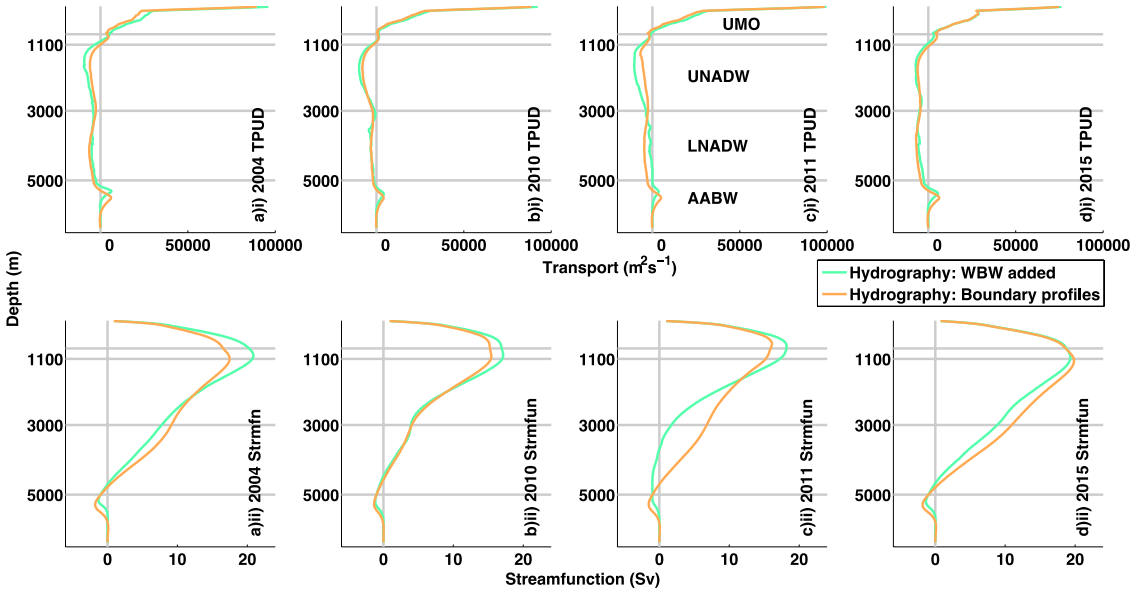

Figure 2.15: Hydrographic TPUD (m^2s^{-1}) profiles (top) & streamfunctions (bottom): a) 2004; b) 2010; c) 2011; d) 2015. All plots include a mean Florida Straits transport profile and mean Ekman transport. Green plotlines show hydrographic transports with WBW absolute transports and gold plotlines show the addition of subsampling to boundary locations.

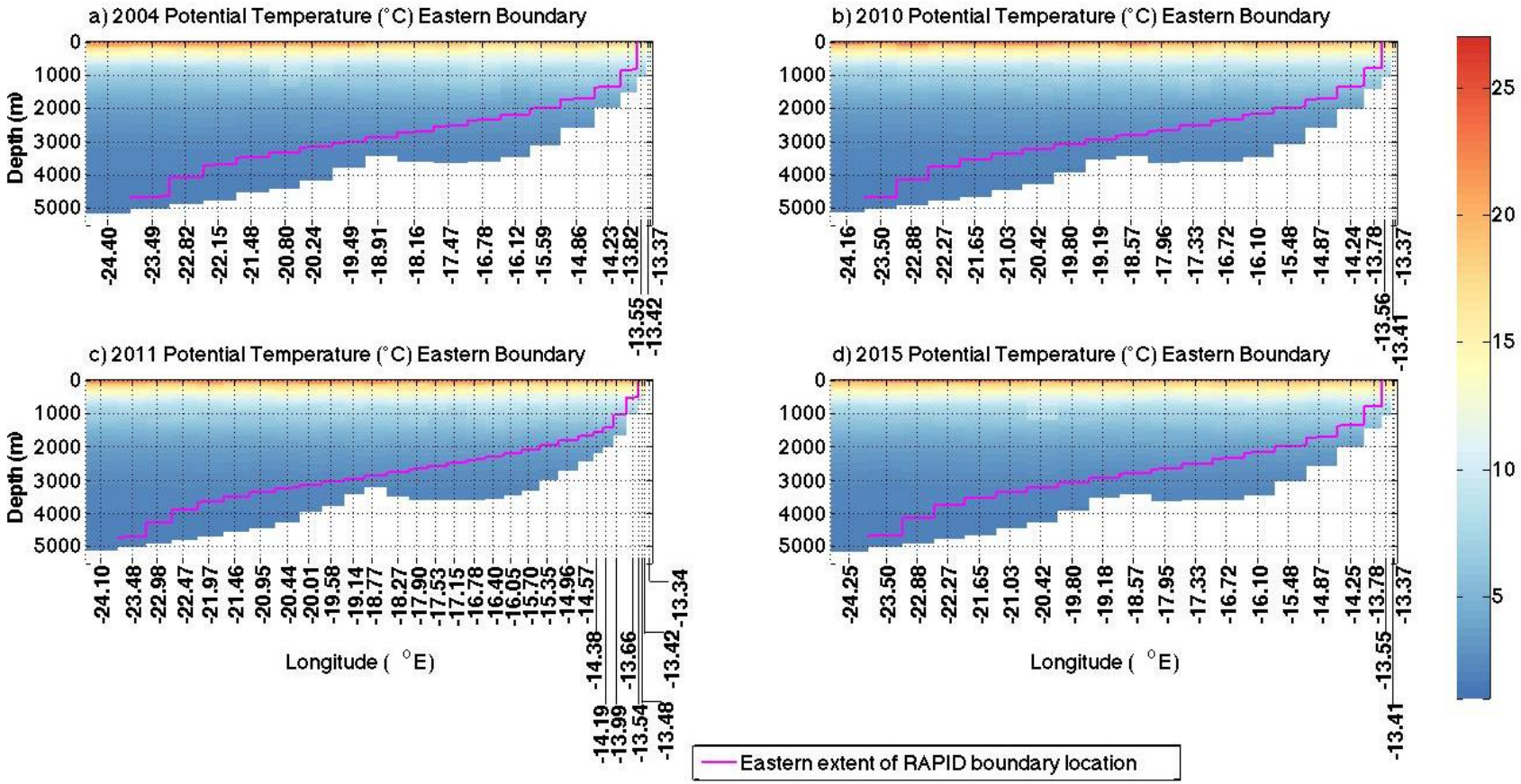

Figure 2.16: Eastern basin hydrographic sections of potential temperature (°C): a) 2004; b) 2010; c) 2011; d) 2015. The edge of the eastern boundary location is superimposed (pink). The eastern boundary location is the temporal average of the RAPID mooring locations, graduated through the depth of the basin. Each Longitudinal value along the x-axis represents the location of each profile/station.

Figure 2.16 illustrates the eastern side of the hydrographic basin with the edge of the eastern boundary location superimposed. The eastern boundary location is the temporal average of the RAPID mooring locations, graduated through the depth of the basin.

Pérez-Hernández et al. (2015) identify the eastern boundary as the source of the AMOC seasonal cycle, which has a magnitude of 6 Sv. Thus, omission of the far eastern hydrographic profiles beyond the RAPID eastern boundary location (Figure 2.16) may reduce this source of seasonal variability. This should enable a more direct comparison between each section.

There is evidence that the spatial pattern of wind stress curl at the bottom of the Canary Islands results in a pumping effect that causes deep density fluctuations (Duchez et al., 2014). This may serve as another salient reason to alter the eastern extent of the section to the RAPID eastern boundary profile.

Where the basin is subsampled in space there is a homogenisation of the TPUD profiles such that there is greater similarity across the 4 sections (Figure 2.15). There are two consistent changes for all four sections: total southward UNADW transports decrease and the compensation becomes a stronger negative value. The lessening distinction between the profiles for each section can be traced to the strengthening southward compensation velocity, as this is applied uniformly across the basin and forces a transport profile onto each section that is relative to section area at each depth level. These un-sampled regions, or bottom triangles, could result in the RAPID AMOC results underestimating AMOC strength by ~1.9 Sv on average. This ~1.9 Sv underestimation caused by subsampling the basin to boundary regions is similar to the bottom triangle error of 1.5 Sv found by McCarthy et al. (2015a) and 1-2 Sv error found by Sinha et al. (2017).

2.3.6 RAPID transports temporally matched to hydrographic transports

To investigate whether the profile structure found with the hydrographic sections (subsampled to boundary locations) persists with regard to RAPID data, RAPID transports are calculated for comparison. RAPID data are selected to mimic the offset in time across the basin inherent in the hydrographic section equivalent. Thus, the outcome of west-east basin aliasing will be prevalent in both to allow direct comparison. The results can be found in Table 2.12 and Figure 2.17. Each segment in Table 2.12 is colour-matched to the profiles found in Figure 2.17. RAPID 12-hourly profiles, without a temporal offset, are also plotted in Figure

2.17 for comparison (grey through cyan lines), in addition to the mean profile for the cruise duration (purple lines). The wide range in the streamfunction maximum amongst the 12-hourly profiles highlights the extent to which temporal aliasing over the course of a month can have an impact on transports. The hydrographic data for all four section profiles falls within the scope of the RAPID 12-hourly profiles (without temporal offset).

	Data	Subsampled hydrography				RAPID			
	Method	1. Bottom triangles ignored & mean AABW 2. Uniform area for each depth layer 3. Reference level 4820 dbar 4. WBW absolute transport (west of WB2)				1. Temporal offset for profiles to match hydrography			
	Year	2004	2010	2011	2015	2004	2010	2011	2015
	Compensation Velocity (m/s)	-0.0012	-0.0006	-0.0008	-0.0012	-0.0011	-0.0003	-0.0001	-0.0011
Transports (Sv)	Ekman	3.5	3.5	3.5	3.5	3.5	3.5	3.5	3.5
	Florida Straits	31.5	31.5	31.5	31.5	31.5	31.5	31.5	31.5
	UMO z ≤ 800 m	-18.5	-19.8	-19.1	-16.4	-18.3	-21.3	-20.3	-17.6
	Upper Total	**16.5**	**15.2**	**15.9**	**18.6**	**16.7**	**13.7**	**14.7**	**17.4**
	AAIW 800 m < z ≤ 1100 m	0.9	0.1	-0.8	1.2	0.5	-0.1	-1.2	0.7
	UNADW 1100 m < z ≤ 3000 m	-8.3	-11.3	-8.4	-8.9	-8.8	-12.3	-12.3	-8.4
	LNADW 3000 m < z ≤ 5000 m	-10.1	-5.1	-7.8	-11.9	-9.4	-2.4	-2.2	-10.7
	AABW >5000m	1.0	1.0	1.0	1.0	1.0	1.0	1.0	1.0
	Lower Total	**-16.5**	**-15.2**	**-15.9**	**-18.6**	**-16.7**	**-13.7**	**-14.7**	**-17.4**

Table 2.12: Hydrographic transports (Sv) and RAPID transports, in depth classes, calculated with the RAPID method. Transports employ long-term mean Florida Straits transport and long-term mean Ekman transport. Transports are calculated for hydrographic (gold) and RAPID (red) data. The hydrography has been subsampled to the RAPID boundary locations then processed with the RAPID method. RAPID transports have been calculated with an offset in time to match the east-west temporal offset of the hydrography. Northward transports are positive. The table is color-matched to Figure 2.17.

Regarding the RAPID 12-hourly profiles without temporal offset (Figure 2.17, grey through cyan lines), the 2010 and 2011 profiles for the first half of both cruise durations display weaker southward LNADW. This may relate to downturn events.

Table 2.12 contains RAPID transports calculated using the data offset in time to match the hydrography (Table 2.12, red), relative to the hydrography (Table 2.12, gold), which convey agreement in both datasets. Both datasets agree that the 2010 MOC is the weakest, the 2011 MOC is stronger than the 2010 MOC, the 2004 MOC is stronger than the 2011 MOC and the 2015 MOC is the strongest.

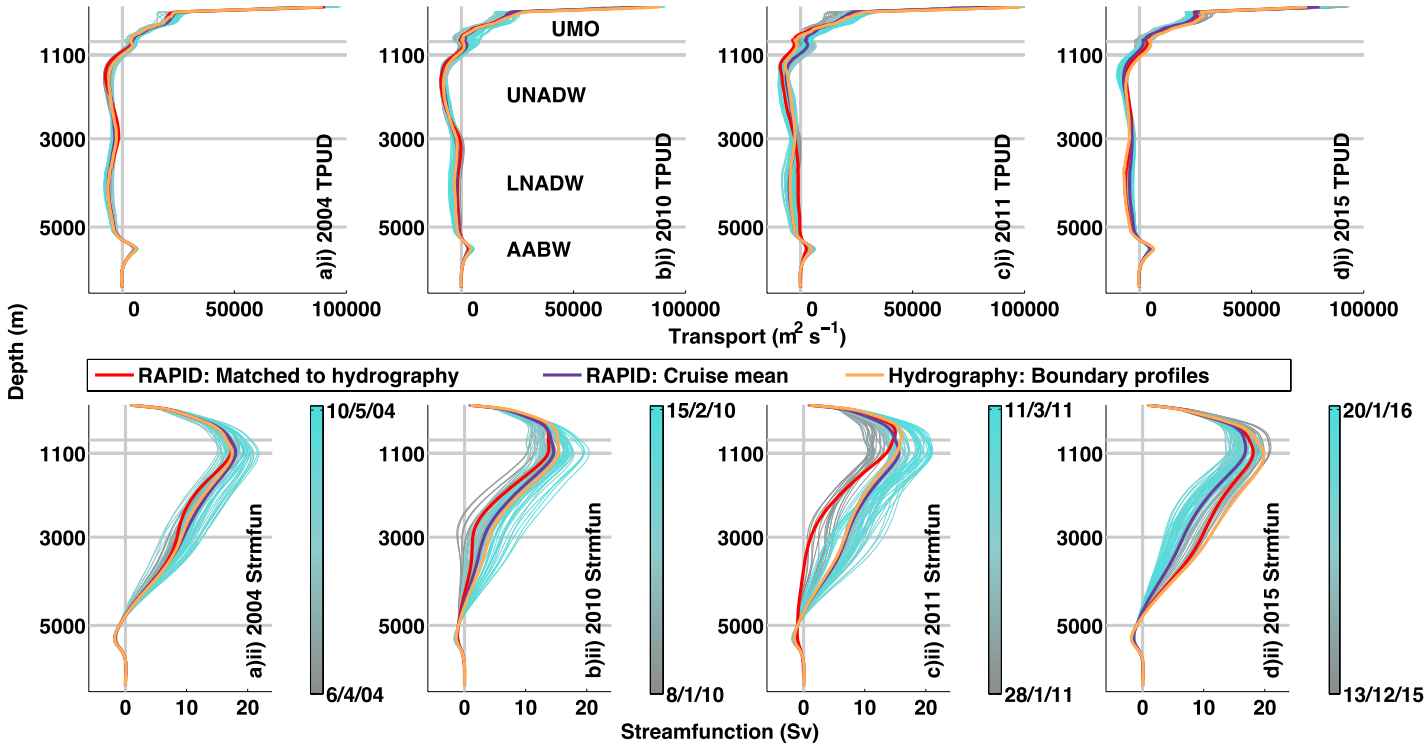

Figure 2.17: Hydrographic TPUD (m^2s^{-1}) profiles (top) and streamfunctions (bottom): a) 2004; b) 2010; c) 2011; d) 2015. All plots include a mean Florida Straits transport profile and mean Ekman transport. Transports are calculated for hydrographic (gold) and RAPID (red) data. The hydrography has been subsampled to the boundary locations. RAPID transports have been offset in time to match the east-west temporal offset of the hydrography. Mean RAPID transports for the cruise duration are also included (purple). The grey-to-cyan profiles are the 12-hourly RAPID transports (10-day low-pass filtered) for the cruise duration (the colour bar denotes the cruise date). Northward transports are positive.

RAPID transports calculated using the time-series data offset in time to match the hydrography (Table 2.12, red), relative to the hydrography (Table 2.12, gold), exhibit reduced southward compensation velocity, by an average of 0.0003 (m/s). A compensation velocity of 0.0003 (m/s) is the equivalent of 8.4 Sv transport. The hydrographic results (spatially sub-sampled to the boundaries, gold lines) are not unlike the RAPID equivalents (red lines), the mean difference in the total MOC is -0.9 ±0.7 Sv. TPUD profiles and corresponding streamfunctions (Figure 2.17) indicate a reasonably good agreement between the datasets. The compensation velocity counterbalances internal transports to produce alignment. The average compensation for the spatially subsampled hydrographic transports is -0.0009 m/s, which equates to -27.3 Sv transport. The average compensation for the temporally subsampled RAPID transports is -0.0007 m/s, which translates to transport of -18.9 Sv. The difference in average compensation between the two datasets is due to the difference in the underlying dynamic height data.

Innate differences between the two datasets are investigated in the dynamic height profiles (Figure 2.18). Analysis of dynamic height profiles can also help to determine the impact of short-term aliasing created by the physical limitation of performing CTD casts on a ship traversing the section. Figure 2.18 contains plots for each boundary profile with respect to the mean of the 12-hourly transports for the duration of the cruise. Profiles are plotted for the spatially subsampled hydrography (gold lines) and temporally subsampled RAPID (red lines) dynamic height values. The 12-hourly transports for the duration of each cruise are underlaid (grey to purple lines). The 2004 and 2011 hydrographic eastern profiles lie outside the range of the RAPID 12-hourly equivalents. The near-surface differences are the result of small-scale distortions, such as eddies, that are mitigated by western boundary profile data, particularly with regard to the 2004 section. The compensation velocity also mitigates the differences in internal transports caused by differences in the dynamic height data, as is the case with the 2011 section.

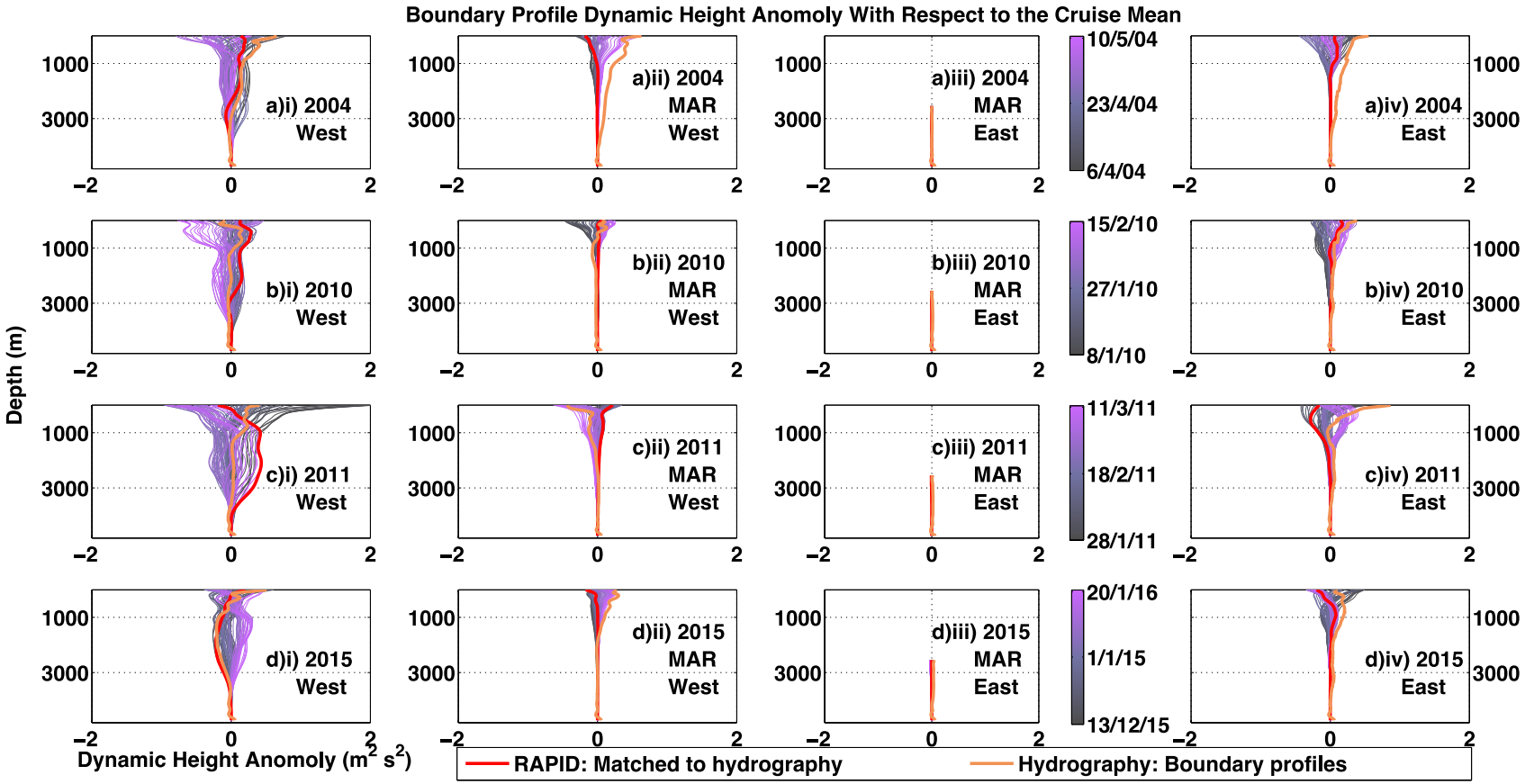

Figure 2.18: Hydrographic (subsampled to boundary locations, gold) and RAPID (red) boundary dynamic height profiles (m^2/s^2) with respect to the RAPID cruise mean at each boundary location: a) 2004; b) 2010; c) 2011; d) 2015. The grey-to-plum profiles represent 12-hourly RAPID dynamic height profiles (10-day low-pass filtered) for the cruise duration (the colour bar denotes the cruise date), with respect to the mean.

2.3.7 The evolution of hydrographic transports

Each cumulative evolutionary change in the methodology from the hydrographic method to the RAPID method, applied to hydrographic data, can be seen in the TPUD profiles and streamfunctions plotted in Figure 2.19. Figure 2.19 includes long-term mean Florida Straits transport and long-term mean Ekman transport. Total layer transports are visualised in Figure 2.20, where the totals are exclusive of long-term mean Florida Straits transport and long-term mean Ekman transport. Transports calculated with RAPID data, where profiles are offset to emulate the hydrographic temporal offset for boundary locations, are included for comparison in Figure 2.19 and Figure 2.20 (plotted in red). Figure 2.19 and Figure 2.20 are colour-matched to Tables 2.5, 2.7, 2.8, 2.9, 2.11 and 2.14, with each plotline/bar representing an additional process applied to the profiles so the cumulative effect of each change can be assessed.

The hydrographic 2004 and 2015 TPUD and streamfunction plots are consistent throughout the evolution of the methodological changes (Figure 2.19a ii & 2.19d ii) and they also match favourably with the RAPID equivalent both qualitatively and quantitatively. The high degree of alignment amongst the 2004 and 2015 streamfunctions supports agreement in the underlying data and increases confidence in the procedures of data collection and processing. This consistency may be a product of lesser short-term variance in flow zonally across the basin and/or temporally over the duration of the 2004 and 2015 hydrographic cruises. The relatively greater clustering of the 12-hourly RAPID transports for the cruise duration (Figures 2.17a & 2.17d) provides evidence for reduced short-term variance. The difference amongst the 2004 hydrographic profiles (Figure 2.19a) are due to initial bias created by a section area that largely differs from the other sections and short-term aliasing of the signal found in the WBW region.

The 2010 and 2011 section profiles (Figures 2.19b & 2.19c) display much greater change through each evolutionary stage from the hydrographic method to the RAPID method. These sections fall during downturn events, thus inherent differences in the internal transports are highly likely to affect the outcome of each methodological alteration.

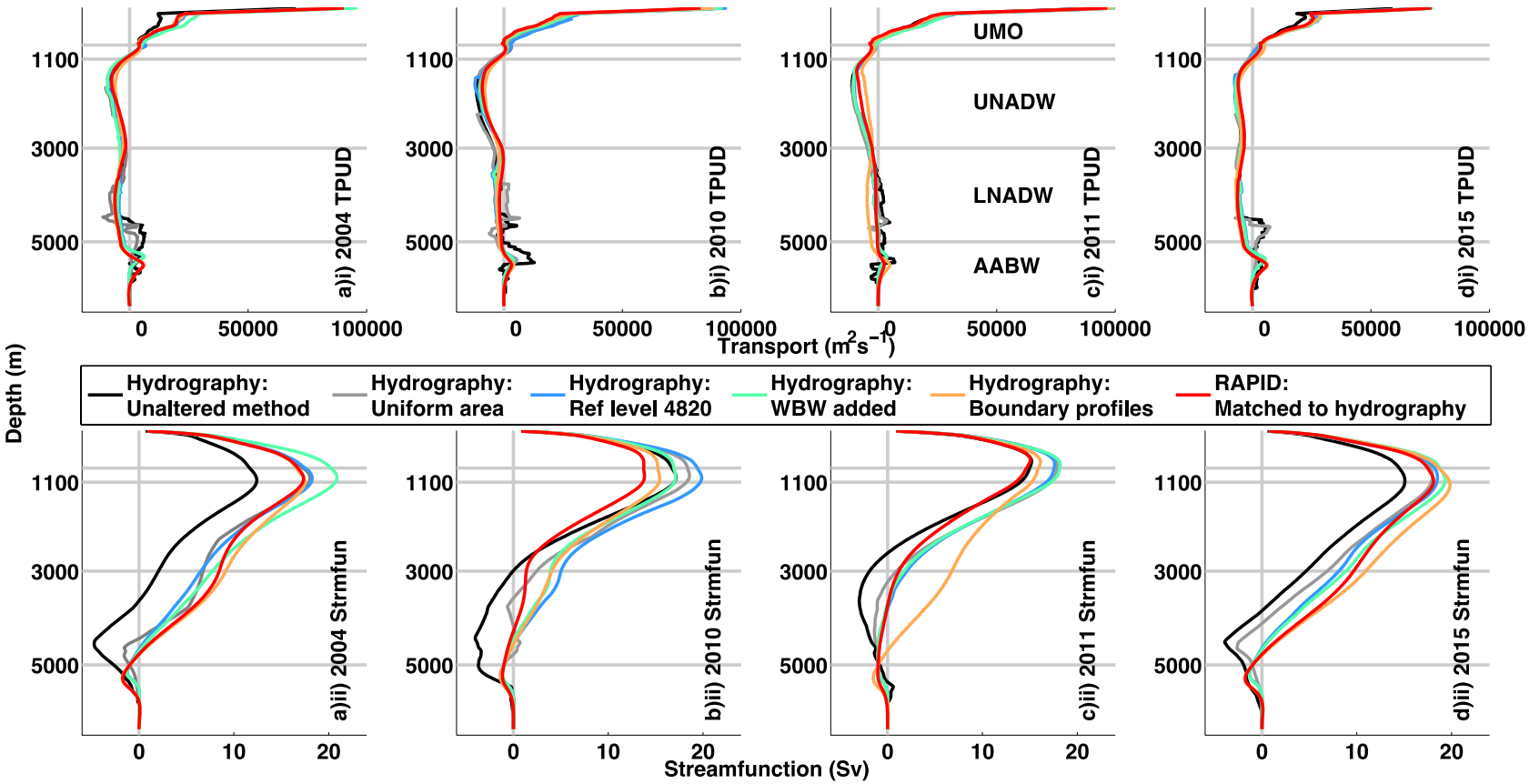

Figure 2.19: Hydrographic TPUD (m^2s^{-1}) profiles (top) and streamfunctions (bottom): a) 2004; b) 2010; c) 2011; d) 2015. All plots include a mean Florida Straits transport profile and mean Ekman transport. Profiles within each subplot (black, grey, blue, green, gold) show the evolutionary change in the results from the hydrographic method to the RAPID method. The RAPID equivalent (red) is included for comparison.

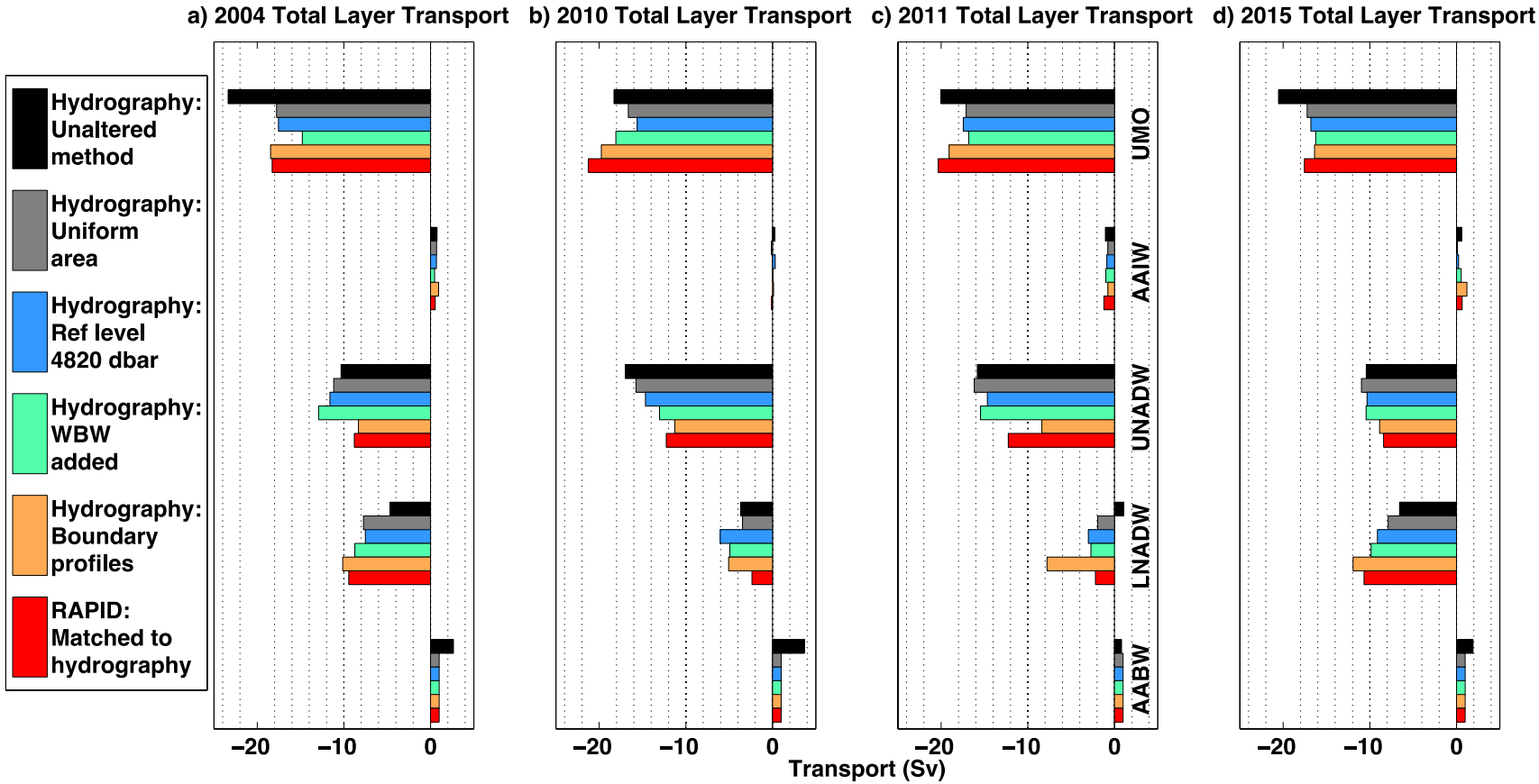

Figure 2.20: Layer transports: a) 2004; b) 2010; c) 2011; d) 2015. All plots exclude both mean Florida Straits transport profile and mean Ekman transport. Bars within each subplot (black, grey, blue, green, gold) show the evolutionary change in the results from the hydrographic method to the RAPID method. The RAPID equivalent (red) is included for comparison.

There is a structural shape in the streamfunctions shared by the 2004 and 2015 (Figures 2.19a ii & 2.19d ii) data that persists regardless of the changes made in the methodology. The structure, beginning at the base of the streamfunction, sets off with strong AABW northward flow that persists from the bottom of the basin up to almost 4500 m. Then, at ~4500 m the streamfunction sharply switches to southward flow due to LNADW and UNADW transports, the maximum streamfunction is reached at 1000 m depth at which point the streamfunction conveys northward flow due to the mean Florida Straits transport profile. The 2010 and 2011 section streamfunctions (Figures 2.21b & 2.21c) do not display the same consistency.

2.3.8 East-west cumulative layer transports

The east-west cumulative layer transports defined by depth class (Figure 2.21) show zonal variation. Hydrographic and RAPID data are not comparable within the AABW depth range and so the plots are not included. It should be noted that the black and grey lines are often co-located within the plots, as are the blue with the green and the gold with the red. Figure 2.22 displays the same data but where the compensation velocity has been subtracted (i.e. just the internal component is summed from east-to-west).

There is a lot of noise on the western side of the 2010 and 2011 UMO layers (Figure 2.21). This is indicative of eddy activity and is backed-up by the oxygen concentration data (Figure 2.8), potential temperature data (Figure 2.3) and absolute salinity data (Figure 2.5). An upward spike of low oxygen levels can be seen at ~65°W in the 2010 oxygen concentration data. The salinity data echoes this upward dip to further confirm high eddy activity, which affects basin-wide total transports. Eddy activity creates ~2.3 Sv root mean square (RMS) variability to upper ocean transports according to Kanzow et al. (2010).

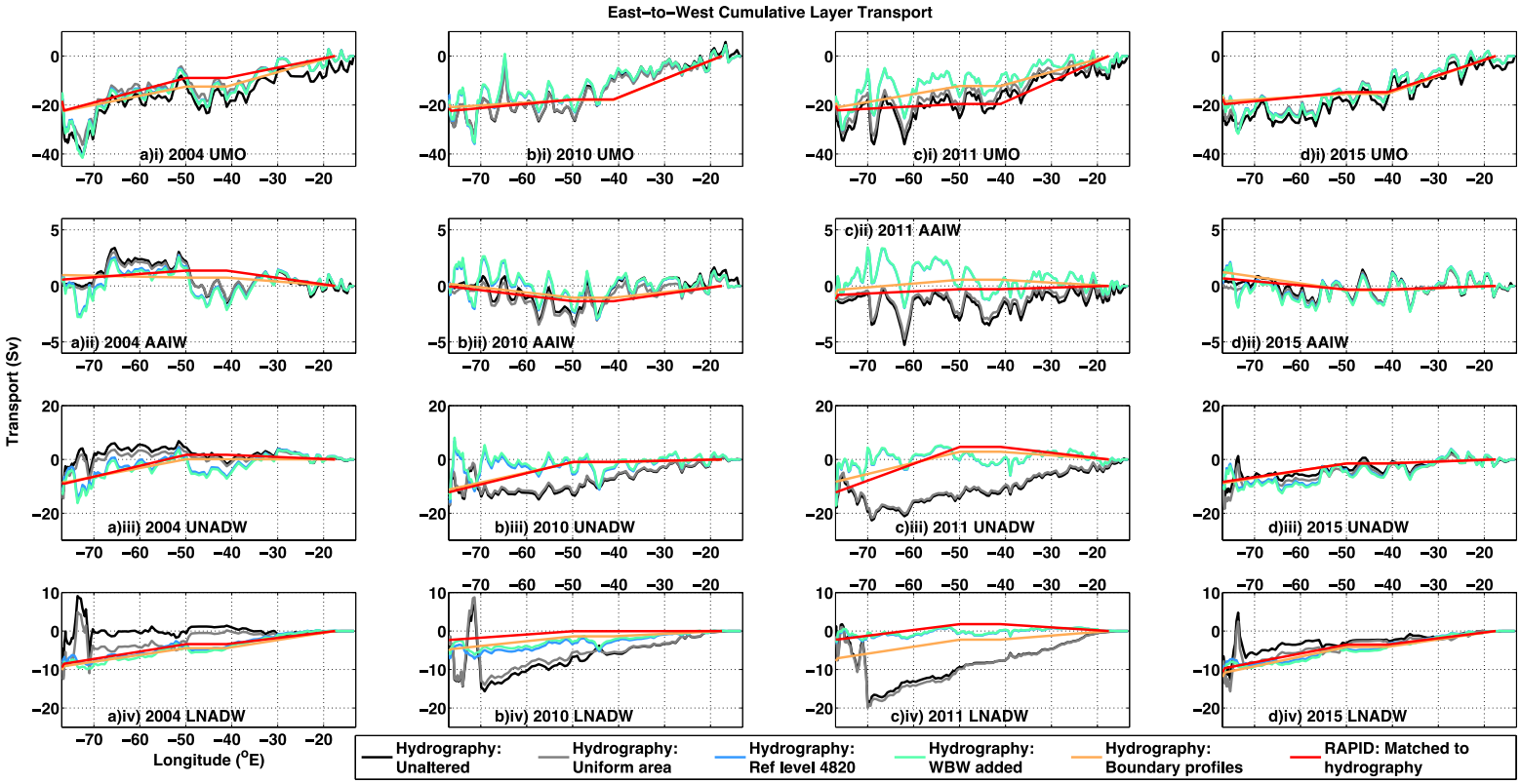

Figure 2.21: Cumulative layer transports, with compensation subtracted, summed from east-to-west for each hydrographic section: a) 2004; b) 2010; c) 2011; d) 2015. All plots exclude mean Florida Straits transport and mean Ekman transport. Plotlines within each subplot (black, grey, blue, green, gold) show the evolutionary change in the hydrographic data from the hydrographic method to the RAPID method. The RAPID equivalent (red) is included for comparison. Plots are displayed for each layer as determined by depth class. Note the different y-axis scaling for each layer. Northward transports are positive.

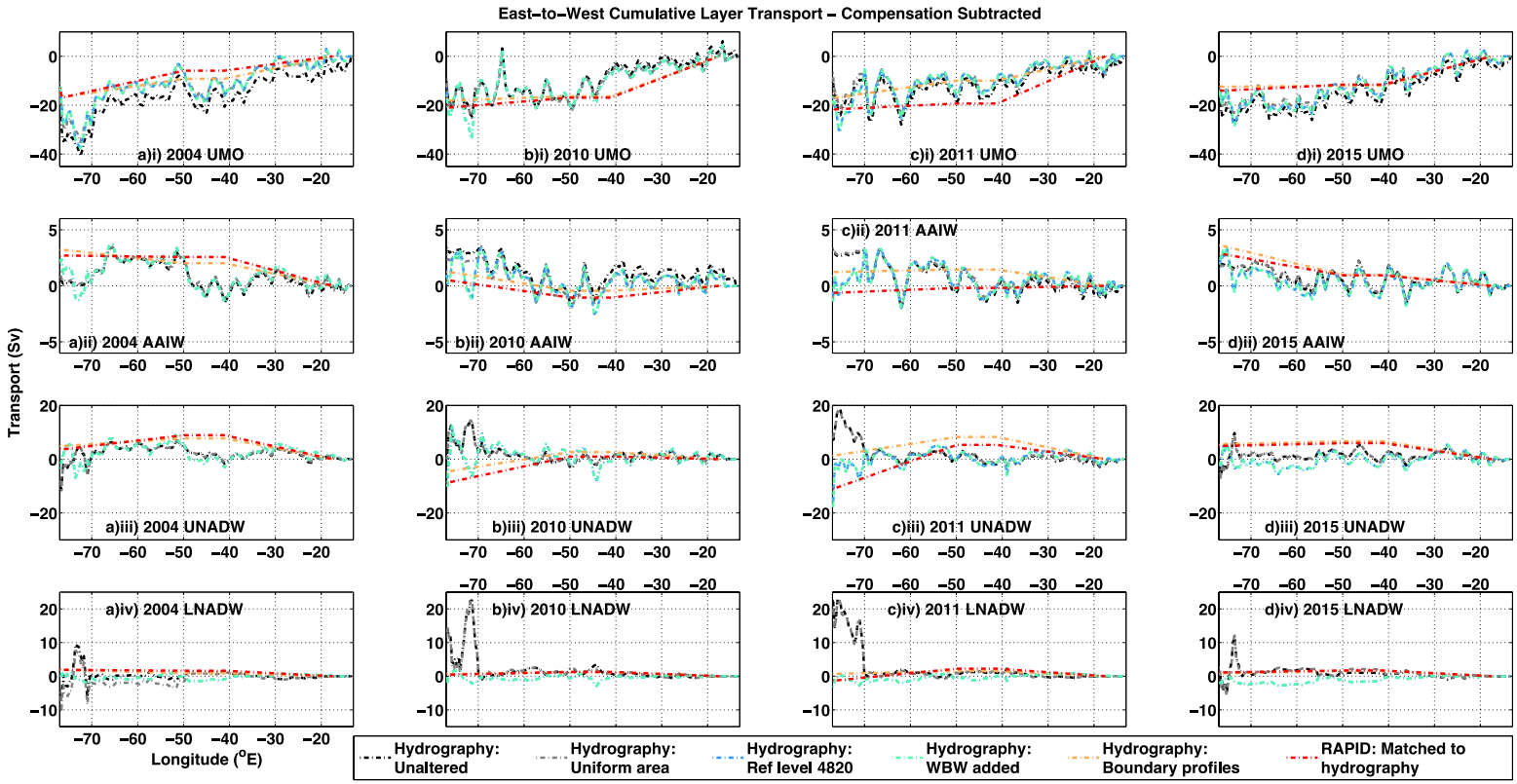

Figure 2.22: Cumulative layer transports, with compensation subtracted, summed from east-to-west for each hydrographic section: a) 2004; b) 2010; c) 2011; d) 2015. All plots exclude both mean Florida Straits transport and mean Ekman transport. Plotlines within each subplot (black, grey, blue, green, gold) show the evolutionary change in the data from the hydrographic method to the RAPID method. The RAPID equivalent (red) is included for comparison. Plots are displayed for each layer as determined by depth class. Note the different y-axis scaling for each layer. Northward transports are positive.

With regard to the 2010 and 2011 sections, the total southward UNADW flow and total southward LNADW flow remain similar for each methodological alteration, despite the large shift within the main basin (Figures 2.21). This accumulation to similar totals is due to the compensation. The compensation adjustment that maintains similar total deep transports comes at the cost of shifting transports zonally across the entire basin. Figure 2.22 shows that, for the deep layers, compensation would be more appropriately applied to just the DWBC region, due to differences when compared to Figure 2.21. Figure 2.22 shows that, where a shallow reference level is employed at the western boundary (dashed black and grey lines), internal transports (without compensation transports) for the UNADW and LNADW layers accumulate to almost zero from the eastern side of the basin until the DWBC region where transports are large. This matches previous findings that show the velocities arising from DWBC fluctuations are spatially highly variable at the western boundary (Johns et al., 2008; Bryden et al., 2009) rather than uniformly distributed over the total basin area. Figure 2.22 also identifies the LNADW and UNADW layers as most affected by the compensation, the UMO layer is relatively unaffected.

The most substantial shift in the accumulated east-west layer transports (Figure 2.21) is seen when the reference level switches from shallow (1000 dbar at the western boundary and 3200 dbar in the main basin) to deep (4820 dbar basin-wide). With regard to the 2010 and 2011 sections, Figure 2.22 shows that total UNADW and LNADW transports are northward flowing with a shallow reference level before compensation is added. The 2010 and 2011 sections are timed within downturn events. This tallies with weaker / restricted DWBC flow seen in oxygen concentration data for the 2010 and 2011 sections (Figure 2.8). For the 2010 and 2011 sections, a shallow reference level needs a larger negative compensation to ensure mass balance. After the reference level is deepened, the 2010 and 2011 UNADW and LNADW total transports are reduced to almost zero and thus are without the need of strong southward compensation (Figure 2.22). The application of a separate reference level at the western boundary would therefore make for an insightful change to RAPID transports, allowing analysis on a temporally continuous dataset.

Switching from a shallow to a deep reference level has little impact on the 2004 and 2015 section layer transports (Figure 2.21 and Figure 2.22). The compensation velocity is able to adjust layer transports such that the end result is very similar regardless of the reference level.

Temporally subsampled RAPID data are in good agreement with the hydrography subsampled to the boundaries (Figure 2.21, red line and gold line, respectively). The exception being 2011 transports (Figure 2.21c & 2.22c). This implies a fundamental disagreement in the geostrophic velocities for the two datasets.

2.3.9 Cruise mean Ekman transports and Florida Straits transports

Cruise mean Ekman transports and cruise mean Florida Straits transports are substituted into the calculation, with a RAPID methodology, seen in Table 2.13. This allows long-term trends in transports to be discerned across time for both the hydrographic (yellow columns) and RAPID (magenta columns) datasets. Cruise mean RAPID transports are calculated for each 12-hourly interval over the duration of the cruise with no temporal offset (Table 2.13, maroon columns). Standard deviations are given in italics. The majority of hydrographic transports (yellow columns) fall within two standard deviations of the hydrographic mean with no temporal offset (maroon columns). Exceptions to this are 2011 and 2015 AAIW transports (underlined in Table 2.13) that reside within 3 standard deviations of the mean, which is a considerable bound. RAPID transports with temporal offset in 2011 (AAIW and LNADW) also fall outside 2 standard deviations of the mean for RAPID transports calculated without a temporal offset. The source of variation between RAPID transports is the temporal offset from west-to-east across the basin. This isolates short-term aliasing as the source of the discrepancy.

The hydrographic and RAPID transports, processed with the same method and isolated to the same time intervals, show similar trends. The 2010 average MOC is the weakest, it also exhibits the weakest southward LNADW flow. Figure 2.23 plots the hydrographic transports over the RAPID time-series transports to show that AMOC short-term variability encompasses those values found with the hydrography.

Data	Subsampled hydrographic data				RAPID boundary data				RAPID boundary data							
Method	1. Bottom triangles ignored & mean AABW 2. Uniform area for each depth layer 3. Reference level 4820 dbar 4. WBW absolute transport (west of WB2)				1. Temporal offset for profiles to match hydrography				1. No temporal offset 2. Mean transport for cruise duration ± 1 standard deviation							
Year	2004	2010	2011	2015	2004	2010	2011	2015	2004		2010		2011		2015	
Compensation Velocity (m/s)	-0.0012	-0.0004	-0.0009	-0.0012	-0.0011	-0.0001	-0.0001	-0.0011	-0.0012	*± 0.0002*	-0.0002	*± 0.0002*	-0.0009	*± 0.0002*	-0.0008	*± 0.0003*
Ekman	4.5	-1.1	3.9	3.8	4.5	-1.1	3.9	3.8								
Florida Straits	31.3	30.3	32.2	31.4	31.3	30.3	32.2	31.4								
UMO (0-800 m)	-18.6	-18.8	-19.3	-16.4	-18.4	-20.3	-20.5	-17.6	-17.9	*± 1.7*	-19.8	*± 2.6*	-20.2	*± 3.5*	-18.4	*± 2.0*
Upper Total	**17.2**	**10.4**	**16.8**	**18.8**	**17.4**	**8.9**	**15.6**	**17.6**								
AAIW (800-1100 m)	0.9	0.5	-0.8	1.2	0.5	0.3	-1.3	0.6	0.8	*± 0.4*	0.8	*± 0.6*	0.5	*± 0.6*	0.1	*± 0.5*
UNADW (1100-3000 m)	-8.6	-9.0	-8.8	-9.0	-9.1	-9.9	-12.7	-8.5	-8.9	*± 1.4*	-9.0	*± 2.0*	-9.1	*± 2.3*	-10.1	*± 1.9*
LNADW (3000-5000 m)	-10.4	-3.0	-8.2	-12.0	-9.7	-0.3	-2.6	-10.7	-10.7	*± 2.2*	-2.0	*± 2.1*	-8.4	*± 2.2*	-7.7	*± 3.4*
AABW (>5000m)	1.0	1.0	1.0	1.0	1.0	1.0	1.0	1.0								
Lower Total	**-17.2**	**-10.4**	**-16.8**	**-18.8**	**-17.4**	**-8.9**	**-15.6**	**-17.6**								

Table 2.13: Hydrographic transports (Sv) and RAPID transports, in depth classes, calculated with the RAPID method. Transports employ cruise mean Florida Straits transports and cruise mean Ekman transports. Transports are calculated for hydrographic (yellow) and RAPID (pink) data. The hydrographic sections have been processed with the RAPID method. RAPID transports have been calculated with profiles offset in time to match the east-west temporal offset of the hydrography. Mean RAPID transports (± 1 standard deviation, highlighted in italics) for each hydrographic cruise, where the profiles have not been offset in time, are also included (maroon). Hydrographic data that fall beyond 2 standard deviations of the RAPID cruise mean are underlined. Northward transports are positive.

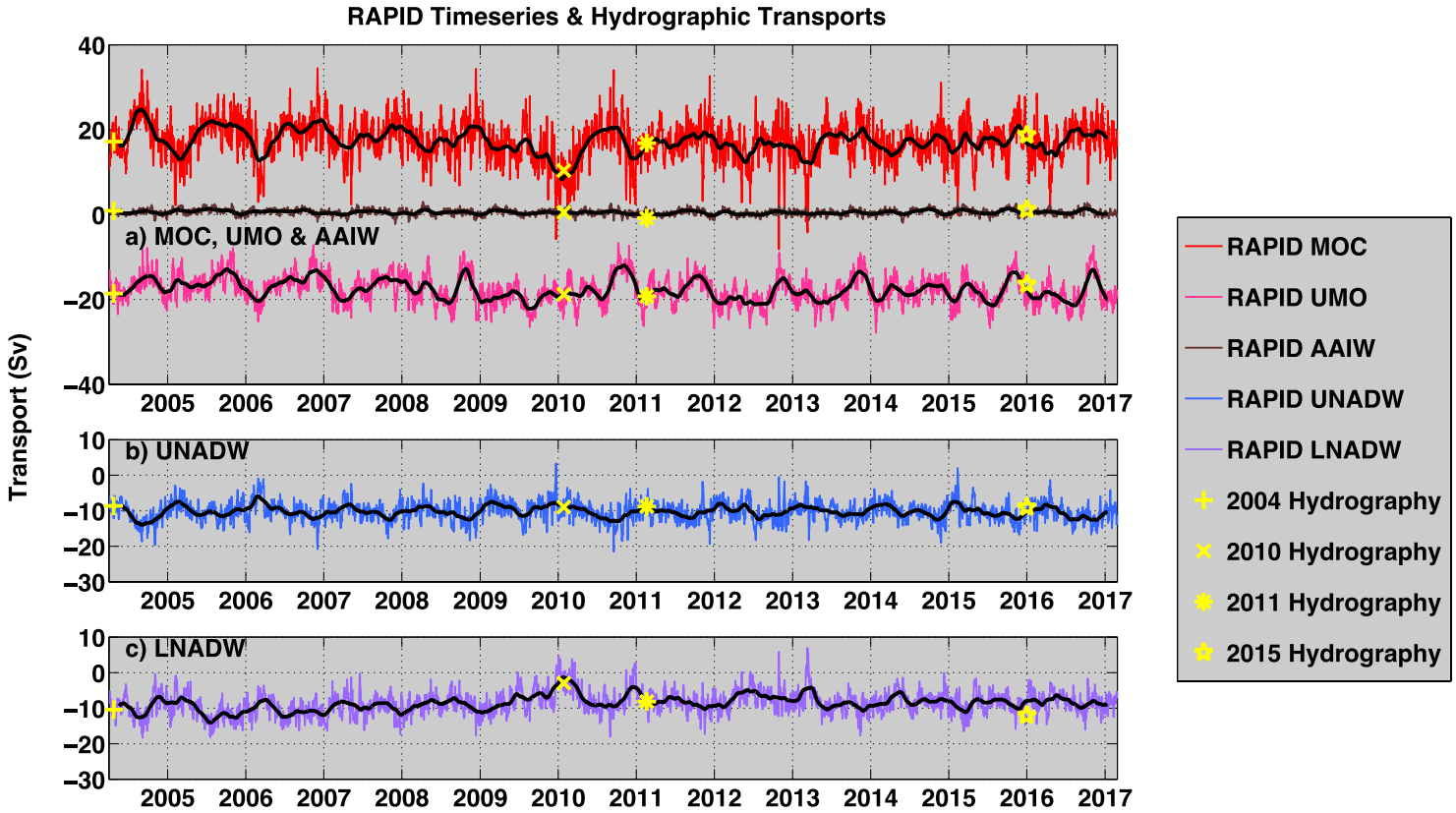

Figure 2.23: RAPID layer transports (10-day low-pass filtered) where hydrographic equivalents have been superimposed (yellow). Transports are inclusive of compensation. Northward transports are positive. Transports are calculated using time variable Florida Straits transports and time variable mean Ekman transports. Transports in black are 3-month low-pass filtered.

2.4 Limitations and uncertainties

Sources of observational data will suffer from measurement errors, missing data, outlying data, different equipment types, instrument bias, different spatial-temporal sampling method and different calibration methods. Hydrographic data are collected during different seasonal conditions, affecting surface and AAIW transports. The hydrography has good spatial resolution but is aliased due to coarse temporal sampling. RAPID data has high temporal resolution but relatively poor spatial resolution, thus the calculation of transports is based on four boundary profiles. These four profiles are the composite of numerous mooring profiles that provide an accurate template of temporal variation at key locations that capture the full MOC. Mooring data errors, due to mooring motion (particularly nearer the surface where there are strong currents) and fouling of sensors by marine life, are eliminated by the gridding and calibration processes. After initial collection, both sources of data are filtered to remove unwanted signals such as those from internal waves and tides so that the remaining signal only relates to the large-scale circulation. For this reason, the RAPID method of merging profiles for each boundary profile may further help to remove unwanted small-scale signals.

The dynamic method of estimating geostrophic velocities necessitates the use of a reference level velocity, the choice of which affects deep transports but not the total MOC. A static level of no motion is not appropriate in shallow regions at the basin edges. In order to address this to a certain extent, the RAPID method uses a profile for the relatively shallow WBW region that is determined by direct current meter measurements. Absolute transports for the WBW region are estimated to be accurate to within ± 0.5 Sv (Johns et al., 2008). The hydrographic method addresses this by employing a shallow reference level within the DWBC region and a deep reference level in the main basin.

The RAPID method works with boundary profiles, the resulting bottom triangles are unaccounted for. The moorings reach down to 4820 dbar, omitting an area of the basin between this and the AABW depth layer that amounts to 2% of the basin. The eastern side of the basin slopes considerably and the boundary profile is therefore a composite of mooring data with a large range in longitude (~24°W to ~14°W). McCarthy et al. (2015a) estimate the measurement error in the RAPID array to be 1.5 Sv. Sinha et al., (2017) quantify the combined error associated with un-sampled deep regions excluded by boundary measurements, the choice

of boundary-wide reference level and unaccounted ageostrophic flow as 1-2 Sv.

The method employed to process hydrographic data, in a manner akin to Atkinson et al. (2012), appears robust but inferences are limited due to the variables affecting each section, such as the difference in basin area. Ganachaud et al. (2003) address the uncertainty of hydrographic MOC estimates, finding a net RMS section-wide uncertainty of order ±6 Sv, which is largely due to internal waves and eddies.

The calculation of transports is based on various assumptions, most notably that there is geostrophic balance below the ageostrophic wind-driven surface boundary layer. Net evaporation and freshwater flux are not accounted for. It is assumed that there is not substantial diapycnal mixing in the deep layers. The response to external forcing due to OBP fluctuations is assumed to be uniform over the section, though it is likely to be near-bottom intensified and zonally non-uniform due to the topography (Kanzow et al., 2007). Another source of uncertainty results from estimates of long-term mean Ekman transport and long-term mean Florida Straits transport, amounting to a combined error of ±2 Sv, as detailed by Longworth (2007). Daily Florida Straits transports are deemed correct to within 1.1 Sv (McCarthy et al., 2015a). Additionally, ignoring the ~0.8 Sv long-term annual mean Bering Straits transport has an associated error. Whilst AABW is a small component of the MOC, it is nonetheless important and is evaluated by Frajka-Williams et al. (2011). AABW flow is distorted by bottom triangle values, due to their greater assignment (in terms of relative area) to the western flank of the MAR, an area of steep topography.

2.5 Discussion and conclusions

High-resolution hydrographic section data are useful for understanding changing water-mass characteristics from section-wide comparisons of various properties. These water-mass variations are a mechanism for decadal change that would advect slowly in the deep layers and would therefore be evident despite data collection limitations. Hydrographic oxygen concentrations support the theory that, in 2004 and 2015, DWBC southward flow west of ~70°W was greater relative to both 2010 and 2011. Zonal sections of potential temperature show that both AABW and UNADW layers, as defined by depth class, have warmed since 2004, suggesting a gradual weakening of these transports. But it cannot easily be concluded which of the deep layers, UNADW or LNADW, is most likely to

compensate for upper ocean variability from the hydrography alone. The degree of variability in water-mass properties is not fully understood and determining changes in transports from these properties is not a straightforward endeavor. Further to this, high spatial resolution hydrography enables division of water-mass transports by potential temperature. Defining layer interfaces by potential temperature class confirms that the chosen depth divisions are a reasonable approximation for each water-mass division. Zonal variation can also be assessed to facilitate greater understanding of RAPID data. These variations within the basin interior can be matched to deductions from section-wide properties such as oxygen concentration. It is evident from such zonal analysis that, during downturn events, a deep reference level of 4820 dbar strengthens the total basin southward internal transports (by reducing deep transports to near-zero, when they are sometimes northward flowing during a downturn event, and applying a southward compensation) such that less southward compensation is needed.

There are differences inherent in both the data and the methods applied to the two datasets. The spatially complex hydrography can be easily manipulated to understand different methodological choices, the effect of which can then be quantified. This informs inferences about the state of the overturning, as it is possible to explore how data from downturn events is affected differently. The evolution of hydrographic transports from the hydrographic method to the RAPID method shows that, largely, the differences impact on inferences for long-term trends within the deep layers. A shallow reference level of 1000 dbar within the DWBC region helps to represent the large short-term variability of the deep southward flow. During downturns, a 1000 dbar reference level in the DWBC region reveals weakened internal southward UNADW and LNADW transports, twinned with strong southward compensation. It would be of interest to see the outcome of a shallow reference level applied to the DWBC region on the temporally replete RAPID time-series. The spatial structure of RAPID data could be supplemented with additional mooring data at key locations, allowing analysis of western boundary transports at high temporal resolution. Though observational changes in deep water formation rates are difficult to reconcile with transports at mid-latitudes due to processes such as mixing during transit from high latitudes.

The main objective, with regard to the hydrography, was to discern whether inferences regarding transports contradict RAPID time-series transports and, if so, to determine a source for the discrepancy. The large short-term variability seen in RAPID transports provides evidence for the difficulty in determining long-term

MOC trends using hydrographic sections. Short-term aliasing of the signal captured by the hydrography is a problem. The spatial and temporal variability of DWBC transports is large. The hydrography suffers from poor temporal resolution that may result in aliasing and thus a distortion of this highly variable component. When differences in the methods are addressed, hydrographic transports fall within 2 standard deviations of RAPID transport means for each cruise but with two notable exceptions: AAIW transports and 2011 LNADW hydrographic transport. With regard to AAIW transports, this layer occupies a wedge shape through the basin that is wider on the east side than the west, this is evident when each layer is separated by potential temperature (as shown by the 5°C to 9.5°C temperature layer in Figure 2.3). Thus, the 800 m to 1100 m depth layer range for AAIW may not accurately relate the divide between AAIW and adjacent water-mass layers. The 2011 section conveys particularly weak southward LNADW that falls 3 standard deviations outside the RAPID mean (where no temporal offset is applied). This appears to be an inherent issue with the base 2011 data. Figure 2.22 conveys strong northward baroclinic flow below 1100 m in the 2011 hydrographic data (without the addition of the compensation component). In summary, for all four hydrographic sections, alignment with the RAPID equivalent is a product of replacing a portion of the hydrography with WBW absolute transports and the counterbalancing effect of the compensation.

With regard to RAPID time-series transports, methodological choices shape the trends that may be discerned. Points of note are as follows:

1. Western Boundary Wedge absolute transports are vital for capturing flow in a region of high-frequency variability;
2. The error associated with un-sampled bottom triangle regions is 1.9 Sv, on average, where data is sub-sampled to RAPID boundary profile locations;
3. The total MOC is unaffected by the choice of reference level due to the compensation component;
4. The choice of reference level is relevant when assessing the strength of the deep transports, particularly when the deep southward baroclinic component is weak (to the extent that it may briefly flow northward).

Employing a high-resolution ocean general circulation model, Sinha et al. (2018) identify and quantify errors associated with RAPID AMOC calculations. They design a virtual RAPID array in the model that closely resembles the real RAPID array so that it may be compared to the model truth. Sinha et al. (2018) find the bias associated with the RAPID estimate of the AMOC to be ~1.5 Sv due to the

combined error of bottom triangle omission, neglect of ageostrophic flow and use of a stationary reference level with the assumption of zero net flow. Error due to bottom triangles (regions beyond the 4 boundary profiles) is largest in the bottom 3000 m at the eastern boundary and on the west side of the MAR (Sinha et al., 2018). They find the total error is at its greatest and most time-variable in the upper 2000 m. Ageostrophic flow is most significant in the top 1000 m but is relatively constant (Sinha et al., 2018). Employing basin-wide constant (but temporally variable) Ekman transports, and constant Coriolis parameter between moorings, make negligible contributions to the error (Sinha et al., 2018). Sinha et al. (2018) conclude that the RAPID AMOC calculation underestimates the total mean MOC but captures the variability of flow to high accuracy.

Kanzow et al. (2007) find that the compensation associated with a deep reference level of 4820 dbar is a good approximation of external transports resulting from OBP fluctuations. The notion of the compensation as a proxy for external transports is a reasonable one, but the way in which it is applied to the basin distorts the signal for each layer. A deep reference level at the base of the moorings ensures the offset required to ensure mass balance is a robust approximation of the external component. However, instead of applying it uniformly according to section area, it may be more salient to add it to the western boundary only, as inferred from east-west cumulative transports in Figures 2.21 & 2.22. This separation of the basin would not be possible for RAPID transports without additional moorings data being included within the calculation. This topic is discussed further in Chapters 3 & 5.

OBP derived from GRACE satellites to determine LNADW and AABW external transports would provide a secondary source of concurrent measurement for comparison. Landerer et al. (2015) show that GRACE-derived LNADW external transports match well with RAPID LNADW transports, this is based on the premise that OBP gradients are the major contributor to average zonal deep transports. This additional source of data could also yield greater understanding of the deep transports below 4820 dbar that are otherwise difficult to capture. With regard to determining which of the deep layers compensates for upper ocean changes, gauging the external transports will be key due to the western boundary sloping bathymetry for the LNADW depth layer (Hughes et al., 2013). GRACE-derived OBP utilised to calculate external transports across the basin for each longitudinal grid-point interval (GRACE grid-points are 300km apart at 26°N) could complement understanding of the deep transports.

Simultaneous observations are important for ratifying results and methods. Given that the methods are adjustable and repeatable, further data will allow the methods to be tested for consistency. The high spatial resolution of hydrographic data enables detection of buoyancy changes through analysis of basin-wide properties. The high temporal resolution of RAPID data provides a reliable measure as to the extent of interannual changes resulting from variation in Ekman transports and can also help to monitor long-term AMOC decline or recovery. Major sources of AMOC variability are wind forcing (Roberts et al., 2013) and buoyancy forcing (Polo et al., 2014). Greater understanding of how these mechanisms alter the density structure and overturning timescales will provide a baseline for comparison with future change. A combination of data from different sources is key to building up a better picture of changing MOC transports. The AMOC is a critical feature of the climate system and long-term trends have implications for the northward transfer of heat through the Atlantic.

Implications for future hydrographic surveys and continuing RAPID array measurements are as follows:

1. Western boundary profile spacing should be relatively tight to allow capture of DWBC flow, where the eastern extent is found at ~70°W, in order to understand the variability of such a large component of the total MOC;
2. Western Boundary Wedge absolute transports are fundamental to capturing flow in a region of high short-term variability and should therefore be used to complement hydrographic measurements;
3. The choice of reference level and application of compensation needs to be explored to understand whether an alternative methodology will convey a different picture of the deep baroclinic flow;
4. External transports need to be explored through various sources of OBP data in order to supplement the MOC calculation.

2.5.1 Summary

- The AMOC has emerged as a focal point in the study of climate change due to its capacity to move heat and other properties. Projections of AMOC decline (IPCC, 2013) motivate continued investigation into AMOC driving mechanisms and transports.
- The AMOC has been measured at 26°N by infrequent hydrographic sections and continuous measurements by the RAPID array since 2004. Both sets of data allow calculation of internal transports. During the first 4 years of

RAPID observations the overturning circulation was, on average, 2.7 Sv stronger than in the subsequent 4 years (Smeed et al., 2014). Transports from hydrographic sections, using a methodology that differs from that of the RAPID AMOC calculation, show contrasting results with stronger overturning in 2010 than 2004 (Atkinson et al., 2012).

- Causes for the apparent discrepancy between the RAPID mooring array and hydrography are explored. These two estimates of the overturning are based on different data and different calculation methods. The limitations and assumptions of the data and methods are examined. The methods are adjusted to eliminate or mitigate differences.
- Fundamental inconsistencies between RAPID data and hydrographic data are uncovered. Hydrographic data aren't always consistent with the scale of flow variation captured by current meters at the western boundary. The western boundary is important in measuring the extent of downturns.
- When differences in the methods are addressed, hydrographic transports fall within 2 standard deviations of RAPID means for each cruise for the 3 major water-mass layers, with the exception of 2011 hydrographic data in the LNADW layer.
- High spatial resolution hydrographic data, such as oxygen concentration, can complement inferences regarding long-term AMOC changes and methodological choices for calculating transports. Hydrographic oxygen concentrations suggest that, during downturn events, DWBC southward flow west of ~70°W is weaker. Calculating transports with a shallow 1000 dbar reference level in the DWBC region reveals weaker internal southward UNADW and LNADW transports during downturns that are partnered with stronger southward compensation. These trends at 26°N have implications for how the larger circulation is viewed.
- It would be of interest to see the outcome of a shallow reference level applied to the DWBC region within RAPID time-series data. The spatial structure of RAPID data could be supplemented with additional mooring data at key locations, allowing analysis of western boundary transports at high temporal resolution.
- OBP derived from GRACE satellites utilised to determine LNADW and AABW external transports would provide a secondary source of concurrent measurement for comparison. This additional source of data could yield greater understanding of the deep transports during periods of weak overturning.

Chapter 3: The relationship between the reference level, Deep Western Boundary Current (DWBC) and the AMOC at 26°N estimated from RAPID array data for 2004-2014

3.1 Introduction

The importance of the AMOC regarding the climate, particularly that of North-West Europe, lies in its capacity to move heat poleward (Srokosz et al., 2012; IPCC, 2013). Continuous observational data from the RAPID array at 26°N since 2004 allow calculation of AMOC strength (McCarthy et al., 2015a). The RAPID array consists of dynamic height moorings across the basin. The moorings are strategically positioned to flank the continental shelf and MAR regions. Four boundary profiles are composed from these dynamic height moorings. Geostrophic transports are calculated between the four profiles, relative to a 4820 dbar level of no motion, before being added to absolute transports for the WBW region between Abaco and the western-most mooring to yield internal transports. The AMOC RAPID time-series transports are composed of four parts: internal transports, northward Florida Straits transports, northward Ekman transports and compensation transports added to ensure zero mass balance.

The necessity of an absolute velocity at the reference level is the main issue when working with geostrophic calculations. This has been investigated through inverse methods (Wunsch, 1978) and hydrographic sections (e.g. Bryden et al., 2005). The solution to assume a level of no motion and apply a time variable barotropic velocity to the basin-wide geostrophic velocity, ensuring zero net transport through the basin, was first proposed by Hirschi et al. (2003). A square ocean basin, with uniform depth and width, would always produce the correct answer for this method, regardless of whether the reference level varied with longitude (Sinha et al., 2018). Given that the basin tapers with depth, the zero net transport assumption is imperfect, and the choice of reference level becomes critical for quantifying each water-mass accurately (Roberts et al., 2013). Ganachaud (2003) found the error associated with the reference level and assumption of zero net transport to be ±3 Sv at 25°N, whereas McCarthy et al. (2015a) estimate that it is 1.5 Sv.

Employing a high-resolution ocean general circulation model, Sinha et al. (2018) identify and quantify errors associated with RAPID AMOC calculations. They design a virtual RAPID array in the model that closely resembles the real RAPID array so that it may be compared to the model truth, which utilises the model pressure gradient to calculate absolute geostrophic flow. The application of a fixed reference level of 4820 dbar with the assumption of zero net transport is explored as a source of error in the RAPID AMOC estimate by Sinha et al. (2018). The true model mean geostrophic streamfunction maximum is 14.7 Sv and the virtual RAPID mean streamfunction maximum is 13.6 Sv, where the difference reflects the degree of reference level error. Sinha et al. (2018) find that the reference level bias is largest and most temporally variable in the top 2000 m, but nonetheless small enough to resolve AMOC variability on interannual and decadal timescales.

Johns et al. (2007) calculate DWBC transports, covering the period March 2004 to May 2005, from the six RAPID western boundary moorings (Figure 3.1) employing a time-varying reference level in the methodology. The five westernmost moorings (WBA-WB3) provide current meter observations, whilst the sixth western boundary mooring (WB5) provides only dynamic height data. At the base of the moorings, bottom pressure recorders (BPRs) provide absolute transports (including the barotropic component) and the time-varying reference level velocity to supplement geostrophic transports for the basin spanning WB3 to WB5. Johns et al. (2007) combine the observational data to calculate transports from the western edge to WB5, covering a distance of 500 km. These transports encompass the southward flowing DWBC and northward flowing Antilles Current in the top 1000 m. Mean net transports above 1000 m, as well as within the UNADW and LNADW layers of the DWBC, are found to be 6 Sv, -13.9 Sv & -12.6 Sv, respectively. Net flow is inclusive of recirculation and is composed of both the barotropic and baroclinic components. Johns et al. (2007) find the temporal variability to be large, the transport range above 1000 m is -15 Sv to 25 Sv and for the deep layer (between 1000 m and 5000 m) is -60 Sv to 3 Sv. The variability occurs on timescales of several days to a few weeks and is largely the result of barotropic fluctuations. Johns et al. (2007) subtract the barotropic variability with the aid of BPR data (the time-mean barotropic flow is retained and just the barotropic fluctuations are filtered out) to highlight baroclinic variability. The resultant, lower-frequency, baroclinic residual reveals a temporary stoppage of LNADW transports within the DWBC in November 2004, with weaker events occurring in February 2005 and April 2005. These sporadic events are deemed by

Johns et al. (2007) to be due to disturbances propagating down the western coast and are likely to be part of the normal variability of the DWBC at this location. It is evident that both the baroclinic and barotropic components of the deep transports are important for understanding AMOC fluctuations, though without reliable BPR data spanning the basin, the time-varying reference level velocity cannot be determined.

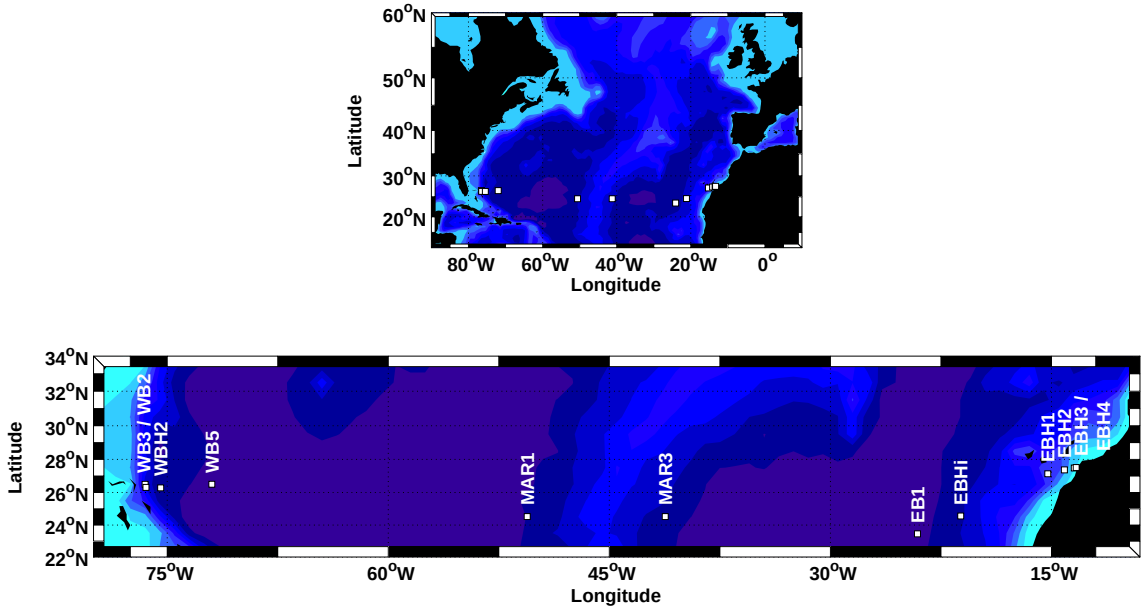

Figure 3.1: Map of the major RAPID moorings. The upper plot shows the majority in relation to the wider North Atlantic. The lower plot conveys a closer view of the mooring locations.

Frajka-Williams et al. (2016) examine covariability between wind-forcing and LNADW flow across the first ten years of the RAPID AMOC record using a basin-wide reference level of 4820 dbar. It is found that isopycnal displacements in the deep ocean at the western boundary, in the top 1000 m and below 2000 m, link to interannual MOC variability. A depression of these isopycnals corresponds to a weakening of southward LNADW flow, but the UNADW layer is unaffected. Frajka-Williams et al. (2016) quantify this: a 42 m isopycnal downward displacement equates to a 1 Sv LNADW weakening. They find that the effect of the winds to alter the basin-wide tilt, and therefore the vertical shear, extends to mooring WB3 (40 km out from the western coast) but not to mooring WB5 (500 km from the coast). The western boundary anomalies are found to be the cause of AMOC downturn events in 2009-10, 2010-11 and 2013, which are typified by weakened northward Ekman Transports, weakened southward LNADW transports and, to a lesser extent, weakened northward Florida Straits transports.

The AMOC decline described by Smeed et al. (2014) whereby the second four years measured by the RAPID array was 2.7 Sv weaker than the first four years, is associated with stronger southward transports in the top 1100 m and weaker southward transports below 3000 m (Smeed et al., 2014). Northward Ekman transports, northward Florida Straits transports and southward LNADW transports were weaker in the subsequent four years of the array by 0.2 Sv, 0.5 Sv & 2.1 Sv, respectively (Smeed et al., 2014). These years of weaker transports coincide with a strengthening of the southward flow above the thermocline (Smeed et al., 2014). Buoyancy changes are expected in association with long-term AMOC changes (e.g. Robson et al., 2014), and thus a corresponding weakening of the DWBC southward flow would be expected.

The estimated geostrophic internal flow calculated between dynamic height profiles is relative to a reference level. The calculation of transports using data gained from the RAPID array employs a deep reference level of 4820 dbar. The RAPID AMOC calculation employs this deep reference level across the basin (WB3 to the east coast), with the addition of current meter absolute transports for the WBW (McCarthy et al., 2015a).

Within Chapter 3, a new perspective of RAPID AMOC transports will be proposed with the inclusion of a fifth profile at 72°W (containing the DWBC between WB3 and WB5) using data from mooring WB5 (Figure 3.1), which is not ordinarily included in the RAPID MOC calculation. This decision to incorporate mooring profile WB5 was made to allow incorporation of the strong and variable DWBC transports found by Johns et al. (2007) into the RAPID MOC. Furthermore, a shallow reference level at the western boundary, as opposed to a basin-wide deep reference level employed in the standard RAPID AMOC calculation, will apply in the methodology. This alteration of the western boundary reference level may change the nature of the reference level bias detailed by Sinha et al. (2018).

Analysis of hydrographic section oxygen concentration data (Longworth 2007; Atkinson et al., 2012) shows that the eastern extent of the DWBC is typically found at 70°W. Variability of the DWBC is between 5 Sv and 75 Sv on a daily basis, with ~13 Sv recirculation (Bryden et al., 2005a). Thus, the inclusion of mooring WB5 in the AMOC calculation should contain the DWBC between WB3 and WB5.

The 1000 dbar reference level choice for the DWBC region corresponds to the zero crossing of the RAPID mean transport per unit depth profile and the hydrographic mean transport per unit depth profile (e.g. Atkinson et al., 2012,

see their Figure 5; Frajka-Williams et al., 2016, see their Figure 2). At the western boundary, at 26°N, the Antilles Current flows northward in the top 1000 m with the southward DWBC below. This shallow reference level in the DWBC region should effectively take the place of the compensation component by increasing deep baroclinic transports. A reference level of 1000 dbar in the DWBC region may also help identify structural changes within the DWBC, an approach that has previously only been employed on hydrographic section data (e.g. Longworth 2007; Atkinson et al., 2012). The reference level choice is vital to quantifying DWBC transports and a 1000 dbar selection will convey an alternative view of these deep flows that may provide additional insight during periods of AMOC weakening.

The choice of shallow reference level will be assessed by:

1. Comparing absolute transports between moorings WB2 and WB3 with the geostrophic equivalent, testing various reference levels to determine the best option;
2. Comparing the transports calculated by Johns et al. (2007) between the western coast and WB5 (a combination of WBW absolute transports and geostrophic transports from WB3 to WB5 with BPR-derived time-varying reference level) with the equivalent calculated for this analysis (i.e. a combination of WBW absolute transports and geostrophic transports from WB3 to WB5 with a fixed 1000 dbar reference level).

Variation in the deep RAPID1000|4820 transports will be related to downturn events in December-April 2009-10, November-January 2010-11 and February-March 2013 that are typified by weakened northward Ekman Transports (below 1 standard deviation of the mean), weakened southward LNADW transports (below 1 standard deviation of the mean) and, to a lesser extent, weakened northward Florida Straits transports (Frajka-Williams et al., 2016). Deep layer variation will also be assessed in terms of the 2.7 Sv AMOC weakening in 2008-2012 relative to 2004-2008 found by Smeed et al. (2014) that is also associated with weakened northward upper ocean transports (top 1100 m) and weakened southward LNADW transports (3000 m – 5000 m) by 2.1 Sv.

Herein, positive transports always indicate northward flow and, for simplicity, the eastern extent of the DWBC region is defined as 72°W, the position of mooring WB5. WB5 data range from April 2004 to March 2014, therefore all transports within Chapter 3 are restricted to the same range. Lastly, transports calculated

with a basin-wide reference level of 4820 dbar will be referred to as RAPID4820 transports. Similarly, transports where a 1000 dbar reference level is employed at the western boundary and a 4820 dbar reference level is employed east of WB5 will be referred to as RAPID1000|4820 transports.

For both basin-wide and isolated western boundary (between the coast and mooring WB5) RAPID1000|4820 transports, the objectives are:

1. To discover whether weak southward LNADW flow continues to serve as a determining factor of the 2009-10, 2010-11 & 2013 downturns (as found with a basin-wide reference level of 4820 dbar by Frajka-Williams et al. (2016));
2. To determine whether southward DWBC transports display a weakening in 2008-2012 relative to 2004-2008 (as found with a basin-wide reference level of 4820 dbar by Smeed et al. (2014));
3. To determine whether the relationship between the internal transports and the compensation transports is altered.

The impact of weak southward flowing LNADW on the AMOC is assessed. Concerns regarding potential AMOC reductions, featuring reduced southward LNADW flow and weak northward Ekman transports, highlight the necessity of continuous monitoring systems and ratification of the methodology employed to calculate transports.

3.2 Data and methods

3.2.1 RAPID4820 transports

RAPID AMOC time-series transports are composed of internal transports, Florida Straits transports, Ekman transports and compensation transports to ensure mass balance (Figure 3.2a). Internal transports are a combination of geostrophic transports employing a basin-wide reference level of 4820 dbar and WBW absolute transports. Lower basin transports (composed largely of UNADW, LNADW and AABW) are equal to upper transports. AABW flow, equating to ~1 Sv northward transport, does not feature within the scope of analysis here in Chapter 3. Downturn events typically feature weak southward flowing LNADW (Figure 3.2, grey shading) and reduced northward Ekman transports. RAPID southward LNADW transports are stronger in the first 4 years (2004-2008) relative to the second 4 years (2008-2012) by 2.1 Sv (Figure 3.2a iii).

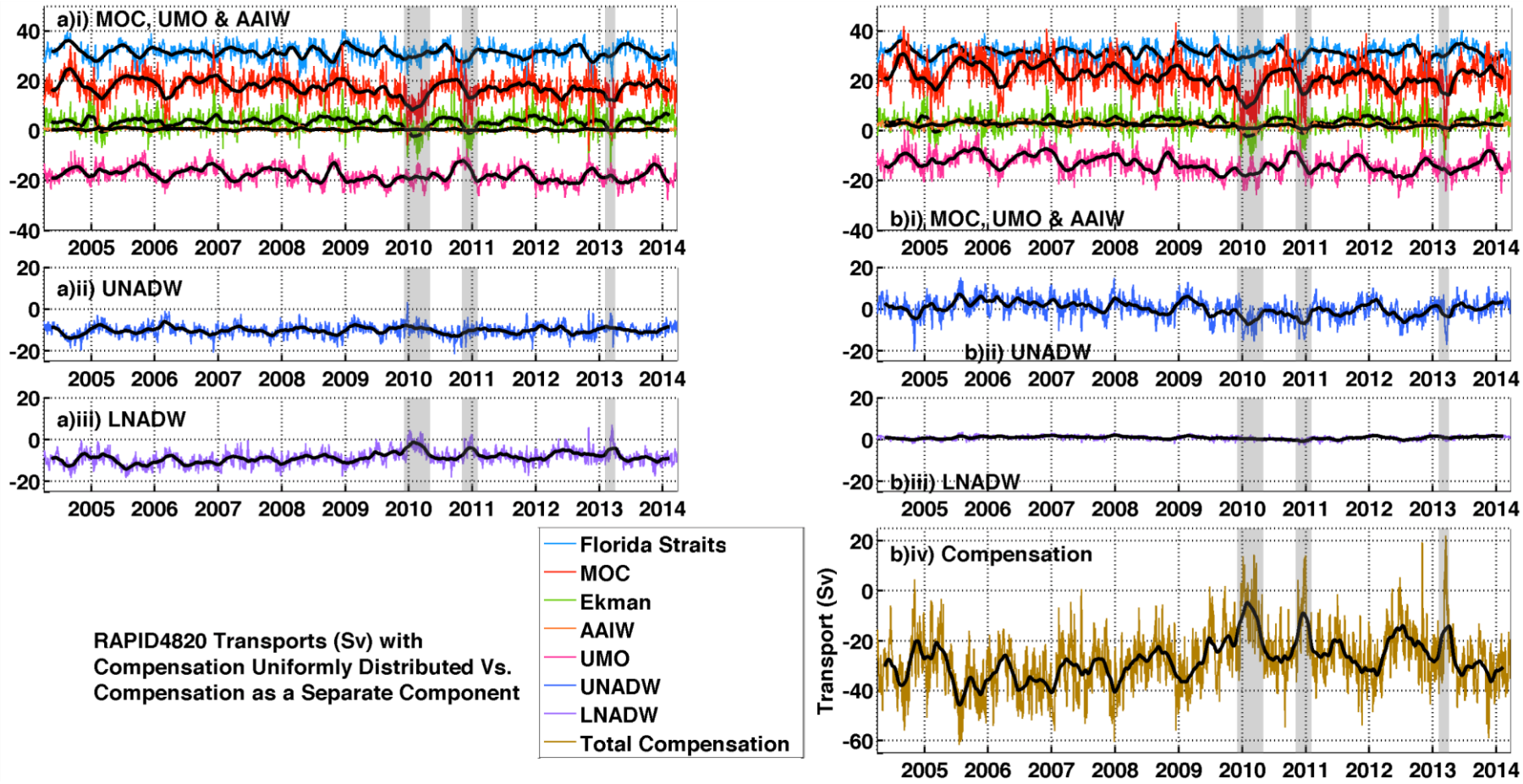

Figure 3.2: RAPID4820 layer transports (Sv): a) total transports; b) total transports with the compensation subtracted from the baroclinic component and plotted separately. Transports are 10-day low-pass filtered and black lines denote the 3-month low-pass filtered equivalent. UNADW and LNADW layers have the same y-axis scale. Shaded regions denote MOC downturn events.

The reference level doesn't just determine the depth of the deep return flow, it also affects the compensation velocity. Where the reference level is deep the result is near-zero LNADW internal transports and a southward compensation acting as counterbalance. Figure 3.2 (right side) displays transports without compensation, the compensation is plotted as a separate component (Figure 3.2b iv). There are instances where a reference level of 4820 dbar yields weak southward compensation such that it is northward flowing. These instances increase in frequency through the time-series but exist on short timescales (days). They are indicative of weak northward Ekman transports (more than one standard deviation below the mean) and weak northward Florida Straits transports. These changes are a feature of downturn events, where weak southward compensation twins with weak southward LNADW flow (more than one standard deviation below the mean). Section 3.3.5 determines whether this relationship between downturn events and compensation transports holds for RAPID1000|4820 transports.

Compensation transports (Figure 3.2b iv) are large and highly variable, as they are a proxy for the large barotropic flow fluctuations that provide mass balance within the basin (Kanzow et al. 2007). This supports the notion that the external transports display the largest short period amplitude change. The compensation component (Figure 3.2b iv) is applied uniformly across the basin to ensure mass balance. Uniform application ensures that the compensation is spread relative to the cross-section area. This alters the ratio between the deep layers because the basin is not square, it tapers toward the bottom. The deep 4820 dbar reference level reduces LNADW transports. The LNADW layer receives proportionately less compensation than the UNADW layer but is overwhelmed by it (comparing Figure 3.2a iii with Figure 3.2b iii). LNADW transports are therefore reflective of the compensation. It is evident that the compensation velocity has a cancelling effect on the UNADW layer (comparing Figure 3.2a ii with Figure 3.2b ii) due to the large degree of anti-correlation. However, Kanzow et al. (2007) utilise differences in bottom pressure at the boundaries to determine the external contribution and compare this to transports calculated with a compensation to ensure mass balance. Kanzow et al. (2007) find that the compensation transports and external transports are comparable. The external component is important, as it partly compensates for variation in Ekman transports (Kanzow et al., 2007). So, a deep reference level of 4820 dbar ensures that the compensation is a close approximation of the external transports.

RAPID4820 layer transports are summarised in Table 3.1. LNADW, occupying the 3000 m to 5000 m depth layer, displays the greatest southward weakening relative to the mean for all three downturn events. Southward LNADW transports are, on average, 4.5 Sv weaker during downturn events relative to the mean (Table 3.1). Southward UNADW transports are weaker by 0.9 Sv, on average, during downturn events, but this lies within 1 standard deviation of the mean.

			Downturn Event Means		
	Mean	SD	Dec 2009 - Apr 2010	Nov 2010 - Jan 2011	Feb 2013 - Mar 2013
	2004-2014*				
Ekman	3.6 ± *3.4*		-0.8	0.0	0.0
Florida Straits	31.4 ± *3.3*		30.1	29.6	29.5
UMO z ≤ 800 m	-17.6 ± *3.3*		-18.8	-15.5	-17.6
AAIW 800 m < z ≤ 1100 m	0.5 ± *0.7*		0.4	0.1	0.2
UNADW 1100 m < z ≤ 3000 m	-10.2 ± *2.7*		-8.7	-10.3	-8.8
LNADW 3000 m < z ≤ 5000 m	-8.7 ± *3.4*		-3.3	-4.9	-4.3
	RAPID4820 Transports (Sv)				

* End date: 21/03/2014

Table 3.1: Mean RAPID4820 layer transports (Sv). Mean transports for the whole time-series, from 2004 to 2014, are given with standard deviations in italics. Mean transports are given for each downturn event in 2009-10, 2010-11 and 2013. Northward transports are positive. Ekman transports and Florida Straits transports are also given.

RAPID4820 transport per unit depth (TPUD) profiles are displayed in Figure 3.3a and the associated streamfunctions are displayed in Figure 3.3b. An appropriate deep level of no motion is difficult to detect, though the vague divide between UNADW and LNADW is visible in the plot of TPUD at ~3000 m. Between the upper and lower components of the basin there appears to be a divide between northward and southward flowing transports at approximately 1000 dbar. This level of no motion at 1000 dbar therefore provides a good estimate for a shallow reference level. This 1000 dbar divide reflects a switch in the internal flow that is not a product of northward Florida Straits flow, as this does not exceed a depth of 740 m.

Across the time-series, there is a weakening southward LNADW trend (Figure 3.3). Brief periods of northward transports in the lower layer persist from a depth of ~2500 m to the bottom of the basin.

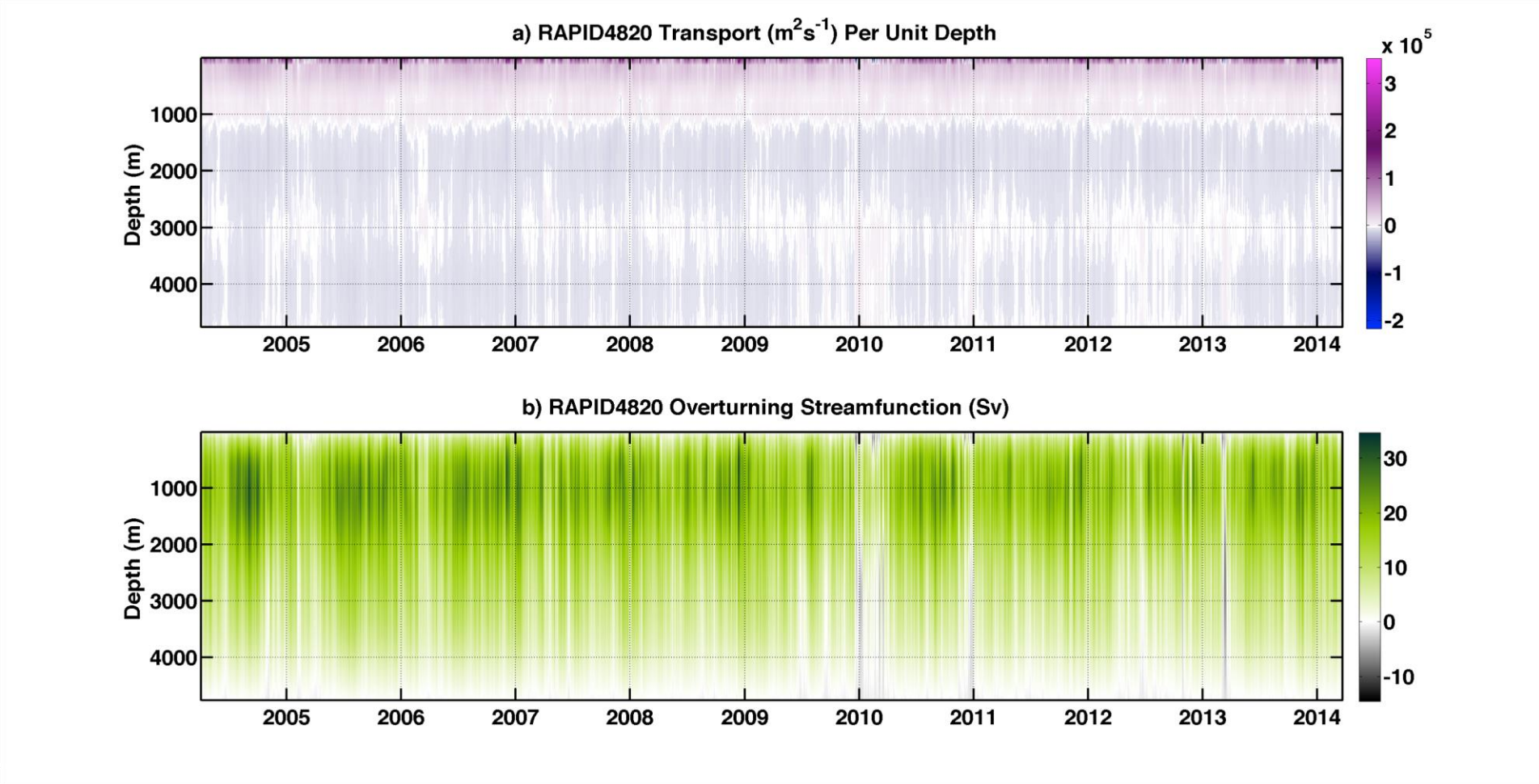

Figure 3.3: RAPID4820: a) TPUD profiles (m^2s^{-1}); b) streamfunctions (Sv), from the surface to 4820 dbar. Transports include time-variable Florida Straits transports and Ekman transports. Transports are 10-day low-pass filtered.

3.2.2 The choice of western boundary reference level: WB2 to WB3

The geostrophic method of calculating transports, with regard to hydrographic sections at 25°N, employs a 1000 dbar reference level at the western boundary up to ~70°W (e.g. Longworth, 2007; Atkinson et al., 2012). This relatively shallow reference level ensures a northward flowing Antilles Current above 1000 m and strengthens southward internal transports at depth. Bryden et al. (2005a) use current meter data from 1986 to 1997 to show the time-averaged velocity structure from the western coast to an offshore distance of 625 km (see their Figure 4). The velocity data encompasses WB5 at ~500 km offshore and an approximate level of no motion is evident at 1000 m depth.

To assess the choice of western boundary reference level, current meter transports can be compared to geostrophic mooring transports at the same mooring locations. Current meter transports are available from the western coast, off Abaco, to mooring WB3 at 76.5°W, but not to mooring WB5. Figure 3.4a displays the current meter TPUD between moorings WB2 and WB3, where the black contour highlights the switch from northward to southward flow between 500 and 1500 dbar. Figure 3.4a conveys the variability of the level of no motion, which shifts slightly lower down in the basin from mid-2010 onwards. The mean current meter TPUD profile between WB2 and WB3 is compared to the mooring geostrophic equivalent using a selection of reference levels from 500 to 1500 dbar in Figure 3.4b. The geostrophic transports are calculated by applying the reference level (500 to 1500 dbar) to the DWBC region, a deep reference level to the main basin (4820 dbar) and calculating the AMOC at each time-interval before isolating the transports between WB2 and WB3. A geostrophic reference level of 900 dbar matches the current meter equivalent most closely, with the smallest RMS difference (Figure 3.5a). Geostrophic reference levels of 800 dbar and 1000 dbar also provide reasonable matches to the current meter equivalent.

Figure 3.5a shows the results of the four closest geostrophic reference level matches compared to the current meter equivalent. The compensations applied between WB2 and WB3 for the four closest geostrophic matches to the current meter equivalent are plotted in Figure 3.5b. These compensations are calculated by performing the AMOC calculation for the whole basin (for each reference level choice) at each time-interval to compute the compensation for the cross-section before isolating the compensation for just the region between WB2 and WB3.

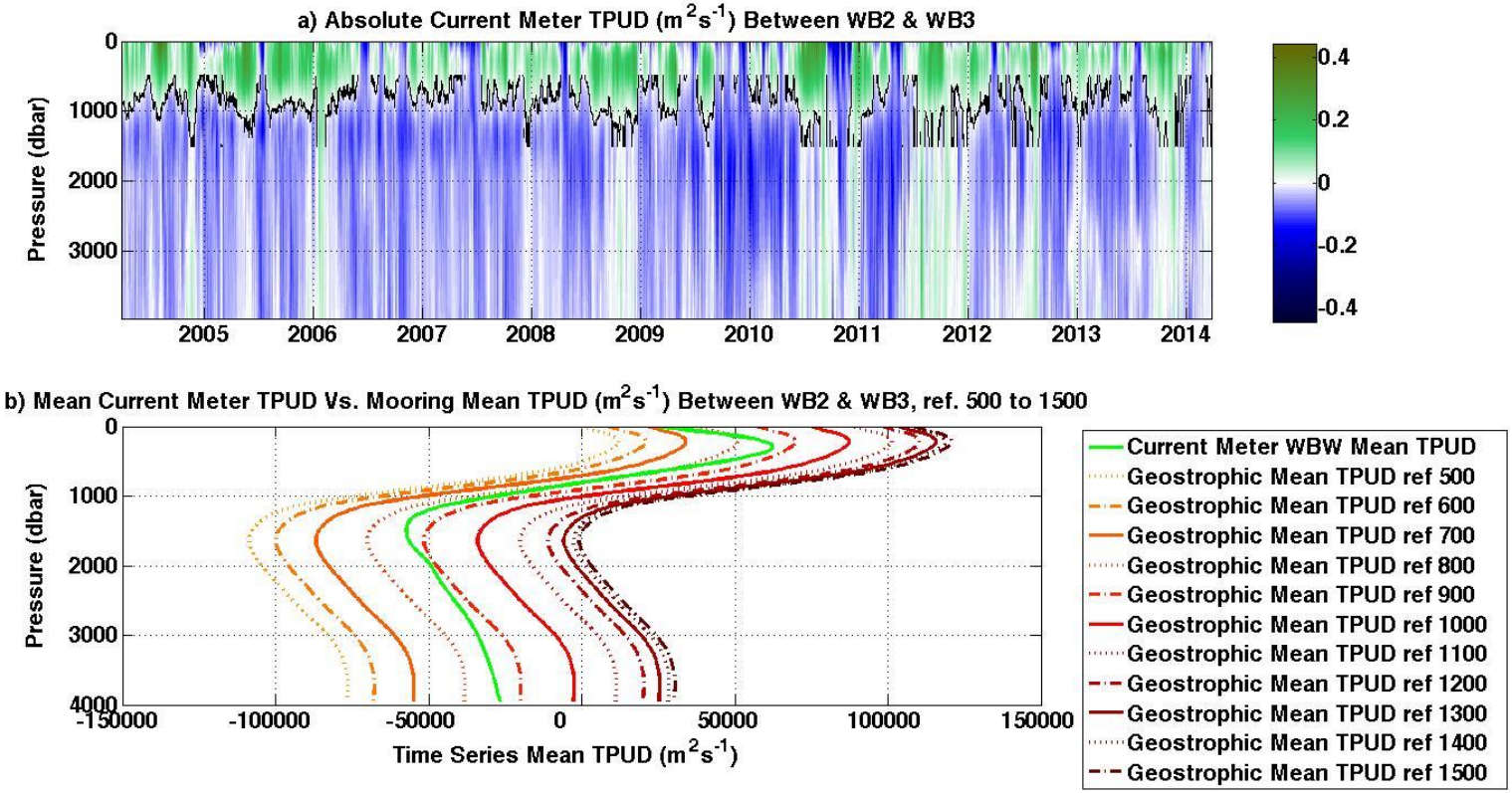

Figure 3.4: Plots of a) current meter absolute TPUD (m^2s^{-1}) between mooring WB2 and WB3; b) mean current meter absolute TPUD (green) and mean geostrophic TPUD with DWBC reference levels ranging from 500 dbar to 1500 dbar, at increments of 100 dbar (yellow to maroon). For all geostrophic transports a reference level of 4820 dbar is applied to the east of WB5 (outside the DWBC region). The black contour in the top subplot denotes the separation between northward and southward transports between 500 dbar and 1500 dbar.

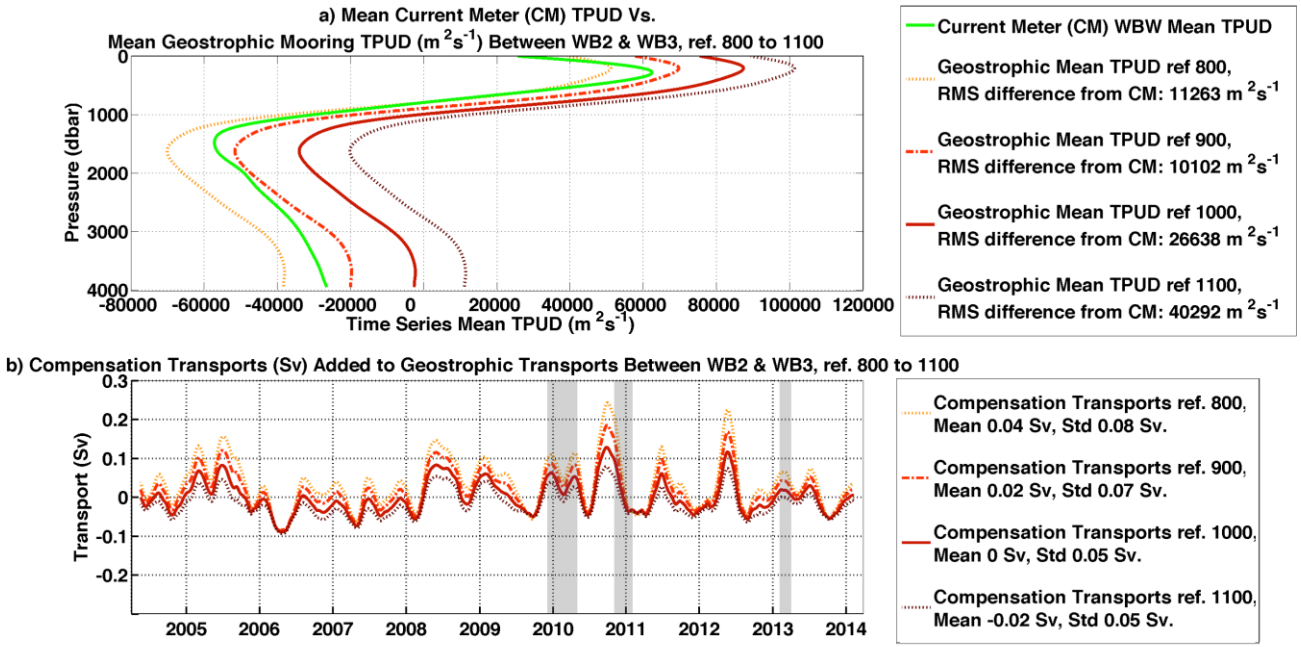

Figure 3.5: Plots of a) mean current meter absolute TPUD (m^2s^{-1}) (green) and mean geostrophic TPUD with DWBC reference levels 800 dbar, 900 dbar, 1000 dbar and 1100 dbar (yellow to maroon); b) associated geostrophic compensation transports (Sv). The geostrophic compensation transports (in the bottom subplot) are the summed compensation applied to the region between WB2 and WB3 at each point in the time-series. The compensation transports are calculated to ensure zero mass balance between the internal transports, Ekman transports and Florida Straits transports, where each DWBC reference level (800 dbar, 900 dbar, 1000 dbar and 1100 dbar) is applied to the west of WB5 and a 4820 dbar reference level is applied to the east. These compensations are calculated by performing the AMOC calculation for the whole basin (for each reference level choice) at each time-interval to compute the compensation for the cross-section before isolating the compensation for just the region between WB2 and WB3.

Typically, the shallower the reference level, the larger the time-series mean compensation and variance (Figure 3.5b). A reference level of 900 dbar applied to the west of WB5 yields mean compensation of 0.02 ±0.07 Sv for the WBW wedge, but this equates to mean 11.1 ±37.5 Sv for the whole basin. A reference level of 1000 dbar applied to the geostrophic transports to the west of WB5 results in time-averaged 0.0 ±0.05 Sv compensation applied to that part of the basin. This equates to mean 0.2 ±30.8 Sv for the whole basin. Thus, a 1000 dbar western boundary reference level will result in the least added basin-wide compensation. This makes a 1000 dbar reference level the best choice because, the smaller the compensation, the less the transports are skewed by a large compensation that is applied according to cross-section area in a basin that tapers with depth (thus the relationship between the deep transports is altered because these layers occupy different areas).

Geostrophic transports between WB2 and WB3 with a 1000 dbar reference level are a relatively close match to the current meter equivalent and also result in zero time-series mean compensation between the moorings (Figure 3.5). Figure 3.6 explores the TPUD difference between the geostrophic mooring transports, with western boundary ref 1000 dbar, and current meter transports. The range in TPUD difference (Figure 3.6d) is -2.1 to 2.5 m^2s^{-1}.

Whilst a geostrophic 1000 dbar reference level creates an approximate match for the current meter level of no motion between WB2 and WB3, this may not extrapolate out to mooring WB5 (Figure 3.1). However, RAPID1000|4820 southward transports reveal anomalously strong flow below 4000 m (an issue discussed in Section 3.3.2) that would be exacerbated by a shallower DWBC reference level.

Section 3.2.3 compares RAPID1000|4820 transports from the western coast up to WB5 to that calculated by Johns et al. (2008) to find a good match. Johns et al. (2008) calculate DWBC transports using current meter data and dynamic height moorings with a time-varying reference level estimated from combined shipboard and lowered-ADCP data as well as bottom pressure data. These factors support the choice of a 1000 dbar reference level in the DWBC region.

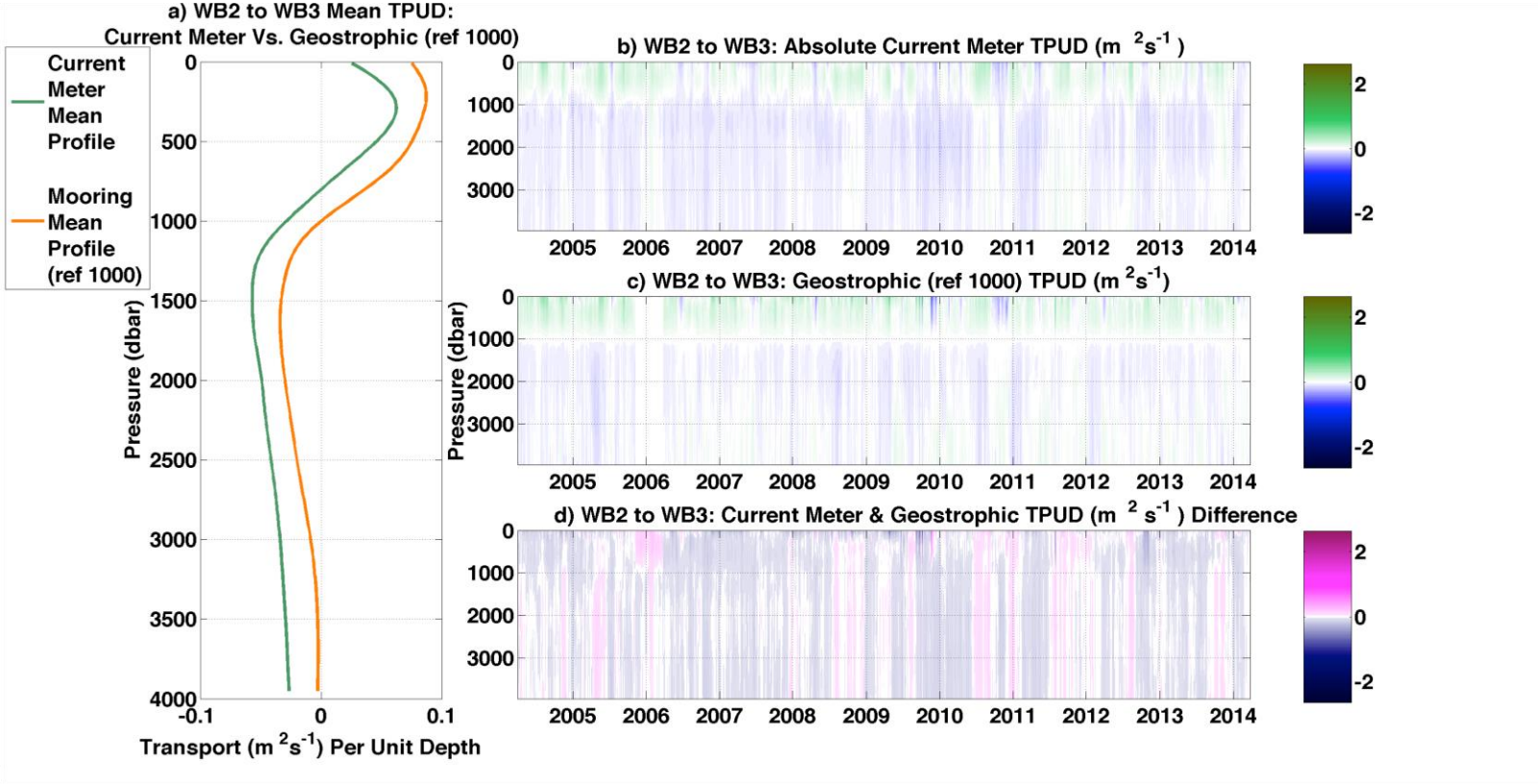

Figure 3.6: Plots of a) mean current meter absolute TPUD (m^2s^{-1}) (green) and mean geostrophic TPUD (orange) with reference level 1000 dbar to the west of WB5; b) current meter absolute TPUD between mooring WB2 and WB3; c) geostrophic TPUD between mooring WB2 and WB3 (with ref 1000 dbar to the west of WB5 and ref 4820 dbar to the east of WB5); d) the difference between current meter absolute TPUD and geostrophic TPUD between mooring WB2 and WB5. The colour bar scales for plots on the right (b, c, d) have the same range (-2.5 to 2.5 m^2s^{-1}).

3.2.3 The choice of western boundary reference level: WB3 to WB5

The isolated RAPID1000|4820 transports up to the eastern extent of the DWBC, approximated by mooring WB5, are displayed in Figure 3.7.

DWBC transports from the coast to WB5, with barotropic / external transports subtracted, calculated by Johns et al. (2008) are superimposed (their Figure 14) in Figure 3.7. Johns et al. (2008) utilise the same current meter data between the western coast and WB3, as well as the same dynamic height data between moorings WB3 and WB5, but their methodology differs. Johns et al., (2008) use a time-varying reference level based on absolute transports estimated from ADCP data and bottom pressure data. For the top 1000 m, there is a 0.95 correlation (confidence level 95%). Transports from 1000 m to 3000 m have a 0.68 correlation and transports from 3000 m to 5000 m have a 0.94 correlation when compared to that of Johns et al. (2008). Correlations are high given that, unlike the results of Johns et al. (2008), the barotropic / external transports have not been removed and a static reference level is employed. The level of correlation lends validity to the choice of reference level and the methodology. Given that we have not removed the external transport signal but nonetheless find high correlation with the results of Johns et al. (2008) (their Figure 14) suggests that the external / compensation component is diluted through uniform application across the basin, where instead, it should be applied largely to the western boundary region.

It is evident that RAPID1000|4820 transports between the coast and WB5 display compensatory behavior between northward transports above 1000 m and southward transports below (Figure 3.7). The correlation between the 0 - 1000 m layer and the 1000 m - 3000 m layer is -0.84. These two layers therefore largely cancel.

It is worth noting that RAPID1000|4820 transports between the coast and WB5 do not convey substantially weakened southward transports between 3000 m and 5000 m during downturn events (Figure 3.7, shaded regions). This suggests that the weak southward LNADW signal found during downturn events (e.g. Frajka-Williams et al., 2016) is carried by the barotropic signal rather than the baroclinic signal.

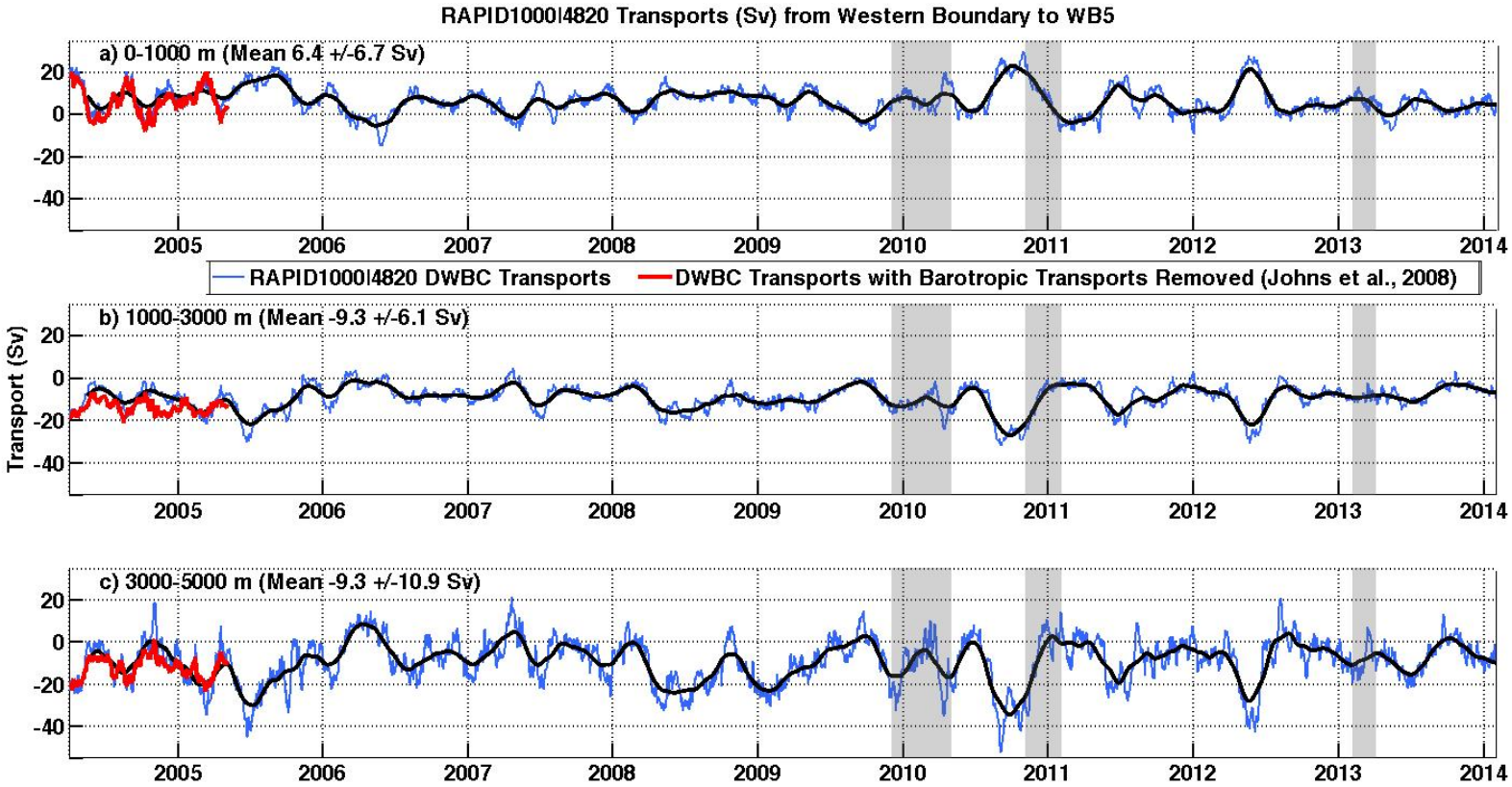

Figure 3.7: RAPID1000|4820 transports (Sv) isolated for the region west of WB5: a) 0 – 1000 m; b) 1000 m – 3000 m; c) 3000 m – 5000 m. Transports are a combination of absolute values from the coast to WB2 and geostrophic transports between WB2 and WB5. Blue lines are 10-day low-pass filtered transports and black lines denote the 3-month low-pass filtered equivalent. Shaded regions denote MOC downturn events. Transports calculated by Johns et al. (2008) for the DWBC region, but with the barotropic component removed, are superimposed in red.

3.3 Results

3.3.1 RAPID1000|4820 transports

A fifth profile is added to the boundary profiles with dynamic height data calculated from temperature, salinity and pressure at mooring WB5 at 72°W. WB5 mooring data are extrapolated to the surface based on the typical shear at the western boundary in the upper ocean for the time of year, based on monthly coefficients. This matches the process employed to extrapolate the four RAPID boundary profiles to the surface (McCarthy et al., 2015a). Internal transports are composed of absolute transports at the western boundary up to mooring WB2 at 77°W, geostrophic transports between WB2 and WB5 with a reference level of 1000 dbar and geostrophic transports east of WB5 with a reference level of 4820 dbar. The shallow reference level and not the compensation velocity thus bolsters transports at the western boundary.

Total layer RAPID1000|4820 transports are displayed in Figure 3.8. Differences between the deep transports below 3000 m in Figure 3.8 when compared to Figure 3.7 are largely due to the added compensation. Several events during which southward LNADW is weak, such as is the case in November 2004, are compensated by strong southward transports in the UMO layer or UNADW layer or both. Johns et al. (2008) identify the November 2004 dip in DWBC southward transports as natural variability that is unlikely to be related to changes in deep water formation.

Combined Ekman transports and Florida Straits transports are plotted in Figure 3.8a. All downturn events (shaded in grey) are accompanied by weakened northward Ekman transports and, to a lesser extent, weakened northward Florida Straits transports. Northward Ekman transports for each downturn event are, on average, 3.8 Sv weaker than the time-series mean, and northward Florida Straits transports are, on average, 1.6 Sv weaker than the time-series mean.

Weak southward RAPID1000|4820 LNADW transports alone are not sufficient to yield a downturn in the MOC, weak northward Ekman transports (weakened by more than 1 standard deviation of the 2004-2014 mean) and weak northward Florida Straits transports are also necessary. There does appear to be an event from mid-October to mid-November 2012 (Figure 3.8, salmon shading) that satisfies the conditions of a downturn event, albeit for a very short time period. However, weakened southward layer transports for this event are not a result of a

change in the internal transports, but are instead a result of a shift in compensation due to weak northward Florida Straits transports. From mid-October to mid-November 2012, mean Florida Straits transport is just 27.2 Sv (4.2 Sv weaker than the mean) and mean Ekman transport is 2.6 Sv (1 Sv weaker than the mean). This is evident in Figure 3.14 (discussed in Section 3.3.5), which illustrates northward compensation from mid-October to mid-November 2012.

Annual mean RAPID1000|4820 transports can be found in Table 3.2. RAPID1000|4820 transports (Figure 3.11b i) reveal a 2.1 Sv stronger MOC for the first 4 years relative to the subsequent 4 years. This is similar to the 2.7 Sv stronger MOC for the first 4 years relative to the subsequent 4 years found by Smeed et al., (2014).

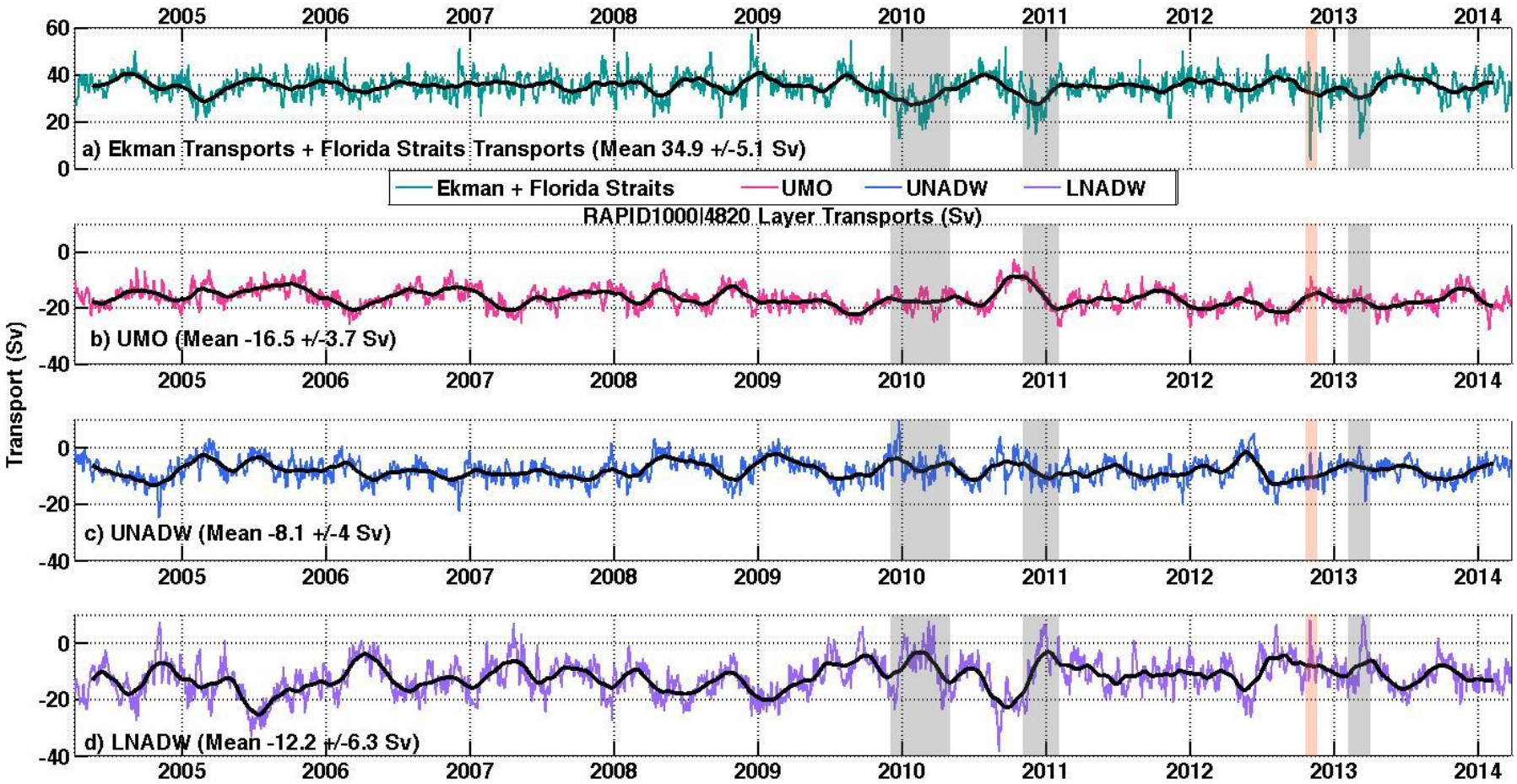

Figure 3.8: RAPID1000|4820 transports (Sv): a) combined Ekman transports and Florida Straits; b) UMO; c) UNADW; d) LNADW. Transports are 10-day low-pass filtered transports and black lines denote the 3-month low-pass filtered equivalent. Grey shaded regions denote MOC downturn events. Salmon shaded region highlights an event featuring weak Florida Straits transports.

	Mean	SD	Annual Means										4-Year Means	
	2004-2014*		2004	2005	2006	2007	2008	2009	2010	2011	2012	2013*	2004-2008	2008-2012
Ekman	3.6	3.4	3.1	3.5	4.0	3.9	4.0	2.2	3.0	4.5	2.9	4.6	3.7	3.2	3.4	3.6
Florida Straits	31.4	3.3	31.8	32.0	31.6	31.6	31.6	30.7	31.0	31.1	30.8	31.6	31.7	3.0	31.1	3.4
UMO z ≤ 800 m	-16.5	3.7	-15.5	-15.2	-15.3	-16.7	-16.0	-18.7	-15.5	-17.3	-17.8	-17.5	-15.7	3.4	-16.9	3.9
AAIW 800 m < z ≤ 1100 m	0.9	1.0	1.0	1.3	0.8	0.6	1.4	0.7	1.0	0.7	0.6	0.7	0.9	1.0	1.0	1.0
UNADW 1100 m < z ≤ 3000 m	-8.1	4.0	-8.0	-7.0	-9.6	-9.6	-5.6	-7.9	-8.1	-8.8	-8.2	-8.2	-8.5	3.7	-7.6	4.2
LNADW 3000 m < z ≤ 5000 m	-12.2	6.3	-13.4	-15.7	-12.6	-10.8	-16.3	-8.0	-12.4	-11.2	-9.3	-12.2	-13.1	6.2	-12.0	6.6
0 m - 5000 m	-35.9	5.1	-35.9	-36.6	-36.6	-36.5	-36.6	-33.9	-35.0	-36.6	-34.7	-37.1	-36.4	4.3	-35.5	5.5
	RAPID1000|4820 Transports (Sv)															

* End date: 21/03/2014

Table 3.2: Mean and annual mean RAPID1000|4820 transports (Sv). Each year begins in April. Mean transports for the whole time-series, from 2004 to 2014, are given with standard deviations in italics. Averages for the first four years (from April 2004) and the subsequent four years (from April 2008) are given in the last two columns. Ekman transports and Florida Straits transports are also given. Northward transports are positive.

Smeed et al. (2014) observe stronger basin-wide southward LNADW by 2 Sv in the first 4 years relative to the second 4 years of the array time-series. Data are contrasted in the interest of determining whether the weakening observed by Smeed et al. (2014) is carried by the DWBC. Table 3.2 conveys stronger basin-wide southward LNADW by 1.1 Sv in the first 4 years relative to the second 4 years of the array time-series, but this is insignificant relative to the standard deviation. Additionally, UNADW southward transports are 0.9 Sv stronger in the first 4 years relative to the subsequent 4 years, this also falls within 1 standard deviation of the time-series mean. RAPID1000|4820 transports convey a deep southward return flow that is distributed higher up in the basin. It should also be noted that southward UMO RAPID1000|4820 transports are weaker in the first 4 years relative to the second 4 years, but only by 1.2 Sv, and again, this is within 1 standard deviation of the mean.

Mean RAPID1000|4820 transports during downturn events can be found in Table 3.3. The average southward LNADW weakening, relative to the time-series mean, for the downturns is 4.7 Sv. This is similar to the average 4.5 Sv LNADW southward weakening seen in RAPID4820 transports during downturns.

			Downturn Event Means		
	Mean	SD	Dec 2009 - Apr 2010	Nov 2010 - Jan 2011	Feb 2013 - Mar 2013
	2004-2014*				
Ekman	3.6	*3.4*	-0.8	0.0	0.0
Florida Straits	31.4	*3.3*	30.1	29.6	29.5
UMO z ≤ 800 m	-16.5	*3.7*	-17.3	-14.9	-16.6
AAIW 800 m < z ≤ 1100 m	0.9	*1.0*	0.9	0.3	0.6
UNADW 1100 m < z ≤ 3000 m	-8.1	*4.0*	-6.0	-9.2	-6.8
LNADW 3000 m < z ≤ 5000 m	-12.2	*6.3*	-7.9	-6.8	-7.7
	RAPID1000|4820 Transports (Sv)				

* End date: 21/03/2014

Table 3.3: Mean RAPID1000|4820 transports (Sv). Mean transports for the time-series, from 2004 to 2014, are given with standard deviations in italics. Mean transports are given for each downturn event in 2009-10, 2010-11 and 2013. Northward transports are positive. Ekman transports and Florida Straits transports are also given.

3.3.2 RAPID1000|4820 TPUD profiles and streamfunctions

To investigate the structure of transports through the profile across the full-width of the basin, TPUD is displayed in Figure 3.9, with the associated streamfunction. The 1000 dbar shallow reference level in the DWBC region has created instances of strong southward flow below 4500 m, such as is the case in mid-2005. The distribution of transports within the depth of the LNADW layer is higher within the basin due to the shallow reference level between WB2 and WB5. Hydrographic transports calculated by Atkinson et al. (2012) also exhibit a high degree of structural profile variation between 4300 m and 5000 m (see their Figure 5), which could be due to the use of a 1000 dbar reference level at the western boundary. However, hydrographic transports are subject to the varying topography created by station locations and depth, thus transports at depth will also vary as a product of non-identical bathymetry for each section.

Lowering the reference level within the DWBC region to 1700 dbar results in TPUD profiles that do not display anomalously strong southward transports below 4000m (Figure 3.9a). However, a 1700 dbar reference level between WB2 and WB5 has the disadvantage of reducing UNADW transports to the extent that the time-series mean LNADW flow is close to zero. The 1000 dbar choice of reference level represents a compromise between ensuring northward transports above 1000 m, preventing anomalously large southward transports below 4000 m and reflecting the level of no motion between upper and lower basin internal flow that varies between 800 m and 1200 m (Figure 3.3).

The downturn events, regarding RAPID1000|4820 transports, all appear to exhibit weakened southward transports from the bottom up to at least 2000 m depth (Figure 3.9b). Thus, there are implications for both LNADW and UNADW. Weak southward flow below ~2000 m depth for the downturn events does not appear to be compensated by greater southward transports in the upper layer.

There are more instances of weak southward flowing LNADW in Figure 3.9 compared to Figure 3.3. Johns et al. (2008) deduce that these events are symptomatic of boundary waves unsettling the divide between UNADW and LNADW as they transmit down topography at the basin edge. The excitation of Rossby waves at the western edge through wind forcing results in an internal flow signal (Polo et al., 2014; Zhao and Johns, 2014). Frajka-Williams et al. (2016) credit southward Ekman flow, and the resultant density changes at the western boundary, for weak southward flowing LNADW events.

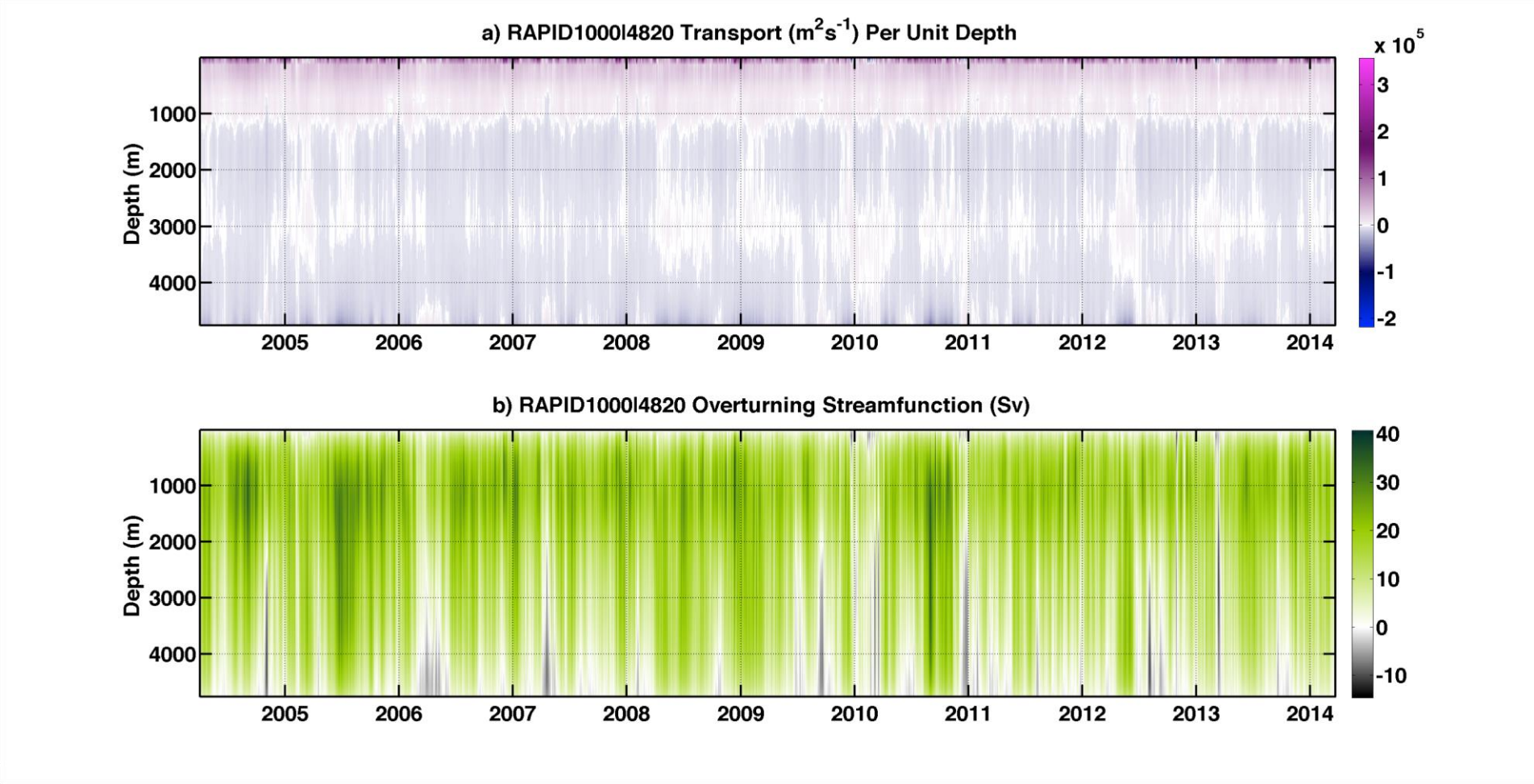

Figure 3.9: RAPID1000|4820 a) TPUD (m^2/s) profiles; b) streamfunctions (Sv). All profiles are from the surface to 4820 dbar. Transports include time-variable Florida Straits transports and Ekman transports. Transports are 10-day low-pass filtered.

3.3.3 RAPID1000|4820 transports from the west coast to WB5

For the purpose of detecting changes in the boundary current that align with downturn events in 2009-10, 2010-11 and 2013 (Figure 3.7, grey shading), mean RAPID1000|4820 transports are displayed in Table 3.4. The 2010-11 and 2013 downturn events convey weakened southward UNADW and LNADW transports relative to the mean. However, due to the large degree of short-term variability, the 2010-11 and 2013 downturn means fall within 1 standard deviation of the time-series mean, thus the differences are not significant. The 2009-10 downturn event doesn't show weakened southward UNADW or LNADW transports relative to the time-series mean. However, this downturn event has a relatively lengthy duration and the large degree of short-term variability in the signal obscures brief periods of weakened transports below 1100 m.

			Downturn Event Means		
	Mean	SD	Dec 2009 - Apr 2010	Nov 2010 - Jan 2011	Feb 2013 - Mar 2013
	2004-2014*				
UMO z ≤ 800 m	6.1 ± *6.4*		7.7	8.2	6.6
AAIW 800 m < z ≤ 1100 m	0.1 ± *0.5*		0.1	0.4	0.2
UNADW 1100 m < z ≤ 3000 m	-9.1 ± *6.1*		-12.1	-8.7	-8.6
LNADW 3000 m < z ≤ 5000 m	-9.3 ± *10.9*		-11.8	-5.5	-8.2
	WestBoundary-to-WB5 RAPID1000|4820 Transports (Sv)				

* End date: 21/03/2014

Table 3.4: Mean RAPID1000|4820 transports (Sv) isolated for the region to the west of WB5. Transports are a combination of absolute values from the coast to WB2 and geostrophic transports between WB2 and WB5. Mean transports for the time-series, from 2004 to 2014, are given with standard deviations in italics. Mean transports are given for each downturn event in 2009-10, 2010-11 and 2013. Northward transports are positive.

The time-varying annual mean RAPID1000|4820 transports are summarised in Table 3.5. The 2004-2014 ratio of mean UNADW to mean LNADW is almost 1:1. DWBC LNADW southward flow has strengthened in the second 4-year interval (2008-2012) relative to the first 4-year interval (2004-2008) by 2.9 Sv. The second 4-year interval also shows strengthened southward western boundary UNADW

transports by 1.7 Sv, on average. This coincides with southward compensation weakening in the latter four-year interval (2008-2012) to provide a counterbalance. However, a strengthening of transports between 1100 m and 5000 m at the western boundary isn't necessarily reflective of strong basin-wide southward flow. There could be substantial recirculation of the DWBC, reducing net southward flow. Additionally, these changes all fall well within 1 standard deviation of the time-series mean.

Bryden et al. (2005a), using direct current meter measurements, estimate means of -12.9 Sv for UNADW flow and -11.3 Sv for LNADW flow at the western boundary. In Table 3.5, 2004-2014 mean southward UNADW and mean southward LNADW at the western boundary up to WB5 are weaker (by 3.8 Sv and 2.0 Sv, respectively). However, standard deviations (Table 3.5) are large and encompass the estimates by Bryden et al. (2005a).

RAPID1000|4820 transports between 1100 m and 5000 m from the coast to WB5 are shown in Figure 3.10. Figure 3.10 also plots combined Ekman transports and Florida Straits transports. Weak northward Ekman transports / weak northward Florida Straits transports (red highlights) are here defined as more that 2 standard deviations below the combined mean (34.9 ±5.1 Sv). Weak southward western boundary RAPID1000|4820 transports between 1100 m and 5000 m (pink highlights) are here defined as northward flowing (positive). Downturn events (grey shading) feature a combination of weak northward Ekman transports / weak northward Florida Straits transports (red highlights) and weak southward transports between 1100m and 5000 m (pink highlights) at the western boundary. For the first 4 years of the time-series, the percentage of weak southward western boundary RAPID1000|4820 transports between 1100 m and 5000 m is 12.2%. For the subsequent 4 years of the time-series, this reduces to 10.8%. This difference is significant at the 95% confidence level. Due to the high level of short-term variability, the 3-month low-pass filtered data is also analysed. For the first 4 years of the time-series, the percentage of weak southward western boundary RAPID1000|4820 3-month filtered transports within 1100 m to 5000 m is 7.7%. For the subsequent 4 years of the 3-month filtered time-series, this reduces to 1.3%. This difference is also significant at the 95% confidence level.

	Mean	SD	Annual Means										4-Year Means	
	2004 - 2014*		2004	2005	2006	2007	2008	2009	2010	2011	2012	2013*	2004-2008	2008-2012
UMO z ≤ 800 m	6.1 ± *6.4*		8.3	9.2	3.7	4.3	7.9	4.2	8.1	4.5	7.2	3.2	6.4 ± *6.2*	6.2 ± *6.7*
AAIW 800 m < z ≤ 1100 m	0.1 ± *0.5*		0.0	0.3	-0.2	-0.1	0.4	0.0	0.4	0.0	0.3	-0.1	0.0 ± *0.5*	0.2 ± *0.5*
UNADW 1100 m < z ≤ 3000 m	-9.1 ± *6.1*		-9.9	-10.4	-6.8	-6.5	-12.1	-8.3	-11.8	-8.3	-10.2	-6.5	-8.4 ± *5.7*	-10.1 ± *6.6*
LNADW 3000 m < z ≤ 5000 m	-9.3 ± *10.9*		-10.9	-12.6	-5.2	-3.9	-18.2	-6.6	-12.3	-7.2	-8.4	-7.3	-8.2 ± *10.4*	-11.1 ± *11.7*
0 m - 5000 m	-12.2 ± *11.9*		-12.5	-13.5	-8.6	-6.3	-22.0	-10.6	-15.7	-10.9	-11.1	-10.6	-10.2 ± *11.1*	-14.8 ± *12.9*
	WesternBoundary-to-WB5 RAPID1000|4820 Transports (Sv)													

* End date: 21/03/2014

Table 3.5: Time-series mean and annual mean RAPID1000|4820 transports (Sv) isolated for the region to the west of WB5. Transports are a combination of absolute values from the coast to WB2 and geostrophic transports between WB2 and WB5. Each year begins in April. Mean transports for the time-series, from 2004 to 2014, are given with standard deviations in italics. Averages for the first four years (from April 2004) and the subsequent four years (from April 2008) are given in the last two columns. Northward transports are positive.

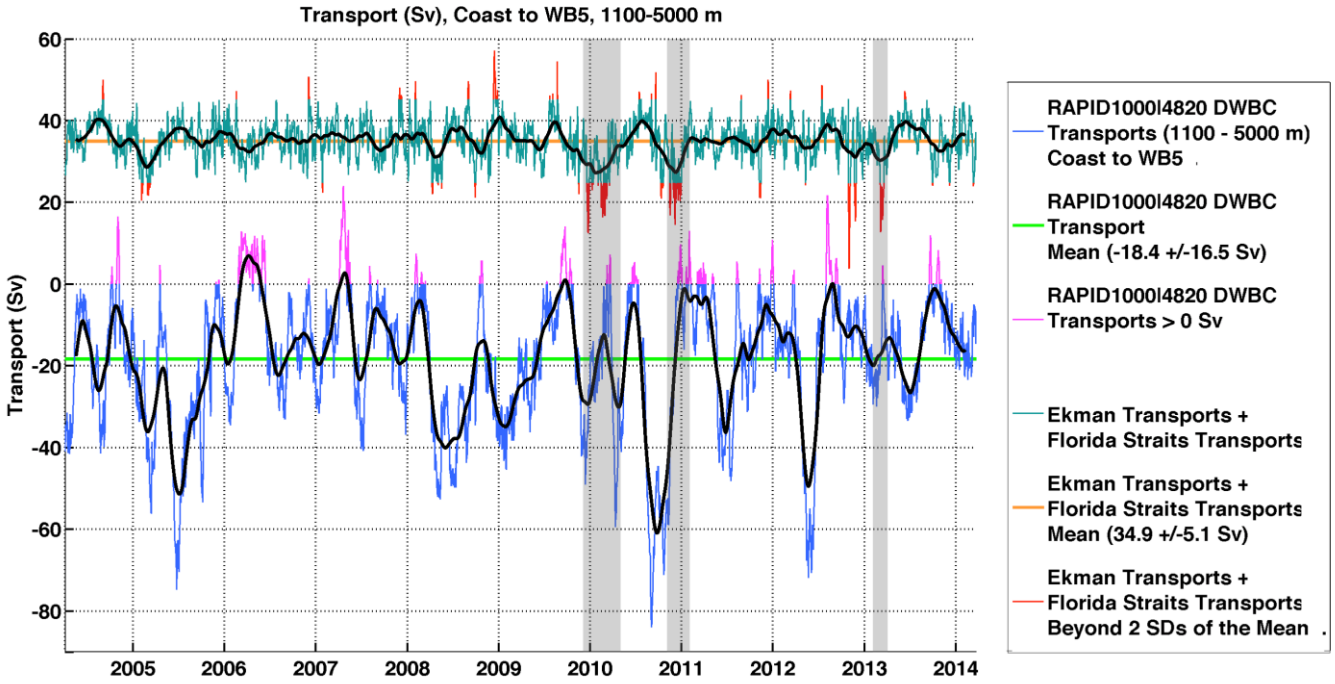

Figure 3.10: RAPID1000|4820 transports (Sv) isolated for the region to the west of WB5 below 1100 m (blue) and combined Ekman and Florida Straits transports (teal) (both are 10-day low-pass filtered). RAPID1000|4820 DWBC transports are a combination of absolute values from the coast to WB2 and geostrophic transports between WB2 and WB5. Instances of northward RAPID1000|4820 DWBC transports are highlighted (pink). Mean RAPID1000|4820 DWBC transports are included (lime). Instances of combined Ekman and Florida Straits transports that are more than 2 standard deviations beyond the mean are highlighted (red). The combined Ekman and Florida Straits time-series mean is included (orange). Black lines denote the 3-month low-pass filtered equivalent. Shaded regions denote MOC downturn events.

Brief moments of northward flowing RAPID1000|4820 transports (Figure 3.10, pink highlights), below 1100 m and west of 72˚W, are less frequent in the 2008-2012 interval relative to the first 4 years. But all events of this nature are short-term. The average duration for each incident of northward flowing western boundary RAPID1000|4820 transports between 1100 m and 5000 m is 6 days, the longest incident is 56 days. Additionally, the link between these incidents and combined Ekman and Florida Straits transports weaker than 2 standard deviations of their combined mean is tenuous given the high degree of short-term variability throughout the time-series.

3.3.4 RAPID4820 compared to RAPID1000|4820 transports

Figure 3.11 displays RAPID1000|4820 transports (on the right) next to normal RAPID4820 transports (on the left). Deep layer transports are drastically altered by the strengthened DWBC. There are many more occurrences of weak southward flowing LNADW (Figure 3.11b iii).

The primary origins of UNADW are the Labrador Sea and Irminger Seas, whereas the primary origins of LNADW are the Nordic Seas. Observations show constant deep-water formation in the Nordic Seas (Jochumsen et al., 2012; Olsen et al., 2008). Conversely, deep-water formation rates for the constituent sources of UNADW display much variability (Yashayaev and Loder, 2009). This suggests that, of the deep southward flows at 26˚N, UNADW will display the greatest variance. Both UNADW and LNADW RAPID1000|4820 transports show great variance throughout the timeline (Figure 3.11, right side).

Mean layer RAPID4820 transports (Figure 3.11, left side) are detailed in Table 3.1. Mean layer RAPID1000|4820 transports (Figure 3.11, right side) can be found in Table 3.3. RAPID1000|4820 transports reveal a stronger southward LNADW mean relative to the UNADW mean. This is a reversal relative to RAPID4820 transports. It should be noted that LNADW displays particularly weak southward transports during downturn events, regardless of the choice of reference level (Figure 3.11).

Differences between RAPID4820 transports verses RAPID1000|4820 transports are shown in Figure 3.12. RAPID4820 MOC transports are compared to RAPID1000|4820 MOC transports in Figure 3.13. MOC transports are little changed by the shallow reference level between WB2 and WB5 (the mean difference is ~ 1 Sv), which increases confidence in the choice of DWBC reference level at 1000 dbar.

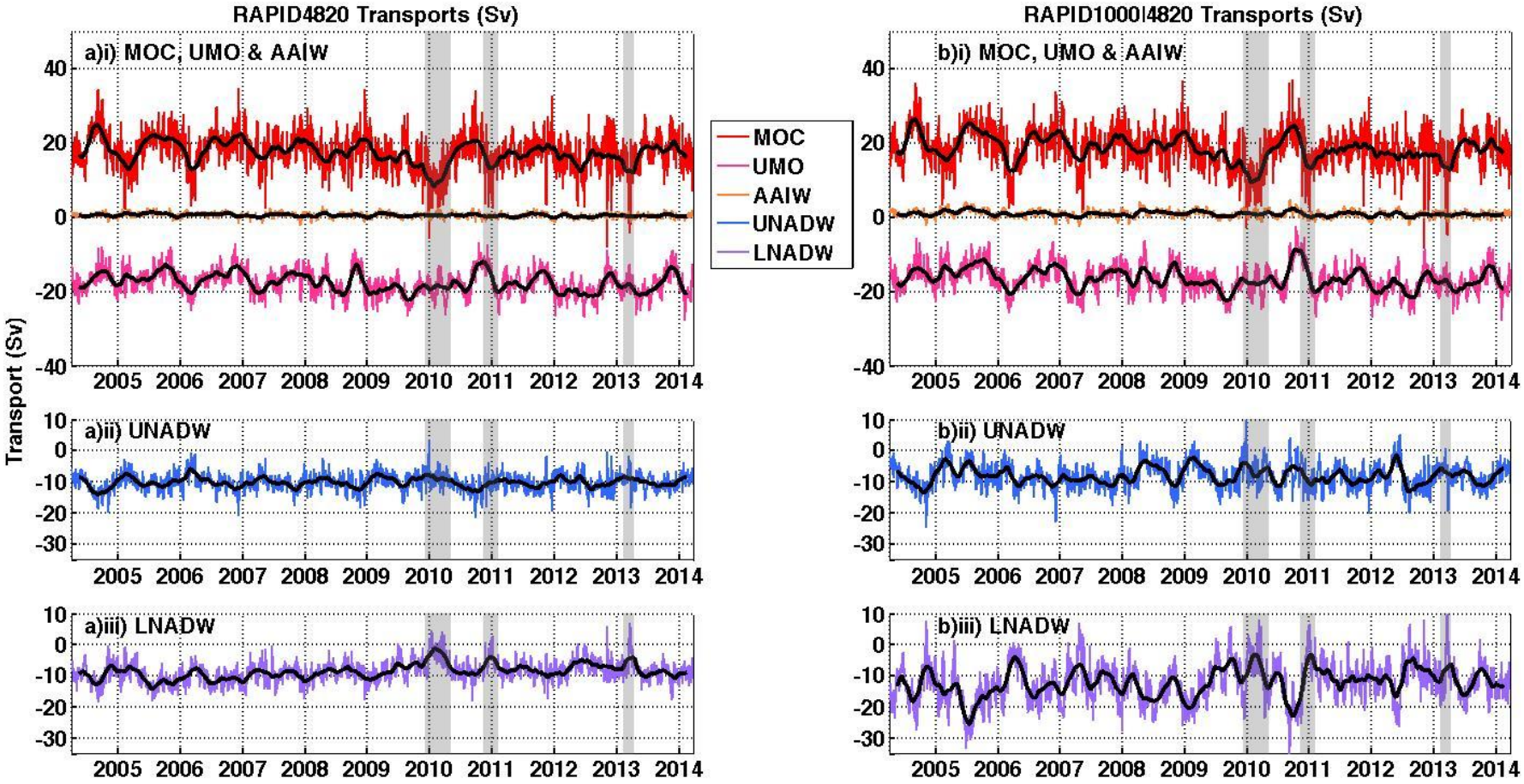

Figure 3.11: Layer transports (Sv): a) RAPID4820; b) RAPID1000|4820. Transports are 10-day low-pass filtered. Black lines denote the 3-month low-pass filtered equivalent. UNADW and LNADW layers have the same y-axis scale. Shaded regions denote MOC downturn events.

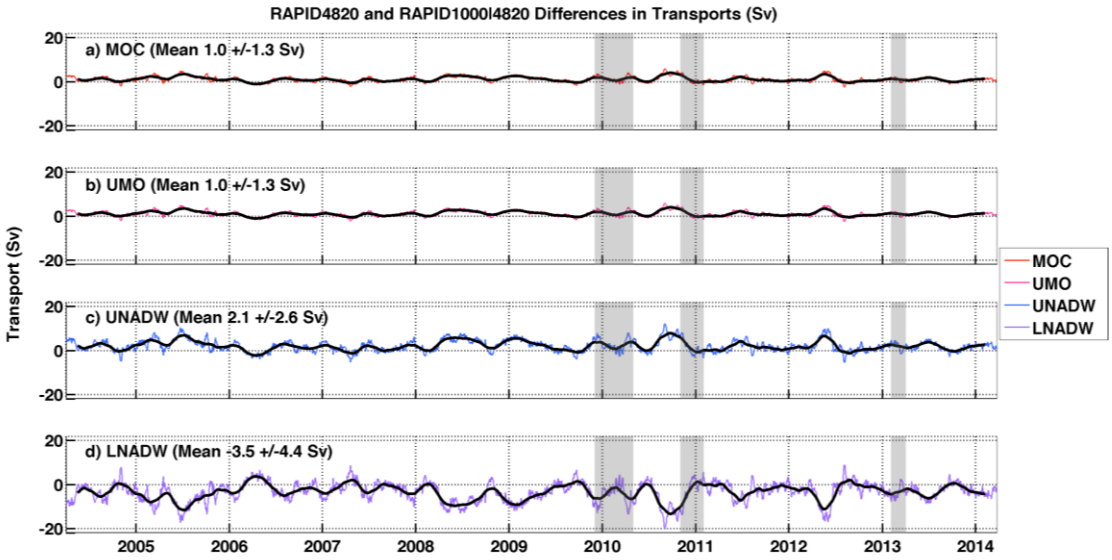

Figure 3.12: Differences in RAPID4820 and RAPID1000|4820 layer transports (Sv): a); MOC b) UMO; c) UNADW; d) LNADW. Transports are 10-day low-pass filtered. Black lines denote the 3-month low-pass filtered equivalent. Shaded regions denote MOC downturn events.

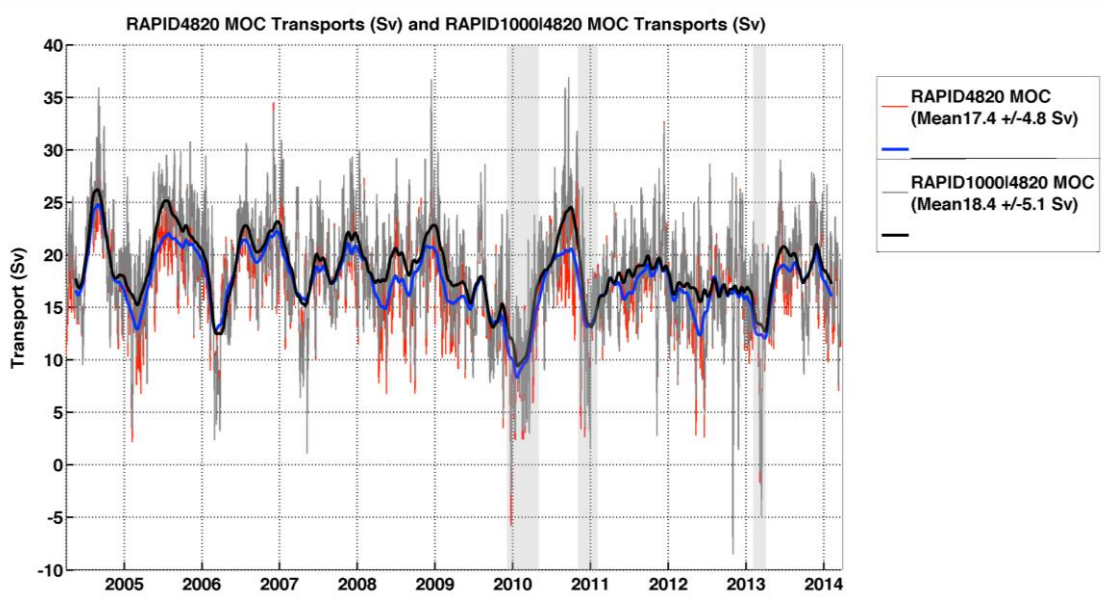

Figure 3.13: RAPID4820 (red) and RAPID1000|4820 (grey) MOC transports (Sv). Transports are 10-day low-pass filtered. The blue line denotes the 3-month low-pass filtered RAPID4820 MOC transports. The black line denotes the 3-month low-pass filtered RAPID1000|4820 MOC transports. Shaded regions denote MOC downturn events, which are typified by weakened northward Ekman transports, weakened southward LNADW transports and, to a lesser extent, weakened northward Florida Straits transports.

3.3.5 RAPID4820 compensation transports compared to RAPID1000|4820 compensation transports

Compensation transports are shown in Figure 3.14. RAPID4820 compensation transports and RAPID1000|4820 compensation transports are summarised in Table 3.6 (gold row and purple row, respectively).

			Downturn Event Means				
	Mean	SD	Dec 2009 - Apr 2010	Nov 2010 - Jan 2011	Feb 2013 - Mar 2013	4-Year Means	
	2004-2014*					2004-2008	2008-2012
RAPID4820	-27.8 ± *11.4*		-10.5	-12.7	-15.2	-32.6 ± *10.3*	-24.4 ± *10.9*
RAPID1000|4820	0.2 ± *33.8*		26.7	2.3	11.4	-8.8 ± *30.3*	9.4 ± *35.6*
	Compensation Transports (Sv)						

* End date: 21/03/2014

Table 3.6: Mean compensation transports (Sv) for RAPID4820 transports and RAPID1000|4820 transports. Mean compensation transports, from 2004 to 2014, are given with standard deviations in italics. Mean transports are given for each downturn event in 2009-10, 2010-11 and 2013. Averages for the first four years (from April 2004) and the subsequent four years (from April 2008) are given in the last two columns. Northward transports are positive.

RAPID1000|4820 compensation transports convey huge short-term variation and large standard deviation (Figure 3.14 & Table 3.6) owing to its purpose as counterbalance to the other transport components, including the large and variable DWBC transports revealed by the shallow western boundary reference level. Johns et al. (2008) find that net transports (inclusive of both the barotropic and baroclinic components) between 1000 m and 5000 m have a range of 3 Sv to -60 Sv, with mean -26.5 Sv at 26.5°N. The results of Johns et al. (2008) cover a relatively short period of time from March 2004 to May 2005, which may not capture the full scale of decadal variability. Johns et al. (2008) employ current meter data from the coast to WB3 and dynamic height data between WB3 and WB5, with time-varying reference level determined by BPR data, to measure the DWBC. They conclude, using BPR data, that DWBC baroclinic fluctuations are low frequency, whereas the barotropic component is large and high-frequency. Bryden et al. (2005a) utilise current meter data, dating from March 1986 to June 1997, to an offshore distance of 625 km at 26.5°N to find that mean DWBC transport from 1000 m to 4860 m depth is -24.2 Sv. Meinen et al. (2004) employ hydrographic

data with Inverted Echo Sounder records and bottom pressure data to measure the DWBC at 26.5˚N between ~807 m and ~4887 m (though their measurements omit the WBW region west of WB2). They find that mean DWBC transport is -25 ±23 Sv. Meinen et al. (2004) surmise that DWBC flow is largely barotropic. Toole et al. (2011) utilise hydrographic data, shipboard ADCP data and a moored array spanning the continental slope around 39˚N, 70˚W to measure the DWBC. They find that DWBC transports range from -3.5 to -79.9 Sv with mean -25.1 ±12.5 Sv. The results of Johns et al. (2008), Bryden et al. (2005a), Meinen et al. (2004) and Toole et al. (2011) highlight the size and short-term variability of DWBC flow, which justifies the large increase in variance found when comparing RAPID4820 compensation transports with RAPID1000|4820 compensation transports.

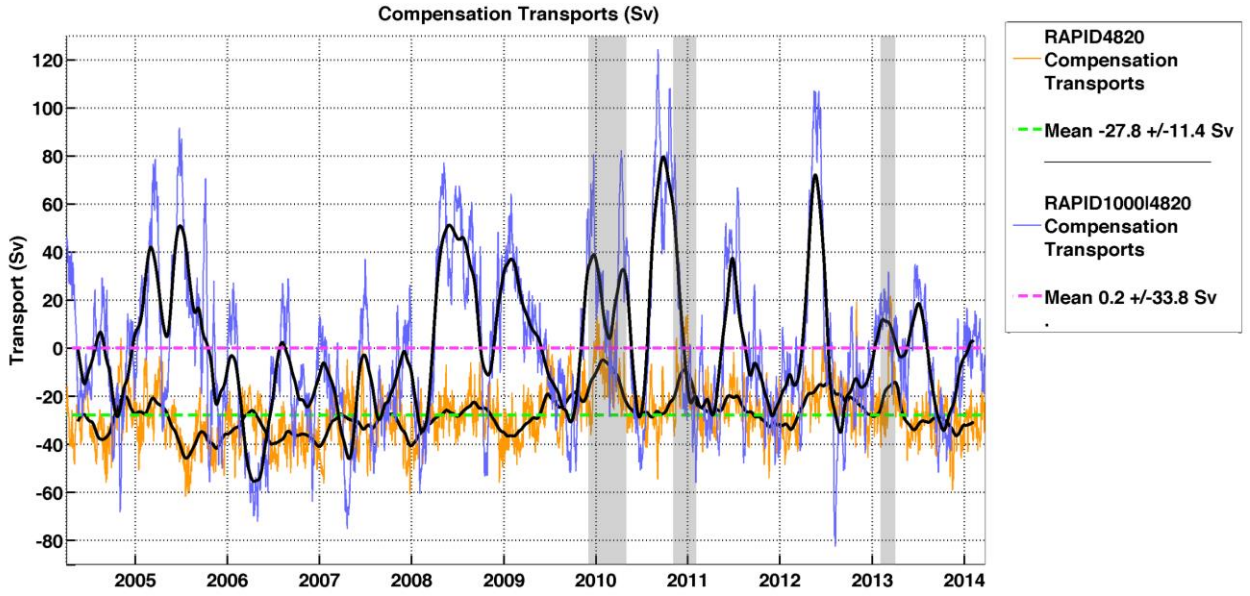

Figure 3.14: Compensation transports (Sv) for RAPID4820 (gold) and RAPID1000|4820 (blue-purple). The means for both RAPID4820 compensation transports (green) and RAPID1000|4820 compensation transports (pink) are included. Transports are 10-day low-pass filtered. Black lines denote the 3-month low-pass filtered equivalent. Shaded regions denote MOC downturn events.

With regard to the three downturn events (Figure 3.14, grey shading), southward RAPID4820 compensation transports are, on average, 15.0 Sv weaker than the mean (Figure 3.14, gold line; Table 3.6, gold row). RAPID4820 compensation transports are 8.2 Sv stronger southward, on average, in the first 4 years relative to the second 4 years (Table 3.6, gold row). However, these changes all fall within 1 standard deviation.

In the centre of the 2009-10 and 2010-11 downturn events and the tail-end of the 2013 downturn, there is a brief negative spike below the mean (Figure 3.14, pink dashed line conveys the mean). These brief moments of RAPID1000|4820 compensation transports below the mean are not indicative of the transports throughout the whole duration of each downturn, as there is a great deal of variance over short timescales. For this reason, mean RAPID1000|4820 compensation transports in Table 3.6 (bottom row) for each downturn are positive and not southward flowing. Four-year mean RAPID1000|4820 compensation transports are stronger southward, by 18.2 Sv, in the first 4 years relative to the subsequent 4 years. But, given the high degree of short-term variability resulting in a large standard deviation of ±33.8 Sv, this is not significant.

RAPID1000|4820 transports result in large and highly variable compensation transports relative to RAPID4820 transports. The results of Landerer et al. (2015) provide verification of RAPID4820 compensation transports. However, their methodology involves averaging bottom pressure values for an entire depth layer (in their case 3000m to 5000 m depth) and calculating the difference between the west side of the basin and the east side. It may therefore be conceivable that bottom pressure differences for the depths and widths relevant to the DWBC (which wouldn't surpass the distance from the western boundary to the MAR) and an altered methodology that only higher resolution bottom pressure data would make possible, could convey a different signal of barotropic transports that correlate with RAPID1000|4820 compensation transports.

3.4 Limitations and uncertainties

There is inevitably an inherent uncertainty regarding the estimation of ocean transports. But while total values will only be approximations, it is possible to determine variability and the extent to which this represents a substantial shift from the norm. The ideal reference level velocity is a concept that does not exist; ocean layer transports vary with time and space, so a static reference level can only result in estimates of the flow. Further uncertainties surround the DWBC and its meandering eastern extent, thus the location of mooring WB5 at 72°W will often capture flow that is a poor representation of the true extent of transports in the DWBC region. Furthermore, the boundary profile data may sometimes be inside an eddy or some other local recirculation. This would yield large internal variability that is not pertinent to the basin-wide flow.

The strength of the overturning circulation is also complicated by recirculating gyres and mesoscale eddies. The RAPID method of calculating transports ignores Bering Straits inflow, ~0.8 Sv, which is small relative to other errors. Additional sources of error, such as the lack of data below 4820 dbar and the omission of bottom triangle transports, further increase the uncertainty regarding MOC estimates. Analysis of some of these uncertainties (Sinha et al., 2017) provides reassurance that reliable conclusions may nonetheless be drawn regarding MOC variability.

3.5 Discussion and conclusions

The strength of the AMOC influences the movement of heat that impacts climate. Changes in the lower southern flowing limb of the AMOC have implications for the total overturning circulation. Data from the RAPID array of moorings along 26.5˚N from 2004 to 2014 are explored. These moorings form the boundary profiles of the RAPID calculation, allowing continuous measurement of the AMOC. In Chapter 3, a new approach to the RAPID AMOC calculation is made by adding a fifth dynamic height profile at location WB5 (located at 72˚W, approximately 500 km offshore from the western boundary). Furthermore, deep western boundary transports are strengthened by means of the reference level rather than compensation to eliminate bias caused by a tapering basin. This alteration of the method allows an alternative estimation of the southward transports in the deep layers.

The choice was made to apply a shallow reference level of 1000 dbar at the western boundary and not across the whole basin because the level of no motion is less clear to the east of the DWBC region. Additionally, this decision ensured that transports in the main basin were not re-distributed higher up, which would shift southward LNADW into the UNADW layer.

DWBC transports are strong relative to the total AMOC (Bryden et al., 2005a; Toole et al., 2011; Meinen et al., 2013) with great recirculation, making estimation of the deep return flow complex. This is nonetheless a valuable pursuit, as the DWBC is likely to provide the main mechanism for transporting deep water from high latitudes. Thus, buoyancy changes and their influence on the AMOC could be discerned. Changes in NADW are likely to be related to long-term changes in North Atlantic deep convection rates. However, water-mass signals tend to weaken as they move further from their source, thus their affect at

subtropical regions is one of slow adjustment. Timescales and pathways of UNADW southward flow, which is largely composed of Labrador Sea Water (LSW), are not fully resolved. Bryden et al. (1996) conclude that LSW takes ~15 years to reach 24.5°N; Curry and McCartney (1996) deem the lag to the subtropics to be 5 to 7 years; a ~10 year lag was found by Molinari et al. (1998); a southward advection time lag of ~9 years is suggested by Van Sebille et al. (2011). LNADW has its source in the Greenland-Iceland-Norwegian Seas and begins at a depth of ~ 3000 m. The deep-water formation rate is not believed to influence the deep layer of the DWBC, but rather, the rate at which these deep waters flow over the sills dividing the Greenland-Iceland-Norwegian Seas and sub-polar North Atlantic is key. The time lag will be a few years longer than that of LSW, making the influence of varying convection rates difficult to discern.

Smeed et al. (2014) remark on UNADW, which can be traced back to the Labrador Sea and Irminger Sea, which exhibits larger variation in deep convection relative to LNADW. LNADW traces back to the Nordic Seas that display stable convection rates. This is a reversal of the expected outcome given that the findings, here, indicate greater variability in DWBC transports below 3000 m.

There is support for the DWBC being disjointed due to recirculation and interior pathways (Boer et al. 2009). This further complicates the task of relating DWBC transports at 26°N to deep-water formation changes. Lozier (2010) goes a step further in advocating the theory that eddy fields create an alternative route in particular regions, which would have implications for the pathways and timescales of the AMOC. The work of Lozier (2010), however, concentrates on a depth of 1500 m, affecting the Labrador Sea Water layer and not Denmark Straits Overflow Water.

Within Chapter 3, dynamic height data at 72°W is added to the boundary profiles and a static reference level of 1000 dbar is employed, in addition to current meter absolute transports for the region west of 77°W, to estimate DWBC flow. The inclusion of strong deep transports in the DWBC region into the AMOC calculation, referred to as RAPID1000|4820 transports, comes with the uncertainty surrounding the choice of fixed reference level. Yet, the attempt to include strong DWBC flow in the internal transports does not affect the UMO layer to a great degree due to the compensation and therefore the total MOC mean is strengthened by just 1 Sv.

For basin-wide RAPID1000|4820 transports, the major deductions are:

1. Weak southward flowing LNADW transports continue to serve as a determining factor of downturn events: southward LNADW transports are weaker during downturn events by, on average, 4.7 Sv;
2. RAPID1000|4820 compensation transports convey huge short-term variation and large standard deviation but with a near-zero mean, there is no easily discernable trend in RAPID1000|4820 compensation transports for downturn events relative to the rest of the time-series;
3. RAPID1000|4820 compensation transports are large and variable, with mean 0.2 ±33.8 Sv, partly due to its purpose as counterbalance to the large and variable DWBC flow.

Regarding RAPID1000|4820 DWBC transports isolated to the west of WB5 at 72°W, the main conclusions are:

1. Brief moments of northward DWBC transports below 1100 m are less frequent in the second 4-year interval relative to the first 4 years, reducing from 12.2% to 10.8% of the time-series for each 4-year interval (95% confidence), but there is a high degree of short-term variability;
2. The mean strength of the RAPID1000|4820 DWBC is 18.4 ±16.5 Sv, which equals the strength of the RAPID1000|4820 MOC (18.4 ±5.1 Sv).

The RAPID1000|4820 DWBC estimate is lower than mean transport measurements made by:

- Johns et al. (2008) of -26.5 Sv (using current meter data, BPR-derived absolute transports and dynamic height moorings at 26.5°N, between 1000 m and 5000 m depth, from the western boundary to WB5 located 500 km offshore, spanning March 2004 to May 2005);
- Bryden et al. (2005a) of -24.2 Sv (using current meter data at 26.5°N, between 1000 m and 4860 m depth, from the western boundary to an offshore distance of 625 km, spanning March 1986 to June 1997);
- Meinen et al. (2004) of -25 ±23 Sv (employing hydrographic data with Inverted Echo Sounder records and bottom pressure data at 26.5°N, between ~807 m and ~4887 m depth, from WB2 to an eastward distance of 82 km, from July 1996 to June 1997);
- Toole et al. (2011) of -25.1 ±12.5 Sv (utilising hydrographic data, ADCP data and a moored array at 39°N, between 678 m to 3575 m depth, from the western boundary to an offshore distance of ~350km, spanning May 2004 to April 2008).

However, RAPID1000|4820 DWBC transports cover a different depth range and / or offshore distance, thus direct comparisons are difficult. Additionally, the time-spans differ and RAPID1000|4820 DWBC transports may cover periods of weakening not seen in the other time ranges. Previous estimates are absolute transports inclusive of both the baroclinic and barotropic components within the DWBC, whereas the RAPID1000|4820 calculation spreads the compensation component (the barotropic proxy) over the whole basin uniformly. Lastly, standard deviations made by previous estimates (listed above) are large and therefore encompass the RAPID1000|4820 DWBC mean.

Compensation applied uniformly, with a single basin-wide reference level, ensures that transports are not dependent on the depth of the chosen level of no motion. Implementing a vertical break in the basin, to apply one reference level in one region and another reference level in the other region, may not suit the application of a single uniform compensation. In Chapter 3, the basin has been split vertically at the eastern edge of the DWBC. The strong and highly variable southward flow in the DWBC region at the western boundary is found to yield equally strong and variable compensation transports. Applying the strong compensation to the basin uniformly makes it difficult to discern regions of recirculation. This is because deep internal transports, to the east of the DWBC, are reduced by the deep reference level then overwhelmed by the compensation. Splitting the compensation for each region, or perhaps applying it solely to the DWBC region, could further develop the methodology and provide insight into DWBC recirculation. Alternatively, a reference level of 3200 dbar (the interface between UNADW and LNADW) to the east of WB5 may boost deep transports in the main basin. This could also reveal insight into DWBC recirculation and alter the magnitude/variance of the compensation transports. Further investigation into how best to apply different reference levels to the basin, and possibly two or more compensation components, would be needed to build up evidence as to whether this is a viable alteration to the RAPID calculation methodology.

Crucial elements of the MOC are concentrated at the western boundary and the strength of these, inferred from current meter and dynamic height data, can be incorporated into the RAPID time-series calculation. The point, here, was to improve the representation of DWBC UNADW and LNADW flow within the RAPID time-series calculation and to characterise instances of reduced overturning. Understanding variation of the deep layers improves analysis of the degree of correlation between upper ocean components. It isn't necessarily the case that a

shallow reference level at the western boundary is inherently better than a basin-wide deep reference level. RAPID1000|4820 transports result in compensation transports that have a near-zero mean but variance is greater than that of standard RAPID4820 transports. Nonetheless, a shallow western boundary reference level does reveal insight into the major ocean components. It would be valuable to present RAPID transports with both a basin-wide deep reference level and a western boundary shallow reference level for comparison. A shallow western boundary reference level enables an alternative view of transports incorporating a more realistic spatial structure of circulation. Whilst the North Atlantic is a highly observed ocean, there remain major gaps in our knowledge as to its circulation. The AMOC resists complete characterisation of its spatial and temporal variability, as well as mechanisms for change, but continuing efforts shed light on long-term trends.

3.5.1 Summary

- The importance of the AMOC regarding the climate, particularly that of North-West Europe, lies in its capacity to move heat poleward (Srokosz et al., 2012). Continuous observational data from the RAPID array at 26°N since 2004 allow determination of AMOC strength (McCarthy et al., 2015a). The RAPID method of calculating AMOC transports reduces lower basin transports with a deep reference level then increases it with a uniformly applied compensation.
- The strong and highly variable DWBC contribution is included in the calculation by taking the novel approach of inserting a profile at 72°W and raising the geostrophic reference level to 1000 dbar for the western boundary region, such that the shallow reference level strengthens deep water transports, as opposed to the compensation component.
- Downturn events occurred in 2009-10, 2010-11 and 2013 and are typified by weakened northward Ekman transports, weakened southward LNADW transports and, to a lesser extent, weakened northward Florida Straits transports (Frajka-Williams et al., 2016). Where the western boundary reference level is raised to 1000 dbar, weak southward LNADW layer transports continue to serve as a determinant of downturn events.
- Smeed et al. (2014) find that, during the first 4 years of RAPID observations, the overturning circulation was 2.7 Sv stronger than in the subsequent 4 years. Basin-wide transports, calculated with a 1000 dbar reference level from the west coast to WB5 and a 4820 dbar reference level

thereafter, show a 2.1 Sv stronger MOC for the first 4 years relative to the subsequent 4 years.

- It would be of value to present RAPID transports with both a basin-wide deep reference level and a western boundary shallow reference level for comparison. A shallow western boundary reference level enables an alternative view of transports incorporating a more realistic spatial structure of circulation. However, the application of compensation transports needs to be assessed, as it is likely these transports should be distributed primarily at the western boundary.

Chapter 4: Estimates of AMOC deep transports using GRACE ocean bottom pressure for 2004-2016

4.1 Introduction

The dynamics of the Atlantic Meridional Overturning Circulation (AMOC) play a key role in the global climate system and the carbon cycle (Meredith et al., 2011). The circulation consists of northward Ekman transports and northward Florida Straits transports of relatively warm waters compensated by southward internal transports. The main water-masses at 26˚N are the UMO, UNADW, LNADW and AABW layers. LNADW is the bottom half of the AMOC deep return flow and has been identified as providing compensatory flow for changes in transports within the top 800 m (Smeed et al., 2014; Frajka-Williams et al., 2016). UNADW is the top half of the deep return flow but has not been found to counterbalance any of the upper ocean flow components using a time-series of continuous basin observations. Deep and dense AABW flow is northward flowing and difficult to observe, so estimates of decline (Johnson et al., 2008) and the impact on the wider AMOC are important areas of investigation. The zonal structure and strength of these layer transports can be assessed using observational data. Hydrographic section data since 1957 have been utilised to estimate AMOC strength (Longworth, 2007; Atkinson et al., 2012, Hernández-Guerra et al., 2014). However, these sections were conducted several years apart, providing poor temporal information. Continuous observations, since 2004, by the RAPID array provide greater temporal data but the dataset is limited by the difficulty of positioning instruments deep within the basin. RAPID array data aren't able to capture deep ocean transports below 4820 dbar and so an estimate of 1 Sv of northward AABW flow is employed in the calculation of internal transports. Compensation transports are added as a residual, uniformly over the basin, to ensure net zero flow. Kanzow et al. (2007) find that these compensation transports are a good approximation for transports driven by ocean bottom pressure (OBP) fluctuations. OBP-derived transports could therefore provide greater insight into MOC trends. The Gravity Recovery and Climate Experiment (GRACE) twin satellites measure ocean mass (Piecuch & Ponte, 2014). GRACE data

(Tapley et al., 2004) therefore provides a source of basin-wide OBP observations. The OBP-derived vertically averaged currents through the section are referred to as the external transports.

GRACE data translated to OBP will contain information on the pressure response at the ocean floor to forces such as atmospheric pressure acting on the bathymetry. Within Chapter 4, commensurate with the task of calculating deep transports, global GRACE data are condensed down to coverage matching that of the RAPID array, spanning the Atlantic Ocean at 26˚N, to produce a time-series. This is complicated by the poor spatial resolution (~300 km) and missing data, due to satellite battery management, within the GRACE dataset. But a major benefit of transports based on OBP is that there is less interference from recirculations or small-scale processes, such as eddies. Furthermore, GRACE OBP can be employed to compute transports globally.

OBP variations derived from bottom pressure recorders (BPRs) may be used as a valuable comparison with satellite measurements of time-variable gravity made by GRACE. However, the deployment of each BPR instrument is relatively short and prone to sensor drift. This creates the additional problems of removing drift and assembling several records to create a time-series. Hydrographic data (employing a deep reference level) also provide useful measures of veracity in the processed GRACE OBP data after conversion to transports.

Concerns regarding the ~5 Sv downturn in 2009-10 motivate the need for a comprehensive estimate of the overturning (McCarthy et al., 2012). The main goal of this work is to further understand trends in AMOC transports using OBP variations. Variability of the depth-averaged transports over time can be calculated by integrating OBP gradients (Hughes et al., 1999). Landerer et al. (2015) demonstrate that GRACE-derived transports correlate well with LNADW transports calculated using RAPID array data. The work in Chapter 4 involves a methodology that differs from that of Landerer et al. (2015), the pre-processing is simplified, and in the latter part of the analysis, time-series de-trending will be removed to preserve the long-term trend (Section 4.3.4). The primary aim, here, is to calculate AABW transports. The secondary aim is to extend the GRACE-derived LNADW layer transports to incorporate recent data. The calculation of AABW transports, in particular, will help to highlight the importance of deep ocean measurements. Chapter 4 explores the variability of AABW transports at regular monthly intervals and the affect on the total MOC.

4.2 Data and methods

4.2.1 GRACE data

GRACE data and its post-processing are described by Watkins et al., (2015) and Wiese et al., (2016). The twin satellites that comprise the GRACE system (Tapley et al., 2004) allow insight into long-term variation of an important ocean parameter, liquid equivalent height, which is related to OBP. The range and range-rate between the satellites allow gravity and mass changes to be determined. The main cause of gravity field change with time over the oceans is assumed to be due to water-mass movement (Wahr et al., 1998). OBP anomalies calculated from equivalent surface elevation are computable owing to the vertical pressure variation between two columns of seawater being dependent on seawater density, elevation change and the acceleration due to gravity. The pressure due to a liquid in a liquid column is represented by:

$$\Delta P = \rho g \Delta h$$

where Δ indicates an anomaly relative to the long-term mean, P is liquid pressure (Newtons/m^2), g is gravity at the surface of the water column (9.8 m/s^2), ρ is seawater density (1.027 x 10^3 kg/m^3) and h is the height from the surface to the ocean floor (m).

The relationship between meridional external transport, $T(y)$, at a given latitude, y, and OBP difference between pressure values for the eastern and western stations, p_e and p_w, (e.g. Kanzow et al., 2007; Bingham and Hughes, 2008; Landerer et al., 2015) is:

$$T(y) = \frac{1}{f\,\rho_0} \int_{z_1}^{z_2} p_e\,(y,z) - p_w(y,z)\,dz$$

where f is the Coriolis parameter, ρ_0 is seawater density (typically 1027 kg/m^3) and z_1, z_2 are the depth levels. Positive flow represents northward movement through the section. OBP, p, is in units of (Newtons/m^2).

GRACE data are available with the 2004-2009, inclusive, mean subtracted from the time-series of liquid water equivalent thickness (cm). Coverage of the anomaly data spans from April 2002 to August 2016. However, some monthly values are missing due to battery management protocols for the instruments. The longitudinal resolution is such that there is a data point for each 3˚ square

covering ~300 km at 26˚N. The 300 km grid elements are known as mass concentration blocks (mascons) and for each mascon there is a monthly mean liquid water equivalent thickness value. Each monthly data value with a low number of constituent days (less than half a month), from which the monthly mean is averaged, is removed. Additionally, part of the very beginning and end of the timeline were omitted due to the number of missing months, creating large gaps in the time-series between which the values would otherwise need to be interpolated. Each mascon transition is smoothed with a Gaussian averaging filter with a 50 km half width, in both longitude and latitude, to remove noise. A 50 km half width was chosen because each mascon is provided on a 50 km grid where the mascon value is repeated across 300 km, so the Gaussian filter creates a gradual transition between each mascon but without changing the central values within them. Data with latitude 26˚N and longitude spanning 77˚W to 13˚W are extracted (Figure 4.1), though it should be noted that data close to the boundaries are not utilised in the transports due to issues with land leakage (an issue where the land signal leaks into the ocean signal). Liquid water equivalent thickness (cm) is converted to pressure in millibars (mbar). Figure 4.2 displays the time-mean pressure at 26˚N for each mascon. Figure 4.3 displays the time-mean pressure at 26˚N projected onto the topography, where each mascon edge is delineated by red markers. The data are de-seasonalised and then, to de-trend the data, a linear least-squares regression is removed from each monthly value. A Lowess low-pass smoothing filter, spanning 10 of the monthly data points, is applied to highlight interannual variation. It should be noted that there is very little difference between a 12-month, a 10-month and a 9-month Lowess low-pass smoothing filter, but a 10-month filter was chosen because it spans approximately 6-7% of the time-series, matching the methodology of Landerer et al. (2015). Figure 4.4 displays GRACE data before processing (after conversion to OBP anomalies) and after processing. Prior to processing, Figure 4.4a shows that the western side of the basin exhibits an OBP strengthening trend that is confined to one side of the basin. Landerer et al. (2015) attribute the western boundary linear trend to uncertainty in corrections for glacial isostatic adjustment (A et al., 2013) and land leakage (Bentel et al., 2015).

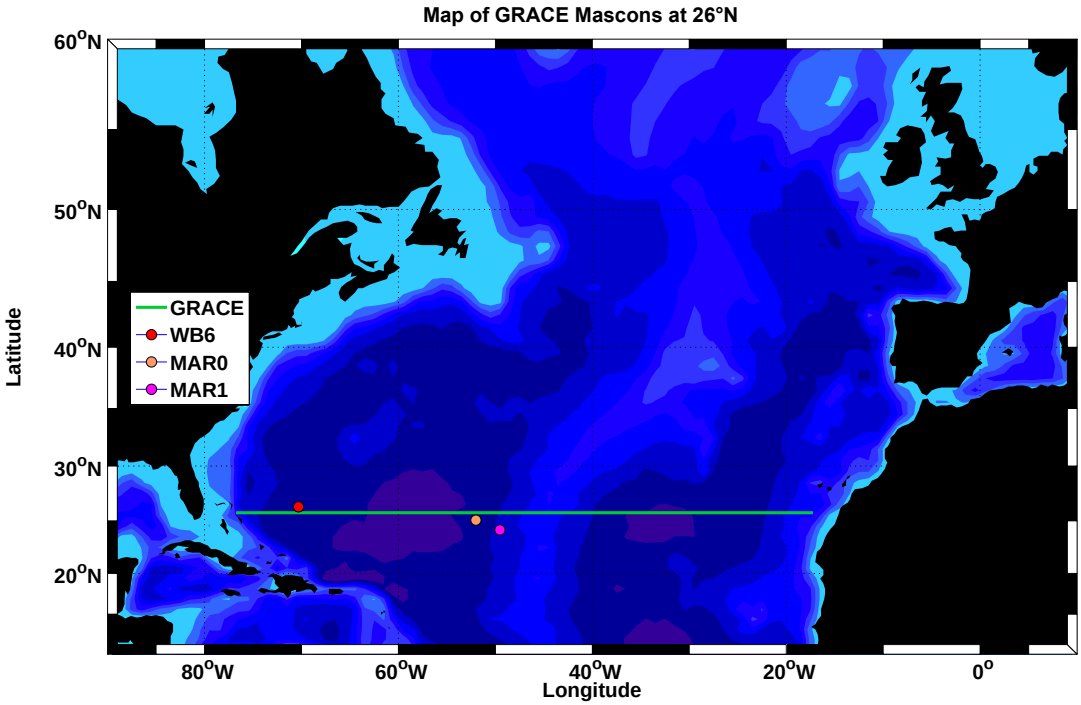

Figure 4.1: Map of GRACE data location, as well as mooring BPR sites WB6, MAR0 & MAR1.

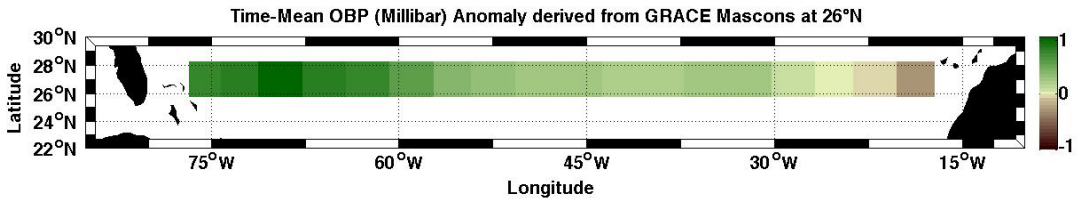

Figure 4.2: Top-down view of GRACE time-mean OBP at 26˚N. Liquid equivalent height data are converted to OBP (mbar) and then averaged from April 2004 to March 2016 for each mascon without any further processing. The colour scale denotes the change in OBP.

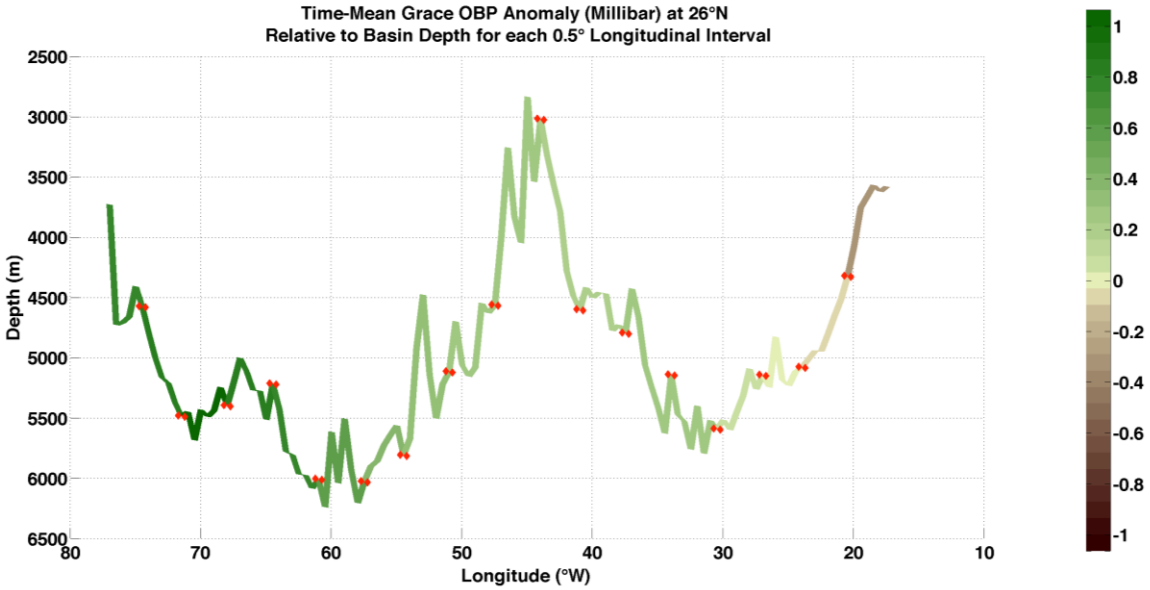

Figure 4.3: Cross-section view of GRACE time-mean OBP at 26˚N. Liquid equivalent height data are converted to OBP (mbar) and then averaged from April 2004 to March 2016 for each mascon, before being projected onto the topography, without any further processing. The colour scale denotes the change in OBP. Each mascon edge is delineated by red markers.

Anomaly transports are calculated by means of the east-to-west differencing of OBP anomalies to infer absolute velocity anomalies. Processing of the data continues by projecting the data onto a topographical map of the basin to pinpoint longitudinal values that match with the walls of the basin for each depth layer: LNADW between 3000 m and 5000 m, as well as AABW below 5000 m. This creation of data representative of each boundary wall includes the walls of the MAR for the LNADW layer but not the AABW layer, which is confined to the left side of the basin. Hydrographic sections of potential temperature show that AABW, separated by a potential temperature contour of 1.9˚C, hugs the western flank of the MAR (Atkinson et al., 2012). Care was taken to ensure that the chosen data for each water-mass boundary wall was isolated to mascons that do not crossover into an adjacent depth layer and thus leakage of nearby land signals is also reduced.

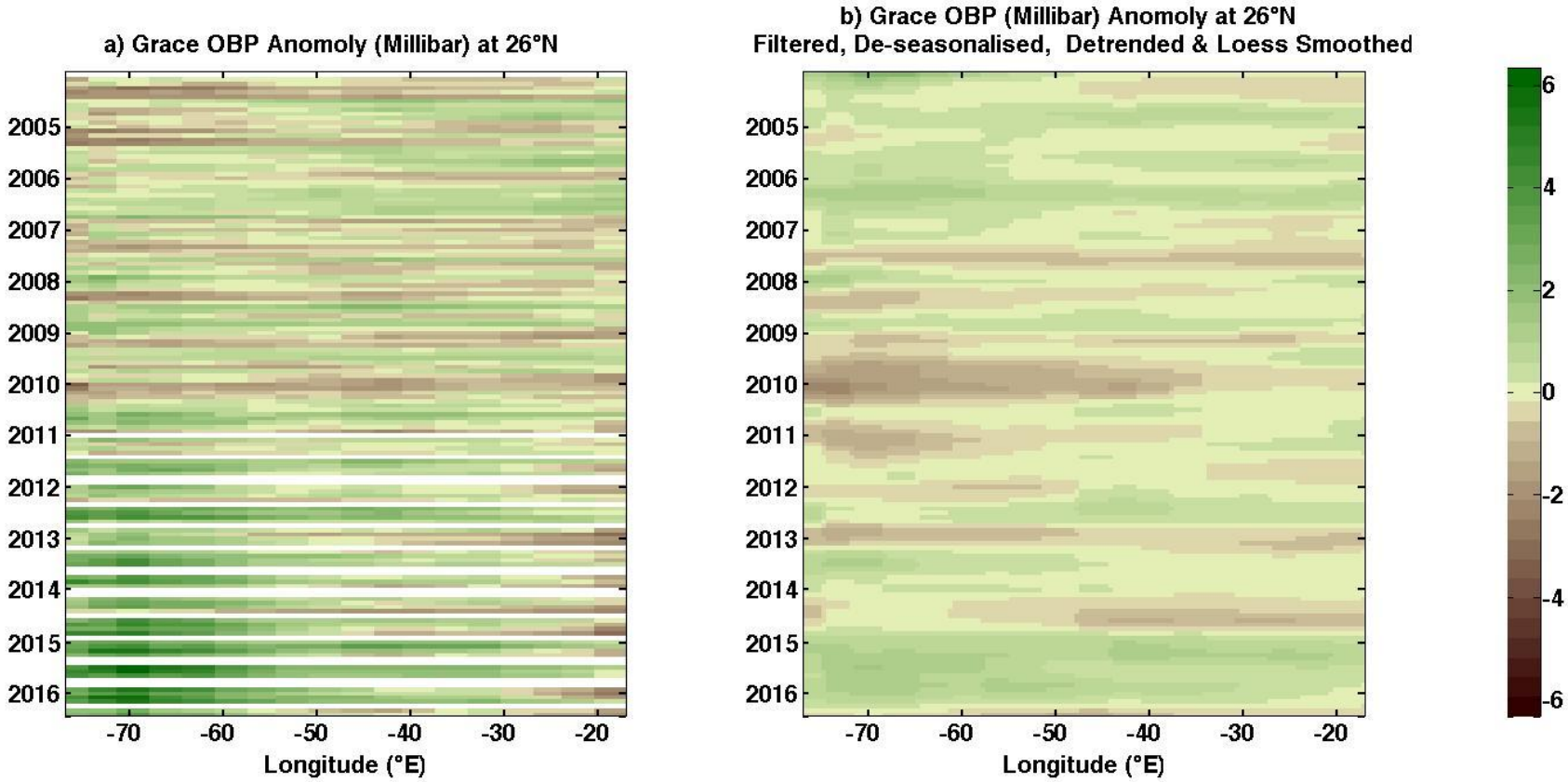

Figure 4.4: Top-down view of GRACE OBP change with time at 26°N: a) liquid equivalent height data are converted to OBP (mbar); b) liquid equivalent height data are Gaussian filtered, converted to OBP, de-seasonalised, de-trended and Lowess smoothed. The colour scale denotes the change in OBP (mbar).

4.2.2 RAPID bottom pressure data

OBP data represents the result of mass variation within the above ocean and atmosphere. In-situ observations from a number of BPRs are investigated for the purpose of authenticating OBP anomaly inferred from GRACE data. The secondary reason for exploring BPR data is to identify whether it is capable of completing gaps in GRACE data created by the continuing need for battery management. BPR measurements from pressure gauges at the ocean bottom require post-processing to remove unwanted signals such as those from tides and internal waves. Additionally, all BPRs drift, which introduces low-frequency error to the signal. Ascertaining long-term OBP variation, with BPR data, is further complicated by the short life span of each device deployment. The life span of a typical BPR instrument is less than three years owing to the need of maintenance and battery replacement, as well as the gradual decay of the sensor in a high-pressure environment.

An array of 12 BPRs at 26.5°N is maintained by the RAPID programme. The BPR locations of primary concern here are in the western side of the basin located at site WB6 at 70.3°W, MAR0 at 52.0°W and MAR1 at 49.8°W. Pairs of instruments are often deployed for each location, with temporal overlap, if possible, to enable data error correction and to ensure there is a back-up in the event of instrument failure. Tidal signals are subtracted (Pawlowicz et al., 2002) and a 2.1-day Gaussian low-pass filter is utilised to eliminate high-frequency variability. Pressure sensor drift has been shown to be exponential-linear in form (Watts and Kontoyiannis, 1990) with a residual uncertainty of ~0.02 dbar. The data for each instrument was fitted to an exponential-linear function, where the exponential element was typically confined to the first 80 days of deployment. The drift was then removed relative to the instrument mean. The instruments were merged into a single timeline using the weighted average of the data. The weighting was determined by the exponential element of the drift, which would receive a 50% lower weighting relative to the linear drift element. This produced a gradual transition from one instrument to the next.

BPR data for three key locations, WB6, MAR1 and MAR0 can be seen in Figure 4.5, Figure 4.6 and Figure 4.7. The average depth of the BPRs situated at WB6, MAR0 and MAR1 is 5372 m, though, with each deployment the depth alters in accordance with topography at each location at the average latitude of 25.2°N. The data have not had drifts removed in Figure 4.5a, Figure 4.6a and Figure 4.7a,

though all data are plotted relative to the estimated exponential-linear drift. Each coloured dataset conveys a different instrument within the plot. The drift of each BPR timespan has been removed in Figure 4.5b, Figure 4.6b and Figure 4.7b, all data are shown relative to the instrument mean. The weighted mean is calculated for overlapping BPR records and the combined timelines are assembled accordingly in Figure 4.5c, Figure 4.6c and Figure 4.7c.

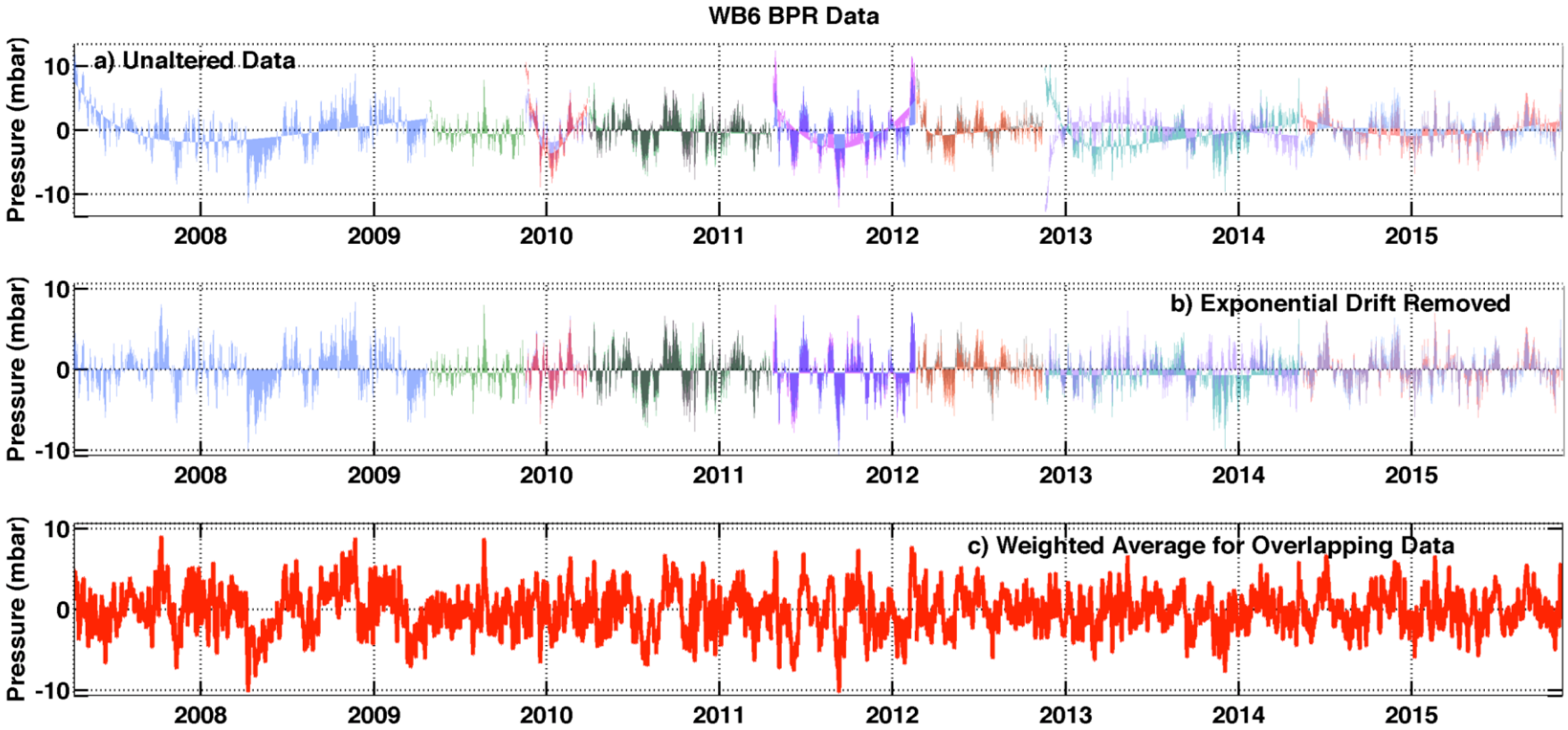

Figure 4.5: WB6 BPR data (mbar): a) prior to drift removal relative to the predicted drift (note the larger y-axis scale); b) after drift removal relative to sensor mean; c) the result of averaging overlapping instruments to create a timeline. Each coloured line in the top two plots represents a different sensor deployment.

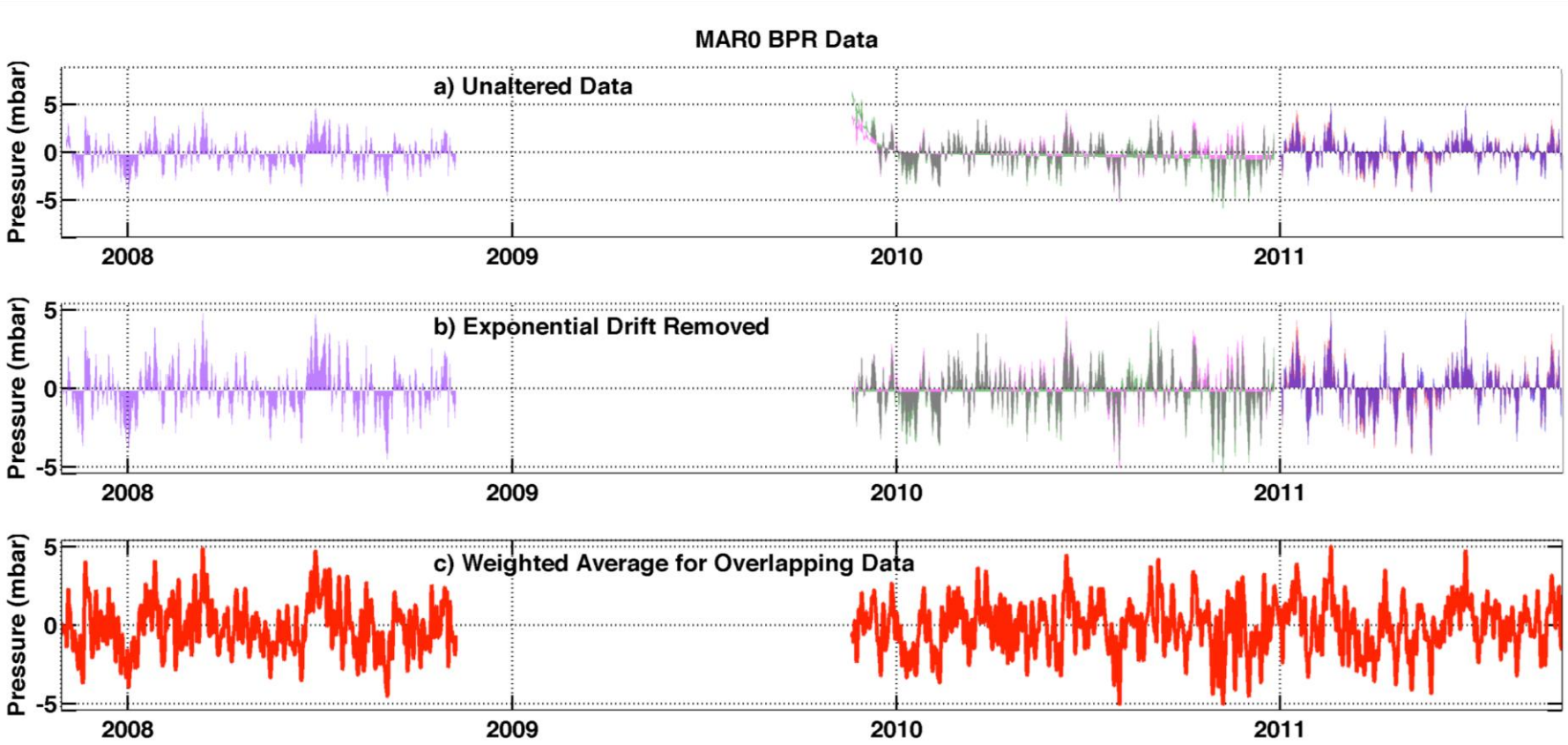

Figure 4.6: MAR0 BPR data (mbar): a) prior to drift removal relative to the predicted drift (note the larger y-axis scale); b) after drift removal relative to sensor mean; c) the result of averaging overlapping instruments to create a timeline. Each coloured line in the top two plots represents a different sensor deployment.

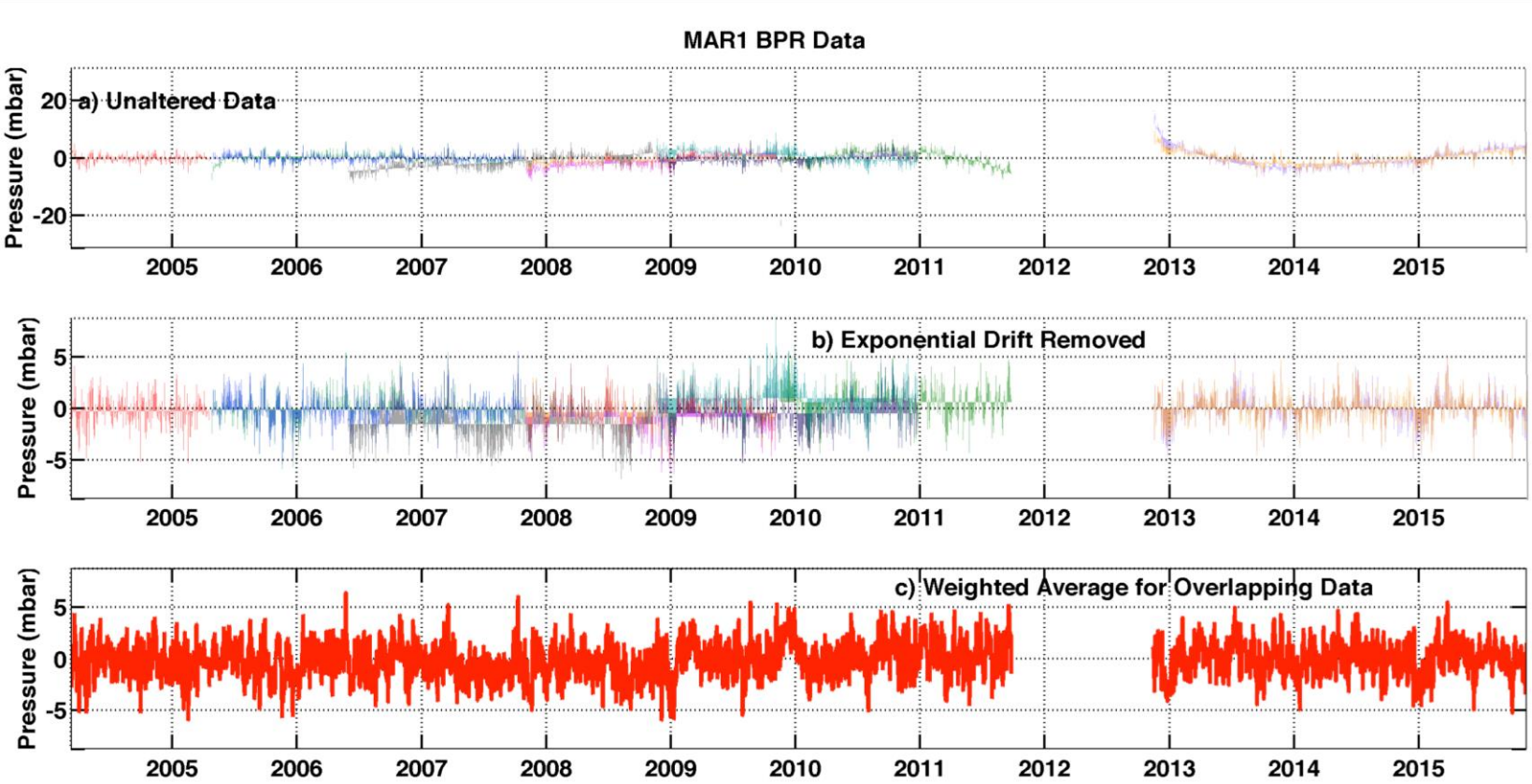

Figure 4.7: MAR1 BPR data (mbar): a) prior to drift removal relative to the predicted drift (note the larger y-axis scale); b) after drift removal relative to sensor mean; c) the result of averaging overlapping instruments to create a timeline. Each coloured line in the top two plots represents a different sensor deployment.

4.2.3 RAPID moorings data

At 26°N the RAPID array has monitored AMOC variability, since 2004, with full-depth continuous measurements made by dynamic height moorings. These moorings are positioned at the continental slopes and the MAR. The dynamic height data are employed to create four boundary profiles. The domain is essentially separated into boxed regions defined by these boundary profiles and internal transports are calculated from the western profile to the profile on the western flank of the MAR (MARwest), from MARwest to the eastern profile above the MAR and from the eastern flank of the MAR (MAReast) to the eastern profile below the peak of the MAR. The MAR height is defined here as 3700 dbar, the depth at which it is permeable to east-west exchange due to fracture zones. Sloping sidewalls are accounted for by combining mooring data that follows the topography and with an area profile that descends in accordance with the bathymetry for each depth level. Velocity is inferred from dynamic height relative to a 4820 dbar reference level, which coincides with the deepest depth of the moorings. Geostrophic transports are calculated using geostrophic velocity for the three boxed regions of the basin between the four profiles. Absolute transports for the region between Abaco and mooring WB2 at ~77°W, referred to as the Western Boundary Wedge (WBW), are added to comprise internal transports. Ekman transports computed from wind stress data and Gulf Stream transports calculated from induced voltages on telephone cables traversing the Florida Straits (Baringer and Larson, 2001) are added to internal transports. Zero net flow through the section is enforced by the application of a compensation component (e.g. Kanzow et al., 2007) to obtain the MOC total at 12-hourly intervals. A thorough description of the methodology is detailed by McCarthy et al. (2015a). RAPID internal transports will be compared with GRACE LNADW external transports, where both datasets are processed to create anomaly transports. Moorings data extend down to a depth of 4820 dbar and therefore AABW flow is not captured. Instead the RAPID calculation enforces a net transport profile of 1 Sv below 5000 m to approximate northward flowing AABW. However, from April 2009 to April 2011, deep moorings captured transports below 4820 dbar (McCarthy et al., 2015a). Mean AABW transport was found to be almost 1 Sv based on deep mooring data.

4.2.4 Hydrographic data

Several hydrographic sections crossing the North Atlantic subtropical gyre at 24.5°N have been conducted since 1957. Those that coincide with the timelines considered herein were dated April-May 2004, Jan-Feb 2010, Jan-March 2011 and Dec-Jan 2015-16. Transports are calculated in a manner akin to that of the RAPID transports time-series, except that there are over 100 vertical profiles of density per section, as opposed to just 4 boundary profiles. To calculate transports using hydrographic data, the geostrophic method is applied to determine velocity shear; absolute velocity requires a choice of level of no motion. The hydrographic method of MOC calculation traditionally employs a deep reference level of 3200 dbar and a shallow reference level of 1000 dbar in the DWBC region, which extends from the west coast to ~71°W (Bryden et al., 2005b; Atkinson et al., 2012). Due to aliasing of the highly variable western boundary transports, the hydrography will employ WBW absolute transports. Many of the hydrographic section profiles extend below 5000 m and thus estimates of AABW transports are possible. These estimates can be compared with GRACE transports.

4.3 Results

4.3.1 Comparison of GRACE ocean bottom pressure anomalies with bottom pressure recorder anomalies

A comparison of GRACE OBP anomalies and BPR OPB anomalies at 3 locations, WB6, MAR0 and MAR1, can be found in Figure 4.8. The two datasets have not been smoothed. The degree of variation between WB6 BPR data and GRACE OBP anomalies is the largest (RMS 1.06 mbar). Watkins et al. (2015) compare GRACE OBP with BPR data in the tropical North Atlantic to show that monthly to interannual variations match well, with RMS differences of 1.1 to 1.4 mbar. RMS differences in Figure 4.8 are relatively low but only because the degree of variation within each signal is similar. Smoothing of the data would produce improved correlation. Data has not been smoothed in order to determine whether BPR data could be employed to fill gaps in the GRACE timeline, but it is clear this would not be possible owing to inadequate agreement between the two datasets. Both the high-frequency variability and long-term variability match poorly, low RMS error isn't a useful measure of agreement. Differences in the structure of the OBP signals observed in the in-situ data and GRACE-derived OBP anomalies result in low correlations. Here, the in-situ data displays greater variance than GRACE

observations. The reasons for the major differences in the structures are twofold: assembling multiple instrument data into one timeline using a weighted mean is not appropriate and elimination of the severe BPR drifts may have also eliminated some of the real signals that mimic drift. To illustrate this point, it is expected that transports for the documented 2009-10 downturn have associated low OBP at the western boundary, and Figure 4.5a displays low OBP accordingly. After removal of drift (Figure 4.5b) low pressure for the downturn event is less evident. Clearly, the cost of error reduction is some signal loss. Though it should be noted that the deployment period for the instruments covering the 2009-10 downturn is very short and a longer deployment would enable better distinction between the exponential components of the drift from the linear component.

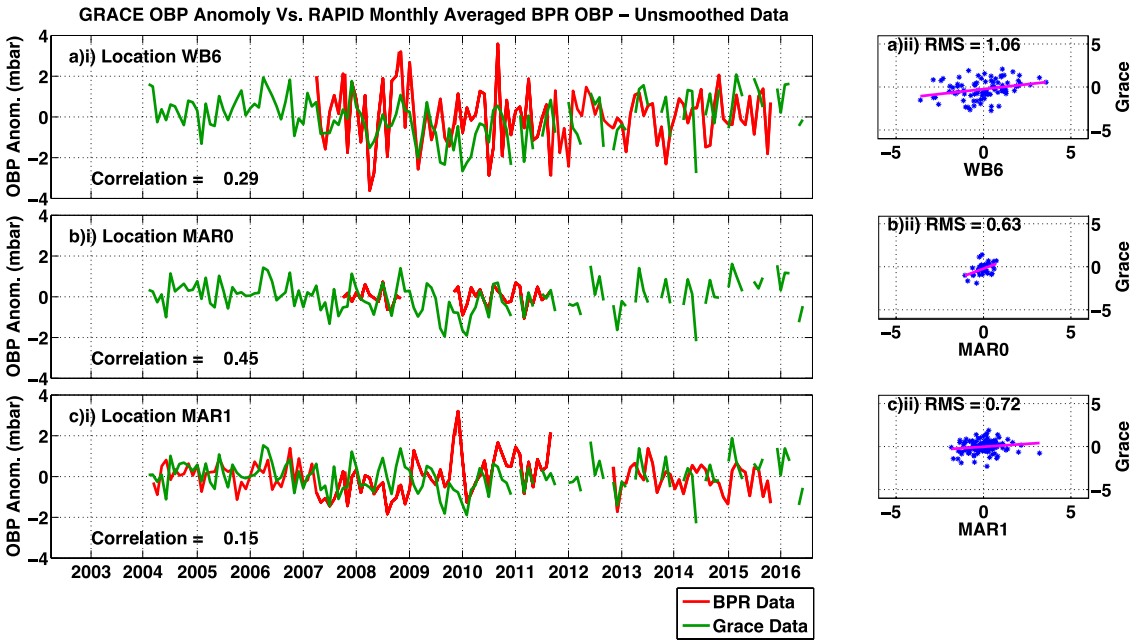

Figure 4.8: Comparison of GRACE OBP anomalies with BPR OBP anomalies (mbar) at three mooring locations: a)i) WB6; b)i) MAR0; c)i) MAR1. GRACE data has been Gaussian filtered, converted from liquid equivalent height to OBP, de-seasonalised and linearly de-trended. BPR data have been processed to remove the exponential-linear drift for each instrument before the weighted averaging of overlapping instrument data. BPR data was then monthly-averaged, anomalised, de-seasonalised and linearly de-trended. Scatter plots of the RMS differences between BPR OBP anomalies and GRACE OBP anomalies can be seen in the adjacent plots: a)ii WB6, b)ii) MAR0 and c)ii) MAR1.

4.3.2 Boundary layer GRACE ocean bottom pressure anomalies

East-west GRACE OBP boundary differences for LNADW layer anomalies (Figure 4.9) are similar to that calculated by Landerer et al., (2015) (confirmed later in Figure 4.11), despite differences in the methodology. Averaging the boundary wall OBP anomalies for an entire depth layer shows that the western boundary dominates the east. To pick LNADW OBP anomalies, firstly all values that overlap the 3000 m boundary are ignored (Figure 4.3), as the basin topography is steep and these mascon values cover more of the UNADW depth range than the LNADW depth range. Then all values on the west, MARwest, MAReast and east walls of the basin are averaged for each monthly bin if they fall within 3000 – 5000 m. To pick AABW OBP anomalies, the division between the west and MARwest walls is chosen as the deepest point on the west side of the MAR at 61˚W. Similarly, the division between the MAReast and east walls is at 32˚W. AABW OBP anomalies are averaged, below 5000 m, for each of the four basin walls and each monthly bin.

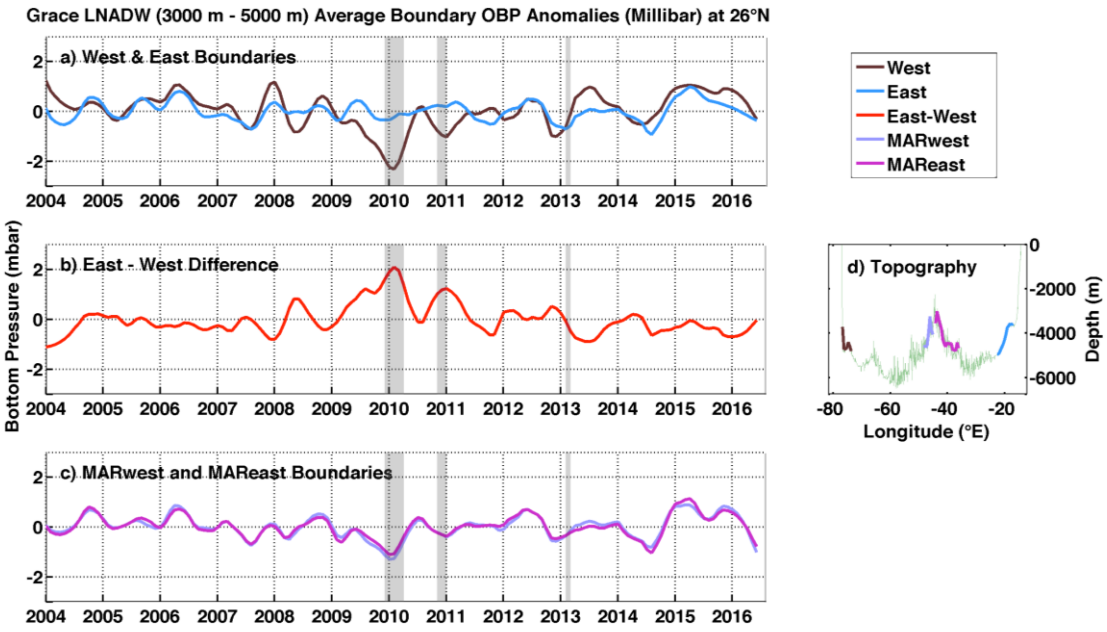

Figure 4.9: LNADW layer average OBP (mbar): a) the west boundary and the east boundary; b) the east-west difference; c) MARwest and MAReast boundaries; d) the topography for each boundary wall. Shaded regions denote periods of weak overturning caused by weakened northward Ekman transports, weakened northward Florida Straits and weakened southward LNADW transports.

LNADW western boundary OBP anomalies have standard deviation ±0.7 mbar with range -2.3 mbar to 1.2 mbar. The LNADW eastern boundary OBP anomalies have

standard deviation ±0.4 mbar with range -0.9 mbar to 1.0 mbar. The contribution of data either side of the MAR largely cancels. The 2013 downturn (all downturn events are highlighted with grey shading) is not evident in western boundary LNADW data with an expected decrease in OBP. This is due to missing months in the GRACE timeline (March 2013 is missing). Figure 4.9e projects the longitudes of the GRACE mascons, from which the averages are drawn, onto the topography. On the western boundary, in particular, the number of mascons is small owing to steep topography and poor spatial resolution of GRACE data. Selecting further mascons would be to utilise those that overlap adjacent depth layers.

The AABW east-west OBP differences over the time-series are much weaker than that of LNADW (Figure 4.10). AABW is contained in the western half of the basin, so the eastern side is omitted. Using hydrographic data, Frajka-Williams et al. (2011) show that northward MOC flow below 4000 dbar and to the east of 46˚W is 0.0 ±0.3 Sv, with a 4100 dbar reference level.

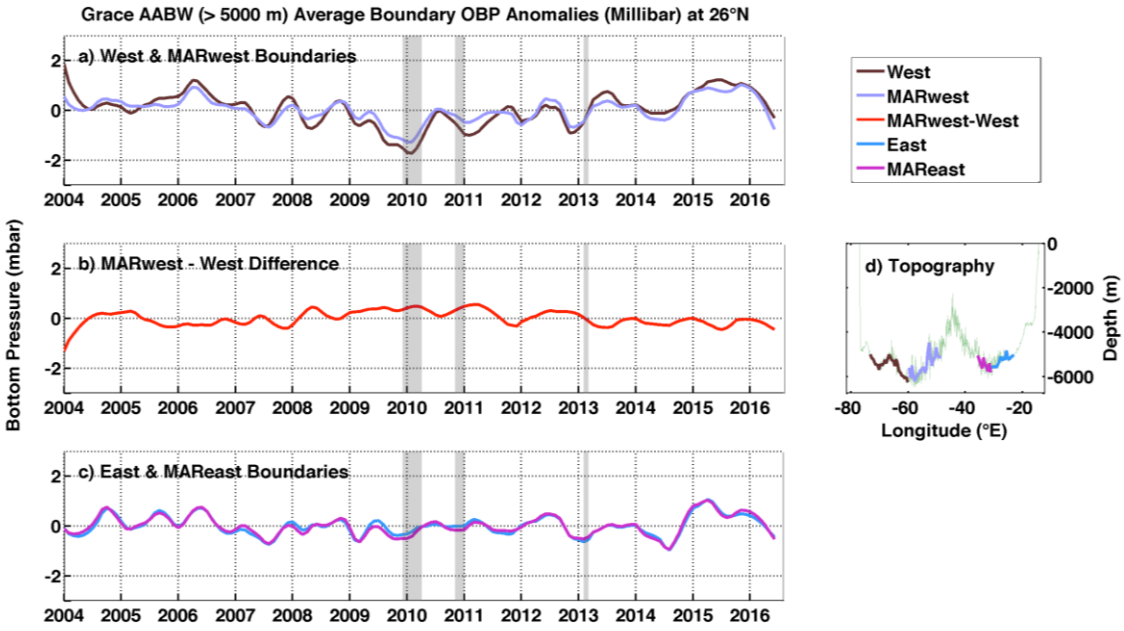

Figure 4.10: AABW layer average OBP (mbar): a) the west boundary and the MARwest boundary; b) the MARwest-west difference; c) east and MAReast boundaries; d) the topography for each boundary wall. Shaded regions denote periods of weak overturning caused by weakened northward Ekman transports, weakened northward Florida Straits and weakened southward LNADW transports.

AABW western boundary OBP anomalies (Figure 4.10) have standard deviation ±0.7 mbar with range -1.7 mbar to 1.9 mbar. The AABW MARwest boundary OBP

anomalies have standard deviation ±0.5 mbar with range -1.3 mbar to 1.0 mbar (both have means of approximately zero mbar). The west to MARwest difference largely cancels and the result is shallow in terms of variance. The west to MARwest anomaly difference has standard deviation ±0.3 mbar with range -1.3 to 0.5 mbar.

4.3.3 GRACE layer anomaly transports

Computing anomaly transports for each depth layer produces results that highlight extreme events (Figure 4.11). The spatial and temporal resolutions of GRACE anomaly transports are smooth relative to RAPID 12-hourly transports. Thus, to reconcile the difference, RAPID transports are processed to match GRACE anomalies and allow equitable analysis (Figures 4.10a and 4.10c). This processing of RAPID transports involves conversion into anomalies with respect to their 2004-2009 mean, averaging into monthly values, de-seasonalising, linearly de-trending and 10-month Lowess low-pass smoothing. Figure 4.11a displays GRACE LNADW anomaly transports and RAPID LNADW anomaly transports, the correlation is above 0.7 (95% confidence) and RMS difference is just 1.1 Sv. The largest differences are found at the beginning and end of the timeline, where there are more intermittent months of missing data. GRACE LNADW anomaly transports have a range of -3.3 Sv to 5.7 Sv. Landerer et al. (2015) show that GRACE-derived transports correlated with RAPID LNADW variation, which itself is a good indicator of upper ocean changes. Results here are consistent with that of Landerer et al. (2015) (correlation 0.9, 95% confidence, Figure 4.11b) despite a methodology that differs, such as inclusion of MAR OBP data.

The comparison of GRACE AABW anomaly transports with RAPID deep mooring transports is much less favourable (Figure 4.11c). The time-series of RAPID AABW estimates from deep moorings is too short in duration to draw any conclusions with regard to agreement with the GRACE AABW estimate. GRACE AABW anomaly transports have a range of -1.8 Sv to 0.9 Sv. This would fit within the 1 Sv to 5 Sv range, predicted by Frajka-Williams et al. (2011), if the mean lay between 2.8 Sv and 4.1 Sv.

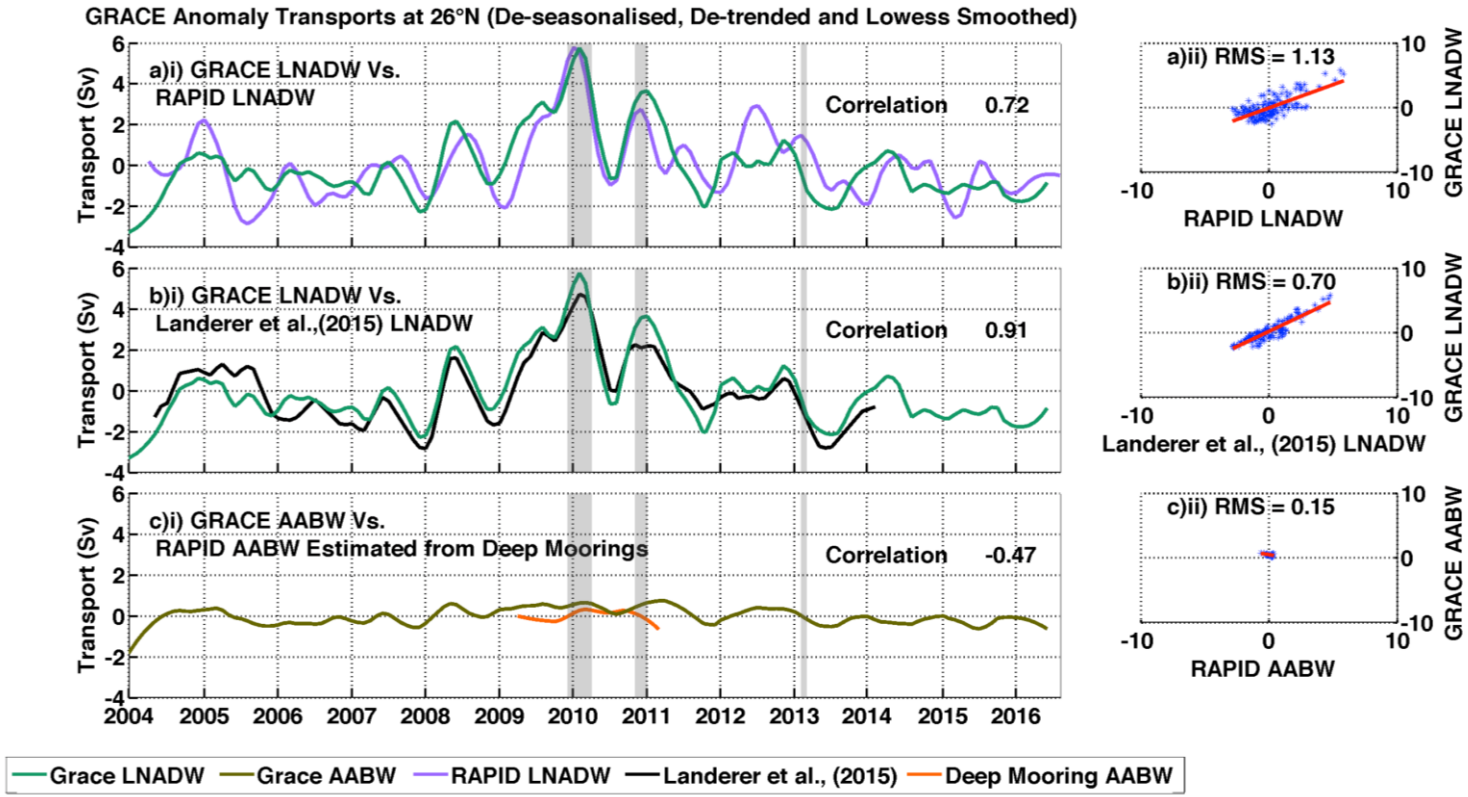

Figure 4.11: GRACE layer anomaly transports (Sv) for LNADW and AABW: a)i) GRACE LNADW and RAPID LNADW; b)i) GRACE LNADW and GRACE LNADW computed by Landerer et al., (2015); c)i) GRACE AABW and RAPID deep mooring AABW estimates by McCarthy et. al., (2015). The scatter plots detail the RMS error difference for each adjacent plot. Shaded regions denote periods of weak overturning caused by weakened northward Ekman transports, weakened northward Florida Straits and weakened southward LNADW transports.

Periods of weak overturning caused by weakened northward Ekman transports, weakened northward Florida Straits and weakened southward LNADW transports are referred to as downturn events. Downturn events (Figure 4.11, grey shading) in 2009-10 and 2010-11 are characterised by weak southward GRACE LNADW anomaly transports relative to the mean (Table 4.1). The 2009-10 and 2010-11 downturns are also characterised by strong northward GRACE AABW anomaly transports relative to the mean. The downturn event in 2013 does not show the same LNADW weakening and AABW strengthening. This is because GRACE data for the 2013 downturn are missing and thus transports have been interpolated over the gap.

			Downturn Event Means		
	Mean 2004-2016	SD 2004-2016	Dec 2009 - Apr 2010	Nov 2010 - Jan 2011	Feb 2013 - Mar 2013
GRACE LNADW	0.0	*1.6*	4.8	3.4	-0.8
GRACE AABW	0.0	*0.4*	0.6	0.5	-0.1
	GRACE Anomaly Transports (Sv)				

Table 4.1: Mean downturn GRACE anomaly transports. Mean transports from 2004 to 2016 are given with the standard deviations in italics. All data are spatially Gaussian filtered, de-seasonalised, de-trended and temporally Lowess low-pass filtered. GRACE data covering the 2013 downturn are not available and so anomaly transports are interpolated from surrounding data.

	Mean 2004-2016	SD 2004-2016	Annual Means												4-Year Means		
			2004	2005	2006	2007	2008	2009	2010	2011	2012	2013	2014	2015	2004-2008	2008-2012	2012-2016
GRACE LNADW	0.0	*1.6*	-0.4	-0.5	-0.8	-1.0	0.6	3.4	1.9	-0.3	0.2	-1.0	-0.7	-1.3	-0.7	*0.8*	1.4	*1.9*	-0.7	*0.9*
GRACE AABW	0.0	*0.4*	0.1	-0.3	-0.3	-0.2	0.3	0.5	0.4	0.1	0.2	-0.3	-0.2	-0.3	-0.1	*0.3*	0.3	*0.3*	-0.1	*0.3*
	GRACE Anomaly Transports (Sv)																

Table 4.2: Mean annual GRACE anomaly transports where each year begins in April. Mean transports from 2004 to 2016 are given with the standard deviations in italics. Averages for each four-year interval (from April 2004, April 2008 and April 2012) are given in the last three columns. All data are spatially Gaussian filtered, de-seasonalised, de-trended and temporally Lowess low-pass filtered.

Average annual GRACE LNADW and GRACE AABW anomaly transports are given in Table 4.2 (where each year begins in April). Increases in GRACE AABW northward anomaly transports coincide with reductions in GRACE LNADW southward anomaly transports, adding to the southward weakening seen in the second four-year interval of the array (2008-2012) relative to the first four years (2004-2008) and the last four years (2012-2016).

4.3.4 GRACE layer estimated transports

GRACE layer estimated transports may be inferred from GRACE anomaly transports by assuming a mean so that they may be included in the RAPID AMOC calculation (Section 4.3.5). Figure 4.12 displays the quantified deep external estimated transports using data from satellite gravity. GRACE estimated transports have not been de-seasonalised, linearly de-trended or Lowess filtered (because they will be compared to hydrographic estimates and unfiltered RAPID compensation transports). GRACE data have been Gaussian smoothed, spatially, to remove noise (prior to conversion to OBP). Gaps in the GRACE time-series are linearly interpolated and then converted to estimated layer transports. Estimated transports are calculated by assuming layer means that are based on RAPID layer transports (-9 Sv for LNADW and 1 Sv for AABW). Figure 4.12 displays the data both before and after de-trending relative to RAPID compensation transports applied to the basin below 3000 m (plots a and b, respectively). RAPID compensation transports were chosen because they have been found to emulate OBP-driven transports when calculated with a reference level of 4820 dbar (Kanzow et al., 2007). It should be noted that de-trending relative to RAPID LNADW internal transports produces almost identical results. Figure 4.12a shows the extent to which GRACE satellite accelerometers suffer from errors like drift and bias.

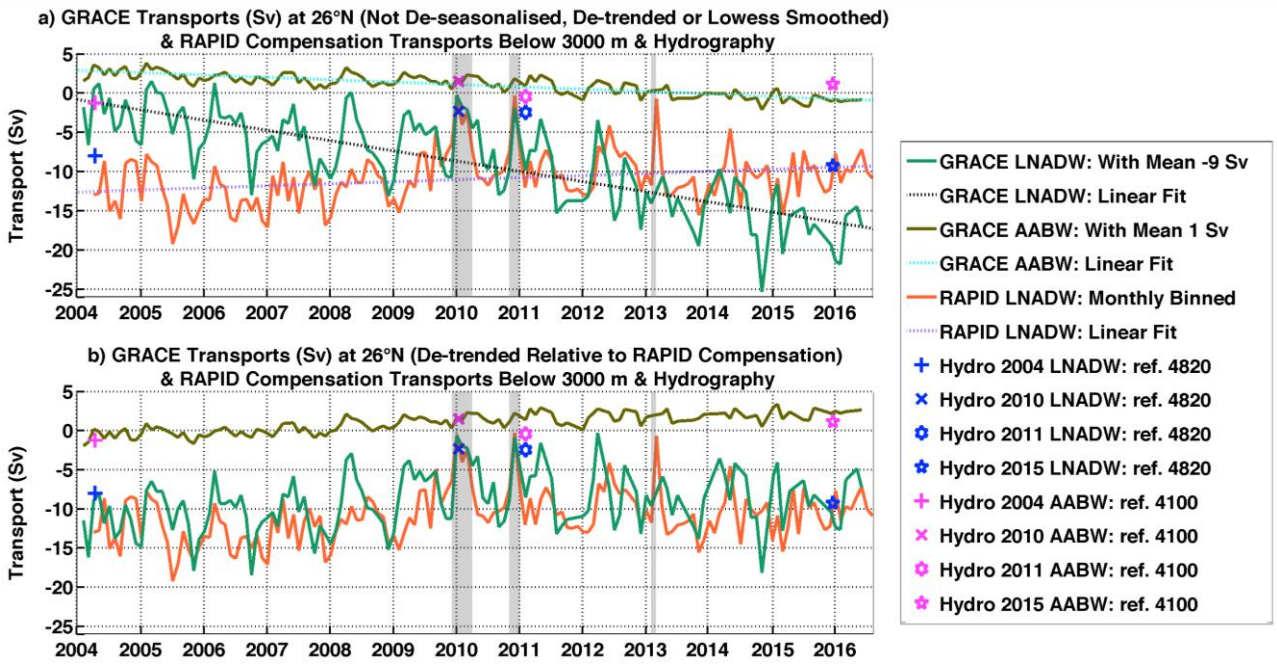

Figure 4.12: GRACE estimated layer transports (Sv) compared to hydrographic data and RAPID compensation transports: a) GRACE LNADW and AABW prior to de-trending; b) GRACE LNADW and AABW after de-trending relative to RAPID compensation transports. GRACE data have been Gaussian filtered before conversion to OBP and then transports. GRACE LNADW is calculated relative to a mean transport of -9 Sv. AABW is calculated relative to a mean transport of 1 Sv, where mean values are based on RAPID AMOC layer transports. Hydrographic transports are calculated with a reference level of 4100 dbar (pink) for the AABW layer and a reference level of 4820 dbar (blue) for the LNADW layer. RAPID compensation transports have been summed for the region below 3000 m (with a reference level of 4820 dbar). Shaded regions denote periods of weak overturning caused by weakened northward Ekman transports, weakened northward Florida Straits transports and weakened southward LNADW transports.

Superimposed on Figure 4.12 are transports estimated from four hydrographic sections calculated with two different reference levels: 4820 dbar and 4100 dbar (Figure 4.12). A hydrographic reference level of 4820 dbar was chosen for the LNADW layer because it is also the reference level traditionally employed for RAPID transports (McCarthy et al., 2015a). A hydrographic section reference level of 4100 dbar was chosen for the AABW layer because it coincides with the approximate depth of the 1.9°C potential temperature divide that often separates AABW from LNADW (see Figure 2.3). A reference level of 4100 dbar is also found to optimise deep AABW transports in the western side of the basin, as opposed to the eastern side, by Frajka-Williams et al. (2011). The results of Figure 4.12 are summarised in Table 4.3 (ref 4820 dbar) and Table 4.4 (ref 4100 dbar) for the hydrography, as well as Table 4.5 for GRACE transports (de-trended according to RAPID compensation transports) timed to match the hydrographic sections. Estimating GRACE transports with an assumed mean (Figure 4.12b) ensures that they match hydrographic transports in the LNADW layer and AABW layer with an average difference of 1.9 Sv and -1.1 Sv, respectively. Hydrographic AABW northward transports do not fit within the 1 Sv to 5 Sv range predicted by Frajka-Williams et al. (2011) because estimates here include flow west of 72°W, which incorporate DWBC southward flow. It is also due to the spatial resolution of the 2004 hydrographic section, which does not extend down to sufficient depth. Thus, temperature and salinity values in the un-sampled regions are assumed to equal the nearest value. Linear extrapolation makes little difference.

Data	Hydrography			
Method	1. Bottom triangles ignored 2. Uniform area 3. Reference level 4820 dbar 4. WBW absolute transport			
Year	2004	2010	2011	2015
Compensation Velocity (m/s)	-0.0009	-0.0003	-0.0002	-0.0009
Ekman	4.5	-1.1	3.9	3.8
Florida Straits	31.3	30.3	32.2	31.4
LNADW 3000 m < z ≤ 5000 m	-8.0	-2.4	-2.5	-9.3
	Transports (Sv)			

Table 4.3: LNADW hydrographic transports calculated with reference level 4820 dbar. Transports employ cruise mean Ekman transports and cruise mean Florida Straits transports and cruise mean WBW absolute transports. A uniform area is enforced for each section.

Data	Hydrography			
Method	1. Bottom triangles ignored 2. Uniform area 3. Reference level 4100 dbar 4. WBW absolute transport			
Year	2004	2010	2011	2015
Compensation Velocity (m/s)	-0.0007	-0.0003	-0.0005	-0.0010
Ekman	4.5	-1.1	3.9	3.8
Florida Straits	31.3	30.3	32.2	31.4
AABW >5000m	-1.3	1.5	-0.5	1.1
	Transports (Sv)			

Table 4.4: AABW hydrographic transports calculated with reference level 4100 dbar. Transports employ cruise mean Ekman transports, cruise mean Florida Straits transports and cruise mean WBW absolute transports. A uniform area is enforced for each section.

Data	GRACE			
Method	1. GRACE LNADW given mean -9 Sv & GRACE AABW given mean 1 Sv 2. De-trended relative to RAPID LNADW			
Year	2004	2010	2011	2015
LNADW 3000 m < z ≤ 5000 m	-8.7	-1.2	-8.5	-11.2
AABW >5000m	0.1	1.5	1.4	2.3
	Transports (Sv)			

Table 4.5: GRACE estimated transports for the LNADW and UNADW depth layers to match the timings of four hydrographic sections (GRACE data are averaged for each cruise duration). GRACE data have been spatially Gaussian filtered and de-trended relative to RAPID compensation transports (ref 4820 dbar). LNADW transports are calculated relative to -9 Sv mean transport. AABW transports are calculated relative to 1 Sv mean transport.

GRACE estimated transports pertaining to Figure 4.12b are summarised in Table 4.6 for the downturns and Table 4.7 for annual results. All GRACE data have been Gaussian filtered (prior to conversion into OBP), linearly interpolated, converted from OBP to estimated transports, converted from anomalies relative to RAPID mean mid-ocean layer transports and de-trended relative to RAPID compensation transports below 3000 m.

	Mean	SD	Downturn Event Means		
	2004-2016		Dec 2009 - Apr 2010	Nov 2010 - Jan 2011	Feb 2013 - Mar 2013
GRACE LNADW	-9.0 ± *3.6*		-4.1	-4.8	-8.8
GRACE AABW	1.0 ± *1.1*		1.5	1.7	1.9
	GRACE Layer Transports (Sv)				

Table 4.6: Mean downturn GRACE estimated transports. Mean transports from 2004 to 2016 are given with the standard deviations in italics. GRACE data have been spatially Gaussian smoothed and de-trended relative to RAPID compensation transports (ref 4820 dbar). GRACE LNADW transports are calculated relative to -9 Sv mean transport. GRACE AABW transports are calculated relative to 1 Sv mean transport. GRACE data covering the 2013 downturn are not available and so transports are interpolated using the surrounding data.

With regard to Table 4.6, the downturn event in 2013 can be ignored because GRACE data for the 2013 downturn are missing and thus transports have been interpolated over the gap. Both the 2009-10 and 2010-11 downturns feature GRACE LNADW estimated transports that are 4.6 Sv weaker than the mean, which is more than 1 standard deviation. This suggests that the nature of LNADW weakening during downturn events is barotropically driven (but this doesn't exclude a concurrent baroclinic change).

Table 4.7 confirms that GRACE LNADW and GRACE AABW estimated transports are 1.4 Sv weaker and 0.3 Sv stronger, respectively, in the 2008-2012 interval relative to the time-series mean but within one standard deviation. GRACE LNADW estimated transports are only 0.5 Sv weaker in the 2012-2016 interval relative to the time-series mean, which may be indicative of a strengthening of the AMOC relative to the weakening observed in 2008-2012.

Whilst it is difficult to infer conclusions from GRACE data given the uncertainty surrounding the method of de-trending (ideally, the data would be de-trended relative to a concurrent OBP dataset), as well as the circular methodology that uses RAPID means and then incorporates the data into the RAPID calculation, the task was performed to determine the difference when time-varying AABW transports are incorporated into the RAPID time-series (see Section 4.3.5). Ideally, the data would be de-trended relative to a concurrent OBP dataset, such as that

from BPRs, then converted from anomalies into estimated transports using a mean derived from a separate source of data, such as deep moorings. However, due to drift problems associated with BPR data (Polster et al., 2009) and the short timescale within which deep moorings captured AABW, their inclusion in this analysis was limited.

	Mean	SD	Annual Means												4-Year Means		
	2004-2016		2004	2005	2006	2007	2008	2009	2010	2011	2012	2013	2014	2015	2004-2008	2008-2012	2012-2016
GRACE LNADW	-9.0 ± *3.6*		-10.8	-10.8	-11.1	-11.0	-8.7	-5.8	-7.1	-8.7	-7.7	-8.6	-8.8	-8.9	-10.9 ± *2.9*	-7.6 ± *3.7*	-8.5 ± *3.3*
GRACE AABW	1.0 ± *1.1*		-0.3	-0.5	-0.3	0.1	0.9	1.3	1.6	1.4	2.0	1.7	2.0	2.2	-0.3 ± *0.6*	1.3 ± *0.8*	2.0 ± *0.6*
GRACE Layer Transports (Sv)																	

Table 4.7: Mean annual GRACE estimated transports where each year begins in April. Mean transports from 2004 to 2016 are given with the standard deviations in italics. Averages for each four-year interval (starting from April 2004, April 2008 and April 2012) are given in the last three columns. GRACE data have been spatially Gaussian filtered and de-trended relative to RAPID compensation transports (ref 4820 dbar). GRACE LNADW transports are converted from anomalies relative to -9 Sv mean transport. GRACE AABW transports are converted from anomalies relative to 1 Sv mean transport.

4.3.5 GRACE layer estimated transports incorporated with RAPID transports

It is of interest to measure variance of GRACE layer transports so that they can be evaluated with regard to the wider AMOC. GRACE AABW transports with net mean northward flow of 1 Sv are added to the internal transports to reveal an almost identical picture (Figure 4.13). Normal RAPID transports are plotted on the left, for comparison, and RAPID transports including GRACE AABW transports are on the right. The results lend support to the methods used to calculate RAPID transports. Figure 4.14 plots the differences, showing that this variance lies within ±1.1 Sv for all depth layers. The degree to which each layer is affected by the inclusion of GRACE AABW estimated transports is relative to the area the layer occupies within the basin, thus the LNADW layer is altered most (Figure 4.14d). Small variations of the deep transports project little onto the upper layer transports due to their magnitude.

Going a step further, both GRACE AABW (relative to 1 Sv mean) and GRACE LNADW (relative to -9 Sv mean) are added to RAPID transports plotted in Figure

4.15b (RAPID transports are plotted on the left, for comparison, and RAPID transports with GRACE AABW and GRACE LNADW are on the right). Further to this, the compensation component is applied above the LNADW depth level (Figure 4.15b, on the right). The choice was made to apply compensation transports above 3000 m depth because the inclusion of GRACE estimated LNADW and AABW transports is a means of incorporating the barotropic component, thus the compensation transports (which are a proxy for the barotropic transports) are deemed unnecessary below 3000 m. The outcome is greater variance in the UNADW layer. But the total MOC is altered by just 0.2 Sv. For the UNADW layer the mean changes from -10.2 ±2.7 Sv to -10.6 ±3.6 Sv. The UMO mean changes from -17.7 ±3.3 Sv to -17.9 ±3.6 Sv. These alterations are small relative to the total MOC. Despite the method of de-trending GRACE data relative to RAPID compensation transports, the method should hopefully capture the scale of variability of the MOC associated with incorporating external transports into the RAPID calculation of transports. The difference between the two sets of transports in Figure 4.15 can be found in Figure 4.16.

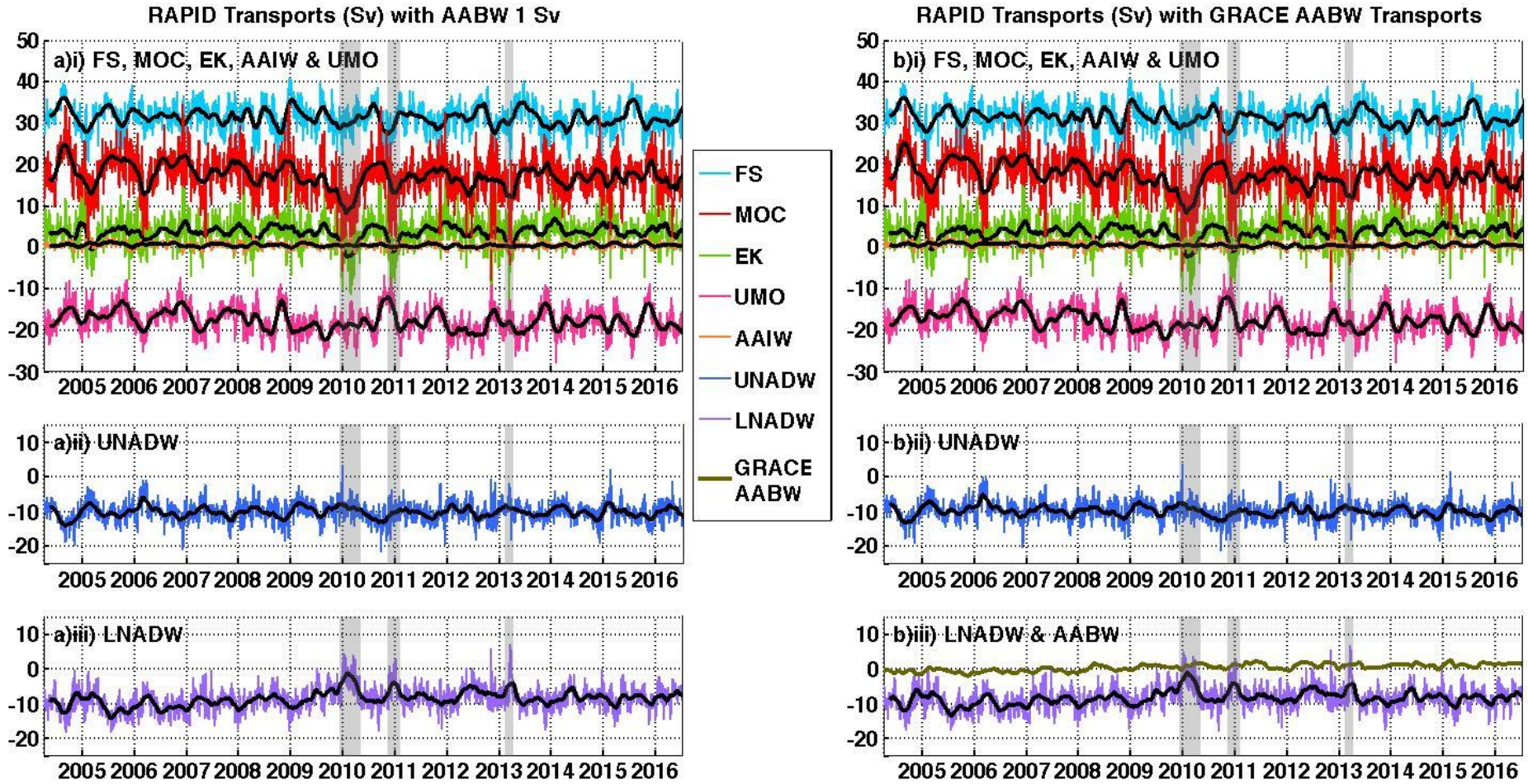

Figure 4.13: RAPID layer transports (Sv): a) with AABW equal to 1 Sv northward flow; b) with GRACE AABW estimated transports (time-series mean 1 Sv).

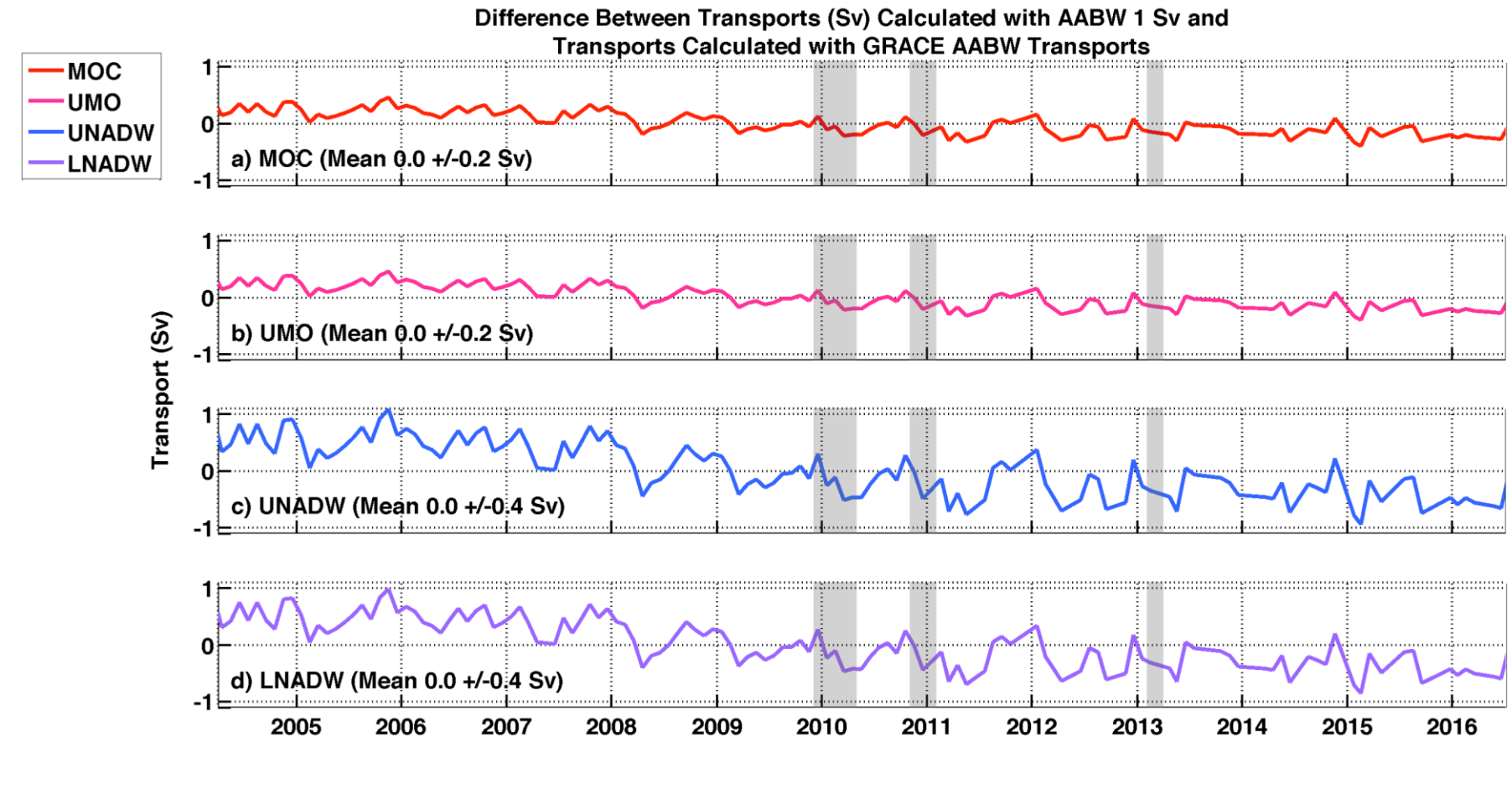

Figure 4.14: Differences between RAPID layer transports (AABW equal to 1 Sv northward flow) and RAPID layer transports with GRACE estimated AABW (time-series mean 1 Sv).

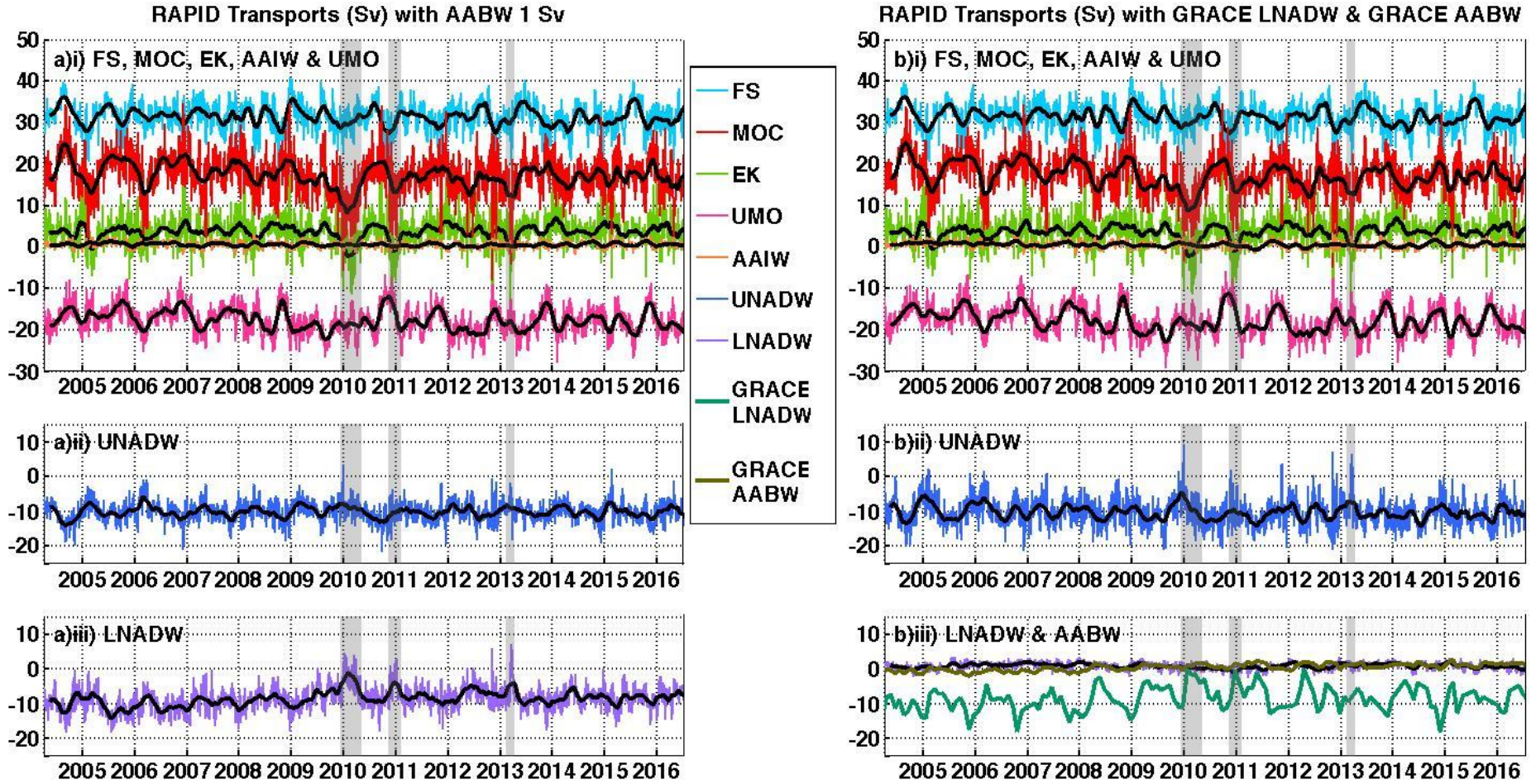

Figure 4.15: RAPID layer transports: a) with AABW equal to 1 Sv northward flow; b) with GRACE AABW estimated transports (time-series mean 1 Sv), GRACE LNADW estimated transports (time-series mean -9 Sv) and the compensation applied above the LNADW layer.

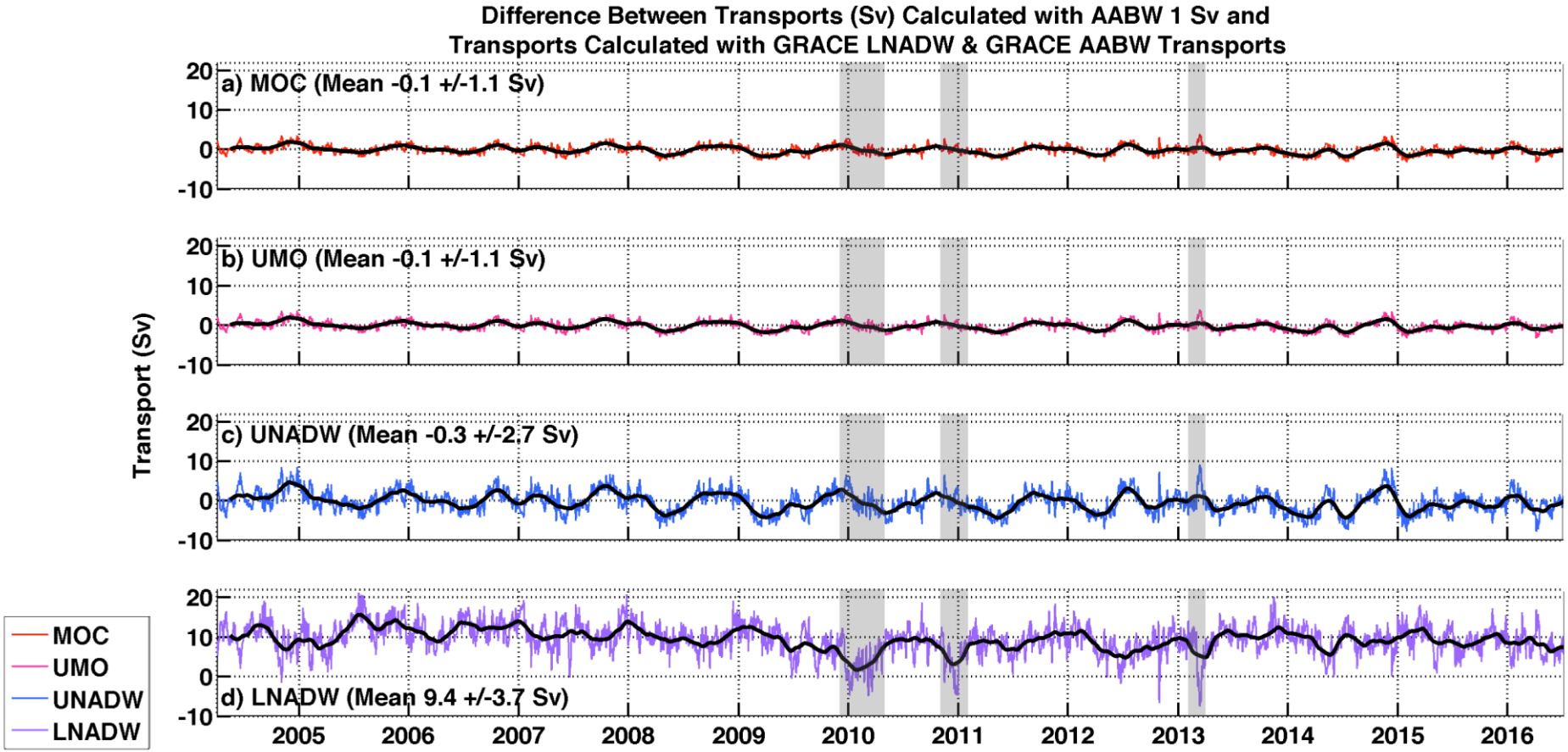

Figure 4.16: Differences between RAPID layer transports (AABW equal to 1 Sv northward flow) and RAPID layer transports with GRACE estimated AABW (time-series mean 1 Sv), GRACE LNADW estimated transports (time-series mean -9 Sv) as well as the compensation applied above the LNADW layer.

4.3.6 Basin-wide GRACE ocean bottom pressure anomalies

A comparison of Ekman transports and RAPID LNADW transports with basin-wide GRACE OBP anomalies is shown in Figure 4.17. There appears to be a prominent AMOC weakening, related to the 2009-10 downturn. The east-west OBP difference during the 2009-10 downturn reaches a peak of 2 mbar. The 2011 downturn displays the second largest east-west OBP difference at just over 1 mbar. The 2013 downturn cannot be accurately evaluated, as the particular month of relevance is missing from GRACE data. Other periods of low western basin OBP anomalies rarely result in a weak overturning, because the eastern side of the basin also exhibits low OBP anomalies and thus the east-west difference is not substantial. The only noteworthy incident of large east-west anomaly difference occurs in spring 2008, which is just under 1 mbar. This is indicative of a weak southward internal component determined by the east-west shear. The spring 2008 OBP pattern could be part of a propagating event. This incident is not associated with a downturn event because it is not accompanied by a sufficient weakening of northward Ekman transports. Thus, the calculation of RAPID AMOC transports will bolster the reduced internal flow by means of the compensation that balances the internal flow with northward Ekman transports and northward Florida Straits transports.

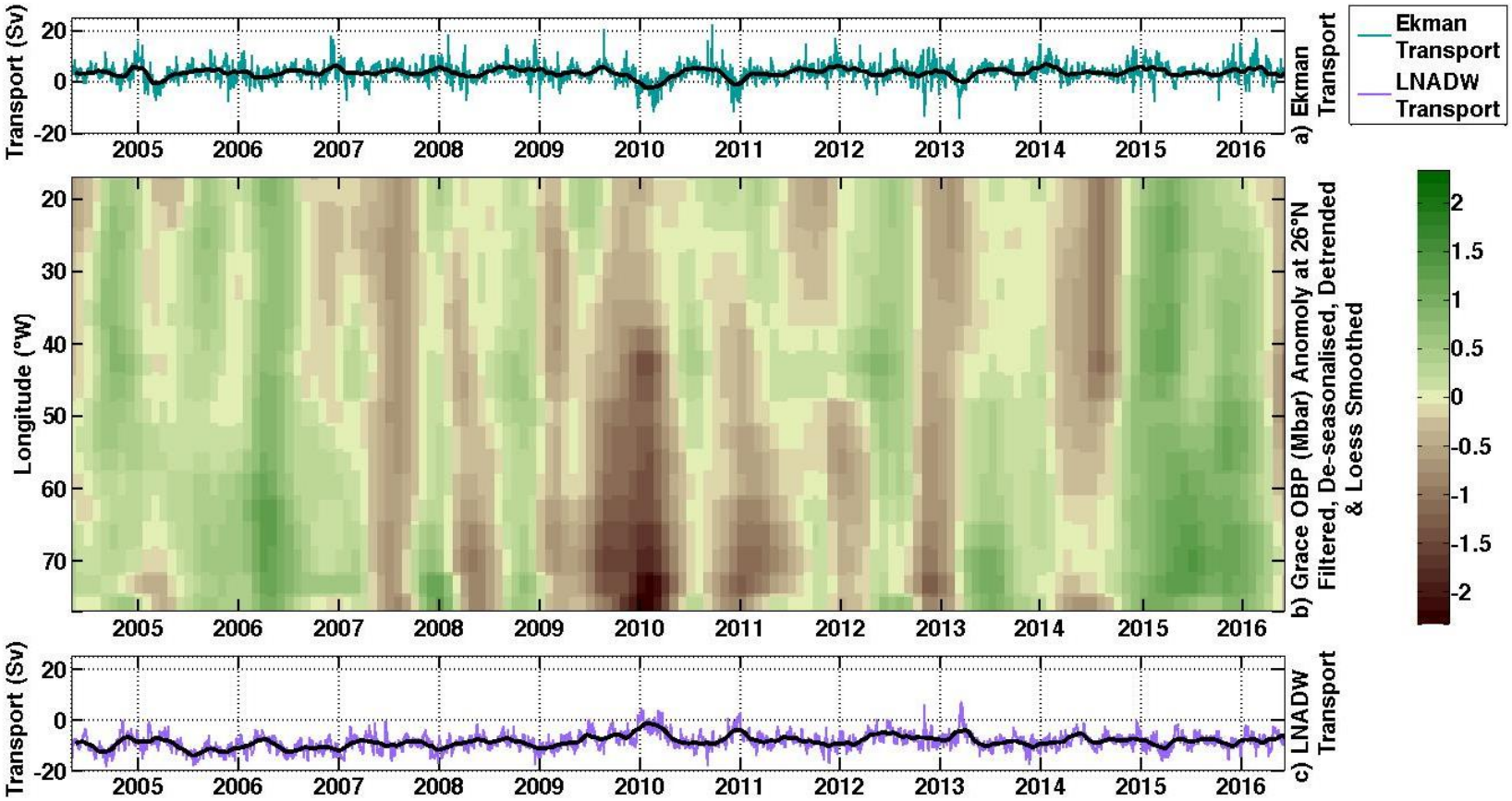

Figure 4.17: Comparison of GRACE OBP anomalies (mbar) with transports (Sv) at 26°N: a) Ekman transports; b) Top-down view of GRACE-derived OBP anomalies from east (top) to west (bottom); c) RAPID LNADW transports. GRACE data has been Gaussian filtered, converted to OBP, de-seasonalised, de-trended and Lowess smoothed. The colour scale denotes the change in OBP (mbar).

4.4 Errors and uncertainties

There are several problems related to inferring ocean mass external transports from GRACE observational data. One such issue is that of signal leakage from land hydrology, whereby mascons near coastlines reflect a merged combination of both the ocean signal and the land signal with no clear separation. Transports estimated using the outermost edges of the basin, affecting the upper water-masses, will be distorted. These leakage signals are of order 50 times greater than ocean mass variations. Transports for the deeper water-masses (AABW and LNADW) are considered to be least affected by signal leakage. The most recent GRACE dataset (Release-05) has reduced the standard leakage error to ~1 cm of equivalent water thickness at ocean mid-latitudes (Chambers and Bonin, 2012; Wiese et al., 2016).

There are vertical stripes in gridded GRACE data that are a manifestation of correlated errors (Swenson and Wahr, 2006). These north-south errors are largely corrected with post-processing smoothing with a 500 km Gaussian filter. There is also a degree of random error that increases at short wavelengths (Wahr et al., 1998). To correct these problems, a set of gain factors was created to restore signals lost by filtering (Landerer and Swenson, 2012). But these gain factors create bias in long-term trends (annual or greater).

Due to battery management, there are several months of missing data and months where the monthly average is estimated from only a few days of data within that month. In these instances, the missing months (or months composed of less than half a month of data) are interpolated over. There is missing data, from 2004 onwards, for January 2011, June 2011, December 2011, May 2012, October 2012, March 2013, August 2013, September 2013, February 2014, July 2014, December 2014, May 2015, June 2015, October 2015, November 2015 and April 2016. Unfortunately, the missing months include March 2013, when there are abnormal northward RAPID LNADW transports.

GRACE can only resolve OBP fluctuations relative to an arbitrary time mean. Anomaly transports allow only the variation to be assessed, inferring long-term trends is not possible. A concurrent dataset is needed to alter GRACE data, relative to a long-term mean and trend, to gain estimated absolute transports.

The use of GRACE OBP is based on the assumption that monthly gravity changes over the ocean are the result of mass distribution above the ocean floor. GRACE

data are temporally sparse relative to RAPID 12-hourly data, which conveys great short-term variance.

GRACE cannot resolve layer transports above LNADW due to the steep boundary walls and relatively poor data resolution and potential leakage of the land signal. Mascons that span multiple water-mass depth layers were omitted in favour of mascons for which their full 300 km span resides within either the LNADW or AABW boundary wall depth layer. This was a particular problem at the western boundary, where the topography is steep. The west side of the basin is crucially where, near the steep topography and confined to a narrow area, much of the signal occurs (Elipot et al., 2014; Smeed et al., 2014). Estimation of UNADW transports is unfeasible due to the resolution of the data in relation to the steep western boundary wall. However, Bentel et al. (2015) find that, despite the spatial resolution issues along steep topography, the associated errors in transports are within ±1 Sv.

Landerer et al. (2015), during their calculation of GRACE LNADW anomaly transports, make long period improvements to account for the pole tide and restore the monthly de-aliasing fields. These steps were not performed during the analysis here, which may impact trend analysis. With this additional processing, Landerer et al. (2015) estimate a monthly uncertainty equating to 0.5 mbar.

4.5 Discussion and conclusions

OBP observations can be used to quantify external transports at ~26°N by looking at east-west pressure differences. By integrating transports between specific AMOC basin depth ranges, it is possible to measure deep water-mass external flow variation. This implies the potential use of these external transports in addition to the internal transports gained by systems such as the RAPID array to build a bigger picture of the overturning circulation.

Landerer et al. (2015) approximated LNADW transports using OBP averaged for the LNADW depth level (3000 m to 5000 m). GRACE transports, here, also ratify the methods employed to compute RAPID transports. GRACE LNADW anomalies and RAPID LNADW anomalies match well, with correlation above 0.7, 95% confidence and RMS difference of just 1.1 Sv. This increases confidence that GRACE data, at greater spatial resolution, would have capacity in recovering layer transports above 3000 m. GRACE AABW transports (below 5000 m) are also approximated to build an estimate of an additional MOC component.

With regard to GRACE transports, the major points are as follows:

- GRACE anomaly transports were computed with GRACE data by Gaussian smoothing (50 km half width) to remove noise before conversion to OBP, de-seasonalising, linearly de-trending, Lowess low-pass filtering to highlight interannual variation and converting OBP to anomaly layer transports;
- GRACE estimated transports were computed with GRACE data by Gaussian smoothing (prior to conversion into OBP), linearly interpolating to fill gaps, converting OBP to layer transports, altering layer means relative to RAPID layer mean transports and de-trending relative to RAPID compensation transports;
- The results of the GRACE anomaly transports and GRACE estimated transports (comparing Table 4.1 to Table 4.6 and comparing Table 4.2 to Table 4.7) are alike in their overriding signal (such as weakened southward LNADW flow by more than 1 standard deviation of the time-series mean during downturns), despite the different processing techniques;
- Downturn events (ignoring the 2013 downturn) convey southward GRACE LNADW weakening of ~3 Sv and northward GRACE AABW strengthening of ~0.5 Sv;
- The first 4 years of the time-series from 2004 convey stronger southward GRACE LNADW than the subsequent 4 years by ~2 Sv, as well as weaker northward GRACE AABW than the subsequent 4 years by ~0.4 Sv;
- There is uncertainty regarding de-trending, which is needed because GRACE data suffers from an error trend caused by glacial isostatic adjustment and land leakage (A et al., 2013; Bentel et al., 2015).

External transports relate to other transports, such as Ekman transports (Frajka-Williams et al., 2016) and the deep internal flow (Landerer et al., 2015). Several studies show that AMOC high-frequency variance is due to wind variability that results in anomalous Ekman transports (Jayne and Marotzke, 2001; McCarthy et al., 2012) or wind stress curl forcing (e.g. Kanzow et al., 2010; Duchez et al., 2014). Frajka-Williams et al. (2016) conclude that the mechanism underlying deep southward transports (LNADW) is wind stress projected onto deep density changes at the western boundary. Yeager (2015) demonstrates, with a numerical model, that sloping topography and wind stress anomalies give rise to wave interactions that project onto the external transports. Roussenov et al. (2008) conclude that boundary waves alter the overturning by affecting OBP. A change in

the wind stress could additionally result in increased eddy energy. Heat and freshwater fluxes also cause density changes that may reinforce or compensate wind changes through heave of isopycnals (Häkkinen et al., 2016).

The North Atlantic plays an important role in the characteristics and variability of the global and regional climate. Changes in the AMOC have far-reaching impacts. External transports are poorly understood relative to internal transports because most ocean data are insensitive to its isolated influence. Separating the external component from mooring data is complex (e.g. Wunsch, 1998). But understanding the dynamics and mechanisms of the internal component is made easier with GRACE data. Chapter 4 shows that external GRACE transports, with estimated long-term trend and long-term mean, can be easily incorporated with RAPID internal transports. Evidence to support incorporation of external transports with that of RAPID internal transports lies with findings that show OBP fluctuations are a result of a combination of processes, such as boundary waves, eddies and density changes arising from wind stress variations. There is also approximate compensation between internal and external transports (Kanzow et al., 2007). Further data is needed to ratify GRACE estimated transports, such as BPR OBP data with longer deployment periods. Additionally, further investigation is required, with the help of additional concurrent datasets, to refine the methodology when incorporating GRACE external transports with RAPID internal transports. Methodological variations include the basin area to which compensation transports should or shouldn't be applied and how to propagate external transports to the layers above 3000 m. Better understanding of the external flow will improve efforts to predict shifts in the overturning and thus climate.

4.5.1 Summary

- Observational systems with adequate spatial and temporal resolution are critical to revealing interannual and decadal AMOC changes. Satellite-derived OBP can be used to determine variability of AMOC external transports (Landerer et al., 2015; Elipot et al., 2014).
- GRACE satellite data are employed to calculate monthly average OBP values from 2003 onwards with a spatial resolution of ~300 km at 26°N. Transports are computed by integrating the gradient of GRACE OBP from east-west basin boundaries for the deep layers.

- GRACE anomaly transports are based on data that is Gaussian filtered to remove noise, linearly de-trended, de-seasonalised and Lowess smoothed to highlight interannual variability before conversion to layer anomaly transports. Results reveal that GRACE LNADW anomalies and RAPID LNADW anomalies match well, with correlation above 0.7 (95% confidence) and RMS difference of just 1.1 Sv.
- GRACE estimated transports are based on data that is Gaussian filtered to remove noise before conversion to estimated layer transports relative to RAPID layer mean transports and de-trended relative to RAPID compensation transports. Results show the ease with which external transports can be combined with RAPID transports to create greater understanding of AMOC flow.
- Despite the differences in the methods employed to calculate GRACE anomaly transports and GRACE estimated transports, common conclusions can be drawn:
    - The 2009-10 and 2010-11 downturns are characterised by southward GRACE LNADW transports that are weaker by ~3 Sv and northward GRACE AABW that are stronger by ~0.5 Sv;
    - The first 4 years (from April 2004) of southward GRACE LNADW transports are stronger than the subsequent 4 years by ~2 Sv and the first 4 years of northward GRACE AABW transports are weaker than the subsequent 4 years by ~0.4 Sv.
- GRACE data suffers from an error trend caused by glacial isostatic adjustment and land leakage (A et al., 2013; Bentel et al., 2015). But there is uncertainty regarding de-trending. An alternative concurrent dataset is needed to ratify GRACE-estimated external transports, such as BPR OBP data with longer deployment periods.
- Evidence to support incorporation of external transports with that of RAPID internal transports lies with findings that show that there is approximate compensation between internal and external transports (e.g. Kanzow et al., 2007).

Chapter 5: Conclusions

The AMOC has emerged as a focal point in the study of climate change due to it carrying heat and other properties poleward (Bryden et al., 2012). Projections of AMOC decline (IPCC, 2013) motivate continued investigation into AMOC driving mechanisms and transports.

The AMOC internal component has been measured at 26°N by infrequent hydrographic sections and, since 2004, continuous measurements by the RAPID mooring array. GRACE satellite-derived and monthly-averaged OBP, from 2003 onwards, can be used to determine AMOC external transports. RAPID transports not only reveal the magnitude of short-term variability but also provide a source of comparison with hydrographic transports and GRACE external transports. This study aimed to better understand the methodological choices employed to calculate transports. This understanding was then utilised to make changes to the methodology and gain further insight into AMOC variation. Concurrent datasets were compared or combined to expand knowledge of the MOC.

During the first 4 years of RAPID observations the overturning circulation was, on average, 2.7 Sv stronger than in the subsequent 4 years (Smeed et al., 2014). RAPID transports also reveal downturn events, occurring in 2009-10, 2010-11 and 2013, that are typified by weak Ekman transports and weak LNADW flow by more than 1 standard deviation of each respective long-term mean (Frajka-Williams et al., 2015). Investigation of datasets measuring the AMOC at 26°N is conducted in this thesis primarily to further understand MOC weakening since 2004, as well as multiple downturn events.

Transports from hydrographic sections show results that contrast with those of RAPID transports, with stronger overturning in 2010 than 2004 (Atkinson et al., 2012). Causes for the apparent discrepancy between the RAPID mooring array and hydrography are explored in Chapter 2. These two estimates of the overturning are based on different data and different calculation methods. The limitations and assumptions of the data and methods are examined. The methods are adjusted to eliminate or mitigate those differences. Fundamental inconsistencies between the datasets are uncovered. The hydrographic profiles aren't always consistent with the scale of flow variation captured by current meter absolute transports at the western boundary. The western boundary is important in measuring the extent of the 2009-10 downturn. When differences in the

calculation methods are addressed, hydrographic layer transports match with RAPID layer transports for the major water-masses (UMO, UNADW and LNADW) within 2 standard deviations of cruise duration means, with the exception of the 2011 hydrographic survey.

High spatial resolution hydrographic data, such as oxygen concentration, can complement inferences regarding long-term MOC changes and methodological choices for the MOC calculation. Hydrographic oxygen concentrations suggest that, during downturn events, DWBC southward flow west of ~70°W is weaker. Calculating hydrographic transports with a 1000 dbar reference level in the DWBC region (with cruise mean Ekman transports and cruise mean Florida Straits transports) reveals weaker internal southward UNADW and LNADW flow during downturns that is partnered with weaker southward compensation. High-resolution hydrographic data (specifically the east-west cumulative transports) reveal that internal transports in the deep layers are near-zero within the main basin with the majority of flow concentrated within the DWBC region. This suggests that the compensation transports should be applied at the western boundary rather than uniformly applied to the whole basin.

RAPID data, explored in Chapter 3, are temporally comprehensive but spatially sparse. The RAPID method of calculation, based around four boundary moorings, reduces lower basin transports by employing a deep basin-wide reference level. This reduction is reversed with a uniformly applied compensation. Chapter 3 takes a novel approach to the current RAPID AMOC calculation methodology by introducing a fifth mooring to the array. The spatial resolution of the RAPID array is supplemented with the addition of data from RAPID mooring WB5 at 72°W. The strong and highly variable DWBC contribution to transports is then included in the calculation by raising the geostrophic reference level to 1000 dbar for the western boundary region up to WB5. Thus, the western boundary shallow reference level strengthens transports, as opposed to the compensation component. For the basin-wide AMOC where a 1000 dbar reference level is employed at the western boundary and a 4820 dbar reference level is employed east of WB5, the objectives were to characterise downturn events and calculate average differences in transports between the first four years and subsequent four years of the RAPID array.

For RAPID transports where the western boundary reference level is raised to 1000 dbar, DWBC flow exhibits too much short-term variability to draw meaningful conclusions with regard to downturn events. However, brief moments

of northward DWBC internal transports below 1100 m are more frequent in the first 4 years relative to the subsequent 4 years (reducing from 12.2% to 10.8% of the time-series for each 4-year interval, significant at the 95% confidence interval). The mean strength of the DWBC is found to be 18.4 ±16.5 Sv, This falls short of estimates found by Johns et al. (2008), Meinen et al. (2004), Bryden et al. (2005a), Toole et al. (2011), who find mean DWBC strength to fall between ~24 Sv and ~27 Sv. However, their estimated DWBC flow standard deviations are large and therefore encompass the DWBC mean found here. Furthermore, previous DWBC estimates are inclusive of both the baroclinic and barotropic components within the DWBC, whereas the methodology detailed in Chapter 3 spreads the external component over the whole basin uniformly. This adds weight to the argument that the compensation transports should be concentrated at the western boundary.

It would be of value to present RAPID transports with both a basin-wide deep reference level and a western boundary shallow reference level for comparison. A shallow western boundary reference level enables an alternative view of transports incorporating a different spatial view of circulation.

GRACE satellite data is employed to calculate external transports for the LNADW and AABW layers in Chapter 4. GRACE data are evaluated from April 2004, to match the start of the RAPID time-series. GRACE layer anomaly transports (with zero mean) are linearly de-trended, de-seasonalised and Lowess smoothed. In contrast, GRACE layer estimated transports are given mean values equal to RAPID deep layer means and de-trended relative to RAPID compensation transports. The results of the GRACE anomaly transports and GRACE estimated transports bear common features regarding MOC weakening, despite the different processing techniques. Downturn events (ignoring the 2013 downturn for which there is a GRACE data gap) convey southward GRACE LNADW weakening (of at least 3 Sv) and northward GRACE AABW strengthening (of at least 0.5 Sv). The first 4 years convey stronger southward GRACE LNADW than the subsequent 4 years (by at least 2 Sv), as well as weaker northward GRACE AABW than the subsequent 4 years (by ~0.4 Sv). There is observational evidence for near compensation between the AMOC mid-ocean components (Kanzow et al., 2007). So, strong southward GRACE external transports are likely to accompany weak southward internal flow. However, these results come with the caveat that there is uncertainty regarding de-trending, which is needed because GRACE data suffers

from an error trend caused by glacial isostatic adjustment and land leakage (A et al., 2013; Bentel et al., 2015).

The results of Chapter 4 show the ease with which external transports can be combined with RAPID transports to create greater understanding of AMOC transports. GRACE data also provide a picture of the longitudinal distribution of barotropic transports, which could inform the distribution of compensation transports employed as a proxy for barotropic flow. However, a concurrent OBP dataset is needed to convert GRACE anomaly transports into absolute transports and to complete data gaps.

Key assessments with regard to the AMOC calculation and the data employed therein, for the purpose of directing future paths of analysis, are as follows:

1. Spatially complex hydrographic section data are a valuable research tool from which the ideas for Chapters 3 and 4 originated. Discovering where the flow is too temporally variable to be captured by hydrographic profiles (such as within the WBW) is just as valuable as understanding where the flow is relatively spatially uniform (such as within the deep layers east of the MAR, highlighting the comparatively large and variable DWBC flow). Further sections will be needed to contrast both with RAPID transports and the 2010 & 2011 hydrographic sections that fall within downturn events. Going forward, WBW absolute transports should be substituted into hydrographic data employed for calculating basin-wide transports at 25°N. WBW absolute transports are key to capturing flow in a region of high short-term variability. Hydrographic sections are the perfect data source with which the choice of reference level and distribution of compensation transports can be experimented. This is due to the understanding that could be gained as to how these changes alter the basin spatially. The resultant alternative methodology could convey a different picture of the deep baroclinic and barotropic flow.
2. Temporally complex RAPID data are an important tool in understanding AMOC variation. The time-series data for mooring WB5 ends in 2014, but it is vital to incorporating high-frequency DWBC flow in the total MOC. The DWBC is the key pathway for NADW to the global ocean; its flow represents the cold-water part of the thermohaline circulation (Bryden et al., 2005a). Incorporation of strong DWBC flow into the RAPID AMOC calculation would thus enable greater understanding of the AMOC driving mechanisms. Due to the prominence of basin-wide monitoring arrays within the Atlantic

Ocean (Lozier et al., 2017), understanding the methods of AMOC calculation, the driving forces, as well as the biases and their magnitude, are vital to our understanding of their accuracy. The current method of calculation remains an accurate and robust representation of the total MOC and its variability. But alternative methods of AMOC calculation may add to the usefulness of the array with regard to understanding deep transports and their impact on the wider issue of climate change. Altering the RAPID AMOC calculation, with a shallow western boundary reference level and non-uniformly applied compensation transports, would make for interesting complementary results. This would necessitate the re-instatement of a mooring located near the eastern extent of the DWBC.

3. GRACE data provide an insightful spatial picture of OBP variation both with longitude and time. Ideally, a concurrent and independent dataset of OBP variation is needed with which to ratify the methods of GRACE data processing and convert GRACE-derived anomaly transports into absolute transports. Nonetheless, GRACE OBP across the North Atlantic at 26°N could be useful as a map determining the longitudinal variation of external transports. The strong and highly variable baroclinic southward flow in the DWBC region is linked to equally strong and, even more variable, barotropic transports. Applying compensation transports to the basin uniformly means that it is difficult to discern regions of recirculation or counterbalancing flow. Splitting the compensation for each longitudinal band represented by a GRACE mascon could further develop the methodology of the RAPID AMOC estimate and provide insight into DWBC flow.

Observational systems with adequate spatial and temporal resolution are critical to revealing AMOC changes. Observational data are our most credible tool with which to form hypotheses and expand our understanding of the spectrum of AMOC variability. Continuing research is needed to assess how the AMOC will evolve and what the repercussions are for regional and global climate. Prediction and attribution of AMOC variability is contingent on our understanding of its natural variability, predominantly for interannual and multidecadal timescales. Thus, the continuing renewal of the RAPID array furthers its scientific merit, particularly if supplemented by additional AMOC observing systems.

Bibliography

Anderson, R. F., Ali, S., Bradtmiller, L. I., Nielsen, S. H. H., Fleisher, M. Q., Anderson, B. E., & Burckle, L. H. (2009). Wind-driven upwelling in the Southern Ocean and the deglacial rise in atmospheric CO_2. Science, 323(5920), 1443-1448.

Atkinson, C. P., Bryden, H. L., Hirschi, J., & Kanzow, T., 2010. On the seasonal cycles and variability of Florida Straits, Ekman and Sverdrup transports at 26°N in the Atlantic Ocean. Ocean Science, 6(4), 837-859.

Atkinson, C. P., 2011. Variability of the Atlantic Meridional Overturning Circulation at 26°N. PhD thesis, School of Ocean and Earth Science, University of Southampton, Southampton, UK, 195.

Atkinson, C. P., Bryden, H. L., Cunningham, S. A., & King, B. A., 2012. Atlantic transport variability at 25°N in six hydrographic sections. Ocean Science, 8(4), 497.

Bader, J., Mesquita, M.D., Hodges, K.I., Keenlyside, N., Østerhus, S. and Miles, M., 2011. A review on Northern Hemisphere sea-ice, storminess and the North Atlantic Oscillation: observations and projected changes. Atmospheric Research, 101(4), 809-834.

Baringer, M. O., Larsen, J. C., 2001. Sixteen years of Florida Current transport at 27°N. Geophys. Res. Lett. 28(16), 3179–3182.

Bates, N.R., 2012. Multi-decadal uptake of carbon dioxide into subtropical mode water of the North Atlantic Ocean. Biogeosciences 9(7), 2649-2659.

Beaugrand, G., Reid, P.C., Ibanez, F., Lindley, J.A. and Edwards, M., 2002. Reorganization of North Atlantic marine copepod biodiversity and climate. Science 296(5573), 1692-1694.

Bentel, K., Landerer, F. W., & Boening, C., 2015. Monitoring Atlantic overturning circulation variability with GRACE-type ocean bottom pressure observations - a sensitivity study. Ocean Science Discussions 12(4).

Bindoff, N., McDougall, T., 1994. Diagnosing climate-change and ocean ventilation using hydrographic data. J. Phys. Oceanogr. 24(6), 1137–1152.

Bingham, R. J., Hughes, C. W., Roussenov, V., Williams, R. G., 2007. Meridional coherence of the North Atlantic Meridional Overturning Circulation. Geophys. Res. Lett. 34(23), L23606.

Black, D.E., Peterson, L.C., Overpeck, J.T., Kaplan, A., Evans, M.N. and Kashgarian, M., 1999. Eight centuries of North Atlantic Ocean atmosphere variability. Science 286(5445), 1709-1713.

Black, R., Adger, W.N., Arnell, N.W., Dercon, S., Geddes, A. and Thomas, D., 2011. The effect of environmental change on human migration. Global Environmental Change 21, S3-S11.

de Boer, G. J., Pietrzak, J. D., & Winterwerp, J. C., 2009. SST observations of upwelling induced by tidal straining in the Rhine ROFI. Continental Shelf Research 29(1), 263-277.

Bryden, H., Griffiths, M., Lavin, A., Millard, R., Parrilla, G., Smethie, W., 1996. Decadal changes in water mass characteristics at 24°N in the subtropical North Atlantic Ocean. J. Climate 9(12), 3162–3186.

Bryden, H. L., Johns, W. E., Saunders, P. M., 2005a. Deep Western Boundary Current east of Abaco: mean structure and transport. J. Mar. Res. 63(1), 35–57.

Bryden, H. L., Longworth, H. R., Cunningham, S. A., 2005b. Slowing of the Atlantic Meridional Overturning Circulation at 25°N. Nature 438(7068), 655–657.

Bryden, H. L., Mujahid, A., Cunningham, S. A., Kanzow, T., 2009. Adjustment of the basin-scale circulation at 26°N to variations in Gulf Stream, Deep Western Boundary Current and Ekman transports as observed by the RAPID array. Ocean Sci. 5(4), 421–433.

Bryden, H. L., Robinson, C., & Griffiths, G., 2012. Changing currents: a strategy for understanding and predicting the changing ocean circulation. Phil. Trans. R. Soc. A 370(1980), 5461-5479.

Bryden, H.L., King, B.A., McCarthy, G.D. and McDonagh, E.L., 2014. Impact of a 30% reduction in Atlantic meridional overturning during 2009-2010. Ocean Science 10(4), 683-691.

Buckley, M.W. and Marshall, J., 2016. Observations, inferences, and mechanisms of the Atlantic Meridional Overturning Circulation: a review. Reviews of Geophysics 54(1), 5-63.

Buizert, C., Gkinis, V., Severinghaus, J.P., He, F., Lecavalier, B.S., Kindler, P., Leuenberger, M., Carlson, A.E., Vinther, B., Masson-Delmotte, V. and White, J.W., 2014. Greenland temperature response to climate forcing during the last deglaciation. Science 345(6201), 1177-1180.

Chambers, D. P., & Bonin, J. A., 2012. Evaluation of Release-05 GRACE time-variable gravity coefficients over the ocean. Ocean Science 8(5), 859.

Cronin, M., & Sprintall, J., 2009. Wind and buoyancy forced upper ocean. Elements of Physical Oceanography: a Derivative of the Encyclopedia of Ocean Sciences, 237-245.

Cunningham, S. A., 2005. Southern Ocean circulation. Archives of Natural History 32, 265-280.

Cunningham, S. A., Kanzow, T., Rayner, D., Baringer, M. O., Johns, W. E., Marotzke, J., Longworth, H. R., Grant, E. M., Hirschi, J. J. M., Beal, L. M., Meinen, C. S., Bryden, H. L., 2007. Temporal variability of the Atlantic Meridional Overturning Circulation at 26.5°N. Science 317(5840), 935–938.

Cunningham, S. A., Roberts, C. D., Frajka-Williams, E., Johns, W. E., Hobbs, W., Palmer, M. D., & McCarthy, G., 2013. Atlantic Meridional Overturning Circulation slowdown cooled the subtropical ocean. Geophysical Research Letters 40(23), 6202-6207.

Curry, R. G., & McCartney, M. S., 1996. Labrador Sea Water carries northern climate signal south. Oceanus 39(2), 24.

Delworth, T.L. and Mann, M.E., 2000. Observed and simulated multidecadal variability in the Northern Hemisphere. Climate Dynamics 16(9), 661-676.

Delworth, T.L., Zhang, R. and Mann, M.E., 2007. Decadal to centennial variability of the Atlantic from observations and models. Geophysical Monograph-American Geophysical Union 173, 131.

Delworth, T. L., Clark, P. U., Holland, M., Johns, W. E., Kuhlbrodt, T., Lynch-Stieglitz, J., Morril, C., Seager, R., Weaver, A., Zhang, R., 2008. The potential for abrupt climate change in the Atlantic Meridional Overturning Circulation. Abrupt Climate Change. U.S. Geological Survey, 258–359.

Dong, B., Sutton, R.T., Woollings, T. and Hodges, K., 2013. Variability of the North Atlantic summer storm track: mechanisms and impacts on European climate. Environmental Research Letters 8(3), 034037.

Duchez, A., Frajka-Williams, E., Castro, N., Hirschi, J., & Coward, A., 2014. Seasonal to interannual variability in density around the Canary Islands and their influence on the Atlantic Meridional Overturning Circulation at 26°N. Journal of Geophysical Research: Oceans 119(3), 1843-1860.

Duchez, A., Courtois, P., Harris, E., Josey, S.A., Kanzow, T., Marsh, R., Smeed, D.A. and Hirschi, J.M., 2016. Potential for seasonal prediction of Atlantic sea surface temperatures using the RAPID array at 26°N. Climate Dynamics 46(9-10), 3351-3370.

Elipot, S., Frajka-Williams, E., Hughes, C. W., & Willis, J. K., 2014. The observed North Atlantic Meridional Overturning Circulation: its meridional coherence and ocean bottom pressure. Journal of Physical Oceanography 44(2), 517-537.

Elsner, J.B., Kossin, J.P. and Jagger, T.H., 2008. The increasing intensity of the strongest tropical cyclones. Nature 455(7209), 92.

Enfield, D.B., Mestas-Nuñez, A.M. and Trimble, P.J., 2001. The Atlantic Multidecadal Oscillation and its relation to rainfall and river flows in the continental US. Geophysical Research Letters 28(10), 2077-2080.

Ezer, T., 2013. Sea level rise, spatially uneven and temporally unsteady: why the US East Coast, the global tide gauge record, and the global altimeter data show different trends. Geophysical Research Letters 40(20), 5439-5444.

Feng, S. and Hu, Q., 2008. How the North Atlantic Multidecadal Oscillation may have influenced the Indian summer monsoon during the past two millennia. Geophysical Research Letters 35(1).

Fine, R.A., 1995. Tracers, time scales, and the thermohaline circulation: the lower limb in the North Atlantic Ocean. Reviews of Geophysics 33(S2), 1353-1365.

Folland, C.K., Knight, J., Linderholm, H.W., Fereday, D., Ineson, S. and Hurrell, J.W., 2009. The summer North Atlantic Oscillation: past, present, and future. Journal of Climate 22(5), 1082-1103.

Frajka-Williams, E., Cunningham, S. A., Bryden, H., & King, B. A., 2011. Variability of Antarctic Bottom Water at 24.5°N in the Atlantic. Journal of Geophysical Research: Oceans 116(C11).

Frajka-Williams, E., 2015. Estimating the Atlantic overturning at 26°N using satellite altimetry and cable measurements. Geophysical Research Letters 42(9), 3458-3464.

Frajka-Williams, E., Meinen, C.S., Johns, W.E., Smeed, D.A., Duchez, A., Lawrence, A.J., Cuthbertson, D.A., Mccarthy, G.D., Bryden, H.L., Baringer, M.O. and Moat, B.I., 2016. Compensation between meridional flow components of the Atlantic MOC at 26°N. Ocean Science 12(2), 481-493.

Ganachaud, A., 2003. Error budget of inverse box models: the North Atlantic. J. Atmos. Ocean. Tech. 20(11), 1641–1655.

Gelderloos, R., Straneo, F., & Katsman, C. A., 2012. Mechanisms behind the temporary shutdown of deep convection in the Labrador Sea: lessons from the great salinity anomaly years 1968–71. Journal of Climate 25(19), 6743-6755.

Goddard, P.B., Yin, J., Griffies, S.M. and Zhang, S., 2015. An extreme event of sea-level rise along the Northeast coast of North America in 2009–2010. Nature Communications 6, 6346.

Goni, G., DeMaria, M., Knaff, J., Sampson, C., Ginis, I., Bringas, F., Mavume, A., Lauer, C., Lin, I.I., Ali, M.M. and Sandery, P., 2009. Applications of satellite-derived ocean measurements to tropical cyclone intensity forecasting. Oceanography 22(3), 190-197.

Gray, S.T., Graumlich, L.J., Betancourt, J.L. and Pederson, G.T., 2004. A tree-ring based reconstruction of the Atlantic Multidecadal Oscillation since 1567 AD. Geophysical Research Letters 31(12).

Häkkinen, S., Rhines, P., 2004. Decline of subpolar North Atlantic circulation during the 1990s. Science 304(5670), 555–559.

Häkkinen, S., Rhines, P. B., & Worthen, D. L., 2016. Warming of the global ocean: spatial structure and water-mass trends. Journal of Climate 29(13), 4949-4963.

Hall, M. M., Bryden, H. L., 1982. Direct estimates and mechanisms of ocean heat transport. Deep-Sea Res. Pt. I 29(3), 339–359.

Hastenrath, S. and Greischar, L., 1993. Circulation mechanisms related to northeast Brazil rainfall anomalies. Journal of Geophysical Research: Atmospheres 98(D3), 5093-5102.

Hernández-Guerra, A., Pelegrí, J. L., Fraile-Nuez, E., Benítez-Barrios, V., Emelianov, M., Pérez-Hernández, M. D., & Vélez-Belchí, P., 2014. Meridional overturning transports at 7.5°N and 24.5°N in the Atlantic Ocean during 1992–93 and 2010–11. Progress in Oceanography 128, 98-114.

Holland, D.M., Thomas, R.H., De Young, B., Ribergaard, M.H. and Lyberth, B., 2008. Acceleration of Jakobshavn Isbrae triggered by warm subsurface ocean waters. Nature geoscience 1(10), 659.

Hughes, C. W., Meredith, M. P., & Heywood, K. J., 1999. Wind-driven transport fluctuations through Drake Passage: a southern mode. Journal of Physical Oceanography 29(8), 1971-1992.

Hughes, C. W., Elipot, S., Morales Maqueda, M. Á., & Loder, J. W., 2013. Test of a method for monitoring the geostrophic meridional overturning circulation using only boundary measurements. Journal of Atmospheric and Oceanic Technology 30(4), 789-809.

IPCC, 2013. Climate change 2013: the physical science basis. Contribution of working group 1 to the fourth assessment report of the IPCC. Cambridge University Press.

Jayne, S. R., Marotzke, J., 2001. The dynamics of ocean heat transport variability. Rev. Geophys. 39(3), 385–411.

Jochumsen, K., Quadfasel, D., Valdimarsson, H., & Jónsson, S., 2012. Variability of the Denmark Strait overflow: moored time series from 1996–2011. Journal of Geophysical Research: Oceans 117(C12).

Johns, E., Fine, R. A., & Molinari, R. L., 1997. Deep flow along the western boundary south of the Blake Bahama Outer Ridge. Journal of Physical Oceanography 27(10), 2187-2208.

Johns, W. E., Kanzow, T., & Zantopp, R., 2005. Estimating ocean transports with dynamic height moorings: an application in the Atlantic Deep Western Boundary Current at 26°N. Deep Sea Research Part I: Oceanographic Research Papers 52(8), 1542-1567.

Johns, W. E., Beal, L. M., Baringer, M. O., Molina, J. R., Cunningham, S. A., Kanzow, T., Rayner, D., 2008. Variability of shallow and deep western boundary currents off the Bahamas during 2004-05: results from the 26°N RAPID-MOC array. J. Phys. Oceanogr. 38(3), 605–623.

Johnson, G. C., Purkey, S. G., & Toole, J. M., 2008. Reduced Antarctic Meridional Overturning Circulation reaches the North Atlantic Ocean. Geophysical Research Letters 35(22).

Kang, I.S., No, H.H. and Kucharski, F., 2014. ENSO amplitude modulation associated with the mean SST changes in the tropical central Pacific induced by Atlantic Multidecadal Oscillation. Journal of Climate 27(20), 7911-7920.

Kanzow, T., Flechtner, F., Chave, A., Schmidt, R., Schwintzer, P., & Send, U., 2005. Seasonal variation of ocean bottom pressure derived from Gravity Recovery and Climate Experiment (GRACE): local validation and global patterns. Journal of Geophysical Research: Oceans 110(C9).

Kanzow, T., Cunningham, S. A., Rayner, D., Hirschi, J. J. M., Johns, W. E., Baringer, M. O., Bryden, H. L., Beal, L. M., Meinen, C. S., Marotzke, J., 2007. Observed flow compensation associated with the MOC at 26.5°N in the Atlantic. Science 317(5840), 938–941.

Kanzow, T., Cunningham, S. A., Johns, W. E., Hirschi, J. J. M., Marotzke, J., Baringer, M. O., Meinen, C. S., Chidichimo, M., Atkinson, C. P., Beal, L. M., Bryden, H. L., Collins, J., 2010. Seasonal variability of the Atlantic Meridional Overturning Circulation at 26.5°N. J. Climate 23, 5678–5698.

Keenlyside, N.S., Latif, M., Jungclaus, J., Kornblueh, L. and Roeckner, E., 2008. Advancing decadal-scale climate prediction in the North Atlantic sector. Nature 453(7191), 84.

Kuhlbrodt, T., Griesel, A., Montoya, M., Levermann, A., Hofmann, M., Rahmstorf, S., 2007. On the driving processes of the Atlantic Meridional Overturning Circulation. Rev. Geophys. 45(1), RG2001.

Kuhlbrodt, T., Rahmstorf, S., Zickfeld, K., Vikebo, F. B., Sundby, S., Hofmann, M., Link, P. M., Bondeau, A., Cramer, W., Jaeger, C., 2009. An integrated assessment of changes in the thermohaline circulation. Climatic Change 96(4), 489–537.

Landerer, F. W., & Swenson, S. C., 2012. Accuracy of scaled GRACE terrestrial water storage estimates. Water resources research 48(4).

Landerer, F. W., Wiese, D. N., Bentel, K., Boening, C., & Watkins, M. M., 2015. North Atlantic Meridional Overturning Circulation variations from GRACE ocean bottom pressure anomalies. Geophysical Research Letters 42(19), 8114-8121.

Larsen, J. C., 1992. Transport and heat-flux of the Florida Current at 27°N derived from cross-stream voltages and profiling data - theory and observations. Philos. T. Roy. Soc. A 338(1650), 169–236.

Lavin, A., Bryden, H. L., Parrilla, G., 1998. Meridional transport and heat flux variations in the subtropical North Atlantic. The Global Ocean and Atmosphere System 6, 269–293.

Lee, T. N., Johns, W., Zantopp, R., & Schott, F., 1990. Western boundary current structure and variability east of Abaco, Bahamas at 26.5°N. Journal of Physical Oceanography 20(3), 446-466.

Longworth, H. R., 2007. Constraining variability of the Atlantic Meridional Overturning Circulation at 25°N from historical observations, 1980-2005. PhD thesis, School of Ocean and Earth Science, University of Southampton, Southampton, UK, 200.

Longworth, H. R., Bryden, H. L., & Baringer, M. O., 2011. Historical variability in Atlantic meridional baroclinic transport at 26.5°N from boundary dynamic height observations. Deep Sea Research Part II: Topical Studies in Oceanography 58(17), 1754-1767.

Lozier, M. S., 2010. Deconstructing the conveyor belt. Science 328, 1507–1511.

Lozier, S.M., Bacon, S., Bower, A.S., Cunningham, S.A., Femke de Jong, M., De Steur, L., deYoung, B., Fischer, J., Gary, S.F., Greenan, B.J. and Heimbach, P., 2017. Overturning in the subpolar North Atlantic program: a new international ocean observing system. Bulletin of the American Meteorological Society 98(4), 737-752.

Marshall, J., Kushnir, Y., Battisti, D., Chang, P., Czaja, A., Dickson, R., Hurrell, J., McCartney, M., Saravanan, R. and Visbeck, M., 2001. North Atlantic climate variability: phenomena, impacts and mechanisms. International journal of climatology 21(15), 1863-1898.

Marshall, J., & Speer, K., 2012. Closure of the Meridional Overturning Circulation through Southern Ocean upwelling. Nature Geoscience 5(3), 171-180.

McCabe, G.J., Palecki, M.A. and Betancourt, J.L., 2004. Pacific and Atlantic Ocean influences on multidecadal drought frequency in the United States. Proceedings of the National Academy of Sciences 101(12), 4136-4141.

McCarthy, G., Frajka-Williams, E., Johns, W. E., Baringer, M. O., Meinen, C. S., Bryden, H. L., & Cunningham, S. A., 2012. Observed interannual variability of the Atlantic Meridional Overturning Circulation at 26.5°N. Geophysical Research Letters 39(19).

McCarthy, G.D., Smeed, D.A., Johns, W.E., Frajka-Williams, E., Moat, B.I., Rayner, D., Baringer, M.O., Meinen, C.S., Collins, J. and Bryden, H.L., 2015a. Measuring the Atlantic Meridional Overturning Circulation at 26°N. Progress in Oceanography 130, 91-111.

McCarthy, G.D., Haigh, I.D., Hirschi, J.J.M., Grist, J.P. and Smeed, D.A., 2015b. Ocean impact on decadal Atlantic climate variability revealed by sea-level observations. Nature 521(7553), 508.

McCarthy, G.D., Menary, M.B., Mecking, J.V., Moat, B.I., Johns, W.E., Andrews, M., Rayner, D., Smeed, D.A., 2017. The importance of deep, basinwide measurements in optimised Atlantic Meridional Overturning Circulation observing arrays. Journal of Geophysical Research: Oceans 122(3), 1808-1826.

McCartney, M.S., 1993. Crossing of the equator by the deep western boundary current in the western Atlantic Ocean. Journal of Physical Oceanography 23(9), 1953-1974.

McCartney, M., 1997. Climate change: is the ocean at the helm?. Nature 388(6642), 521.

McManus, J.F., Francois, R., Gherardi, J.M., Keigwin, L.D. and Brown-Leger, S., 2004. Collapse and rapid resumption of Atlantic meridional circulation linked to deglacial climate changes. Nature 428(6985), 834.

Meinen, C. S., Garzoli, S. L., Johns, W. E., & Baringer, M. O., 2004. Transport variability of the Deep Western Boundary Current and the Antilles Current off Abaco Island, Bahamas. Deep Sea Research Part I: Oceanographic Research Papers 51(11), 1397-1415.

Meinen, C. S., Baringer, M. O., Garcia, R. F., 2010. Florida Current transport variability: an analysis of annual and longer-period signals. Deep-Sea Res. Pt. I 57, 835–846.

Meinen, C. S., Johns, W. E., Garzoli, S. L., van Sebille, E., Rayner, D., Kanzow, T., & Baringer, M. O., 2013. Variability of the Deep Western Boundary Current at 26.5°N during 2004–2009. Deep Sea Research Part II: Topical Studies in Oceanography 85, 154-168.

Meredith, M. P., Gordon, A. L., Naveira Garabato, A. C., Abrahamsen, E. P., Huber, B. A., Jullion, L., & Venables, H. J., 2011. Synchronous intensification and warming of Antarctic Bottom Water outflow from the Weddell Gyre. Geophysical Research Letters 38(3).

Metzl, N., Corbière, A., Reverdin, G., Lenton, A., Takahashi, T., Olsen, A., Johannessen, T., Pierrot, D., Wanninkhof, R., Ólafsdóttir, S.R. and Olafsson, J., 2010. Recent acceleration of the sea surface fCO_2 growth rate in the North Atlantic subpolar gyre (1993–2008) revealed by winter observations. Global Biogeochemical Cycles 24(4).

Miles, M.W., Divine, D.V., Furevik, T., Jansen, E., Moros, M. and Ogilvie, A.E., 2014. A signal of persistent Atlantic Multidecadal Variability in Arctic sea ice. Geophysical Research Letters 41(2), 463-469.

Mohtadi, M., Prange, M. and Steinke, S., 2016. Palaeoclimatic insights into forcing and response of monsoon rainfall. Nature 533(7602), 191.

Molinari, R., Fine, R., Wilson, W., Curry, R., Abell, J., McCartney, M., 1998. The arrival of recently formed Labrador Sea Water in the Deep Western Boundary Current at 26.5°N. Geophys. Res. Lett. 25(13), 2249–2252.

Munk, W., & Wunsch, C., 1998. Abyssal recipes II: energetics of tidal and wind mixing. Deep Sea Research Part I: Oceanographic Research Papers 45(12), 1977-2010.

Olsen, S. M., Hansen, B., Quadfasel, D., Osterhus, S., 2008. Observed and modelled stability of overflow across the Greenland-Scotland ridge. Nature 455(7212), 519– U35.

Osborn, T.J., 2011. Winter 2009/2010 temperatures and a record-breaking North Atlantic Oscillation index. Weather 66(1), 19-21.

Ottersen, G. and Stenseth, N.C., 2001. Atlantic climate governs oceanographic and ecological variability in the Barents Sea. Limnology and Oceanography 46(7), 1774-1780.

Palter, J.B. and Lozier, M.S., 2008. On the source of Gulf Stream nutrients. Journal of Geophysical Research: Oceans 113(C6).

Park, J. H., Watts, D. R., Donohue, K. A., & Jayne, S. R., 2008. A comparison of in situ bottom pressure array measurements with GRACE estimates in the Kuroshio Extension. Geophysical Research Letters 35(17).

Pawlowicz, R., Beardsley, B., & Lentz, S., 2002. Classical tidal harmonic analysis including error estimates in MATLAB using T_TIDE. Computers & Geosciences 28(8), 929-937.

Pérez-Hernández, M. D., McCarthy, G. D., Vélez-Belchí, P., Smeed, D. A., Fraile-Nuez, E., & Hernández-Guerra, A., 2015. The Canary Basin contribution to the seasonal cycle of the Atlantic Meridional Overturning Circulation at 26°N. Journal of Geophysical Research: Oceans 120(11), 7237-7252.

Peterson, L.C., Haug, G.H., Hughen, K.A. and Röhl, U., 2000. Rapid changes in the hydrologic cycle of the tropical Atlantic during the last glacial. Science 290(5498), 1947-1951.

Pickart, R. S., 1994. Interaction of the Gulf Stream and deep western boundary current where they cross. Journal of Geophysical Research: Oceans 99(C12), 25155-25164.

Piecuch, C. G., & Ponte, R. M., 2014. Non-seasonal mass fluctuations in the mid-latitude North Atlantic Ocean. Geophysical Research Letters 41(12), 4261-4269.

Piecuch, C. G., Fukumori, I., Ponte, R. M., & Wang, O., 2015. Vertical structure of ocean pressure variations with application to satellite-gravimetric observations. Journal of Atmospheric and Oceanic Technology 32(3), 603-613.

Polo, I., Robson, J., Sutton, R., & Balmaseda, M. A., 2014. The importance of wind and buoyancy forcing for the boundary density variations and the geostrophic component of the AMOC at 26°N. Journal of Physical Oceanography 44(9), 2387-2408.

Polonsky, A.B., Basharin, D.V., Voskresenskaya, E.N., Worley, S.J. and Yurovsky, A.V., 2004. Relationship between the North Atlantic Oscillation, Euro-Asian climate anomalies and Pacific variability. Pacific Oceanography 2(1-2), 52-66.

Polzin, K.L., Toole, J.M., Ledwell, J.R. and Schmitt, R.W., 1997. Spatial variability of turbulent mixing in the abyssal ocean. Science 276(5309), 93-96.

Rayner, D., Hirschi, J. J. M., Kanzow, T., Johns, W. E., Wright, P. G., Frajka-Williams, E., & Beal, L. M., 2011. Monitoring the Atlantic Meridional Overturning Circulation. Deep Sea Research Part II: Topical Studies in Oceanography 58(17), 1744-1753.

Reuveny, R., 2007. Climate change-induced migration and violent conflict. Political Geography 26(6), 656-673.

Rietbroek, R., LeGrand, P., Wouters, B., Lemoine, J. M., Ramillien, G., & Hughes, C. W., 2006. Comparison of in situ bottom pressure data with GRACE gravimetry in the Crozet-Kerguelen region. Geophysical Research Letters 33(21).

Rignot, E., and P. Kanagaratnam, 2006. Changes in the velocity structure of the Greenland Ice Sheet. Science 311(5763), 986–990.

Roberts, C. D., Waters, J., Peterson, K. A., Palmer, M. D., McCarthy, G. D., Frajka-Williams, E., & Blockley, E. W., 2013. Atmosphere drives recent interannual variability of the Atlantic Meridional Overturning Circulation at 26.5°N. Geophysical Research Letters 40(19), 5164-5170.

Robson, J., Hodson, D., Hawkins, E., & Sutton, R., 2014. Atlantic overturning in decline?. Nature Geoscience 7(1), 2-3.

Roemmich, D. and Wunsch, C., 1985. Two transatlantic sections: meridional circulation and heat flux in the subtropical North Atlantic Ocean. Deep Sea Research Part A. Oceanographic Research Papers 32(6), 619-664.

Roussenov, V. M., Williams, R. G., Hughes, C. W., Bingham, R. J., 2008. Boundary wave communication of bottom pressure and overturning changes for the North Atlantic. J. Geophys. Res. 113(C8), C08042.

Sabine, C.L., Feely, R.A., Gruber, N., Key, R.M., Lee, K., Bullister, J.L., Wanninkhof, R., Wong, C.S.L., Wallace, D.W., Tilbrook, B. and Millero, F.J., 2004. The oceanic sink for anthropogenic CO_2. Science 305(5682), 367-371.

San Antolín Plaza, M.Á., Pelegrí, J.L., Machín, F.J., Benítez-Barrios, V., 2012. Inter-decadal changes in stratification and double diffusion in a transatlantic section along 7.5°N. Scientia Marina 76, 189–207.

Schmittner, A., 2005. Decline of the marine ecosystem caused by a reduction in the Atlantic overturning circulation. Nature 434(7033), 628–633.

Schuster, U. and Watson, A.J., 2007. A variable and decreasing sink for atmospheric CO_2 in the North Atlantic. Journal of Geophysical Research: Oceans 112(C11).

Serreze, M.C., Holland, M.M. and Stroeve, J., 2007. Perspectives on the Arctic's shrinking sea-ice cover. Science 315(5818), 1533-1536.

Servain, J., 1991. Simple climatic indices for the tropical Atlantic Ocean and some applications. Journal of Geophysical Research: Oceans 96(C8), 15137-15146.

Sinha, B., Smeed, D.A., McCarthy, G., Moat, B.I., Josey, S.A., Hirschi, J.M., Frajka-Williams, E., Blaker, A.T., Rayner, D. and Madec, G., 2018. The accuracy of estimates of the overturning circulation from basin-wide mooring arrays. Progress in Oceanography 160, 101-123.

Slater, D. R., 2003. The transport of Mediterranean Water in the North Atlantic Ocean. PhD thesis, School of Ocean and Earth Science, University of Southampton, Southampton, UK, 127.

Smeed, D. A., McCarthy, G. D., Cunningham, S. A., Frajka-Williams, E., Rayner, D., Johns, W. E., & Bryden, H. L., 2014. Observed decline of the Atlantic Meridional Overturning Circulation 2004-2012. Ocean Science 10(1), 29.

Smeed, D.A., Josey, S.A., Beaulieu, C., Johns, W.E., Moat, B.I., Frajka-Williams, E., Rayner, D., Meinen, C.S., Baringer, M.O., Bryden, H.L. and McCarthy, G.D., 2018. The North Atlantic Ocean is in a state of reduced overturning. Geophysical Research Letters 45(3), 1527-1533.

Srokosz, M., Baringer, M., Bryden, H., Cunningham, S., Delworth, T., Lozier, S., & Sutton, R., 2012. Past, present, and future changes in the Atlantic Meridional Overturning Circulation. Bulletin of the American Meteorological Society 93(11), 1663-1676.

Steinfeldt, R., Rhein, M., Bullister, J.L. and Tanhua, T., 2009. Inventory changes in anthropogenic carbon from 1997–2003 in the Atlantic Ocean between 20°S and 65°N. Global Biogeochemical Cycles 23(3).

Straneo, F. and Heimbach, P., 2013. North Atlantic warming and the retreat of Greenland's outlet glaciers. Nature 504(7478), 36.

Sutton, R.T. and Hodson, D.L., 2007. Climate response to basin-scale warming and cooling of the North Atlantic Ocean. Journal of Climate 20(5), 891-907.

Sutton, R.T. and Dong, B., 2012. Atlantic Ocean influence on a shift in European climate in the 1990s. Nature Geoscience 5(11), 788.

Swenson, S., & Wahr, J., 2006. Post-processing removal of correlated errors in GRACE data. Geophysical Research Letters 33(8).

Talley, L. D., 1999. Some aspects of ocean heat transport by the shallow, intermediate and deep overturning circulations. Mechanisms of Global Climate Change at Millennial Time Scales, 1-22.

Talley, L., 2003. Shallow, intermediate, and deep overturning components of the global heat budget. J. Phys. Oceanography 33(3), 530–560.

Talley, L. D., 2013. Closure of the global overturning circulation through the Indian, Pacific, and Southern Oceans: schematics and transports. Oceanography 26(1), 80-97.

Takahashi, T., Sutherland, S.C., Wanninkhof, R., Sweeney, C., Feely, R.A., Chipman, D.W., Hales, B., Friederich, G., Chavez, F., Sabine, C. and Watson, A., 2009. Climatological mean and decadal change in surface ocean pCO_2, and net sea–air CO_2 flux over the global oceans. Deep Sea Research Part II: Topical Studies in Oceanography 56(8-10), 554-577.

Tapley, B. D., Bettadpur, S., Watkins, M., & Reigber, C., 2004. The gravity recovery and climate experiment: mission overview and early results. Geophysical research letters 31(9).

Toole, J. M., Curry, R. G., Joyce, T. M., McCartney, M., & Peña-Molino, B., 2011. Transport of the North Atlantic deep western boundary current about 39°N, 70°W: 2004–2008. Deep Sea Research Part II: Topical Studies in Oceanography 58(17), 1768-1780.

Van Sebille, E., Baringer, M. O., Johns, W. E., Meinen, C. S., Beal, L. M., De Jong, M. F., & Van Aken, H. M., 2011. Propagation pathways of classical Labrador Sea water from its source region to 26°N. Journal of Geophysical Research: Oceans 116(12).

Vellinga, M., Wood, R. A., 2002. Global climatic impacts of a collapse of the Atlantic thermohaline circulation. Climatic Change 54(3), 251–267.

Visbeck, M., Chassignet, E.P., Curry, R.G., Delworth, T.L., Dickson, R.R. and Krahmann, G., 2003. The ocean's response to North Atlantic Oscillation variability. The North Atlantic Oscillation: Climatic Significance and Environmental Impact 134, 113-145.

Wahr, J., Molenaar, M., & Bryan, F., 1998. Time variability of the Earth's gravity field: hydrological and oceanic effects and their possible detection using GRACE. Journal of Geophysical Research: Solid Earth 103(B12), 30205-30229.

Wahr, J. and Zhong, S., 2012. Computations of the viscoelastic response of a 3-D compressible Earth to surface loading: an application to Glacial Isostatic Adjustment in Antarctica and Canada. Geophysical Journal International 192(2), 557-572.

Wang, C., Dong, S., Evan, A.T., Foltz, G.R. and Lee, S.K., 2012. Multidecadal covariability of North Atlantic Sea Surface Temperature, African dust, Sahel rainfall, and Atlantic hurricanes. Journal of Climate 25(15), 5404-5415.

Ward, M.N., Lamb, P.J., Portis, D.H., El Hamly, M. and Sebbari, R., 1999. Climate variability in Northern Africa: understanding droughts in the Sahel and the Maghreb. Beyond el Niño, Springer, Berlin, Heidelberg, 119-140.

Watkins, M. M., Wiese, D. N., Yuan, D. N., Boening, C., & Landerer, F. W., 2015. Improved methods for observing Earth's time variable mass distribution with GRACE using spherical cap mascons. Journal of Geophysical Research: Solid Earth 120(4), 2648-2671.

Watson, A.J., Schuster, U., Bakker, D.C., Bates, N.R., Corbière, A., González-Dávila, M., Friedrich, T., Hauck, J., Heinze, C., Johannessen, T. and Körtzinger, A., 2009. Tracking the variable North Atlantic sink for atmospheric CO_2. Science 326(5958), 1391-1393.

Watts, D. R., & Kontoyiannis, H., 1990. Deep-ocean bottom pressure measurement: drift removal and performance. Journal of Atmospheric and Oceanic Technology 7(2), 296-306.

Waugh, D.W., Hall, T.M., McNeil, B.I., Key, R. and Matear, R.J., 2006. Anthropogenic CO_2 in the oceans estimated using transit time distributions. Tellus B: Chemical and Physical Meteorology 58(5), 376-389.

Weise, A., Kroner, C., Abe, M., Ihde, J., Jentzsch, G., Naujoks, M., & Wziontek, H., 2009. Gravity field variations from superconducting gravimeters for GRACE validation. Journal of Geodynamics 48(3), 325-330.

Wunsch, C., & Roemmich, D., 1985. Is the North Atlantic in Sverdrup balance?. Journal of Physical Oceanography, 15(12), 1876-1880.

Wunsch, C., 1998. The work done by the wind on the oceanic general circulation. Journal of Physical Oceanography 28(11), 2332-2340.

Wunsch, C., & Heimbach, P., 2013. Dynamically and kinematically consistent global ocean circulation and ice state estimates. International Geophysics 103, 553-579.

Yashayaev, I., & Loder, J. W., 2009. Enhanced production of Labrador Sea Water in 2008. Geophysical Research Letters 36(1).

Yeager, S., Karspeck, A., Danabasoglu, G., Tribbia, J., & Teng, H., 2012. A decadal prediction case study: late twentieth-century North Atlantic Ocean heat content. Journal of Climate 25(15), 5173-5189.

Yeager, S.G. and Robson, J.I., 2017. Recent progress in understanding and predicting Atlantic decadal climate variability. Current Climate Change Reports 3(2), 112-127.

Zhao, J., & Johns, W., 2014. Wind-forced interannual variability of the Atlantic Meridional Overturning Circulation at 26.5°N. Journal of Geophysical Research: Oceans 119(4), 2403-2419.